Advanced X-ray characterization for the development of low consumption power transistors

Victor Yon

THÈSE

Pour obtenir le grade de

DOCTEUR DE L'UNIVERSITE GRENOBLE ALPES

Spécialité : PHYSIQUE DES MATERIAUX

Arrêté ministériel : 25 mai 2016

Présentée par

Victor YON

Thèse dirigée par **Patrice GERGAUD**, ingénieur HDR, Université Grenoble Alpes – CEA-Leti, encadrée par **Emmanuel NOLOT**, ingénieur docteur, Université Grenoble Alpes – CEA-Leti et par **Matthew CHARLES**, ingénieur docteur, Université Grenoble Alpes – CEA-Leti

préparée au sein du **CEA – Leti**
dans **l'École Doctorale de Physique de Grenoble**

Caractérisation avancée par rayons X pour le développement de transistors de puissance basse consommation

Advanced X-ray characterization for the development of low consumption power transistors

Thèse soutenue publiquement le **19 février 2021**,
devant le jury composé de :

M. Olivier DURAND
Professeur, INSA Rennes, Rapporteur

M. Alexandre BOULLE
Directeur de recherche, Institut de recherche sur les céramiques, Rapporteur

Mme. Maud NEMOZ
Ingénieur de recherche, CRHEA-CNRS, Examinatrice

Mme. Magali MORALES
Maître de conférences, Université de Caen Normandie, Examinatrice

M. Hubert RENEVIER
Professeur, Université Grenoble-Alpes - Grenoble INP, Président du jury

Acknowledgments

I would like to warmly thank the many people at CEA-Leti laboratory that helped me to bring this PhD work to fruition.

My thesis director Patrice Gergaud and thesis supervisors Matthew Charles and Emmanuel Nolot gave me their attentive and enthusiastic support during these three years. I am grateful for their many advices and true kindness.

I had the chance to benefit from the active assistance of my managers Cécile Moulin, Lucille Roulet, Céline Lapeyre, Laurent Vandroux, Bernard André and Nicolas Lhermet, from my arrival until my last year during the 2020 pandemic.

Many of my collegues at the CEA-Leti cleanroom facility and Nano-characterization platform participated in my works. I would especially like to thank Jérôme Richy, Yann Mazel, Simona Torrengo, Névine Rochat, Denis Rouchon, Amal Sediri as well as my work-neighbors Myriam Le Guen, Laura Sauze, Tom Vethaak, Lucie Prazakova, Walter Batista Pessoa, Vincent Huynh, Sylvie Favier and Yann Meier for their permanent good humour. This work also greatly benefited from fruitful discussions with Joël Eymery, Pierre Ferret and Guy Feuillet.

I also cordially thank all the members my thesis committee, Olivier Durand, Alexandre Boulle, Maud Nemoz, Magali Morales and Hubert Renevier, for assessing this work and for their constructive comments and remarks.

Finally, a warm thank you to my partner Clara Garnier, my parents Jean-Jacques and Pilar Yon, my sister Alexia Yon, my brother-in-law Laurent Bertholle and the rest of my family for their love, their support, their time (even for checking my calculations) and much more.

Table of contents

List of figures

List of tables

List of abbreviations

2DEG: Two-dimensional gas of free electrons

3D: Three-dimensional

III-N: Semiconductors composed of atoms of nitrogen and of group-III elements

AFM: Atomic force microscopy

CL: Cathodoluminescence

FWHM: Full width at half maximum

GaN-on-Si: Gallium nitride layer grown on silicon substrate

HEMT: High electron mobility transistors

HRXRD: High resolution X-ray diffraction

HVPE: Hydride Vapor Phase Epitaxy

LED: Light emitting diode

MBE: Molecular Beam Epitaxy

MOCVD: Metalorganic Chemical Vapor Deposition

MOVPE: Metalorganic Vapor Phase Epitaxy

RHEED: Reflection high energy electron diffraction

RMS: Root mean square

RSM: Reciprocal space map

TEM: Transmission electron microscopy

TD: Threading dislocation

UC: Unit cell

UV: Ultra-violet

XRD: X-ray diffraction

General Introduction

Nitride semiconductors of the III-N group are renowned materials for the production of optoelectronics and power electronics components. In particular, they are increasingly employed to fabricate high power and high frequency transistors with excellent energy efficiency, owing to their adapted physical properties such as high electron mobility, breakdown field and thermal conductivity.

These devices are made of III-N thin film structures, whose base typically consists of a µm-thick layer of gallium nitride (GaN). In the past decades, growth of GaN crystals has mainly been performed on foreign substrates of sapphire or silicon carbide (SiC), which allow for a good compromise between costs and material quality. More recently, CEA-Leti has chosen to develop the fabrication of III-N materials and components on 200 mm diameter wafers of (111)-oriented silicon, for power electronics applications. This substrate material renders the manufacturing of III-N components compatible with the standards of microelectronics industry, while dramatically decreasing production costs. The downside is the low coefficient of thermal expansion of Si(111), responsible for the incorporation of tensile stress in III-N materials, which might lead to film cracking. This issue is fixed by growing a complex stack of intermediate III-N buffer layers between GaN and the substrate.

This specific stack results in the generation of a gradient of in-plane stress within GaN and buffer layers underneath. This evolution of stress throughout the thickness of III-N films affects the curvature of wafers, and even their propensity to crack. In addition, GaN and buffer layers possess a high concentration of crystal defects, consisting in threading dislocations (TDs) extending throughout films thicknesses. Dislocations stem from the high mismatch between lattice parameters of Si(111) substrate and III-N crystals. Their density is a critical parameter for the quality of produced devices.

Hence, dislocations and gradients of stress are two defects of prime interest when studying GaN layers on silicon substrates (GaN-on-Si). In order to support the development of this material, it is essential to have access to quick characterizations of both defects, readily usable in the LETI cleanroom facility, where the batch of wafers are processed. To this end, X-ray diffraction (XRD) is an acknowledged technique for the study of monocrystalline thin films, allowing for non-destructive characterizations. However, the existing XRD analyses of the defects of interest are either imprecise, non-adapted to GaN-on-Si layers or non-achievable with equipment available in the LETI cleanroom.

This PhD work aims at developing XRD characterizations adapted to our needs. We chose to focus on analyzing the GaN layer, which is the cornerstone of III-N power electronics components. Nevertheless, the methods were developed with a concern for their future extension to the analysis of buffer layers. We present our studies throughout five chapters.

The first chapter consists in a description of the physical properties of III-N materials, in particular of GaN, including crystallographic, mechanical, polarization and electronic properties. The benefits and limits of these characteristics for the main applications of nitride

semiconductors are discussed, especially for the production of high electron mobility transistors (HEMTs). We then provide a discussion about the impact of the choice of substrate on the properties of GaN films and detail the buffer layer structure used at CEA-Leti for GaN-on-Si samples. The methods of epitaxial growth of III-N crystals are briefly explained. Finally, the main defects affecting GaN-on-Si layers are reviewed, with focuses on TDs, including a large theoretical background, and stress gradients.

The second chapter provides basic knowledge about XRD, required for characterization of III-N layers. Interactions between X-rays and matter are detailed, and the reader is introduced to the theory of diffraction through descriptions of physical phenomena, reciprocal space representation and the kinematical model, including the case of a distorted crystal. A justification is given of the validity of kinematical model versus dynamical model of diffraction for the analysis of III-N epitaxial layers. We then introduce high-resolution X-ray diffraction (HRXRD) measurements and associated experimental setups, including details of the diffractometers used during this PhD. The last section of the chapter is dedicated to elemental analyses of the diffraction signal, especially in the framework of nitride semiconductor characterization.

In the third chapter, we examine analyses of stress gradients that we carried out in GaN layers. Firstly, we show different basic estimates of stress/strain profiles, obtained from Raman, in-situ sample curvature during growth and XRD measurements. We discuss the existing XRD methods to analyze stress gradients and their limits in the case of our samples and diffractometers. We propose to answer these issues by developing a program of simulation of XRD profiles stemming from our materials. This numerical tool relies on the modelling of unit cells (UCs) displacement throughout the GaN layer. The corresponding XRD radial $2\theta - \omega$ scans are simulated for several symmetric reflections, by means of the kinematical theory of diffraction. We analyze the evolution of simulated diffraction profiles when integrating effects of instrumental resolution, of X-ray correlation length, or modifying the shape of the input strain profile. We find that a key parameter to obtain realistic diffraction signals is the local variation of displacement profiles. Hence, we propose a simple model to simulate local displacement fields, which are assumed to be affected by the surrounding distribution of TDs.

Threading dislocations are the subject of the fourth chapter. These defects have been extensively studied in the XRD literature. However, analyses of TD densities either rely on complex simulation procedures, which might in addition require high quality XRD measurements, or on lattice misorientation measurements, which translate into TD density through simple but imprecise models. In this work, we explore an alternative analysis, based on the measurement of the micro-strain field surrounding TDs. Despite allowing for a simple estimate of TD density, this method has only been reported a few times for GaN studies, to analyze specimens grown on sapphire substrates and without taking into account the particular mechanical properties of GaN crystals. Hence, we properly adapt the model of conversion of micro-strain measurements into TD density to the low Poisson ratio of GaN layers. In the case of GaN-on-Si samples, our characterizations are complicated by the alteration of micro-strain measurements due to the presence of a strong stress gradient. We highlight the impact of this stress profile and demonstrate how to bypass it. The accuracy of TD density micro-strain measurements is assessed by a comparison with cathodoluminescence (CL), transmission

electron microscopy (TEM) and XRD lattice misorientation measurements on GaN-on-Si samples, on a freestanding GaN substrate and on GaN films grown on sapphire and SiC substrates. The impact of the reduction of TD density throughout the thickness of GaN, which is different on XRD measurements than on CL and TEM counterparts, is discussed.

The in-depth evolution of TD density and stress is complex to analyze with XRD characterization. To better understand the limitations of our analyses and improve them, we performed measurements on progressively etched layers of GaN, as reported in the last chapter. The profile of strain/stress is successively calculated from curvature, Raman and XRD measurements. XRD results are then input into the program developed in the third chapter, in order to achieve the best fit of measured data. The evolution of TD density is also estimated with XRD measurements of lattice misorientation and micro-strain. We discuss the good agreement between both measurements close to the sample surface and their divergence at a deeper position in GaN. A comparison with surface CL measurements is also performed. Finally, the correlation between profiles of strain and of TD density is studied, allowing us to analyze the mechanism of relaxation of compressive stresses within GaN.

1. Properties and growth of III-N materials

III-N crystals are semiconductor materials, forming part of the III-V alloys category, like a number of other usual semiconductors such as GaAs, GaP or InP. Hence, their crystal lattice is formed by equal parts of group-V atoms (nitrogen atoms in this case) and group-III atoms (usually gallium, aluminum and indium). The III-N family is therefore composed by the binary alloys GaN, AlN, InN, the ternary alloys $Al_xGa_{(1-x)}N$, $In_xGa_{(1-x)}N$ and $In_xAl_{(1-x)}N$ and quaternary alloys $In_xGa_yAl_{(1-x-y)}N$).

This chapter gives an overview of III-N materials physical properties, including their crystalline structure (focusing on the most common wurtzite structure), mechanical behavior, polarization and key properties for the fabrication of electronic devices. Some useful basic knowledge on crystallography and mechanics is provided. The main applications of III-N semiconductors are detailed, especially in the field of power electronics. The fabrication of these materials by epitaxy is briefly explained and the choice of the substrate is discussed, thus introducing GaN-on-Si materials, on which this work focuses. Finally, the main crystal defects affecting GaN-on-Si layers, such as threading dislocations and in-plane stress gradients are reviewed.

1.1. Physical properties and applications of III-N materials

1.1.1. Crystallographic description

a) Crystalline structure

III-N materials can adopt three different crystal structures, namely rocksalt, zincblende and wurtzite structures. Among these, wurtzite is the thermodynamically stable phase at ambient conditions. Conversely, the growth of rock rocksalt structure can only be achieved under very high pressures: 12.1 GPa for InN, 22.9 GPa for AlN and 52.2 GPa for GaN.[1] These conditions are incompatible with an epitaxial growth,[2] so this structure is not suited for industrial applications. III-N zincblende crystals are also metastable under ambient conditions. Their stabilization requires a heteroepitaxial growth on cubic substrates of SiC, Si, MgO or GaAs.[1]

Wurtzite phase is usually preferred to rock-salt and zincblende, as its growth is simpler. The research presented in this thesis focus on III-N layers, mostly of GaN, with this crystal structure. Wurtzite has a hexagonal lattice system, with a unit cell composed of two pairs of atoms (two atoms of group-III and two N atoms for III-N materials). The unit cell of III-N crystal with wurtzite structure can be defined in several equivalent ways. In the following, we will use the definition depicted in **Figure 1.1 b)**. The cell is defined by a base of three vectors: two vectors $\vec{a}$ and $\vec{b}$ of length a, separated by an angle of 120°, and an orthogonal vector $\vec{c}$ of

length c. Group-III atoms are placed at coordinates (0,0,0) and $(\frac{2}{3},\frac{1}{3},\frac{1}{2})$, while N atoms are placed at $\left(0,0,\frac{3}{8}\right)$ and $(\frac{2}{3},\frac{1}{3},\frac{7}{8})$.

The structure can be seen as two interpenetrating hexagonal close packed sublattices, of group-III cations and anions N respectively, shifted from each other along the c-axis by a parameter u (see **Figure 1.1 a)**). Each atom is placed at the center of a tetrahedron composed of atoms of the other group. In an ideal wurtzite crystal, the ratio between lattice parameters c/a is equal to $\sqrt{8/3} = 1.633$ and the length of a cation-anion bond is $u = 3/8c$.[1] The real values of c/a and u depart from these ideal ratios, in particular because they are linked to the difference of electronegativity between the atoms forming the crystal.[3]

A wide set of lattice parameters, with no consistent reference value,[4] can be found in the literature. Indeed, these parameters depend on the concentration in the crystal of free electrons, foreign atoms and defects, on the residual strain in the lattice and on the temperature.[4],[1] Extensive reviews of lattice parameters measurements can be found in[4],[1], and show variations at the fourth significant digit between the different estimates of a and c, while the c/a ratio is more consistent. **Table 1.1** gives the values used in this thesis for the for the three III-N wurtzite binary alloys.

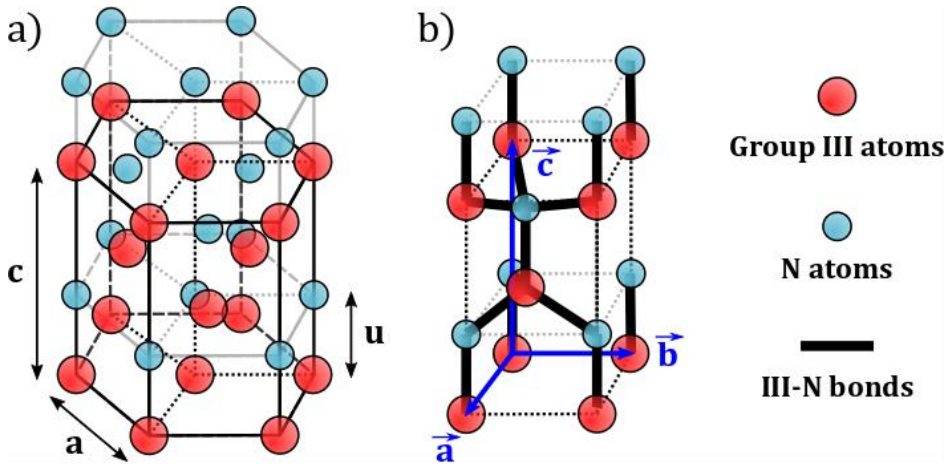

Figure 1.1 : Wurtzite structure. a) Illustration of the two interpenetrating hexagonal sublattices of group-III atoms (black lines) and N atoms (grey lines), the lattice parameters a and c and the cation-anion length u. b) Unit cell of a III-N wurtzite crystal (black dotted lines) and its basis vectors $(\vec{a},\vec{b},\vec{c})$

Crystal	a (Å)	c (Å)	c/a
GaN	3.1896	5.1855	1.6258
AlN	3.1106	4.9795	1.6008
InN	3.5378	3.7033	1.6121

Table 1.1 : Lattice parameters of III-N wurtzite binary alloys. Parameters are taken from measurements on a GaN substrate,[5] a bulk AlN[6] and an InN powder,[7] due to the difficulty of growing monocrystalline thin films with the latter material.

b) Miller-Bravais notation

In the field of crystallography, three-index Miller notation is widely used to describe crystallographic directions and crystal planes. This notation relies on the coordinate system defined by the three vectors $\vec{a}, \vec{b}, \vec{c}$ forming the lattice unit cell. The direction of a line passing through the origin of the lattice and a point of coordinates U, V, W is indexed as $[UVW]$. Note that UVW indices are taken as the combination of smaller integer possible. Furthermore, the negative indices are usually noted with a bar over the number. For example, the direction of a line passing through the coordinates $(0,0,0)$; $\left(\frac{-1}{3}, 1, \frac{2}{3}\right)$; $(-1,3,2)$; $(-2,6,4)$ is indexed as $[\bar{1}32]$. Some directions are related by symmetry, in such a way that each of them can be indexed by a family of $[UVW]$ triplets, depending on which orientation is chosen for the $\vec{a}, \vec{b}, \vec{c}$ base when defining the unit cell. An example of this is the equivalent directions of a cubic unit cell diagonals: $[111]$, $[\bar{1}11]$, $[1\bar{1}1]$ and $[\bar{1}\bar{1}1]$. Such a family of directions is called directions of a form and is denoted with angle brackets $\langle 111 \rangle$. Crystal planes are indexed by a similar triplet (HKL), distinguished by the use of parentheses. HKL indices are linked to the intercepts xyz of the plane and the unit cell vectors in the following way: $x = ||\vec{a}||/H$; $y = ||\vec{b}||/K$; $z = ||\vec{c}||/L$, with the index being equal to zero when the plane does not intercept a vector. Hence, by using the three-index Miller notation, a direction $[UVW]$ is normal to a plane (HKL) when $U = H$; $V = K$ and $W = L$. As for families of directions, families of crystal planes can be defined and are denoted by braces $\{HKL\}$.

In the case of III-N crystals and other hexagonal systems, three equivalent crystallographic directions are separated by 120° rotations about the c-axis. Due to this particular symmetry, the directions of a form and the families of planes are not intuitively distinguishable by using the Miller indexation (see **Figure 1.2 a)**). Hence, an alternative four-index $[uvtw]/(hkil)$ Miller-Bravais notation, initially proposed by *Weber*,[8] is used. It relies on a base of four vectors $\overrightarrow{a_1}, \overrightarrow{a_2}, \overrightarrow{a_3}, \vec{c} = \vec{a}, \vec{b}, (-\vec{a} - \vec{b}), \vec{c}$, which define the unit cell as shown in **Figure 1.2 b)**. With the Miller-Bravais notation, we have $\overrightarrow{a_3} = -(\overrightarrow{a_1} + \overrightarrow{a_2})$, $t = -(u + v)$ and $i = -(h + k)$, so the families of directions and planes are identified by permutations of the values of the indices uvw and hkl. The relationships between Miller triplets and Miller-Bravais quadruplets are given by:[9],[10]

$$\begin{cases} [uvtw] = [(2U - V)\ (-U + 2V)\ (-U - V)\ 3W] \\ [UVW] = [(u - t)\ (v - t)\ w] \end{cases} \quad (1.1)$$

$$\begin{cases} (hkil) = (H\ K\ (-H - K)\ L) \\ (HKL) = (hkl) \end{cases} \quad (1.2)$$

An additional benefit of using the Miller-Bravais notation for hexagonal systems is a more intuitive representation of the reciprocal lattice. Indeed, the four reciprocal lattice basis vectors $\vec{a_1^*}, \vec{a_2^*}, \vec{a_3^*}, \vec{c^*}$ are oriented in the same direction as the basis vectors $\vec{a_1}, \vec{a_2}, \vec{a_3}, \vec{c}$ of the direct lattice. This is not true with the 3-index Miller notation, for which the basis vectors $\vec{a^*}, \vec{b^*}$ are separated by a 60° angle. The relation between the reciprocal lattices basis vectors of both systems of indexation is given by:

$$\begin{cases} \vec{a_1^*}, \vec{a_2^*}, \vec{a_3^*}, \vec{c^*} = \dfrac{2\vec{a^*} - \vec{b^*}}{3}, \dfrac{-\vec{a^*} + 2\vec{b^*}}{3}, \dfrac{-\vec{a^*} - \vec{b^*}}{3}, \vec{c^*} \\ \vec{a^*}, \vec{b^*}, \vec{c^*} = \left(2\vec{a_1^*} + \vec{a_2^*}\right), \left(\vec{a_1^*} + 2\vec{a_2^*}\right), \vec{c^*} \end{cases} \quad (1.3)$$

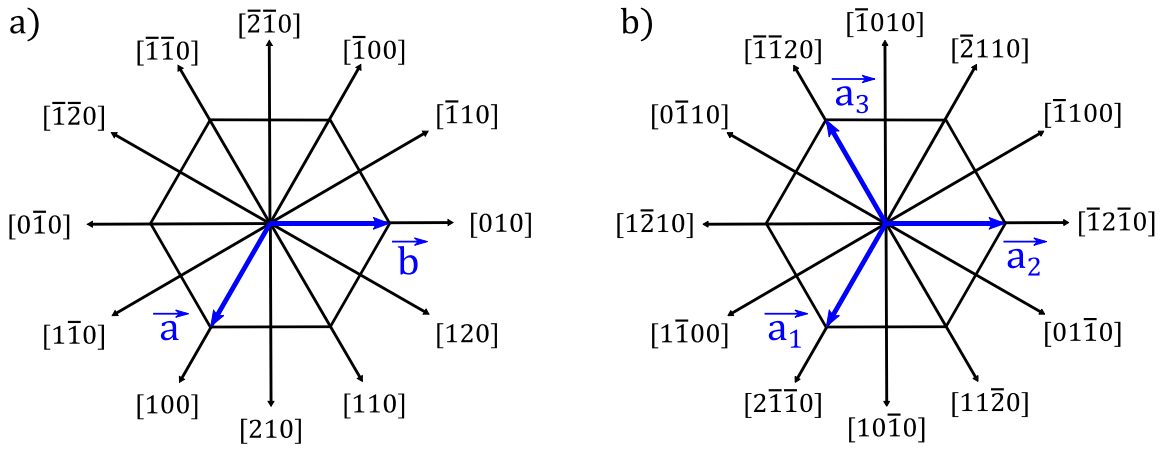

Figure 1.2 : Crystallographic directions in a basal plane of a hexagonal crystal. a) Miller notation [UVW], based on the basis vectors $\vec{a}, \vec{b}, \vec{c}$. b) Miller-Bravais notation [uvtw], based on the basis vectors $\vec{a_1}, \vec{a_2}, \vec{a_3}, \vec{c}$. For both figures, the vector $\vec{c}$ is normal to the sheet plane.

1.1.2. Mechanical properties

According to the theory of linear elasticity, the relation between fields of elastic strain and stress in a material is given by the general Hooke's law:

$$\sigma_{ij} = \sum_{k,l} C_{ijkl}\, \varepsilon_{kl} \tag{1.4}$$

C_{ijkl} are the elastic stiffness constants of the material, usually given in GPa. These constants linearly relate the stress components σ_{ij} to the strain components ε_{kl}, each of them being identified by the pairs of subscripts ij and kl. Each index has three possible values (1,2,3), corresponding to the three axes of the chosen coordinate system. i/k denotes the direction along which the stress/strain component applies and j/l indicates the normal of the surface which undergo the stress or the direction of the force inducing the strain. Hence, $\sigma_{ij}/\varepsilon_{kl}$ correspond to a normal tensile ($\sigma_{ij} > 0/\varepsilon_{kl} > 0$) or compressive ($\sigma_{ij} < 0/\varepsilon_{kl} < 0$) stress/strain if $i = j\ /\ k = l$ and to a shear stress/strain if $i \neq j\ /\ k \neq l$. Alternatively, the usual notations of the coordinate system axes can be used to write these indices: $(1,2,3) = (x, y, z)$ for a Cartesian coordinate system, $(1,2,3) = (r, \theta, z)$ for a cylindrical coordinate system or $(1,2,3) = (r, \theta, \phi)$ for a spherical coordinate system.

Equation (1.4) can be rewritten with a tensor notation $[\sigma] = [C][\varepsilon]$, where the stiffness tensor $[C]$ gathers the 81 constants C_{ijkl}. By considering the symmetry of the stress and strain tensors $[\sigma]$ and $[\varepsilon]$ and the interchangeable nature of ij and kl pairs of indices, the number of different constants C_{ijkl} can be reduced to 21. The writing of equation (1.4) is usually simplified by using Voigt convention,[11] which consists in a change of notation of the four ij and kl subscripts by two mn indices in the following way: $11 \rightarrow 1$, $22 \rightarrow 2$, $33 \rightarrow 3$, $23 = 32 \rightarrow 4$, $13 = 31 \rightarrow 5$ and $12 = 21 \rightarrow 6$. In hexagonal crystals like III-N wurtzite, the number of independent elastic coefficients is further reduced by the lattice symmetries. In Cartesian coordinates and using Voigt notation, equation (1.4) becomes:

$$\begin{bmatrix} \sigma_{xx} \\ \sigma_{yy} \\ \sigma_{zz} \\ \sigma_{xy} \\ \sigma_{yz} \\ \sigma_{zx} \end{bmatrix} = \begin{bmatrix} C_{11} & C_{12} & C_{13} & 0 & 0 & 0 \\ C_{12} & C_{11} & C_{13} & 0 & 0 & 0 \\ C_{13} & C_{13} & C_{33} & 0 & 0 & 0 \\ 0 & 0 & 0 & C_{44} & 0 & 0 \\ 0 & 0 & 0 & 0 & C_{44} & 0 \\ 0 & 0 & 0 & 0 & 0 & C_{66} \end{bmatrix} \begin{bmatrix} \varepsilon_{xx} \\ \varepsilon_{yy} \\ \varepsilon_{zz} \\ \varepsilon_{xy} \\ \varepsilon_{yz} \\ \varepsilon_{zx} \end{bmatrix} \tag{1.5}$$

where $C_{66} = (C_{11} - C_{12})/2$

In a similar way, we define a set of elastic compliance coefficients S_{mn}:

$$\begin{bmatrix} \varepsilon_{xx} \\ \varepsilon_{yy} \\ \varepsilon_{zz} \\ \varepsilon_{xy} \\ \varepsilon_{yz} \\ \varepsilon_{zx} \end{bmatrix} = \begin{bmatrix} S_{11} & S_{12} & S_{13} & 0 & 0 & 0 \\ S_{12} & S_{11} & S_{13} & 0 & 0 & 0 \\ S_{13} & S_{13} & S_{33} & 0 & 0 & 0 \\ 0 & 0 & 0 & S_{44} & 0 & 0 \\ 0 & 0 & 0 & 0 & S_{44} & 0 \\ 0 & 0 & 0 & 0 & 0 & S_{66} \end{bmatrix} \begin{bmatrix} \sigma_{xx} \\ \sigma_{yy} \\ \sigma_{zz} \\ \sigma_{xy} \\ \sigma_{yz} \\ \sigma_{zx} \end{bmatrix} \tag{1.6}$$

where $S_{66} = (S_{11} - S_{12})/2$

Hence, the mechanical properties of wurtzite III-N materials are fully defined either by their elastic stiffness coefficients C_{11}, C_{12}, C_{13}, C_{33}, C_{44} and C_{66} or their elastic compliance

coefficients S_{11}, S_{12}, S_{13}, S_{33}, S_{44} and S_{66}. **Table 1.2** gives the values of these coefficients for GaN, AlN and InN.

Stiffness constants (Gpa)	GaN	AlN	InN	Compliance constants (Tpa^{-1})	GaN	AlN	InN
C_{11}	396	345	271	S_{11}	3.01	3.53	5.03
C_{12}	144	125	124	S_{12}	-0.962	-1.01	-1.77
C_{13}	100	120	94	S_{13}	-0.522	-0.765	-1.53
C_{33}	392	395	200	S_{33}	2.82	3.00	6.44
C_{44}	91	118	46	S_{44}	11.0	8.47	21.7
C_{66}	126	110	74	S_{66}	7.94	9.09	13.5

Table 1.2 : Elastic stiffness and compliance constants of III-N wurtzite materials. Values are taken from[12] for GaN and InN and from[13] for AlN.

Nevertheless, it is also interesting to define an additional elastic constant of III-N materials, namely the Poisson ratio ν. This constant is defined for the case of a uniaxial stress and corresponds to a ratio between the strain in the unstressed plane and the strain along the stressed direction. In anisotropic materials like III-N crystals, three Poisson ratios can be defined, along each of the three axis orthogonal axes of the Cartesian system. However, measurements and calculations of Poisson ratio are usually limited to the [0001] direction, as this parameter $\nu_{[0001]}$ is the relevant one in the case of [0001]-grown films, for example to relate lattice parameters in the (0001) plane and along the c-axis in the case of stressed layers.[4] $\nu_{[0001]}$ is linked to C_{mn} and S_{mn} parameters by the relationships:[14],[15]

$$\nu_{[0001]} = \frac{C_{13}}{C_{11} + C_{12}} = \frac{-(S_{12} + S_{13})}{2S_{11}} \tag{1.7}$$

Table 1.3 gives the reference values[4] for Poisson ratio of III-N binary alloys. Note that the GaN Poisson ratio is impacted by the density of edge type threading dislocations (see section 1.3.1), which tend to reduce the in-plane strain resulting from biaxial in-plane stresses.[16] This can result in significant differences between a near perfect GaN crystal ($\nu_{[0001]} = 0.212$)[17] and a MOVPE-grown GaN (see section 1.2.1) with a medium density of threading dislocations of $5 \times 10^8\ cm^{-2}$ ($\nu_{[0001]} = 0.183$).[16]

Crystal	$\nu_{[0001]}$
GaN (Low dislocation density)	0.212
GaN (Medium dislocation density)	0.183
AlN	0.203
InN	0.272

Table 1.3 : C-axis Poisson ratios of III-N wurtzite materials. Values are taken from[17] for low dislocation density GaN or calculated from elastic stiffness constants by means of equation (1.7), from[16] for high dislocation density GaN and from[18] for AlN and InN.

We should note that the Poisson ratio is quasi-isotropic in GaN crystals,[14],[16] thus allowing the use of the corresponding values of **Table 1.3** independently of the stressed axis. This is not true in the case of AlN and InN crystals, which have a significant anisotropic behavior.[14]

1.1.3. Polarity and polarization

From **Figure 1.1**, we observe that the wurtzite structure of III-N crystals is not symmetric about the basal plane (0001). Hence, in a III-N crystal, the two interfaces normal to the c-axis are distinguished by their polarity, which corresponds to the nature of the terminal atoms. In the $[000\bar{1}]$ direction, the face is referred to as N-polar, while in the [0001] direction it is named Ga-polar face, regardless of which type of group-III atom is present.[2] III-N layers grown along the c-axis can either have a Ga polarity or an N polarity at their top surface, depending on the conditions adopted for the epitaxy process.

Additionally, the high difference of electronegativity between group-III cations and anions N (i.e. values on the Pauling scale of 1.61 for Al, 1.81 for Ga and 1.78 for In versus 3.04 for N),[19] induces dipole moments, oriented from anions toward cations. As discussed before, III-N crystal structures deviate from the ideal wurtzite structure, causing a slight deformation of the tetrahedra of anions and cations. In the resulting non-regular tetrahedra, the barycenters of positive and negative charges do not coincide, thus generating a global dipole moment. The sum of all dipole moments along the c-axis leads to a macroscopic spontaneous polarization of III-N crystals, oriented toward the N-polar face. The values of this spontaneous polarization are $-0.090\ C/m^2$ for AlN, $-0.034\ C/m^2$ for GaN and $-0.042\ C/m^2$ for InN,[2] where the negative sign corresponds to an orientation of the polarization vector opposed to the growth direction [0001] of the Ga-polar layer.

In addition to the spontaneous polarization, a piezoelectric polarization arises from the strain state in the material, which further modifies the equilibrium of charges within the tetrahedra composing the crystal, as these tetrahedra are deformed. In the case of III-N heterostructures, this strain often arises from the growth of layers with different lattice constants in the plane, such as GaN and AlGaN. The epitaxy process imposes the in-plane lattice parameter of the substrate on the grown layers, thus inducing a strain which can be either tensile or compressive. Such a strain is associated with an isotropic biaxial stress state

(i.e. applied with equal values along two orthogonal directions of the surface plane). With this assumption, the value of the piezoelectric polarization P_{PE} along the c-axis is:[20]

$$P_{PE} = 2\frac{a - a_0}{a_0}\left(e_{31} - \frac{C_{13}}{C_{33}}\, e_{33}\right) \tag{1.8}$$

where a and a_0 are the lattice parameters of the strained crystal and the unstrained crystal, associated to the in-plane strain ($\varepsilon_x = \varepsilon_y = (a - a_0)/a_0$). C_{13} and C_{33} are the elastic stiffness constants while e_{31} and e_{33} are the piezoelectric coefficients of the material, given in **Table 1.4**.

Crystal	e_{31}	e_{33}
GaN	-0.34	0.67
AlN	-0.53	1.5
InN	-0.41	0.81

Table 1.4 : Piezoelectric coefficients of III-N wurtzite materials. Values are taken from reference[2].

Spontaneous and piezoelectric polarizations add together to give the overall polarization of a III-N film. For a layer grown with Ga surface polarity, both polarizations have a negative sign and are therefore oriented in the same direction if the strain is tensile. In the case a compressive strain, spontaneous and piezoelectric polarizations have an opposite sign, thus limiting the total polarization of the layer. These polarizations have important consequences for the electronic properties of the materials, as described below.

1.1.4. Large Bandgap and properties for electronic applications

The suitability of a semiconductor material for electronic device conception is based on various physical properties, depending on the targeted application. A number of them are compiled in **Table 1.5** for III-N materials and other well-known semiconductors. The first of these characteristics is the band structure of the material. As shown in **Figure 1.3**, III-N wurtzite alloys cover a large range of bandgap values, from 0.7 eV for InN to 6.2 eV for AlN. Despite the small band gap of InN, the III-N materials are usually classified as large gap semiconductors, in contrast to small gap Si (1.1 eV) or GaAs (1.4 eV) semiconductors. Furthermore, III-N crystals are direct bandgap semiconductors, which implies that a transition of carriers between the conduction and valence band happens without any change in their wavenumber, thus enabling radiative recombination of electrons and holes. This property is essential for optoelectronic applications, such as the generation of light with light emitting diodes.

Physical properties	GaN	AlN	InN	Si	4H-SiC	GaAs	Diamond
Bandgap (eV)	3.4	6.2	0.8	1.1	3.2	1.4	5.6
Gap Nature (Direct – Indirect)	D	D	D	I	I	D	I
Breakdown field ($MV\ cm^{-1}$)	3.3	8.4	1.2	0.3	3.5	0.4	5.0
Electron mobility ($cm^2\ V^{-1}s^{-1}$)	990	135	3000	1350	650	8500	1900
Saturation velocity ($10^7 cm\ s^{-1}$)	2.5	2.2	1.8	1.0	2.0	2.0	2.7
Thermal conductivity ($W\ cm^{-1}K^{-1}$)	2.3	2.85	0.45	1.6	3.30	0.54	20-25

Table 1.5 : Physical properties of various semiconductors at 300 K. Values are taken from reviews from[21],[22],[23],[24].

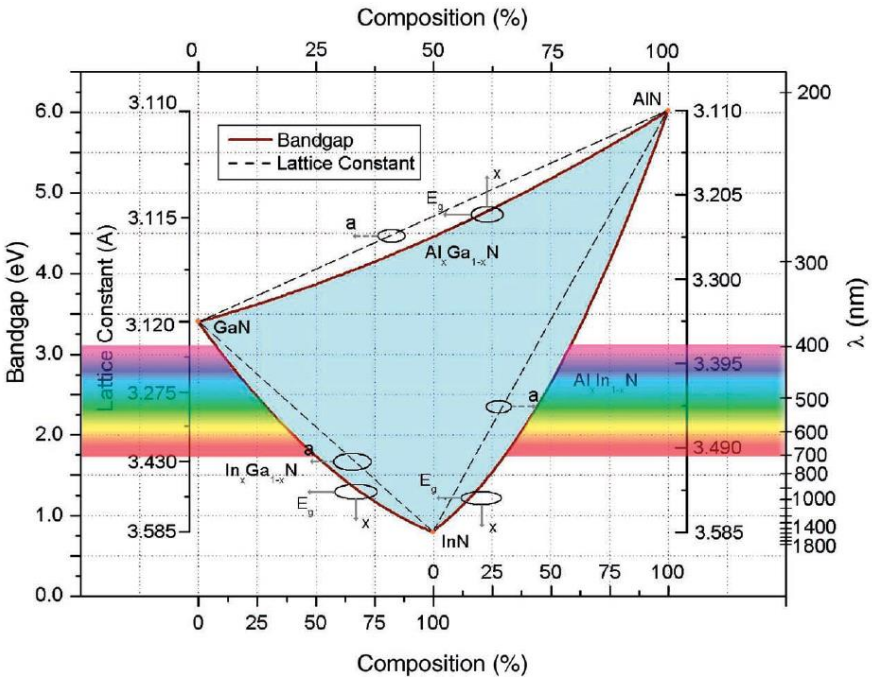

Figure 1.3 : Bandgap of ternary III-N alloys. The bandgap is plotted versus the lattice constant a and the composition and the percentages of Al and In for ternary alloys. The figure is reproduced from[2].

The bandgap value affects several other properties of the semiconductor, such as the breakdown voltage or the supported operating temperature. Both properties are essential for applications in high power electronics, as they impact the maximum operating power of the devices. Power and high frequency electronics also require good transport properties, such as high electron mobility (i.e. the displacement speed in the material of an electron accelerated by an electric field) and electron saturation velocity, which is the speed reached under very high electric field (typically 50-300 kV/cm).

1.1.5. Applications of III-N materials

a) Optoelectronics

Light emitting diodes (LEDs) have been the main driving force for the development of III-N based devices in the past thirty years. Back in the early 1990's, most of the existing LEDs were based on cubic III-V materials, such as GaAs and GaP, able to emit red and yellow-green light. The efforts made to develop the growth of good quality p-type doped GaN layers[25],[26] led to the fabrication of the first efficient blue LED.[27] This opened the way for the high scale production of white light LEDs systems which are nowadays massively used for various lighting applications, from domestic lightening to back-illumination of displays. III-N based LEDs have continued to develop, with increasing interest in devices such as direct light displays, were LCD pixels are replaced by GaN-based LEDs pixels, or efficient ultra-violet (UV) LEDs, for applications including water purification and medical treatments.[28] Additionally, blue laser diodes have been produced for applications such as optical data storage systems. Beyond the large range of bandgaps accessible with III-N materials, allowing for emissions from the near infrared to UV lights (see **Figure 1.3**), LEDs based on this family of semiconductors benefit from great conversion efficiencies, owing to high breakdown fields and carrier velocities.[21]

b) High electron mobility transistors

Following the advances in the in the field of optoelectronics, the first GaN based high electron mobility transistors (HEMTs) were developed in 1993 and 1994.[29],[30] These devices rely on the polarization properties of III-N crystals. They are made of heterojunctions of III-N layers, typically formed by a GaN channel on top of which an AlGaN barrier layer is grown, although this top-film can also be made of InAlN or InGaAlN. At the interface of these layers, the spontaneous and piezoelectric polarizations P_{SP} and P_{PE} generate a two-dimensional charge density σ defined by:[20]

$$\sigma = P^{channel} - P^{barrier} = P_{SP}^{channel} + P_{SP}^{channel} - P_{SP}^{barrier} - P_{SP}^{barrier} \qquad (1.9)$$

In the case of an AlGaN on Ga-polar GaN heterojunction, σ is positive and the interface charge is compensated by the formation, in the Ga channel, of a two-dimensional gas of free electrons (2DEG). A high concentration of electrons, typically around $1 \times 10^{13}\ cm^{-2}$,[2],[21] is found within such a 2DEG, which is about five times higher than for GaAs HEMTs.[21] Note that the formation of the 2DEG does not require any doping of the III-N heterostructure, although such an operation can be carried out to further increase the free electron density.

The physical properties of GaN, presented in **Table 1.5**, make GaN-based HEMTs excellent candidates for applications in high power and high frequency electronics. Indeed, GaN have good electron transport properties, with a saturation velocity of $2.5\ 10^7\ cm/s$[31] and a mobility within the 2DEG significantly improved compared to bulk GaN, reaching values of $2000\ cm^2\ V^{-1}s^{-1}$[32] instead of $990\ cm^2\ V^{-1}s^{-1}$.[33] Furthermore, the wide bandgap of GaN

leads to a high breakdown field of 3.3 MV/cm, which is one order of magnitude higher than the values found for Si or GaAs. Finally, GaN is able to handle the high temperatures associated to high power electronics. Its rather good thermal conductivity, which enables much more efficient evacuation of temperature than in GaAs, is associated to a tolerance of high operating temperatures. Indeed, low drain current losses have been reported on transistors operated at 300°C, limited to 30% of the currents at 25°C.[34]

Thanks to their high performances, GaN-based HEMTs are gaining an increasing part of power electronics market. Power amplifiers for future communication systems and radars are the core of high frequency applications. The need for high output powers of these systems is met by GaN components, with performances about an order of magnitude higher than GaAs based components.[35] GaN is also increasingly used for lower frequency power devices, owing to its better performances than Si and lower price than SiC, especially for devices grown on 200 mm diameter Si substrates. Main applications include fast chargers for cell phones and laptop computers, electrical converters for electric vehicles and airplanes, power supply of data centers or photovoltaic inverters for solar panels. In the following studies of this thesis, we will focus on the characterization of few-micrometers thick GaN layers forming the base structure of power electronics HEMTs.

1.2. Epitaxy of III-N materials

1.2.1. Impact of the substrate

Epitaxial growth designates the growth of a crystal, initiated on the surface of another crystal, in which the orientation of the initial crystal conditions the orientation of the expanding new crystal. This process allows for the growth of large monocrystalline layers, required for the fabrication of transistors. In the case of GaN-based devices, an initial substrate serves as a base for the epitaxial deposition of a succession of III-N layers. The choice of the substrate has a crucial impact on the quality of the III-N layers on top of it, as well as the performances and cost of the manufactured devices. As summarized in **Table 1.6**, four main materials are used as substrates for power electronics III-N stacks, namely GaN, sapphire (Al_2O_3), silicon carbide (SiC) and silicon (Si).

Properties	GaN	Sapphire	SiC	Si
Lattice mismatch (%)	0	16	3.1	-17
Thermal expansion coefficient ($10^6\ K^{-1}$)	5.6	7.5	4.4	2.6
Thermal conductivity ($W\ cm^{-1}\ K^{-1}$)	2.3	0.25	4.9	1.6
Optimized dislocation density on GaN films (cm^{-2})	10^4-10^6	Low 10^8	Low 10^8	Low 10^8
Wafer cost per area ($\$\ cm^{-2}$)	200	1	4	0.06
Maximum available wafer diameter (mm)	100	300	150	300

Table 1.6 : Benefits and limitations of different substrates used for epitaxial growth of III-N materials. The cost of wafers is a 2010 estimate, from reference[36]. Other properties are taken from reference[24].

Typically, semiconductors such as Si, GaAs, SiC or InP are grown on their corresponding native substrates, in a process designated as homoepitaxy. The use of such bulk/freestanding GaN substrates is highly desirable, as the substrate/layer lattice matching enables to obtain III-N epitaxial layers of excellent quality, with low densities of threading dislocations (see section 1.3.1) typically of the order of $10^6\ cm^{-2}$ to $10^7\ cm^{-2}$, with reported values down to $10^4\ cm^{-2}$.[24] However, GaN substrates are extremely expensive and only available in small diameters, up to 100 mm.

Historically GaN substrates were not available, so initial III-N LEDs and power devices were developed on hexagonal (0001)-oriented sapphire and SiC substrates, which corresponds to a heteroepitaxial growth. Both substrates have a lattice mismatch with GaN crystals (16% for sapphire, 3.1% for SiC), leading to the generation of high densities of threading dislocation defects at the heterointerface. A further issue induced by the use of foreign substrates is the difference of thermal expansion coefficients between the two crystals. As the epitaxy process is carried out at high temperatures (see section 1.2.1), a discrepancy in the contraction behavior of both lattices arises during the cooling step, thus generating additional stresses in the two crystals. Within the epitaxial GaN layer, the resulting in-plane stress is compressive for sapphire substrates and tensile for SiC substrates, respectively due to their higher and lower thermal expansion coefficients compared to GaN. This phenomenon leads to a bowing of wafers, which is in turn responsible for difficulties of growing additional ternary layers on large wafers, due to temperature inhomogeneities.[37] Hence, although some large sapphire wafers up to 300mm are available, the growth of devices on sapphire substrates has typically been confined to sample diameters of 150 mm or less. Overall, SiC appears as the adapted solution for better quality epitaxial layers owing to its better matching with GaN lattice, but sapphire substrates have often been preferred due to their significantly lower cost and easier availability.

More recently, III-N community focused on Si substrates to replace Sapphire and SiC, motivated by the considerably cheaper cost of this material, its availability in large diameter wafers, and its simple integration in a standard microelectronics fabrication chain. (111)-oriented Si substrates are used to match the hexagonal structure of GaN. Si has a rather large mismatch of -17% with GaN. This is similar to the sapphire/GaN mismatch, although the interatomic distance in Si (111) plane (3.84 Å) is higher than the lattice parameter a of GaN

(3.19 Å). Despite this, good quality GaN-on-Si layers can be grown with threading dislocation densities of the order of $10^8\ cm^{-2}$, which is comparable to sapphire and SiC. Following the same arguments as for active layers, substrates used to fabricate III-N HEMTS are expected to possess a high capacity of heat dissipation. This point represents an additional benefit of Si compared to sapphire, as its thermal conductivity is one order of magnitude higher. Thermal conductivity of SiC substrates is even better at $4.9\ W\ cm^{-1}\ K^{-1}$ and this has been one reason for it being as the favored substrate for RF applications. The main difficulty for GaN on silicon (GaN-on-Si) development is its low thermal expansion coefficient of $2.6 \times 10^{-6} K^{-1}$, which induces large amounts of tensile stress during cool down from growth temperatures, resulting in the apparition cracks in the GaN layer.

To avoid this cracking, a set of intermediate layers are typically grown between Si and GaN crystals, as shown in **Figure 1.4**. This stack structure is typical of the GaN-on-Si samples studied in this thesis. A few hundred nm thick AlN nucleation layer is first grown on top of the Si substrate, typically at a temperature around 1100°C to obtain a highly crystalline structure.[38] The first interest of this film is to form a barrier between the GaN and the Si, which would otherwise react chemically, leading to the formation of large defects referred to as meltback etching.[39],[40] Additionally, AlN has a smaller lattice parameter than GaN, which enables the latter layer to be grown under compressive strain, thus compensating the tensile strain brought by the cooling down of the substrate after growth. On top of the AlN, two to three AlGaN layers are grown, with a progressive decrease in Al content, to gradually adapt the lattice parameters of AlN and GaN, thus improving the quality of GaN layer. These buffer films also contribute to the compressive strain input within the top of the sample. As it will be explained in the section 1.3.2, no relaxation of this compressive stress can occur through the generation of dislocations, as the only slip planes of the wurtzite structure are parallel to the [0001] growth direction.[41] This allows for large compressive strain to be built into the layers.

Figure 1.4 : Typical structure of a GaN-on-Si epitaxial stack.

In the III-N stacks presented in **Figure 1.4**, GaN orientation is such that the GaN (0001) plane is almost parallel to Si (111) plane, and the $[11\bar{2}0]$ direction of GaN lattice is parallel to [110] direction of Si substrate.[38]

1.2.2. Growth methods

Besides the choice of the substrate, the fabrication of a GaN-on-Si template requires the use of an epitaxial growth technique, typically molecular beam epitaxy (MBE), hydride vapor phase epitaxy (HVPE) and metal organic vapor phase epitaxy (MOVPE), also designated by the generic term metalorganic chemical vapor phase deposition (MOCVD).

In MBE growth, III-N elements are heated in effusion cells so that a beam of evaporated matter is generated and directed toward the substrate, where it reacts to form the epitaxial layers. The process is carried out at relatively low temperatures (500-900 °C) and in an ultra-high vacuum environment, about $10^{-8}\ Pa$. This extremely low pressure allows to employ in-situ characterization methods, such as reflection high energy electron diffraction (RHEED), to precisely monitor the thicknesses of the epitaxial films. MBE process permits to grow homogeneous layers with sharp interfaces, but with the drawback of low growth rates of $0.1 - 2\ \mu m/h$, which are not suitable for a large volume production.

HVPE relies on the reaction between sources of group-III atoms, hydrogen chloride (HCl) and ammonia (NH_3) or 1.1-dimethylhydrazine (DMHy) on the surface of the sample heated at a temperature of 900-1100°C. The main benefit of this technique is the rapid growth of III-N layers, from $10\ \mu m/h$ up to $300\ \mu m/h$. The weaknesses of the HVPE technique are the use of corrosive HCl gas and the difficult control of the growth.

MOVPE principle is close to HVPE, although it uses organometallic gases as group-III precursors, typically trimethylgallium (TMGa) (C_3H_9Ga), trimethylaluminum (TMAl) (C_3H_9Al) and trimethylindium (TMIn) (C_3H_9In). These react with ammonia (NH_3), the N-source precursor, leading to the deposition of the epitaxial layers on the hot (700-1100 °C) surface of the sample. The main parameters of the MOVPE process are the temperature of deposition, the ratio of injected precursors and the global pressure within the reactor, which is in the range of 50 to 800 mbar. MOVPE technique is associated with high growth rate, usually in the range of $1 - 10\ \mu m/h$ but reaching values up to $56\ \mu m/h$,[42] and a good quality of the epitaxial layers in terms of purity and uniformity. Moreover, this process can be carried out in large growth chambers, suited for the growth on large or multiple samples. Hence, MOVPE is a very appropriate method for high scale production of III-N devices. The GaN-on-Si samples used in this thesis are grown within two MOVPE reactors adapted to epitaxial deposition of III-N layers on 200 mm diameter wafers, namely an Aixtron Crius R200 single wafer reactor of research and development and an Aixtron G5+ multi-wafer production reactor. The typical density of threading dislocations (see the following section 1.3.1) at the surface of GaN-on-Si layers grown on Crius and G5+ reactors are respectively in the high $10^8\ cm^{-2}$ and low $10^9\ cm^{-2}$.

1.3. Defects in heteroepitaxial III-N materials

1.3.1. Dislocations

The substantial mismatch between lattices of III-N layers and Si, sapphire or SiC heterosubstrates leads to the formation at the interface of numerous crystalline defects, called

dislocations. Indeed, the nucleation process of III-N films typically starts with the formation of crystalline islands with slightly misoriented lattices.[38] These nuclei subsequently coalesce, thus generating at the misoriented crystal interfaces a dense distribution of dislocations, usually of the order of 10^{10} units per square cm. As the epitaxy process progresses, dislocations expand through the growing layers, in the direction normal to the surface, and are referred to as threading dislocations (TDs).

Their density progressively decreases as dislocations recombine, especially in the 400 first nm of GaN layers in the case of GaN-on-sapphire,[43] typically leading to densities of dislocations of the order of $10^8 - 10^9 cm^{-2}$ at the surface of GaN layers. This recombination can be enhanced by either strain in the layer, or by the growth of 3D layers. With 3D growth, the inclined facets of the pyramids grown tend to bend the dislocations into the plane, allowing easier recombination. Growth on sapphire typically uses this strategy of 3D then 2D growth to reduce the dislocation density, while this is not possible for GaN on silicon due to the need of keeping a compressive strain in the layers during growth.

These defects highly impact the performances of III-N based power electronics devices. In particular, dislocations have been shown to increase current leakage[44], as they act as a vertical current paths through the GaN layer. This effect is lowered by carbon or iron doping of GaN layers, although the density of threading dislocations might still affect the dynamical behavior of GaN-on-Si transistors, such as the trend of channel conductance decrease under a drop of applied voltage.[45] Threading dislocations also lead to a decrease of GaN breakdown voltage[46] as they act as electron traps.[47] Additionally, dislocations densities above $10^8\ cm^{-2}$ cause a reduction of electron mobility in GaN layers,[48] with dramatic drops for dislocation densities over $10^9\ cm^{-2}$.[49] Nevertheless, this effect is observed at low temperature or at low sheet carrier concentrations in the 2DEG, which are not typical conditions of operation for power devices. [41] This is the reason why the fabrication of efficient HEMTs on GaN-on-Si is possible.

Dislocations also play an essential role in the relaxation of compressive stress through GaN and buffer layers (see section 1.3.2). Hence, a high density of TDs lowers the amount of compressive stress supposed to compensate the tensile stress introduced during post epitaxy cooling, thus leading to layer cracking.

a) Basic theory of dislocations

Dislocations are described as one-dimensional defects, as they consist of a linear disruption of the lattice perfection, which extends through the whole crystal or part of it. This dislocation line can follow either a straight or a curved path in the lattice. Along with its line, a dislocation is defined by its Burgers vector, which corresponds to the shift induced along a circuit surrounding the dislocation line (see **Figure 1.5**).

Based on the direction of the Burgers vector with respect to the direction of the dislocation line, we can describe different types of dislocations.

Edge dislocations, as illustrated in **Figure 1.5 a)**, can be seen as a half plane inserted in a perfect lattice. The dislocation line is localized next to the unbounded atoms, at the edge of the half plane. The Burgers vector of such dislocation is perpendicular to the dislocation line.

Screw dislocations consist in a shear of the lattice, so the plane initially normal to the dislocation line adopts a helicoid shape (**Figure 1.5 b)**). The Burgers circuit around this type of dislocations shows a shift of one lattice parameter in the direction of the dislocation line. Hence, the Burgers vector is parallel to the dislocation line.

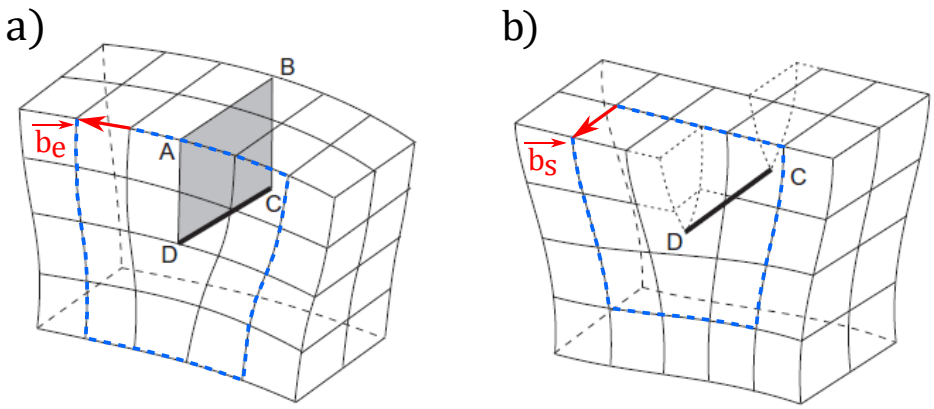

Figure 1.5 : Geometry of dislocations within a crystal lattice. a) Edge dislocation. The departure from a perfect lattice is shown with the extra half plane ABCD. b) Screw dislocation between the points C and D. Figures are adapted from reference.[50] Dislocations are depicted in a cubic lattice for a simple understanding of dislocations geometries. Burgers vectors $\vec{b_e}$ and $\vec{b_s}$ of edge and screw dislocations are shown in red and their construction paths are outlined in blue.

Finally, dislocations with their Burgers vector forming an intermediate angle between the two previous cases are called mixed dislocations. Their Burgers vector can be described by the sum of its two vector components in the direction normal and parallel to the dislocation line, showing the mixed character of such dislocations between screw and edge cases.

It should be noted that the Burgers vector of a dislocation remains constant along the whole dislocation line, which implies that a curved dislocation can change its type along its path. For example, a screw dislocation would become mixed in the area where its line bends, as the direction of this line would deviate from the direction of the Burgers vector. On the other hand, a straight dislocation maintains its character along its whole length.

Under the action of a mechanical stress, dislocations can move through the crystal lattice. We can distinguish two mechanisms of dislocation displacement:

- Dislocation glide. It consists in the movement of a dislocation in the plane containing its line and its Burgers vector. At a macro scale, gliding of dislocations can lead to a slip mechanism, corresponding to a plastic deformation of the crystal when two planes of atoms slide over each other. This phenomenon can only happen on slip planes, which are usually the planes of the crystal with higher atomic density.

- Dislocation climb. It corresponds to a displacement of a dislocation out of the glide plane and typically occurs at high temperature.

b) Mechanical elastic fields surrounding dislocations

By locally disrupting the crystal lattice perfection, dislocations create a strain field around them, that can be described by elasticity theory. This is usually done by considering a straight dislocation in an isotropic crystal, with its line direction oriented along the z axis of a cylindrical coordinate system (r, θ, z), as represented in **Figure 1.6**.

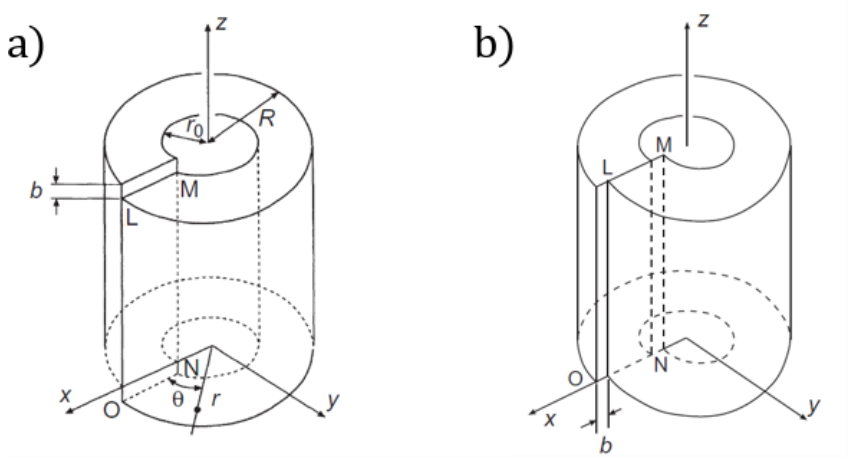

Figure 1.6: Distortion induced by dislocations on a surrounding hollow cylinder of crystal lattice. a) Screw dislocation. b) Edge dislocation. b is the Burgers vector. r_0 and R represent respectively the inner and outer radius of the hollow cylinder, in which the elastic mechanic fields apply. Figures are reproduced from reference.[51]

The vector of displacement around a screw dislocation with Burgers vector b_s can be found from **Figure 1.6** (a):

$$\begin{pmatrix} u_r \\ u_\theta \\ u_z \end{pmatrix} = \begin{pmatrix} 0 \\ 0 \\ \frac{b_s \theta}{2\pi} \end{pmatrix} \tag{1.10}$$

From Equation (1.10), we obtain the strain and stress tensors, assuming a linearly elastic isotropic crystal with shear modulus G:

$$\begin{pmatrix} \varepsilon_{rr} & \varepsilon_{r\theta} & \varepsilon_{rz} \\ \varepsilon_{\theta r} & \varepsilon_{\theta\theta} & \varepsilon_{\theta z} \\ \varepsilon_{zr} & \varepsilon_{z\theta} & \varepsilon_{zz} \end{pmatrix} = \begin{pmatrix} 0 & 0 & 0 \\ 0 & 0 & \frac{b_s}{4\pi r} \\ 0 & \frac{b_s}{4\pi r} & 0 \end{pmatrix} \tag{1.11}$$

$$\begin{pmatrix} \sigma_{rr} & \sigma_{r\theta} & \sigma_{rz} \\ \sigma_{\theta r} & \sigma_{\theta\theta} & \sigma_{\theta z} \\ \sigma_{zr} & \sigma_{z\theta} & \sigma_{zz} \end{pmatrix} = \begin{pmatrix} 0 & 0 & 0 \\ 0 & 0 & \dfrac{Gb_s}{2\pi r} \\ 0 & \dfrac{Gb_s}{2\pi r} & 0 \end{pmatrix} \tag{1.12}$$

According to equation (1.11), the linear elasticity theory predicts a strain around screw dislocations consisting of pure shear. However, when second order terms of nonlinear elasticity theory are taken into account, tensile/compressive strain arises, as demonstrated by *Stehle et Seeger*:[52]

$$\begin{pmatrix} \varepsilon_{xx} & \varepsilon_{xy} & \varepsilon_{xz} \\ \varepsilon_{yx} & \varepsilon_{yy} & \varepsilon_{yz} \\ \varepsilon_{zx} & \varepsilon_{zy} & \varepsilon_{zz} \end{pmatrix} = \begin{pmatrix} \Delta\, cos^2\theta & -\Delta \sin\theta \cos\theta & \dfrac{b_s \sin\theta}{4\pi r} \\ -\Delta \sin\theta \cos\theta & \Delta\, sin^2\theta & \dfrac{-b_s \cos\theta}{4\pi r} \\ \dfrac{b_s \sin\theta}{4\pi r} & \dfrac{-b_s \cos\theta}{4\pi r} & 0 \end{pmatrix} \tag{1.13}$$

where $\Delta = Kb_s^2/(4\pi r^2)$, K being a factor depending on second order atomic forces, close to 1.

Determining the displacement field of an edge dislocation is not as straightforward as for a screw dislocation. The expressions have been derived from Volterra's works on hollow cylinders[53] and adapted to the case of a straight dislocation in an isotropic crystal, described in Cartesian coordinates.[54],[55] We give adapted equations replacing the Lamé parameters used in this historical literature with the Poisson ratio ν:

$$u_x = \frac{b_e}{2\pi}\left(arctan\frac{y}{x} + \frac{1}{4(1-\nu)}\frac{xy}{x^2+y^2}\right) = \frac{b_e}{2\pi}\left(\theta + \frac{sin\,2\theta}{4(1-\nu)}\right) \tag{1.14}$$

$$u_y = \frac{b_e}{4\pi(1-\nu)}\left(\frac{2\nu-1}{2}ln(x^2+y^2) + \frac{y^2}{x^2+y^2}\right) = \frac{b_e}{4\pi(1-\nu)}\left((2\nu-1)ln(r) + \frac{1-cos\,2\theta}{2}\right) \tag{1.15}$$

$$u_z = 0 \tag{1.16}$$

The corresponding strain field is a plane strain, as it expands in the plane normal to the dislocation line (i.e. $\varepsilon_{rz} = \varepsilon_{\theta z} = \varepsilon_{zz} = 0$). The stress field around edge dislocations is:[56]

$$\begin{pmatrix} \sigma_{rr} & \sigma_{r\theta} & \sigma_{rz} \\ \sigma_{\theta r} & \sigma_{\theta\theta} & \sigma_{\theta z} \\ \sigma_{zr} & \sigma_{z\theta} & \sigma_{zz} \end{pmatrix} = \frac{Gb_e}{2\pi(1-\nu)}\begin{pmatrix} \dfrac{-\sin\theta}{r} & \dfrac{\cos\theta}{r} & 0 \\ \dfrac{\cos\theta}{r} & \dfrac{-\sin\theta}{r} & 0 \\ 0 & 0 & \dfrac{-2\nu\sin\theta}{r} \end{pmatrix} \tag{1.17}$$

Note that equations (1.10) to (1.17) are valid for a hollow cylinder of inner radius r_0 surrounding the dislocations, as depicted in **Figure 1.6**. Indeed, near to the core of the dislocations (i.e. when $r \to 0$), the stress field values would diverge, due to the $1/r$ tendency shown in equations (1.12) and (1.17). The value of r_0 is considered to lie between one to four times the Burgers vector,[51] with a typical assumed value of $10^{-7} cm$. Hence, the study of strain and stress fields in the core region of a dislocation needs to rely on atomic models, whose description is beyond the scope of the present work.

c) Threading dislocations in III-N layers

III-N materials grown in the form of hexagonal (0001) layers are crossed by threading dislocations, whose lines usually follow a path perpendicular to the surface (along the [0001] direction). **Figure 1.7** shows the three different groups of threading dislocations that coexist in hexagonal (0001) III-N layers. Screw TDs are divided into two dislocation types, depending on the orientation of their Burgers vector, which is normal to the surface ($b_s = \langle 0001 \rangle$). Edge TDs are separated into three types, with Burgers vectors ($b_e = 1/3\ \langle 11\bar{2}0 \rangle$) parallel to the surface plane. Finally, six types of mixed dislocations constitute the last group ($b_m = 1/3\ \langle 11\bar{2}3 \rangle$), with their Burgers vector forming an intermediate angle between the two previous cases. Hence, in terms of lattice parameters a and c, the magnitude of screw, edge and mixed dislocations is respectively $b_s = c$, $b_e = a$ and $b_m = \sqrt{a^2 + c^2}$. Edge and mixed TD are predominant in hexagonal GaN layers, while pure screw ones generally account for less than 2% of the total TD density.[4]

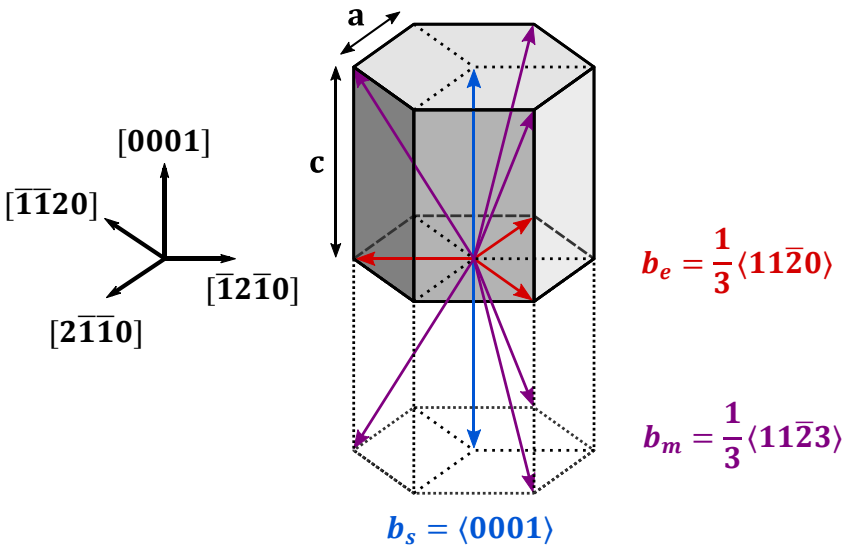

Figure 1.7: Schematic of the Burgers vectors of threading dislocations in a hexagonal unit cell of GaN. *a* and *c* are the lattice parameters, respectively in the surface plane and in the direction normal to the surface plane. The Burgers vectors are drawn in red

(b_e) for the set of three edge TD, in blue (b_s) for the two kinds of screw TD and in purple (b_m) for the family of mixed TD.

1.3.2. Macro-stress fields

We have seen in the section 1.2.1 that the use of heterosubstrates for GaN epitaxy may require the growth of intermediate III-N buffer layers. The small lattice mismatch between these buffers films and the GaN layer leads to the introduction of a biaxial compressive stress in the (0001) plane of GaN. Before the post-epitaxy cooling step, the GaN layer is therefore under a compressive strain within its (0001) plane, and under a tensile strain along the c-axis ([0001] direction), by Poisson's effect. As the GaN layer grows up to a few µm thick, the lattice relaxes, thus leading to a gradient of in-plane stress along the normal to the surface plane.

Most of usual semiconductors, such as Si, Ge or GaAs, have a close packed cubic structure, characterized by {111} planes with high atomic densities. In these crystals, the relaxation of compressive stress typically happen through a slip mechanism (see section 1.3.1.a)). However, in the case of wurtzite structure, the slip phenomenon is restricted to the planes of the $\{10\bar{1}0\}$ family. In (0001) oriented GaN layers, these planes are normal to the surface, thus preventing any relaxation of in-plane stress by slip. Instead, two other mechanisms have been proposed for the progressive relaxation of compressive stress, and thus the formation of a stress gradient:

- The bending of TDs with an edge component away from the [0001] direction. The projection of the bended dislocation segments on the (0001) plane corresponds to a segment of misfit dislocation (i.e with both the line and the orthogonal Burgers vector comprised in the (0001) plane), known for relaxing in-plane stresses.[57] Dislocation bending is promoted by rough surfaces of growing films, in particular in the case of Si-doped III-N layers.[58]
- The recombination of TDs. In III-N layers, part of the TDs annihilate by progressively recombining with each other throughout the film thickness. It has been suggested that the density at the core of dislocations is smaller than in the rest of the lattice, thus forming a free volume that disappears when TDs annihilate, allowing for compressive stress relaxation.[59],[60]

The magnitude of this gradient has been observed to be especially strong in MOVPE-grown GaN-on-Si layers. **Figure 1.8** gives an example of in-plane stress gradient, estimated from measurements of sample curvature evolution during the epitaxy process.[61] We note that the mechanism described before generates a stress gradient in both the AlGaN films and the GaN layer, although the magnitude of the latter is higher.

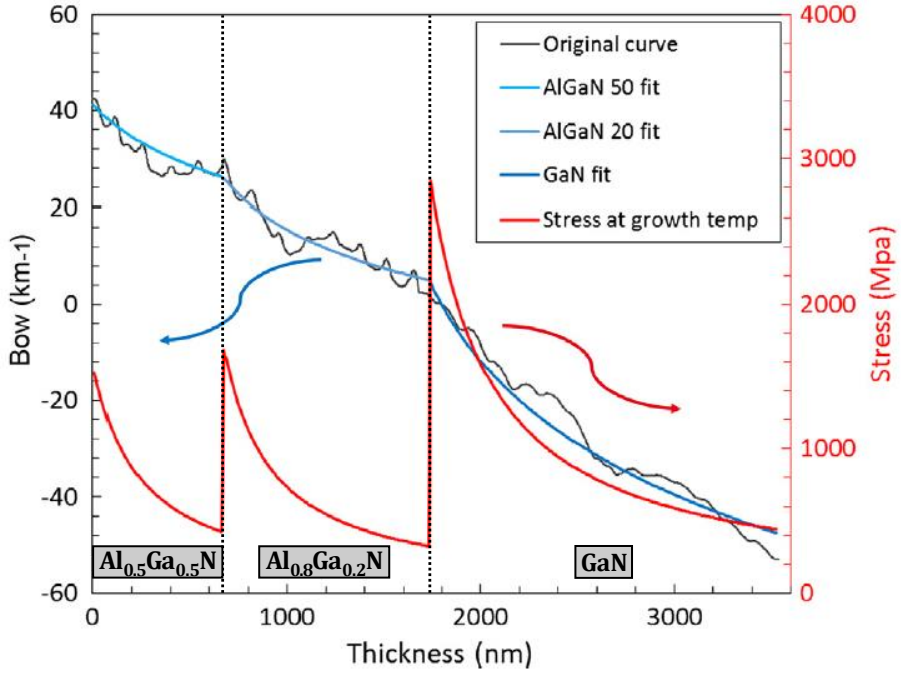

Figure 1.8 : Stress gradient in a GaN-on-Si sample estimated from in-situ bow measurements. Black curve: Bow of the sample, measured by optical reflectance during the epitaxial growth of the two AlGaN buffers and the GaN layer. Blue curves: Logarithmic fits of bow measurements on each layer. Red curve: Stress calculated using the Stoney equation.[62] Reproduced from reference.[61]

1.3.3. Stacking faults

Unlike one-dimensional dislocations, planar defects extend through two dimensions of the crystal lattice. Beyond the surfaces and interfaces of a crystal, this two-dimensional category includes defects such as grain boundary (i.e. the interface between two highly misoriented lattices, whether constituted of the same crystal phase or not) or twin, which is a plane of inversion of lattice orientation, acting as the interface between two lattice areas related by a mirror symmetry. These two latter defects are not common in III-N layers, unlike the last main type of planar defect, namely stacking faults.

In III-N wurtzite crystals, stacking faults occur in the basal (0001) plane and thus are called basal plane stacking faults (BSFs). As depicted in **Figure 1.9**, BSFs consist of a disruption of the *ABABAB* hexagonal closed pack stacking along the c-axis, to locally adopt a face-centered cubic close packed *ABCABC* sequence, which is normally characteristic of stacking along the [111] direction of zincblende III-N crystals. BSFs are only observed in III-N layers grown along semi-polar and non-polar directions (i.e. $[hkil] \neq [000l]$), with typical densities of the order of $10^5 cm^{-1}$. Hence, this type of defect will not be considered for the [0001]-grown layers studied throughout this thesis.

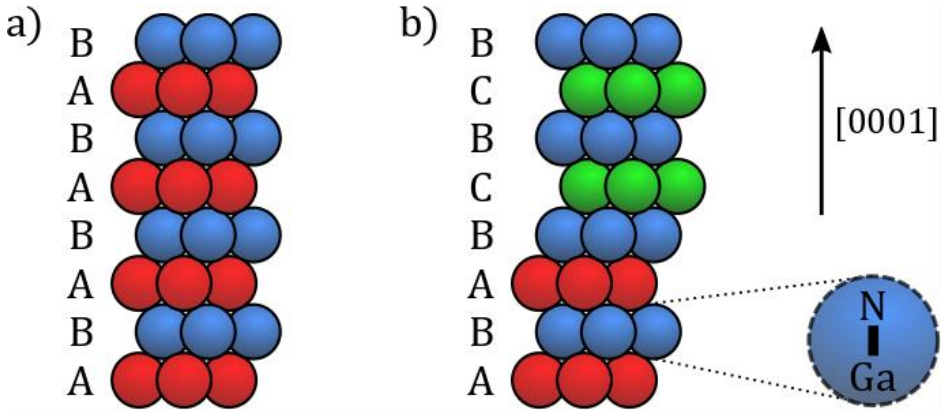

Figure 1.9 : Stacking fault in a wurtzite III-N layer. a) Standard wurtzite hexagonal closed pack sequence b) Example of BSF sequence of type I_1, which represents about 90% of BSFs in wurtzite III-N layers, owing to its low formation energy.[55] Each letter ABC letters represents a group-III/N bilayer and each sphere represents a group-III/N doublet of atoms.

GaN-on-Si appears to be well positioned to respond to the challenge of supporting the upcoming massive expansion of power electronics, as it is with a practical, affordable and highly-performant semiconductor. Nevertheless, this material is affected by substantial densities of threading dislocations, known for deteriorating the performances of devices, and a strong gradient of stress with a magnitude specific to GaN-on-Si. The study of these defects is of crucial interest to improve the quality and understanding of grown layers and electrical performance. The following chapter will detail the background knowledge to carry out these characterizations by using X-ray diffraction techniques.

2. X-ray diffraction characterizations

X-Ray Diffraction (XRD) is a widely used method of materials characterization, in particular for investigation of crystal structures. The study of monocrystals requires the use of high-resolution X-ray diffraction (HRXRD) techniques. They rely on the measurement of the distances between crystal planes and the strain to which they are subject. A large set of structural information can be deduced from these measurements, from the examination of the crystal structure and the lattice parameters to the study of the strain fields and defects present in the crystal.

Besides this wide variety of measurements, X-ray diffraction is an ideal answer to the constraints of a metrological monitoring of III-N wafers. The technique is indeed non-destructive, rather fast and easy to implement, especially when using fully automated measurement tools adapted to cleanroom processes.

The following chapter contains an overview of the basic knowledge needed to understand XRD characterizations and analyses applied to III-N epitaxial layers. It includes considerations on the nature of X-rays, their interactions with matter and an introduction to the diffraction theory, by means of the simple kinematical model. This theory is illustrated using the reciprocal space representation, which allows a relevant depiction of XRD measurements on monocrystals. A description of the diffractometers used for these measurements is provided, as well as the setups used in this thesis. Finally, elemental analyses are made of the links between the measured diffraction peaks characteristics (position and width) and the crystalline structure of the sample. They give the required theoretical bases for the specific studies of subsequent chapters, on dislocation distributions and strain gradients.

2.1. X-ray - matter interactions

2.1.1. Production of X-rays

X-rays is the name given to the category of electromagnetic waves with wavelengths ranging from 10 pm to 10 nm. More specifically, the typical wavelengths used for XRD characterizations are of the order of the ångström.

Different sources are used to produce X-ray photons. In the laboratories, the radiation is produced in an X-ray tube by the strike of highly accelerated electrons on a metallic anode. These electrons are generated by heating a filament, typically made of tungsten, and then accelerated by applying a strong electric field. When hitting the anode, the electrons eventually undergo a deceleration, thus generating a continuous X-ray radiation called Bremsstrahlung. At the same time, an X-ray emission in the form of intense characteristic lines is also observed. These lines are the result of electronic transitions, induced in the metal of the anode by the incident radiation.

This characteristic line emission is the one used for XRD. The wavelength of the lines depends on which metal the anode is made of. Usually, the $K_{\alpha 1}$ radiation of a copper anode is used, as it will be the case throughout this thesis. According to the recommendations of the international union of crystallography, its wavelength is estimated to be equal to 1.54059 Å.[63] An example of the spectra emitted by a copper anode is presented in Figure 2.1. It should be noted that the efficiency of these sources is highly limited , as 99% of the energy of the electron beam is dissipated as heat at the anode.[64]

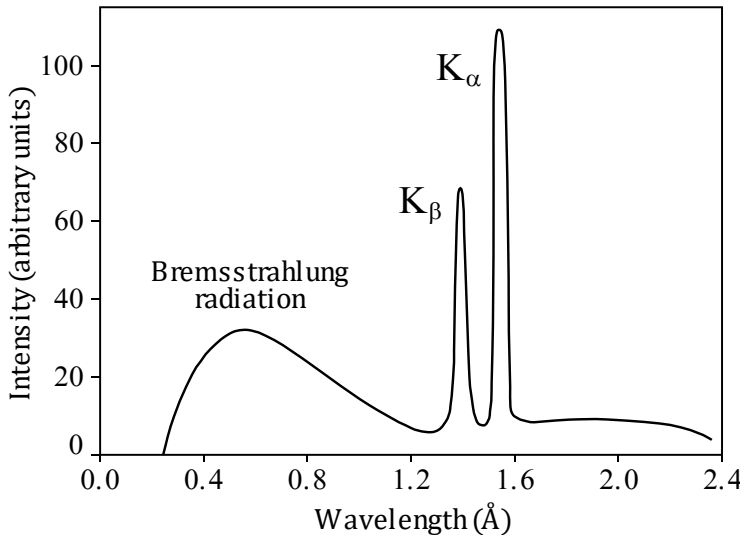

Figure 2.1 : Emission spectrum of a copper anode hit by an electron beam. Schematic representation for a 50kV potential applied on the X-ray tube, including the K_α, K_β and continuous Bremsstrahlung radiations. K_α radiation is composed by two lines $K_{\alpha 1}$ and $K_{\alpha 2}$. Wavelength values are taken from reference.[65] Relative intensities between the peaks are arbitrary.

The synchrotrons form a second type of artificial X-rays sources. They are constituted of a storage ring where electrons are injected and turn at high speed, their trajectory being deviated by magnetic fields. The electrons thus undergo a centripetal acceleration and emit an electromagnetic radiation, called synchrotron radiation, which is extremely brilliant and is composed by a large spectrum of frequencies. This source is a few orders of magnitude more powerful than X-ray tubes but require the construction of large and expensive facilities. To better adhere to the metrological framework of this thesis, synchrotrons are not used and the experiments focus on laboratory-compatible X-ray tube systems.

2.1.2. Absorption

The main interest of X-ray production is the characterization of matter. When an X-ray beam travels through a material, different effects are observed. The more obvious is the absorption of the X-rays, property which is used for example in medical radiology, or for the human protection against X-radiations. At low and medium X-ray energy (i.e. below 1 MeV), three effects should be considered to explain the X-rays absorption:[66]

- The photoelectric effect. This phenomenon consists in the absorption of an X photon by an atom, partially compensated by the emission of an electron. As the energy transmitted from the incident photon is higher than the binding energy of the electron, the atom loses the energy surplus by emitting an X-radiation or a second electron called Auger electron. This effect is predominant at low energy.

- The Rayleigh scattering effect. It is the result of the oscillation of the electron cloud around the irradiated atom. This motion leads to the re-emission of X-rays with the same wavelength in all the directions around the atom, which is the source of the diffraction phenomenon. The loss of intensity due to this phenomenon is higher at low X-ray energy. However, its relative importance compared to the photelectric effect increases with the rise of energy.

- The Compton scattering effect. It describes the loss of energy of the photons when hitting an electron of the external shells of the atoms. This effect is more important at high energies.

The X-ray absorption is described by the sum of these three effects. Its magnitude depends on the atomic density of the absorbing material. Hence, for a given X-radiation energy, we associate to each material a linear attenuation coefficient μ, which describes the loss of intensity of a beam of initial intensity I_0 travelling through a length x of material. The transmitted intensity I is given by the Beer-Lambert law:

$$I = I_0 \exp(-\mu x) \tag{2.1}$$

For the Cu K_α radiation, which has a photon energy of 8.04 keV, μ of GaN is equal to 271 cm^{-1},[67] corresponding to an 1/e attenuation length of 36.9 µm.

2.1.3. Diffraction

a) Diffraction and Bragg's law

Like other electromagnetic waves, X-rays undergo a phenomenon called diffraction when passing through apertures with a size of the order of their wavelength. For X-rays, this happens when travelling through materials with interatomic distances of the order of the ångström. For the particular case of crystalized materials, the separation between atoms is ruled by the interplanar distances between crystalline planes. Hence, irradiating a crystal with X-rays leads to the scattering of the incident beam all around in space, generating spots of diffracted intensity separated by zones of beam extinction. Most of XRD techniques focus on the measurement of these crystal-scattered signals, which are used to characterize the crystallographic structure of the material.

When the X-ray source is located far enough from the diffracting material (i.e. at a distance much greater than the wavelength value), we can consider that the incident wave is plane. In

the same way, the diffracted wave can be treated as a plane wave when it is detected at a high distance from the crystal. These criteria correspond to the Fraunhofer diffraction conditions. The diffraction phenomenon is caused by the Rayleigh effect detailed previously, which transforms each irradiated atom into a sub-X-ray source that scatters the incident beam in all space directions. The waves coming from different atoms may have different phases when encountering one another due to the unequal lengths of the covered paths. Two waves with opposite phases will cancel each other, leading to a destructive interference and an extinction of the beam. Conversely, two waves with the same phase will add together to generate a constructive interference, which can be measured by a detector.

This phenomenon is represented in **Figure 2.2**. A constructive interference is formed when the additional path covered by a first wave compared to a second wave is a multiple of the wavelength, so the two waves have the same phase after the diffraction. Using the notations of **Figure 2.2**, the length of this additional path is $2d_{hkl}\ sin\ \theta$.

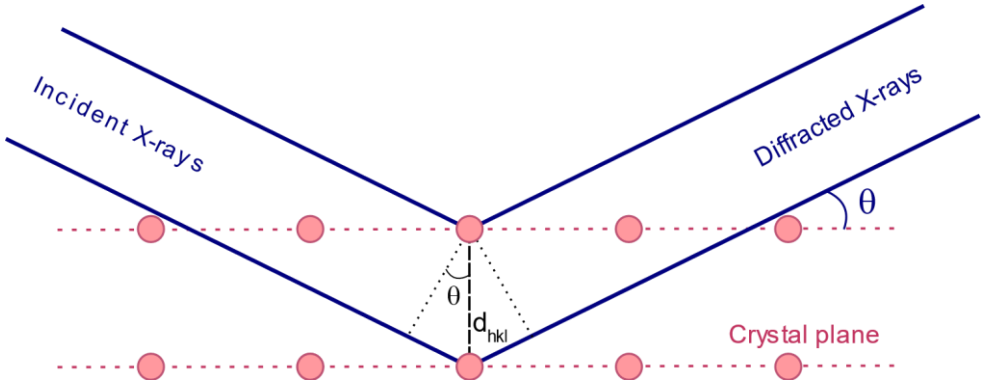

Figure 2.2 : Representation of the Bragg's law. The two series of red points represent the atoms of two crystal planes separated by a distance d_{hkl}. θ angle is equal to half of the angle between transmitted and diffracted rays.

One can therefore deduce the Bragg's law, which links the wavelength λ to the interplanar distance d_{hkl} and the angular position θ at which a diffraction spot is observable:

$$n\lambda = 2d_{hkl} \sin\theta \qquad (2.2)$$

where n is the diffraction order.

Usually, a monochromatic beam of known wavelength is used. The θ angle is therefore measured to deduce the distance between two planes of Miller indices (h, k, l). The diffraction phenomenon on this set of crystal planes is called the (h, k, l) reflection.

b) Reciprocal space representation

To describe the diffraction phenomenon, it is appropriate to use a vectorial representation. Hence, we define a new frame of reference $R_c^* = (\vec{a}^*, \vec{b}^*, \vec{c}^*)$ for the crystal lattice, called reciprocal lattice. It is defined by means of the direct lattice reference frame $R_c = (\vec{a}, \vec{b}, \vec{c})$,

which gives the three unit vectors whose linear combinations form the crystal lattice in the real space (see section 1.1.1). For a unit cell of volume V_c in the real space, we have:

$$\begin{cases} \vec{a}^* = \dfrac{\vec{b} \wedge \vec{c}}{V_c} \\ \vec{b}^* = \dfrac{\vec{c} \wedge \vec{a}}{V_c} \\ \vec{c}^* = \dfrac{\vec{a} \wedge \vec{b}}{V_c} \end{cases} \tag{2.3}$$

The reciprocal lattice is in turn generated by a linear combination of these $(\vec{a}^*, \vec{b}^*, \vec{c}^*)$ vectors. Hence, the expression of a vector $\overrightarrow{h_{hkl}}$ linking the space origin to a lattice point is:

$$\overrightarrow{h_{hkl}} = h\vec{a}^* + k\vec{b}^* + l\vec{c}^* \tag{2.4}$$

Due to the definition of the reciprocal space, the distances in this system are inverse to the distances in the direct lattice system. Hence:

$$\left\|\overrightarrow{h_{hkl}}\right\| = \frac{1}{d_{hkl}} \tag{2.5}$$

where d_{hkl} is the interplanar distance between the (hkl) planes.

In the reciprocal space, the diffraction of a monochromatic beam of wavelength λ is described by a scattering vector $\vec{q}$. This scattering vector is defined by $\overrightarrow{k_\iota}$ and $\overrightarrow{k_d}$, the wave vectors before and after the diffraction of length $\left|\overrightarrow{k_\iota}\right| = \left|\overrightarrow{k_d}\right| = 1/\lambda$:

$$\vec{q} = \overrightarrow{k_d} - \overrightarrow{k_\iota} \tag{2.6}$$

As shown in **Figure 2.3**, the scattering vector's components $\overrightarrow{q_x}$ and $\overrightarrow{q_z}$ are often used as unit vectors of a reciprocal space system to illustrate the diffraction phenomena on monocrystals. In this system, we can represent the reciprocal lattice points, indexed by their Miller indices (h, k, l). The diffraction angles, such as the Bragg angle θ, can also be incorporated to this representation.

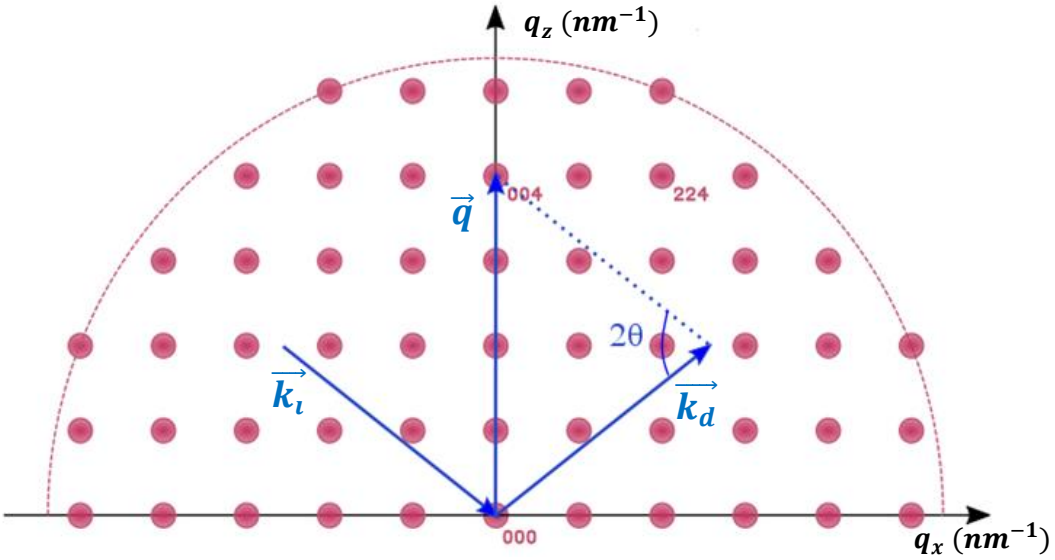

Figure 2.3 : Representation of the lattice points, diffraction vectors and diffraction angles in the reciprocal space.

In **Figure 2.3**, $\overrightarrow{k_i}$ and $\overrightarrow{k_d}$ are represented with a length $1/\lambda$. According to equation (2.5), when $\vec{q}$ links the reciprocal space origin to a point (h,k,l) of the reciprocal lattice, its length is inverse to the interplanar distance d_{hkl}. Graphically, we easily find that this condition leads to $\vec{q} = \frac{\sin\theta}{\lambda} + \frac{\sin\theta}{\lambda} = \frac{1}{d_{hkl}}$, which corresponds to Bragg's law (equation (2.2)). Hence, the vectorial translation of Bragg's law, called the Laue condition, is defined for any (hkl) reflection by:

$$\vec{q} = \overrightarrow{h_{hkl}} \tag{2.7}$$

Thus, on every point of the reciprocal lattice of a perfect monocrystal is located a diffraction spot, associated to the reflection of the corresponding (hkl) plane (except for forbidden (h,k,l) reflections, as detailed in the following section 2.1.3c)). For an imperfect crystal, the diffraction spot may slightly move away from the reciprocal lattice point, as the real interplanar distances differ from their ideal values.

c) Diffracted intensity

When the angles between the X-ray source, the sample and the detector are set according to the condition of Bragg/Laue, a diffracted signal is measured. A crucial parameter of this measurement is the diffracted intensity, which can vary by several orders of magnitude and imposes very long measurements when it is low. We shall describe this diffracted intensity using the simple model of the kinematical theory. This model assumes that an X-ray wave hitting a crystal only undergoes a single scattering and potentially some absorption.

We should remember that the diffracted wave originates from a scattering of the incident beam by electron clouds around each atom of the irradiated material. The diffracted amplitude can be expressed as the sum of the contributions of each of these atoms to the scattering. The

contribution of an atom j is quantified by an atomic scattering factor f_j, which increases with the atomic number of the atom, as more electrons are involved in the Rayleigh scattering process. Furthermore, due to partial interferences between X-rays scattered by each electron of an atom, f_j is lowered by the increase of the diffraction angle θ and the decrease of the wavelength.[68]

Let's consider a wave diffracted by a crystal.

As stated earlier, we can write the amplitude $A(\vec{q})$ scattered during the diffraction process at a point $\vec{q}$ of reciprocal space by the J atoms forming the crystal:

$$A(\vec{q}) = \left| \sum_{j}^{J} f_j(\vec{q}) e^{i2\pi \vec{q}.\overrightarrow{r_j}} \right| \tag{2.8}$$

r_j is the vector connecting the atom j to the origin of the lattice.

It is useful to decompose the diffracting crystal into its elementary components, called unit cells. In a perfect crystal, all the unit cells are identical as each of them contains the same number and kind of atoms, whose positions with respect to the origin of the cell are described by a set of vectors $\overrightarrow{r_n}$. For a crystal of finite size containing M cells, each of them containing n atoms, the equation (2.8) becomes:

$$A(\vec{q}) = \left| \sum_{m}^{M} e^{i2\pi \vec{q}.\overrightarrow{r_m}} \right| \left| \sum_{n}^{N} f_n(\vec{q}) e^{i2\pi \vec{q}.\overrightarrow{r_n}} \right| = |L(\vec{q})||F(\vec{q})| \tag{2.9}$$

The vectors $\overrightarrow{r_m}$ give the positions of the origin of each unit cell with respect to the origin of the lattice.

The term $L(\vec{q})$ is the form factor. It reflects the increase in amplitude of the scattered wave with the amount of diffracting material. Alternatively, $L(\vec{q})$ can be defined as the Fourier transform of the crystal shape function $V(\vec{r})$.

$$L(\vec{q}) = \mathrm{FT}[\, V(\vec{r})] \tag{2.10}$$

The crystal shape function permits to transform the sum over lattice sites of unit cells (equation (2.9)) into an integral over the entire continuous space (equation (2.10)).[69] It is defined as:

$$V(\vec{r}) = Y^{\infty}(\vec{r})\, s(\vec{r}) \tag{2.11}$$

The function $s(\vec{r})$ defines the boundaries of the crystal, as it is equal to unity within the crystal and to zero outside the crystal. The function $Y^{\infty}(\vec{r}) = \sum_{m=-\infty}^{\infty} \delta(\vec{r} - \overrightarrow{r_m})$ reproduces the periodic contribution to the scattered amplitude originating from each unit cell lattice site.

The second term $F(\vec{q})$ of equation (2.9) is called the structure factor. It describes the wave diffracted by one unit cell, in terms of amplitude and phase. Its absolute value corresponds to the amplitude scattered by the unit cell. As shown in the equation (2.9), the structure factor is composed by the sum of the contributions to the diffracted wave of each atom of the unit cell. These contributions are expressed in the form of a series of complex numbers, which can add together or cancel one another. We can rewrite the structure factor, by developing the scalar product $\vec{q}.\overrightarrow{r_m}$, to express it with the Miller indices (h,k,l) of the considered reflection and the coordinates (u_n, v_n, w_n) of each atom in the unit cell:

$$F(h,k,l) = \sum_{n}^{N} f_n(h,k,l) e^{i2\pi(hu_n + kv_n + lw_n)} \tag{2.12}$$

For a GaN crystal with wurtzite structure (see section 1.1.1 a)), equation (2.12) becomes:

$$F_{GaN}(h,k,l) = f_{Ga}(h,k,l)\left(1 + e^{i2\pi\left(\frac{2h}{3}+\frac{k}{3}+\frac{l}{2}\right)}\right) + f_N(h,k,l)\left(e^{i2\pi\left(\frac{3l}{8}\right)} + e^{i2\pi\left(\frac{2h}{3}+\frac{k}{3}+\frac{7l}{8}\right)}\right) \tag{2.13}$$

The reader is referred to the section *6.1.1* of the International tables of crystallography Volume C[70] for the calculation of $f_{Ga}(h,k,l)$ and $f_N(h,k,l)$.

Like for a simple hexagonal closed-packed crystal, the structure factor of GaN is equal to zero when the Miller coefficients combination follows both the two rules below:

- l coefficient is odd
- $2h + k = 3n\,, n \in \mathbb{N}$

Hence, (h,k,l) reflections following these two conditions show theoretically no intensity, preventing their use for XRD characterizations.

Table 2.1 gives the different accessible reflections of a GaN crystal, for 2θ angles up to 138°.

Reflection	d_{hkl} (Å)	2θ (°)	χ (°)	Reflection	d_{hkl} (Å)	2θ (°)	χ (°)
(100)	2.762	32.39	90.00	(210)	1.044	95.11	90.00
(002)	2.593	34.57	0.00	(211)	1.023	97.65	78.62
(101)	2.438	36.84	61.96	(114)	1.006	99.95	39.11
(102)	1.890	48.10	43.19	(105)	0.971	105.01	20.58
(110)	1.595	57.77	90.00	(212)	0.968	105.40	68.07
(103)	1.465	63.43	32.04	(204)	0.945	109.17	43.19
(200)	1.381	67.81	90.00	(300)	0.921	113.59	90.00
(112)	1.358	69.10	58.41	(213)	0.894	119.09	58.87
(201)	1.334	70.52	75.09	(302)	0.868	125.22	70.45
(004)	1.296	72.91	0.00	(006)	0.864	126.07	0.00
(202)	1.219	78.40	61.96	(205)	0.829	136.52	36.91
(104)	1.174	82.05	25.14	(106)	0.825	138.10	17.38
(203)	1.079	91.12	51.38				

Table 2.1 : Allowed XRD reflections for a GaN crystal. The interplanar distance d_{hkl} , twice the Bragg angle 2θ and the inclination ψ of the diffracting planes with respect to the surface are given for each reflection, for a Cu $K_{\alpha 1}$ radiation of wavelength $\lambda = 1.54059$ Å.

The wave summation described in the equations (2.8) and (2.9) happen in a crystal domain, whose dimensions ideally correspond to the whole size of the crystal, but can be reduced by lattice defects such as grain boundaries or heavy distortions. The width of a domain in the surface plane of the sample is called lateral X-ray correlation length and its height along the normal to the surface is called normal or vertical X-ray correlation length. Within such a domain, the wave amplitudes add together and the diffraction is described as coherent. However, if the correlation lengths are lower than the crystal dimensions, this one is divided in several diffraction domains. In this case, the sum of the signals coming from each domain is not anymore an addition of amplitudes but a sum of their intensities.

For a crystal divided in D domains of coherent diffraction, each of them containing M_d atoms, the total diffracted intensity is expressed as a sum of the squared amplitudes scattered by each domain. With I_0 being a reference intensity, we have:

$$I(\vec{q}) = I_0 \sum_{d}^{D} A_d^2(\vec{q}) = I_0 |F(\vec{q})|^2 \sum_{d}^{D} \left| \sum_{m}^{M_d} e^{i2\pi \vec{q}.\overrightarrow{r_m}} \right|^2 \qquad (2.14)$$

d) Case of a distorted crystal

In the case of a distorted crystal, the positions $\overrightarrow{r_m}$ of unit cells are modified. By assuming that the structure factor remains constant within the crystal, Equation (2.9) becomes:

$$A(\vec{q}) = |F(\vec{q})| \left| \sum_{m}^{M} e^{i2\pi\vec{q}.(\overrightarrow{r_m}+\overrightarrow{u_m})} \right| \tag{2.15}$$

$\overrightarrow{u_m}$ corresponds to the displacement field induced by the distortion on each unit cell of the crystal.

When the scattering vector $\vec{q}$ slightly deviates from the closer reciprocal lattice vector $\overrightarrow{h_{hkl}}$ by $\vec{s} = \vec{q} - \overrightarrow{h_{hkl}}$ and $|\vec{s}| \ll |\overrightarrow{h_{hkl}}|$, the scalar product $(\vec{s}.\overrightarrow{u_m})$ can be neglected to write equation (2.15) as:

$$A(\vec{q}) = |F(\vec{q})| \left| \sum_{m}^{M} e^{i2\pi\vec{q}.\overrightarrow{r_m}} e^{i2\pi\overrightarrow{h_{hkl}}.\overrightarrow{u_m}} \right| \tag{2.16}$$

This approximation enables to write the scattered amplitude around a reflection (hkl) in terms of a Fourier transform:

$$A(\vec{q}) = |F(\vec{q})| \, | \, FT[V(\vec{r})G(\vec{r})] \, | \tag{2.17}$$

where $V(\vec{r})$ is the crystal shape function of equations (2.10) and (2.11) and $G(\vec{r})$ is the correlation function $G(\vec{r}) = \exp\left(2\pi\overrightarrow{h_{hkl}}.\overrightarrow{u(\vec{r})}\right)$

e) Dynamical XRD model

The previous description of the intensity scattered by a diffracting crystal relies on the simplified model of the kinematical theory. While this theory gives in many cases a very good approximation of the real scattered intensity, some diffraction processes require a comprehensive model, called dynamical theory.

Unlike the kinematical theory, the dynamical model takes into account different second order effects, such as the interaction between the incoming and diffracted waves, the multiple scattering of a wave, or its partial reflection on the material. This results in changes in the modeled intensity and width of the diffraction peaks.

Among the main results of the dynamical theory, it is worth mentioning the prediction of an elementary width of the diffraction peaks. This broadening is usually called Darwin width, in reference to the pioneering works of this author.[71],[72] It corresponds to the breadth encountered for the peak of a perfect and infinite crystal, independently of the instrumental

resolution of the diffractometer. The Darwin width β_0 directly depends on the nature of the crystal and on which planes are used for the diffraction:[73]

$$\beta_0 = r_e \frac{\lambda |F(h,k,l)|(1 + |\cos 2\theta|)}{V_c \, \pi \sin 2\theta} \tag{2.18}$$

The constant r_e is the classical electron radius, equal to $2.818 \times 10^{-15}\, m$. θ and $F(h,k,l)$ are the Bragg angle and the structure factor corresponding to the considered (h,k,l) reflection and V_c is the volume of a unit cell.

The use of the dynamical theory is required to describe diffraction processes on quasi-perfect crystals, which means large crystals (micrometric dimensions) with very few defects. This quasi-perfection condition does not appear to be met in the rather highly defective III-N crystals studied in this work, especially regarding their density of threading dislocations.[4] The kinematical theory is therefore used in the studies of a wide variety of III-N layers, like GaN layers grown on sapphire substrates by MOVPE[74] or HVPE,[75] laterally overgrown (ELO) GaN structures[76] or InGaN/GaN quantum wells.[77] Similarly, this model will be assumed to be sufficient to describe most of the diffraction results presented in this thesis.

2.2. HRXRD measurements

2.2.1. Diffraction in the real space

X-ray diffraction is a widely used characterization method, which is divided in a large range of sub-techniques, using their own measurement geometries. For simple reviews of these techniques, the reader is referred to the following references[78],[79]. In this work, we will focus on a rotational measurement method, using a measurement geometry usually designated as Bragg-Brentano geometry.

The Bragg-Brentano geometry is shown in **Figure 2.4**. The diffracting crystal is placed on a sample-holder, in the center of a goniometer circle containing the X-ray source and the X-ray detector. Hence, both the source and the detector are placed at the same fixed distance from the sample. This set-up allows the measurement of diffracted beams with high resolution and intensity, despite the substantial divergence of the beams produced by the X-ray tubes.

Once produced by the source, the incident beam irradiates the top-surface of the sample, undergoes the diffraction process and emerges from the same top-surface before being measured by the detector. Due to the path followed by the beam, the technique is described as using a reflection geometry, by contrast with the transmission geometry, for which the beam goes through the sample. On thick samples, the reflection geometry allows the use of less brilliant beams than the ones required for diffraction in-transmission. This enables once again the use of X-ray tubes as sources for the beam, which are compatible with a laboratory diffractometer.

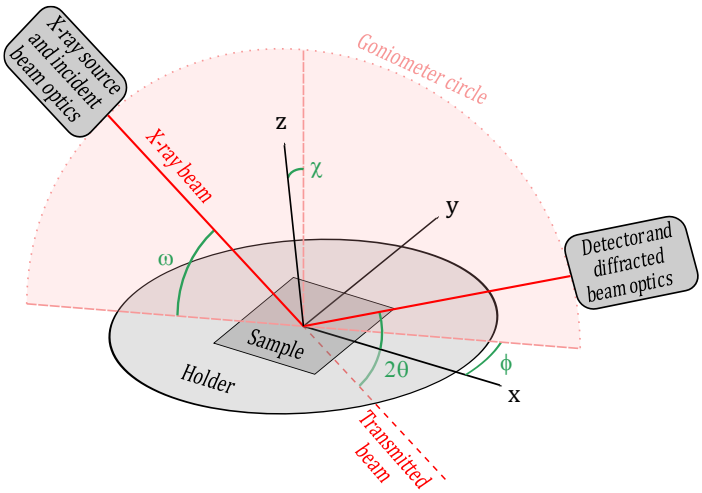

Figure 2.4 : Sketch depicting the main components of a diffractometer in Bragg-Brentano geometry. The angles associated to the four rotations of the diffractometer and the three movement axes of the sample holder are shown. The plane containing the goniometer circle and the X-ray beam is highlighted in red.

For HRXRD measurements on large crystals, diffractometers typically adopt a four-circle configuration, as it uses four different rotations to set the sample in diffracting conditions:

- The rotation associated to the ω angle between the surface of the sample and the incident beam. Either the X-ray source or the sample can be rotated to set this angle, depending on the model of the diffractometer.

- The detector rotation. In a Bragg-Brentano geometry, the detector is placed at the same distance from the sample than the source. Instead of the angle between the surface of the sample and the emergent beam (i.e. the angular position of the detector), the diffractometer user typically monitors the angle 2θ between the virtually transmitted beam and the emergent beam. For a given value of ω, this 2θ angle is directly determined by the angular position of the detector. However, it is simpler to set the sample in diffraction conditions by using 2θ angles, which correspond to twice the Bragg angle of equation (2.2), than by using the position of the detector.

- The sample rotation about the axis normal to the surface plane of the sample. The associated angle is designated as ϕ angle.

- The sample rotation about the projection of the incident and emergent beams on the sample surface. The corresponding angle is usually called χ angle.

Additionally, the sample holder can be moved in space along three axes (x, y, z), enabling the alignment of the sample height with the beam, as well as the selection of the zone of the surface plane (x, y) to be analyzed.

2.2.2. Measurement scans and reciprocal space mappings

To characterize a monocrystal with diffraction, HRXRD measurements on a four circles diffractometer are used. In the reciprocal space representation, the endpoint of the scattering vector $\vec{q}$ can be seen as a probe of the diffracted intensity, which is moved across the reciprocal space by modifying the diffraction angles. A rotation of the crystal (i.e. a modification of ω) leads to a rotation of the scattering vector $\vec{q}$, while a modification of 2θ changes the length of $\vec{q}$. By acquiring the diffracted intensity at different angular positions, we thus obtain a scan of the reciprocal space, with a direction depending on the diffraction angles used. The three most common scan types, represented in **Figure 2.5**, are:

- ω scans (also called rocking curves). This scan consists in a variation of the incident beam angle ω while keeping 2θ constant. The path of the scan in the reciprocal space is a circular arc centered on the space origin.

- 2θ scans. The ω angle is kept constant while 2θ varies. The scan follows a circular arc of radius $1/\lambda$ centered on the endpoint of $\overrightarrow{k_d}$.

- $2\theta - \omega$ scans. Both the angular positions of the source and the detector with respect to the sample vary, so 2θ changes twice as fast as ω. We obtain a linear scan along $\vec{q}$. These measurements are also referred to as radial scans.

Although they are less usual, other scan types like ϕ scans or scans along $\overrightarrow{q_z}$ at a non-zero $||\overrightarrow{q_x}||$ value can be used.

When the path of the scan (i.e. the endpoint of the probe $\vec{q}$) crosses a diffraction spot, a peak of diffracted intensity is measured and associated to a position in the reciprocal space through the values of the diffraction angles.

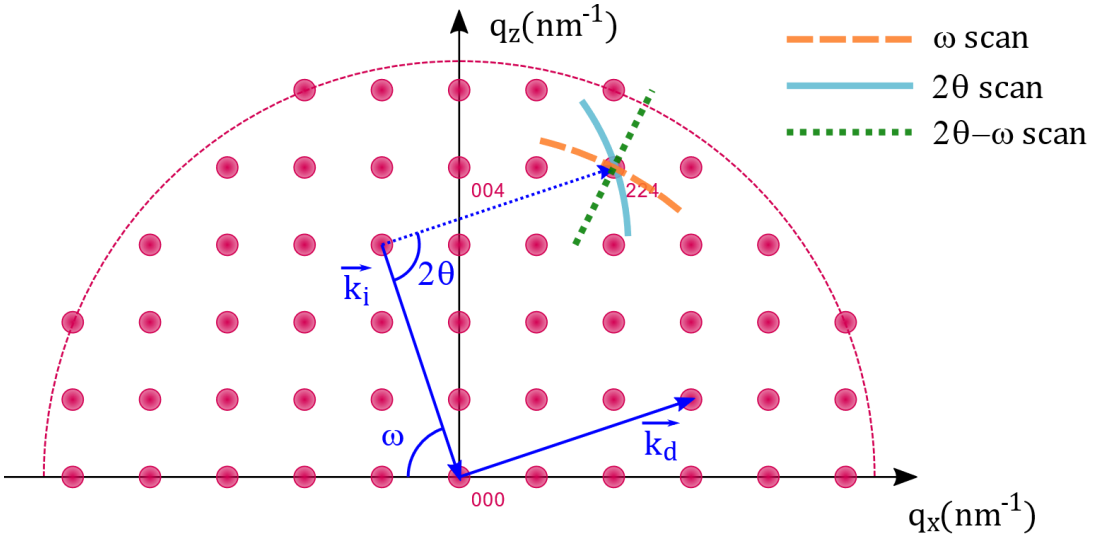

Figure 2.5: Representation in the reciprocal scape of the path of different HRXRD scans.

By carrying out several scans, we can obtain a two-dimensional mapping of a portion of the reciprocal space, around a given reflection. This process is illustrated in Figure 2.6 for a series of ω scans measured at different $2\theta - \omega$ values. Alternatively, series of 2θ or $2\theta - \omega$ scans can be used to acquire these reciprocal space maps (RSM). This type of measurement enables much more comprehensive analyses of the diffraction spots than a simple scan. However, RSM can be really long to carry out, due to the multiple scans to measure. Nevertheless, the measurement time can be dramatically decreased by using 1D or 2D detector, capable of measuring multiple 2θ positions simultaneously (see section 2.3.1).

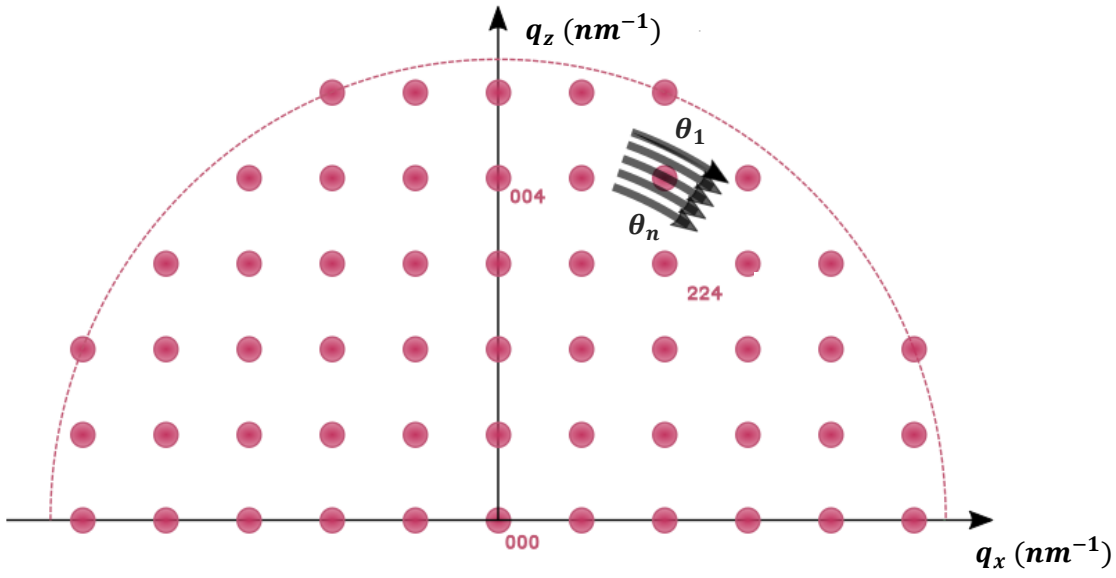

Figure 2.6 : Representation in the reciprocal space of an RSM measurement.

Like for simple scans, the data obtained when measuring an RSM are diffracted intensities at different angular positions. To obtain an image of the (q_x, q_z) reciprocal space system, this data needs to be transposed using the following expressions:

$$\begin{cases} q_x = \frac{2}{\lambda}\sin(\theta)\sin(\theta-\omega) \\ q_z = \frac{2}{\lambda}\sin(\theta)\cos(\theta-\omega) \end{cases} \quad (2.19)$$

The measurement of the XRD scans can be carried out either in absolute or in relative mode. In the absolute mode, the "true" calibrated values of θ and ω are used. The calibration of θ is made by matching its zero value with the peak of intensity of the direct beam (i.e. the beam directly arriving from the source without interacting with the sample). ω calibration consists of an alignment of the sample with this direct beam. First, the specimen's height is set by aligning its surface with the middle of the beam's height, resulting in a loss of half the intensity of the direct beam. The beam intensity is then recorded while rocking the sample about the ω axis. The measured peak of intensity corresponds to the ω position for which the sample surface is aligned with the incoming beam. This angle is chosen as the zero value of ω. This ω calibration is not rigorous as the inclination of the sample with the incident beam can vary with ϕ. Furthermore, the specimen may not be flat, especially when considering hetero-epitaxial III-N layers, due to the wafer curvature. In this case, the real value of ω varies with the chosen surface area of the specimen.

In order to avoid the limitations of angle calibrations, one can carry out XRD measurements in relative mode. In this case, the zero-values of θ and ω correspond to the angular positions measured on a reference diffraction peak. This reference peak needs to come from the substrate or any layer for which the lattice parameters are accurately known, so the relative measurement can be correctly repositioned in the reciprocal space. This kind of measurement is uncommon when characterizing III-N hetero-epitaxial layers, due to the lack of reliable reference peak. Indeed, the diffraction peaks of the substrates are widely separated from the III-N peaks. Additionally, these substrates and all the layers are strained, as shown by the curvature of the wafers, and their lattice parameters are therefore not known.

2.2.3. Measurement geometries

The HRXRD scans are normally limited to the reciprocal space area surrounding the diffraction spot of a given reflection (h, k, l). This is due to the wide angular separation between the different reflections and to the need of scans with high resolution and therefore low angular steps. Hence, before carrying out an HRXRD scan, one needs to access the reciprocal space area corresponding to the desired reflection by applying an appropriate rotation of the diffraction angles.

As shown in **Figure 2.7**, we distinguish different measurement geometries depending on which reflections are measured and how the diffraction angles are set to access it:

- The symmetric geometry concerns the measurements of the planes parallel to the surface of the sample. In this case, the angles ω and θ are equal.

- The asymmetric measurements are made on crystal planes tilted with respect to the surface of the sample. Compared to the symmetric case, an additional rotation ω_0 is applied on the crystal, so $\omega = \theta + \omega_0$. The ω_0 offset can either be chosen to be positive or negative. In the first case, the incidence angle of the beam is higher than its exit angle, and the geometry is described as having a grazing incidence. Otherwise, we say that the beam has a grazing exit. Measurements with both geometries are equivalent although grazing incidence is better suited to increase the measurement intensity, as the beam footprint is bigger and thus more material diffracts. Conversely, grazing exit geometry may improve the measurement resolution, due to a contraction the diffracted beam width.

- The skew symmetric geometry is an alternative to the asymmetric geometry to access the reflections of the planes non-parallel to the surface. The crystal is rotated 90° about the ϕ axis and tilted about the χ axis with an angle equal to the inclination of the diffracting planes with respect to the surface.

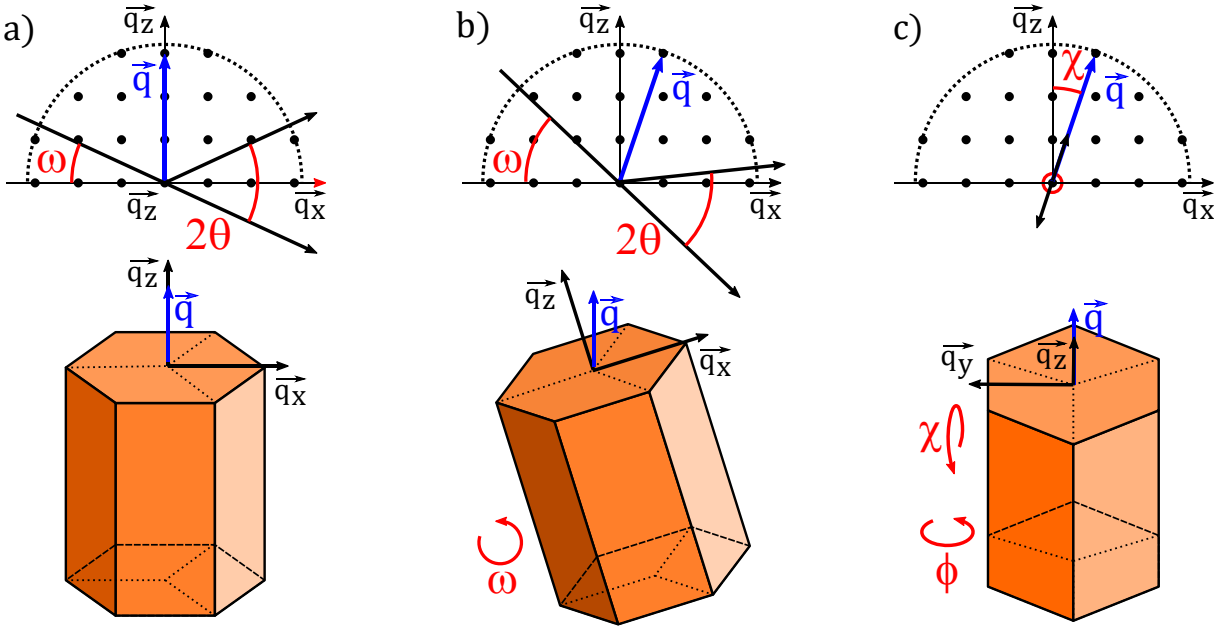

Figure 2.7 : The HRXRD measurement geometries. a) Symmetric geometry. b) Asymmetric geometry (grazing exit). c) Skew symmetric geometry. For each geometry are shown the rotation of the scattering vector $\vec{q}$ in the reciprocal lattice and the rotations of a unit cell of the crystal in the real space. For the skew symmetric geometry, the angles ω and 2θ are depicted with a red circle as their axis of rotation coincides with the $\vec{q_x}$ axis and they are out of the plane of the sheet.

The terms employed for the measurement geometries are often extended to the (h,k,l) reflections used for diffraction. Hence, we designate as symmetric the reflections of the planes parallel to the surface, while the ones tilted with respect to the surface are referred to as asymmetrical reflections.

We have seen in the section 2.1.3.c) that some (h,k,l) reflections cannot be used in diffraction measurements as their structure factor is equal to zero and they have no intensity.

Besides this forbidden reflection rule, the geometry of measurement induces further limitations on which (k, k, l) planes can be measured. Due to the reflection geometry used, no signal is detected when the path of the X-ray goes through the sample depth. This can happen either when the incident beam hits the back surface of the sample ($\omega < 0$) or if the direction of the diffracted beam points below the surface of the sample ($2\theta < \omega$).

Further constrains are brought by the angular limitations of the diffractometer, like the angular ranges of the source (ω angle), the detector ($2\theta - \omega$ angle) and the χ rotation, or the minimum distance between the source and the detector ($\pi - 2\theta$ condition).

2.3. Experimental setup

2.3.1. Detectors

Since the first developments of XRD techniques to analyze the matter structure, in the early 20th century, diffractometers have gradually evolved to rather complex machines, such as the four-circles diffractometers used for this thesis. The success of XRD techniques have led to the apparition of numerous variants of each of the diffractometer components, from source to detector.

X-ray detection systems are a good example of these evolutions, from the photographic films which used to be employed to modern detectors. Nowadays, three different technologies of X-ray detectors are usually used on laboratory diffractometers: the scintillation counters, the solid-state detectors and the gas-filled proportional counters. The scintillation counters contain a fluorescent crystal, usually made of NaI activated with 1% of Tl.[80] When the diffracted beam passes through the aperture of the detector, an amount of X photons proportional to the intensity of the incoming beam is generated by fluorescence. This fluorescence signal is eventually detected by a photomultiplier tube. The detected diffracted intensity is thus expressed as a quantity of counted photons. The scintillation counters have a high efficiency, which means a high ratio of detected photons to entering photons.

Unlike scintillation counters, the solid-state detectors carry out a direct measurement of the diffracted beam intensity. Their sensitive material is made of a semi-conductor, usually of Si or Ge. When the diffracted beam hits this crystal, the photoelectric effect induces the excitation of electrons from the valence band to the conduction band. The created electron-hole pairs are then collected and taken as a measurement of the beam intensity. These solid-state detectors are sometimes coupled with a scintillator and use the fluorescence signal to make an indirect measurement of the diffracted intensity, as described earlier. The efficiency of these detectors is also high, although they may saturate earlier than scintillation counters when measuring highly intense beams.

The proportional counters are made of a cathode chamber filled with an inert gas and containing a wire anode in its center. The chamber has a cylindrical shape with an X-ray transparent window on one side. When the X-ray beam passes through this window, it ionizes the detector's gas, generating electrical charges which are accelerated toward the anode, for

the electrons, and the cathode, for the positive charges, by applying a 600 to 900 volts potential.[81] While moving toward the anode, the electrons strike the non-ionized atoms of the gas, causing additional ionization and therefore an amplification of the signal measured by the wire anode. The efficiency of proportional counters is lower than the one of scintillation and solid-state devices. Nevertheless, they are highly linear. This means that from low to high intensity beams, they are able to keep a constant proportion between the number of incoming and measured photons.

Independently of the technology of fabrication, the X-ray detectors are classified in three categories, depending on their dimensions of observation. The punctual detector, or zero-dimension (0D) detector, allows an intensity measurement at a given angular position. The one-dimension (1D) and two-dimensions (2D) detectors carry out simultaneous measurements at multiple points in space, respectively along one and two space directions. This enable faster scan measurements, which is especially useful to achieve a reciprocal space mapping, as presented in the section 2.2.2.

2.3.2. Optics and beam properties

The beams produced by X-ray tubes are far from being perfect. When leaving the source, the beam is non monochromatic, due to the emission of several characteristic lines and the continuous Bremsstrahlung signal (see **Figure 2.1**). Even when focusing on the K_α line, the emission is divided in a doublet $K_{\alpha1}$ and $K_{\alpha2}$, only separated by in the wavelength spectrum by 0.0038 Å (i.e. a relative separation $\delta\lambda/\lambda$ of 0.25%).[82] The two contributions of the doublet are therefore found on the diffracted pattern, which can lead to imprecisions in the measurement of diffraction peak positions and widths. The X-ray beams also have a significant divergence, which means that the rays composing the beam are slightly non-parallel, as shown in **Figure 2.8**. This effect can induce a loss of resolution in the diffraction measurements. One last property of the beam that needs to be considered is the dimension of its footprint on the sample. Its size depends on the angle of incidence ω of the X-rays, on the dimensions of the beam (width and height) and on the corresponding beam divergences. The dimensions of a typical X-ray beam of a laboratory diffractometer is a rectangle of 10 mm × 1.5 mm. Several issues can arise from an excessively large dimension of the beam footprint, such as the measurement of unwanted areas of the sample or a substantial alteration of the diffracted signal due to the sample curvature (see section 2.4.2). Conversely, an undersized beam footprint means less diffracting material and thus a deterioration of the measured signal.

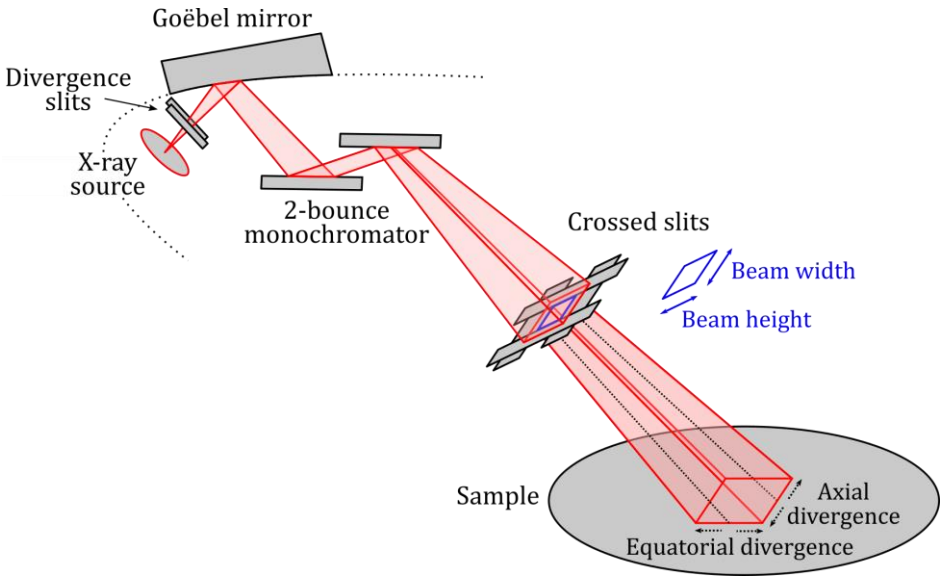

Figure 2.8: Modifications of the incident beam by a set of HRXRD optics.

In order to improve the quality of the beam, several X-rays optics can be added in the beam path. Their use is essential to allow a high-resolution X-ray diffraction (HRXRD), which is required for the study of monocrystals, such as the III-N layers studied in this thesis. The most important optics for HRXRD applications are described below:

- The attenuators and filters. The X-ray beam can sometimes be so intense that it saturates the detector. This is especially true for the intense reflections of quasi-perfect monocrystals, like Si. It may also happen during the alignment of the goniometer, when measuring the direct beam, which means a beam that has not undergone any interaction with the crystal. To solve this issue, an X-ray attenuator can be added in the X-ray path, usually between the source and the sample. It consists of a thin metallic foil which absorbs a portion of the beam intensity. Some attenuators can also be used as selective filters to absorb a part of the X-ray spectrum, like the K_β line of copper which is absorbed by titanium foils.

- The mirrors. For X-radiations, the total reflection of the beam with conventional mirrors can only be obtained at very low incidences. The X-ray mirrors use instead the diffraction phenomenon to “reflect” the beam. They are made of multilayered materials, with controlled interlayer distances, having an elliptical or a parabolic shape. The most common of these optics for HRXRD applications is the Göbel mirror. It is placed after the X-ray source, which is located at the focus of its parabolic shape. This enables a large collection of the highly divergent beam coming from the source and its transformation in a much more parallel reflected beam, with less than 0,1° of equatorial divergence. Due to the high amount of X-rays turned parallel, the mirror permits the obtention of a much more intense incident beam than by collimating it to reduce the divergence. Furthermore, the wavelength of the beam is monochromatized around the K_α line during the process.

- The monochromators. These optics are made of perfect crystals which diffract the incident beam with a reflection geometry. Hence, only the rays with an angular direction following

the Bragg's law of the monochromator's crystals are guided toward the sample. This results in a highly monochromatic beam, as these devices are able to separate the $K_{\alpha 1}$ and $K_{\alpha 2}$ lines of copper. Furthermore, the beam divergence is also reduced. The use of this optic is therefore mandatory for an HRXRD measurement, even though it substantially reduces the intensity of the incident beam. There are a wide variety of monochromators, differentiated by the number of diffracting crystals they contain, the nature of these crystals, their orientation and the (h, k, l) diffracting planes that are used. A four-bounce monochromator (also called Bartels monochromator), containing four diffracting crystals, will generate a beam with a lower divergence than a two-bounce monochromator, at the cost of a higher loss of intensity (see **Figure 2.9 a)**). Furthermore, the instrumental resolution of ω scans measured with monochromators varies with the Bragg angle[83] (**Figure 2.9 b)**) . Two-bounce monochromators have an optimal θ value, for which their resolution is minimal. Conversely, four-bounces models keep a rather constant resolution below a high θ threshold.

a)

Monochromator	Divergence (arcsec)	Relative intensity
2-bounce Ge(220)symmetric	36	100
4-bounce Ge(220) asymmetric	25	80
4-bounce Ge(220)symmetric	12	20
4-bounce Ge(440) symmetric	5	0.7

b)

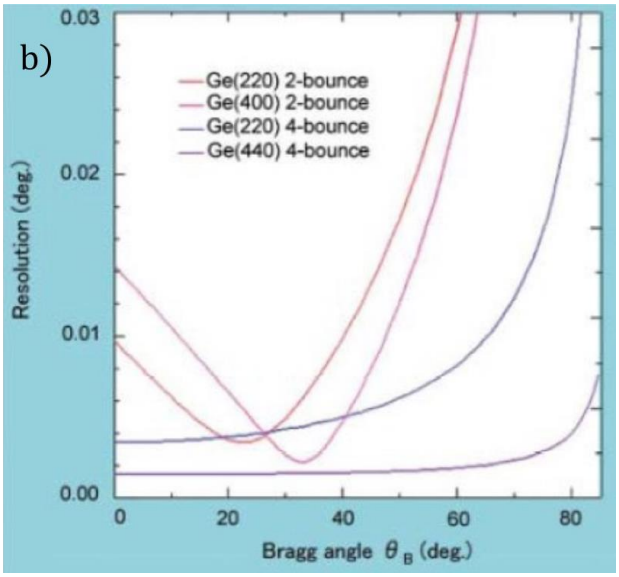

Figure 2.9 : Characteristics of a set of monochromators. a) Table of the beam divergence and beam relative intensities. b) Evolution of the resolution of ω scans with the Bragg angle. The figure is reproduced from reference.[83]

- The analyzer crystal. This device is similar to a monochromator although it is placed in the diffracted beam path, just before the detector. Its purpose is to only select the diffracted rays which arrive toward the detector with a quasi-exact 2θ angle. This eliminates the divergent rays of the beam, thus improving the measurement resolution and precision of the scan in the reciprocal space. When the analyzer crystal is used, the diffractometer is described as set in triple axis mode. When the analyzer crystal is removed, the measurements have a higher intensity. In this case, we say that the diffractometer is set in double axis mode.

- The slits. The purpose of these optics is to cut a portion of the X-ray beam. They are either made of two metallic absorbing foils, separated from each other by a gap, or of a single metallic piece in which an aperture has been made. Either way, the aperture/separation

has a large height and a small and precisely controlled width. We distinguish several types of slits. The divergence slits are usually placed right after the source and reduce the equatorial divergence of the beam (see **Figure 2.8**). Conversely, the receiving slits are located right before the detector, in double axis mode, to increase the resolution of the measurement. Finally, variable crossed slits can be added to the incident beam path. This pair of adjustable slits allows a precise control of the two dimensions of the beam footprint on the sample.

2.3.3. Diffractometers used during the PhD

In order to develop characterizations methods compatible with a metrological framework, three laboratory diffractometers were used for this thesis. All of them use the general structure and measurement geometry presented in the section 2.2.1. Their sources are X-ray tubes producing a Cu $K_{\alpha 1}$ radiation from a copper anode.

The first diffractometer is a Bruker JV-DX, designed for the characterization of wafers of 200 mm and 300 mm diameter in a cleanroom facility. This tool is fully automated (samples handling, alignments and recipe-based measurements) and therefore ideal for metrological measurements on a batch of up to 25 wafers. It has two copper anode X-ray sources, a classical one producing a beam with millimetric dimensions and a second one generating a micro-beam for the study of patterned samples. Its automated package of optics includes a set of slits, a mirror, two interchangeable monochromators 2-bounce Ge(220) and 2-bounce Ge(004) and an analyzer crystal. As shown in the **Figure 2.9 b)**, the Ge(220) monochromator is relevant for measurements at low Bragg angle (θ<30°), like for the (002), (101) or (102) reflections of GaN. Beyond this limit, the Ge(004) monochromator should be used to maximize the measurement resolution, at the cost of a slight reduction of the beam intensity. Due to the space occupied by the two sources, the angular ranges of this diffractometer are limited (-5°<ω<95° and -5°<χ<45°). This blocks the measurement of some reflections on GaN samples like the symmetric (006), the asymmetric (213) and (205) or, in skew symmetric geometry, all the diffracting planes tilted with respect to the surface by an angle higher than 45°.

To overcome these limitations, we used a second cleanroom diffractometer, a Panalytical X'Pert Pro. This tool is also adapted to the measurement of 200 mm and 300 mm wafers, although the sample and components handling is manual, and the alignment procedures are not automated. The incident beam optics used for the measurements include a divergence slit and a hybrid mirror/4-bounce monochromator. On the diffracted beam side, two optical paths are mounted simultaneously to switch between double and triple axis modes. The double axis path has a 1mm wide receiving slit while the triple axis is equipped with a 3-bounce Ge(220) analyzer crystal. Two similar 0D scintillation detectors are mounted on both paths.

Finally, we used a third diffractometer located outside of the cleanroom facility. This diffractometer is also a Panalytical X'Pert Pro, but adapted to a wide range of sample sizes, from a 200 mm wafer to a millimetric sample. This tool is not suited for a cleanroom metrology framework but enables to work on small samples and to carry out more diverse measurements,

as its configuration can be adapted as desired. In its usual configuration, the components of this diffractometer are the same than for the first X'Pert Pro, except for the hybrid monochromator which is replaced by a mirror and an asymmetrical 4-bounce Ge(220) monochromator with higher resolution and lower intensity, the addition of cross slits and the double axis 0D scintillation counter replaced by a 2D solid state detector, allowing for easier RSM measurements.

2.4. Characteristics of diffraction peaks and HRXRD analyses

2.4.1. Peak position analyses

HRXRD techniques focus on the measurement of the diffraction spots of a set of chosen (h,k,l) reflections. The obtained data is often analyzed along a line of the reciprocal space, either corresponding to a 1D scan, or to a cut in a 2D RSM. The resulting 1D diffraction peak is characterized both by its position and its shape.

The position of a diffraction peak is directly linked to the mean distance between the crystal planes by Bragg's law (equation (2.2)). This peak position is widely analyzed, as it permits to obtain the main information on the crystal structure. For III-N materials, the position of diffraction peaks is usually used to evaluate the lattice parameters, the composition of an alloy or the mean strain in the layers. These characterizations, which are already well known and widely used, are not further developed in this thesis. Nevertheless, due to their importance, a brief summary of the main measurement methods is given in the following. For a fully comprehensive description, the reader is referred to the third chapter of the review of *Moram et Vickers* on XRD measurements on III-N crystals.[4]

The lattice parameters a_0 and c_0 of a hexagonal III-N crystal are linked to the interplanar distance d_{hkl} by the expression:[84]

$$\frac{1}{d_{hkl}^2} = \frac{4}{3}\frac{h^2+hk+k^2}{a_0^2} + \frac{l^2}{c_0^2} \tag{2.20}$$

c_0 is obtained from one or several measurements of interplanar distances d_{00l} on symmetric XRD reflections, using equations (2.2) and (2.20). High 2θ reflections, like (004) and (006) should be used to reduce the measurement errors.[4] The parameter a_0 is then deduced from the value of c_0 and one or several interplanar distances measured on asymmetrical reflections. The diffracting planes should ideally be chosen highly tilted with respect to the surface, so d_{hkl} is highly impacted by a_0.

Any addition of tensile or compressive strain to a relaxed crystal leads to a modification of the interplanar distances in the strained direction, and therefore to a shift of XRD peaks along the same direction in the reciprocal space. This is readily understandable by assuming that a constant strain ε_{hkl} is applied to the crystal in the direction normal to a set of (h,k,l) planes. By definition:

$$\varepsilon_{hkl} = \frac{d_{hkl} - d^0_{hkl}}{d^0_{hkl}} \quad (2.21)$$

where d_{hkl} is the interplanar distance in the strained crystal and d^0_{hkl} the interplanar distance in of a relaxed crystal. If the lattice parameters a_0 and c_0 of the relaxed crystal are known, one can calculate d^0_{hkl} using equation (2.20). By measuring the θ position of the peak and using Bragg's law (equation (2.2)), d_{hkl} and thus ε_{hkl} can be determined.

In hetero-epitaxial III-N layers, this analysis can be used to determinate the tensile or compressive strain arising from the differences in thermal expansion coefficients between the substrate and the film (see section 1.2.2), or to measure the relaxation state of a film in a stack of mismatched III-N layers.[4]

Variations in III-N alloys composition induce a global expansion or contraction of the crystal lattice. The lattice parameters of the alloy can be estimated using the mole fractions and lattice parameters of its binary III-N compounds. For a ternary $A_xB_{1-x}N$ compound, the following Vegard's law is commonly used on c_0 lattice parameters:[85]

$$c_0^{A_xB_{1-x}N} = x\, c_0^{AN} + (1-x)\, c_0^{BN} \quad (2.22)$$

The mole fraction x of the AN elementary compound is easily determined from this relationship and a measurement of $c_0^{A_xB_{1-x}N}$ on a symmetric reflection.

2.4.2. Peak width analyses

a) Sources of peak broadening

The shape of the diffraction peaks contains a lot of supplementary information to the one apported by the peak position. We can divide the diffraction peak in two zones: its central part and the tails.

The intensity of the tail zone is scattered by parts of the matter where the structure varies widely from the rest of the crystal structure, like in highly strained zones immediately surrounding a lattice defect. In the tails, the intensity does not follow the same trends than in the central part. This peculiar signal is called diffuse scattering.

However, XRD analyses usually focus on the central signal of the peak, which contains most of the diffracted intensity. It is useful to characterize this peak by its width, which indicates whether the diffraction is ideal or imperfect. Indeed, an infinite perfect crystal has, in every area, constant interplanar distances, associated to constant θ angles. Hence, the diffraction peaks of such a crystal are extremely narrow. Conversely, broad diffraction peaks are found when measuring small or highly defective crystals.

The width of XRD peaks can be quantified by its integral breadth, which is equal to the peak area divided by the intensity maximum. This corresponds to the width of a rectangle of

same height than the peak. A simpler and more common approach consists in measuring the width of the peak at half of the maximum intensity. This width is called FWHM, which means full width at half maximum. The two breadth values are close in the case of a diffraction peak with gaussian shape, as the ratio FWHM on integral breadth is 0.94, while it is equal to 0.64 in the case of a peak with a Lorentzian shape.[86]

The breadth of a diffraction peak is impacted by numerous factors. The measured width β_m of a peak is usually described as a quadratic sum of all these broadening components:[87],[88],[4]

$$\beta_m^2 = \beta_0^2 + \beta_d^2 + \beta_\alpha^2 + \beta_\varepsilon^2 + \beta_L^2 + \beta_r^2 \tag{2.23}$$

where β_0 is the Darwin intrinsic peak width associated to the measured crystal and β_d the instrumental resolution of the diffractometer. β_α, β_ε, β_L and β_r are the respective broadenings due to misorientations of the lattice, to the local strain, to the limited correlation lengths (also called size effect) and to the curvature of the sample.

All these sources of broadening are found in III-N layers diffraction. While β_0 and β_d are often considered as negligible, β_L and β_r can substantially impact the measured breadth, which is usually driven by β_α and β_ε.

While a global strain, which remains constant in the whole crystal, results in a shift of the diffraction peaks, the broadening β_ε comes from variations of the strain throughout the lattice, owing to the presence of stress gradients or lattice defects like dislocations.

The broadening β_α is the consequence of a rotational disorder within the crystal lattice. This can be understood by means of the mosaic block model. The crystal is considered as being composed by a set of subdomains, misoriented with respect to one another because of lattice rotations. In the case of a monocrystalline layer, we distinguish two kinds of lattice rotations. As represented in **Figure 2.10**, the misorientation caused by rotations of subdomains about the normal of the surface plane is called twist, while the rotations about the axes lying in the surface plane induce a tilt of the lattice.

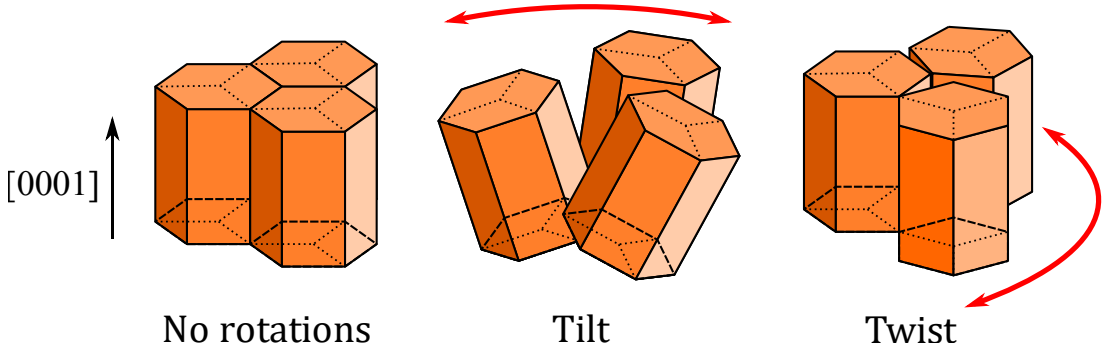

Figure 2.10 : Mosaic tilt and twist. The rotated domains are represented for a [0001]-oriented III-N layer.

The spread of XRD spots in the reciprocal space is oriented along one or several directions, which depend on the nature of the broadening effect (see **Figure 2.11**). Lattice rotations broaden the diffraction spots along an arc-shaped direction. The broadening orientations

corresponding to tilt and twist are easily understandable, as they correspond to the real-space rotations of the domains in the mosaic blocks representation. Hence, lattice tilt induces a broadening oriented about the lines of the (q_x, q_y) plane passing through the reciprocal space origin, while the twist broadening spreads about the q_z axis. Conversely, strain variations along a lattice direction generate a distribution of interplanar distances. The resulting broadening happens along a straight line passing through the XRD spots and oriented in the strained direction. The same happens for the size effect, which causes a straight broadening in the direction of limited correlation length.

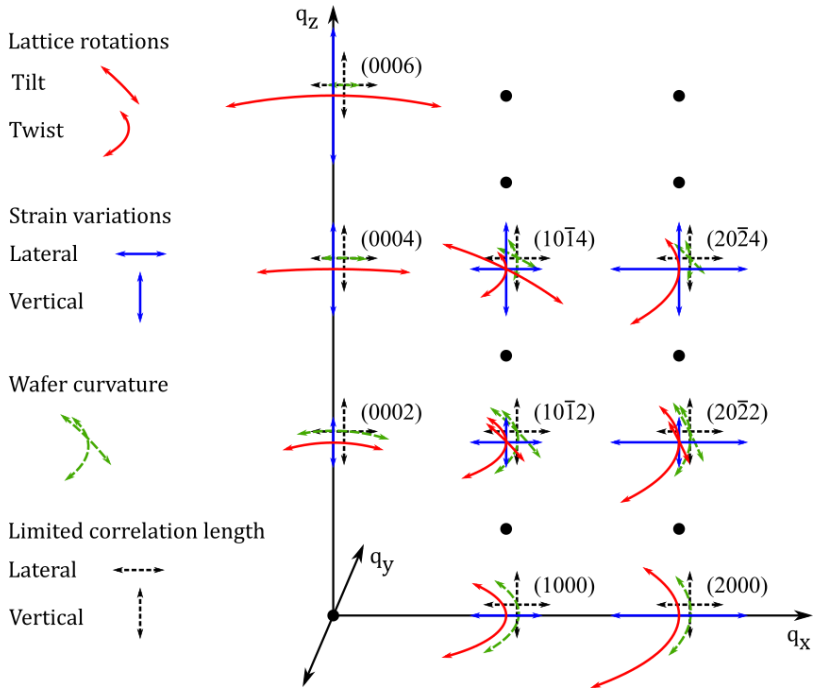

Figure 2.11 : Directions of broadening of diffraction spots in the reciprocal space.

b) Estimating the impact of the broadening effects

Although the broadening effects spread the diffraction spots in a variety of directions, their contributions may add together, as expressed in the equation (2.23). For example, an ω scan on a symmetric reflection can undergo a simultaneous broadening from the lattice tilt, the wafer curvature and a limited lateral correlation length. In order to decorrelate these contributions, it is useful to evaluate the impact of each broadening effect.

In HRXRD, the instrumental resolution β_d is highly reduced by using monochromators and analyzer crystals. Its value, which depends on the chosen optics, the direction in the reciprocal space and the 2θ angle, is normally of the order of a few tenths of arcsec.

The Darwin width β_0 is usually considered to be negligible in III-N materials, as it is equal to a few arcsec. Its FWHM value can nevertheless be calculated using the equation (2.18). For GaN, it is equal to 8.5 arcsec for the (002) reflection, 2.3 arcsec for the (004) and 2.7 arcsec for the (006).

An estimated value of β_r can be calculated in the case of a uniform spherical bending of the measured wafer:[87],[88],[89]

$$\beta_r = \frac{w}{\mathrm{R}^2 \sin^2 \theta} \tag{2.24}$$

R is the radius of curvature of the sample and w the dimension of the beam footprint on the diffracting plane, in the direction parallel to the χ axis. w can be lowered by limiting the size of the X-ray beam with cross-slits, or by reducing the surface of the specimen by using a mask or cutting the sample.

The broadening β_L arises from the presence of diffraction domains of limited size (see section 2.1.3.c), with dimensions of a few micrometers or less. Historically, this broadening has been studied for the analysis of polycrystalline materials, where the diffraction domains are associated to the crystallites forming the samples. In 1918, *Scherrer* was the first to publish an eponym relationship between β_L (given in units of 2θ) and the domain size L:[90]

$$\beta_L = \frac{K\lambda}{L \cos \theta} \tag{2.25}$$

In this equation, K is the Scherrer constant. *Scherrer* derived its value using the FWHM as a breadth measurement of a diffraction peak with gaussian profile. Assuming a diffracting domain with spherical shape, he found $K = 0.94$. The actual value of the Scherrer constant depends on the definition adopted or the breadth β_L (FWHM or integral breadth), on the average shape of the diffracting domains and on the reflection (h, k, l) considered when the domains are non-spherical.[86] Nevertheless, K remains relatively close to the value given by *Scherrer* as it ranges, for the most common domain shapes, from 0.73 to 1.03 when using the FWHM and from 0.98 to 1.39 when using the integral breadth.[86]

The β_α breadth can be quantified by means of the misorientation α, which corresponds to the mean angle between the mosaic blocks.[91] For β_α corresponding to the integral breadth and α being related either to a lattice tilt or twist, we have:[4]

$$\beta_\alpha = \alpha \tag{2.26}$$

A deeper derivation of β_α estimations is provided in the section 4.1.1 a), as the rotational disorder in the lattice is tightly linked to the distribution of dislocations in the crystal.

An expression linking the root mean square (RMS) strain ε of a crystal to the broadening of a $2\theta - \omega$ scan diffraction peak was given in 1944 by *Stokes et Wilson*, by neglecting the effect of rotations of the crystal cells.[92] For a broadening β_ε given in units of 2θ angle, this relation is equivalent to:

$$\beta_\varepsilon = 4\varepsilon \tan \theta \tag{2.27}$$

In practice, XRD peaks may undergo both strain and domain size broadenings. *Williamson et Hall* suggested a graphical method to decorrelate these two effects.[93],[94] By

using equations (2.25), (2.27) and assuming that the measured breadth corresponds to a direct summation of the strain and domain size broadenings ($\beta_m = \beta_\varepsilon + \beta_L$), they obtained:

$$\frac{\beta_m \cos\theta}{\lambda} = \frac{4\sin\theta}{\lambda}\,\varepsilon + \frac{1}{L} \tag{2.28}$$

Note that the Scherrer constant is taken equal to unity, which is fully acceptable owing to the uncertainties on its value.

By drawing on a graph $\beta_m \cos\theta\,/\lambda$ against $4\sin\theta/\lambda$ for a set of reflections, one obtains a linear plot with the slope corresponding to ε and the y-axis intercept corresponding to L. β_ε and β_L are then straightforwardly derived from equations (2.25) and (2.27).

A similar analysis can be carried out on ω scan peaks to separate the broadenings β_α and β_L due to the misorientation of the lattice and the limited correlation lengths. A plot of $\beta_m\, 2\sin\theta\,/\lambda$ against $2\sin\theta/\lambda$ gives a line with a slope α and a y-intercept $1/L$.[95]

Unlike the polycrystalline metals analyzed in the works of *Scherrer, Stokes et Wilson or Williamson et Hall*, a monocrystalline III-N layer is divided in a set of diffraction domains with similar orientation. It is therefore possible to analyze the strain and domain size in a direction orthogonal to a chosen set of diffracting planes, by collecting the XRD data on several orders of diffraction. On a III-N layer, by applying a Williamson-Hall plot to the $2\theta - \omega$ scans of a set of symmetric reflections, one obtains ε along the normal to the surface and the vertical size $L_\perp$ of the diffraction domains. The analogous Williamson-Hall plot on the ω scans of symmetric reflections gives the mean tilt α and lateral correlation length $L_{//}$.

It should be noted that the Williamson-Hall analyses presented here are strictly valid for diffraction peaks with Lorentzian shapes, due to the direct addition employed to sum the broadening contributions. The actual peak shapes of the strain, misorientation and sometimes domain size contributions are actually better represented by gaussian functions,[96] as assumed in the equation (2.23), or by Voigt functions[86] (i.e. the convolution of a Lorentzian and Gaussian function). A more accurate addition of β_L and $\beta_\varepsilon - \beta_\alpha$ should therefore lye in between the direct summation ($\sum\beta$) associated to Lorentzian profiles and the quadratic summation ($\sum\beta^2$) specific to gaussian profiles. As a consequence, the values of X-ray coherence length found using Williamson-Hall plots may be overestimated.[97] Further inaccuracy is brought by the uncertainties on the value real value of the Scherrer constant, which is usually taken equal to 1 (equation (2.28)). Williamson-Hall plots should therefore be used as an estimation of the magnitude of ε, α and L, rather than a precise determination of these parameters.

2.4.3. Orders of stress and comparative impact on the diffracted signal

Lattice distortions within a crystal are either caused by applied stresses, due to forces which originate from outside of the material, or by residual stresses independent of these

outside forces. Heteroepitaxial III-N materials are highly affected by residual stresses, especially owing to the high lattice mismatch and difference of coefficient of thermal expansion between substrate and layers.

We have seen in the sections 2.4.1 and 2.4.2 that a strained lattice can cause both a shift in position and a broadening of diffraction peaks. It is useful to adopt a classification of the residual stresses responsible for this strain to clarify the impact of lattice distortions on XRD signal. Three orders of stress are usually distinguished:[98]

- The first-order stress (σ_I) corresponds to the average residual stress within the material. If the crystal has a volume V, it is defined by:

$$\sigma_I = \frac{1}{V}\int_V \sigma(\vec{r})\, dV \tag{2.29}$$

where $\sigma(\vec{r})$ is the stress value at a position $\vec{r}$ of the volume V. This macroscopic stress (or macro-stress) is responsible for a global change in the interplanar distances of some ($hkil$) planes, and thus a macroscopic strain along the normal to these planes. This results in a global shift of XRD peaks for the corresponding ($hkil$) reflections (**Figure 2.12 b)**). The biaxial stress in heteroepitaxial III-N layers, stemming from differences in thermal contraction behavior compared to the substrate, is an example of first order stress.

- The second-order stress (σ_{II}) is defined as the mean deviation, at a local scale from the first order macro-stress. In polycrystalline materials, the local scale is typically taken as the volume V_L of a single crystallite. This stress is therefore equal to:

$$\sigma_{II} = \frac{1}{V_L}\int_{V_L} (\sigma(\vec{r}) - \sigma_I)\, dV \tag{2.30}$$

By analogy, we can divide the lattice of a monocrystals in a set of areas within which the mean strain differs from its macroscopic value. This treatment is relevant in the case of gradients of biaxial stress which form along the normal to the surface of III-N layers, owing a progressive relaxation of the lattice. Such local variations induce a broadening of XRD peaks, which can possibly be asymmetric (**Figure 2.12 c)**).

- The third-order stress (σ_{III}) corresponds to a deviation from the mean local strain value:

$$\sigma_{III} = \sigma(\vec{r}) - \sigma_I - \sigma_{II} \tag{2.31}$$

σ_{III} is a micro-stress, as it acts at a very local scale (i.e. small compared to a local volume V_L). It is necessarily due to a crystal defect whose stress field has a mean value of zero. In III-N crystals, this is typically the case of threading dislocations (see section 1.3.1 b)). By analogy, the strain stemming from third order stresses is called micro-strain. The mean value of third order micro-strain is also equal to zero, as the expansions of the lattice are

compensated by its contractions. Hence, σ_{III} results in a symmetrical broadening of XRD peaks, as shown in **Figure 2.12 d)**.

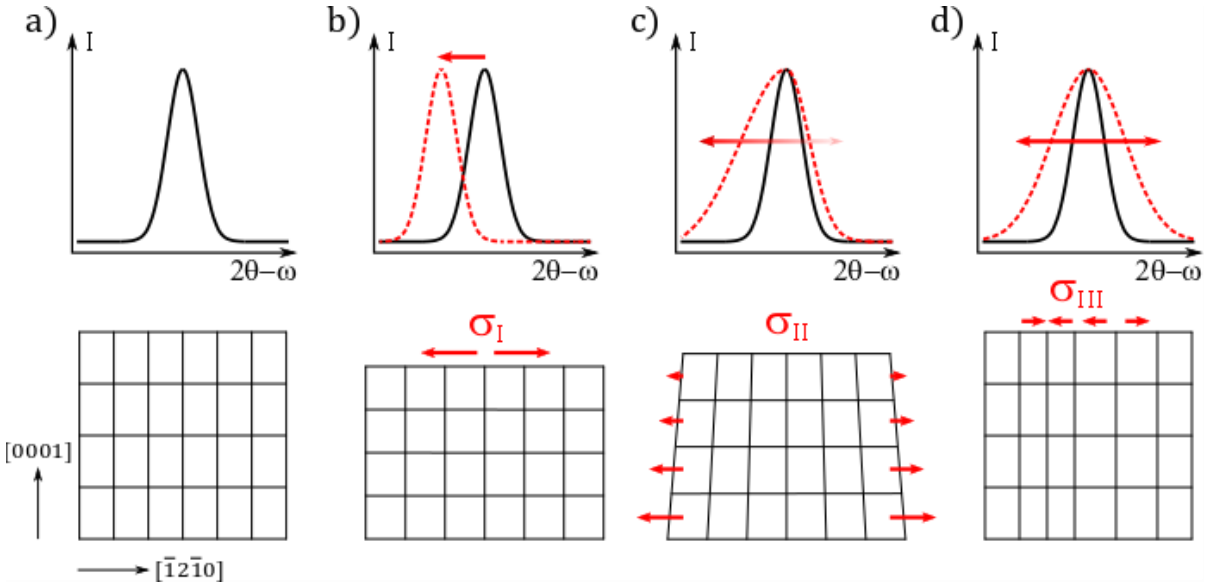

Figure 2.12 : Impact of mechanical stresses on diffraction peaks. For each order of stress, an example of lattice distortion in the $[10\bar{1}0]$ plane and the associated impact on the $2\theta - \omega$ scan a $(\bar{1}2\bar{1}0)$ reflection is depicted. a) No stress. b) First order stress σ_I. c) Second order stress σ_{II}. d) Third order stress σ_{III}.

The theory of XRD peak broadening presented above provides a fast and accessible solution to study the strain field of a crystal. Despite the wide use of these analyses, the accuracy of the results may be reduced by the numerous hypotheses made on the shape of the diffracting domains and the characteristics of the diffraction profiles. Furthermore, this treatment only allows a determination of the RMS value of strain. In heteroepitaxial GaN-on-Si layers, the presence of stress gradients through the layer thickness leads to complex asymmetrical XRD peak profiles, whose shape contains information on the evolution of strain within the lattice. To accurately measure these stress gradients, it is necessary to go beyond the classical analyses presented previously. To this end, we will present in the next chapter an approach based on the numerical simulation of the diffraction signals.

3. Stress gradient analysis

Gradients of in-plane stress of III-N layers have not seen significant analysis, likely due to the low magnitude of such gradients in the traditional III-N specimens, such as GaN layers grown on sapphire or SiC substrates. However, in GaN layers grown on silicon substrates, which is an increasingly common III-N usage, strong stress gradients are reported.[61] Hence, it is worth analyzing these stress gradients, considering that they are directly linked to crucial parameters of nitride crystals growth process, such as the profile of threading dislocation density, the curvature of wafers and even sample fragility.

In this chapter, we first demonstrate the presence of a stress gradient within a GaN-on-Si sample by Raman measurements, curvature measurements and XRD measurements. We then propose a simulation-based analysis of this stress gradient, relying on a program developed in Python language. The method aims at extracting profiles of strain along the c-axis from simple XRD radial scans on (002), (004) and (006) reflections (as it is sufficient for symmetrical measurements, three-index Miller notation will be used throughout this chapter). This computing tool differs from classic commercial XRD simulation software, as it is specifically designed for imperfect epitaxial layers such as GaN materials, in order to generate simulated data which better match the real XRD measurements.

3.1. Highlight of the stress gradient in our layers

To analyze stress gradients in GaN layers, we chose to focus our efforts on a GaN-on-Si sample grown at CEA-Leti, in an AIXTRON Crius R200 reactor. This sample of limited quality has a GaN film thickness of 1.85 µm, grown on an AlN/$Al_{0.5}Ga_{0.5}N$/ $Al_{0.25}Ga_{0.75}N$ stack of buffer layers. We chose this sample as it possesses a stress gradient of high magnitude, due to relaxation of compressive stresses during layers growth.

3.1.1. Raman measurements

Raman spectroscopy is a method of characterization frequently used for the determination of stresses in semiconductors. The technique consists of irradiating the analyzed sample with a monochromatic photon beam, and to measure the energy shift between this incoming beam and the beam scattered by the material. By doing so, one can measure the frequency of several modes of vibration of the crystal lattice. These frequencies are characterized in terms of the Raman shift, which is the difference of wavenumber between the laser source and the scattered beam. The Raman shift is directly linked to the strain state of the material.

In GaN crystals, this kind of measurement is usually performed by using the E_2 mode,[99] with an incoming beam oriented toward the c-axis. The beam (typically a green

laser),[99],[100],[101] normally scatters through a whole µm-thick GaN layer, thus giving a measurement of the main value of stress in the film.

In order to observe the variation of strain along the film thickness, we needed to carry out a cross section measurement of the film. This was achieved by using the alternative $E_1(LO)$ mode of vibration, which is compatible with this geometry of measurement. A 700 nm wide micro-beam, with a wavelength of 488 nm (green laser), was used to perform a series of measurements along the layer thickness, with a step of 100 nm between each point. The result of this experiment is shown in **Figure 3.1**. The evolution of Raman shift along the layer thickness clearly demonstrates the presence of a gradient of stress in the sample. However, unlike the E_2 mode, a conversion of Raman shift profile into a stress profile cannot be performed with the $E_1(LO)$ mode, as the corresponding phonon deformation potential has not yet been determined in the literature. In addition, despite the clear evolution of strain, the result is difficult to interpret due to the beam width, which covers roughly one third of the layer thickness for each measurement.

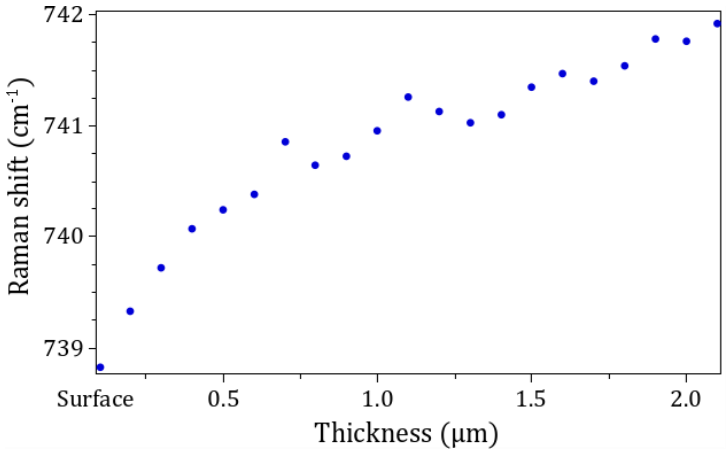

Figure 3.1 : Demonstration of the presence of a strain gradient in a GaN layer with a cross-section micro-Raman measurement.

3.1.2. Curvature measurement

The relaxation of stressed thin films is typically hindered by the substrate on which they are deposited/grown. To reach a mechanical equilibrium of forces and bending moments, such layer/substrate systems tend to bow, so the thin-film face adopts a concave shape when the film is under tension or a convex shape when it is under compression. The relationship linking the curvature κ of the sample to the stress in the film σ^f, is known as the Stoney equation:[62]

$$\sigma^f = \frac{E_s t_s^2 \kappa}{6 t_f (1 - \nu_s)} \tag{3.1}$$

In this equation, t_f and t_s are the thicknesses of the film and the substrate, E_s and ν_s are the Young's modulus and Poisson ratio of the substrate. The Stoney equation assumes that the

mechanical properties of the substrate are isotropic in the surface plane, that the deflection of the substrate is small compared to its thickness, that the total thickness $t_f + t_s$ of the system is small compared to its lateral dimensions, that $t_f \ll t_s$ and that the film perfectly adheres to the substrate. In addition, if the stress is treated as being constant across the film, one should verify that the thicknesses are uniform across the sample and that the curvature is spherical (equal in all the directions). Equation (3.1) can also be expressed in terms of the curvature radius $R_c = 1/\kappa$.

The curvature of the sample can easily be measured by XRD. The method consists in measuring the variation of ω angle position of an (hkl) diffraction peak along a line corresponding to the sample diameter. Several ω scans are carried out at points separated by a distance x. The curvature radius R_c between two points diffracting at angles ω_1 and ω_2 is:

$$R_c = \frac{x}{\omega_2 - \omega_1} \tag{3.2}$$

When analyzing global film stresses with the Stoney equation, it is best to measure R_c along at least two different diameters of the sample, to verify that the curvature is spherical.

Alternatively, the bow of samples can be measured by optical reflectance, for example by measuring the distance between two parallel beams reflected off the wafer.[61] Such a measurement can be carried out in-situ during the epitaxy of III-N layers, in adapted growth reactors. By monitoring the variation of sample curvature $\Delta\kappa$ during the growth of epitaxial layers, one can apply Stoney's equation on thin slices Δt_f of the growing film. Hence, the local stress σ_l^f in the film slice is obtained by:

$$\sigma_l^f = \frac{E_s t_s^2 \Delta\kappa}{6\Delta t_f (1 - \nu_s)} \tag{3.3}$$

This procedure has been applied in reference[61] to analyze the stress gradient in our GaN-on-Si sample. The result is shown in **Figure 3.2**. This method has frequently been used to determine stress gradients within GaN films, see for example references[60],[102]. Note that curvature measurements determine the global stress throughout the thickness of the GaN film. Hence, equation (3.3) assumes that no relaxation occurs within the layers previously deposited. This assumption seems reasonable in the case of compressive stress relaxation controlled by growing TDs (see section 1.3.2).

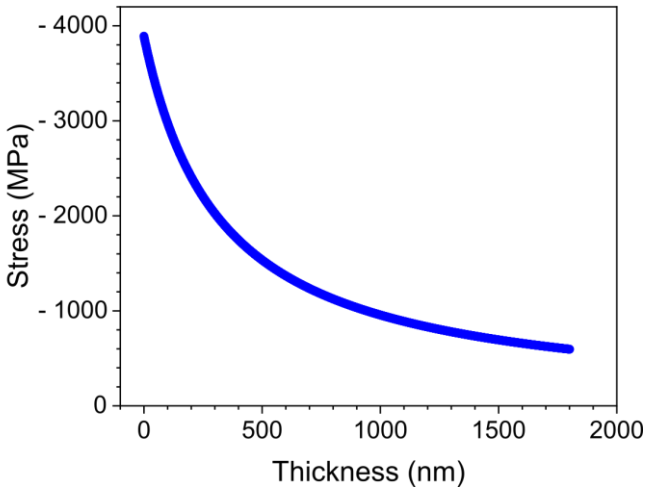

Figure 3.2 : Stress gradient in a GaN layer estimated from in-situ bow measurements. Negative stress values correspond to a compressive biaxial in-plane stress, positive values to a tensile stress. Optical reflectance measurements of bow acquired for the publication of the article[61] have been used to construct the stress gradient. A thickness step of $\Delta t = 1$ nm is used.

3.1.3. XRD peak position measurements

As explained in the section 2.4.1, the crystal strain can be readily deduced from measurements of the 2θ position of XRD peaks, for binary alloys such as GaN or AlN. The actual value of strain varies depending on the direction $\phi\chi$ of measurement, where χ corresponds to the inclination with respect to the surface of the sample, and ϕ to the azimuth, as represented in **Figure 2.4**. For a homogeneous and isotropic crystal, with Poisson ratio ν and Young's modulus E, the equation linking the strain $\varepsilon_{\phi\chi}$ in this particular direction to the stress field is given by:[98]

$$\begin{aligned}\varepsilon_{\phi\chi} = (1+\nu)/E\ (&\sigma_{11}\cos^2\phi\sin^2\chi + \sigma_{22}\sin^2\phi\sin^2\chi + \sigma_{33}\cos^2\chi \\ &+\sigma_{12}\sin 2\phi\sin^2\chi + \sigma_{13}\cos\phi\sin 2\chi + \sigma_{23}\sin\phi\sin 2\chi) \\ &-\nu/E(\sigma_{11}+\sigma_{22}+\sigma_{33})\end{aligned} \tag{3.4}$$

In thin films, out of plane stress components σ_{i3} $(i \in \{1,3\})$ are equal to zero at the surface and can only differ from this value inside of the film if there is a variation of in-plane stress components σ_{ij} $(i,j \in \{1,2\})$.[103] Hence, outside from thin film lateral edges, we have $\sigma_{13} = \sigma_{23} = \sigma_{33} = 0$, so equation (3.4) becomes:

$$\varepsilon_{\phi\chi} = (1+\nu)/E\ (\sigma_{11}\cos^2\phi + \sigma_{22}\sin^2\phi + \sigma_{12}\sin 2\phi)\sin^2\chi \\ -\nu/E(\sigma_{11}+\sigma_{22}) \tag{3.5}$$

The linear dependence of $\varepsilon_{\phi\chi}$ on $\sin^2\chi$ shown in equation (3.5) is used to determine the stress components σ_{ij}. This is achieved by constructing $\varepsilon_{\phi\chi}$ vs $\sin^2\chi$ plots from XRD measurements on various reflections and calculating their slope $(1+\nu)/E\ (\sigma_{11}\cos^2\phi + \sigma_{22}\sin^2\phi + \sigma_{12}\sin 2\phi)$.

In the case that the stress field is not constant through the thin film's thickness, the linear dependence of $\varepsilon_{\phi\chi}$ vs $\sin^2\chi$ may be replaced by a curved trend. Some methods aim at extracting stress gradients from the curvature of such $\varepsilon_{\phi\chi}$ vs $\sin^2\chi$ plot, such as in reference.[104] However, this kind of analysis cannot be applied in the case of thin layers with a thickness inferior to the penetration depth of X-rays. In such cases, $\varepsilon_{\phi\chi}$ vs $\sin^2\chi$ plots keep a linear trend even in the case of steep stress gradients.[103] This is the case in the GaN layers studied throughout this thesis, whose thicknesses are between 1 µm and 3µm, and in particular on the GaN-on-Si sample studied throughout this chapter, as shown in **Figure 3.3**.

In order to reach a shallower X-ray penetration depth, several alternative measurement geometries can be used.[103] However, these analyses are either not adapted to the measurement of strongly textured/monocrystalline samples, or require measurement geometries such as the in-plane mode or η-mode (rotation of the sample around the diffraction vector), which are not accessible on the diffractometers used during this PhD.

Further issues with these methods of extraction of stress gradient include the large number of measurements needed and the high precision required for the determination of interplanar distances.[103] The latter point is of special concern in the case of asymmetric line profiles caused by steep strain gradients, such as found in our samples (see the following section 3.1.4). In such samples, the shape of XRD peaks changes with the inclination χ and their global 2θ position should therefore not be used for the calculation of interplanar distances.[105] An example of this issue can be seen in **Figure 3.3**, were the calculated strain greatly varies for the three $(00l)$ reflections, despite having the same tilt $\chi = 0°$.

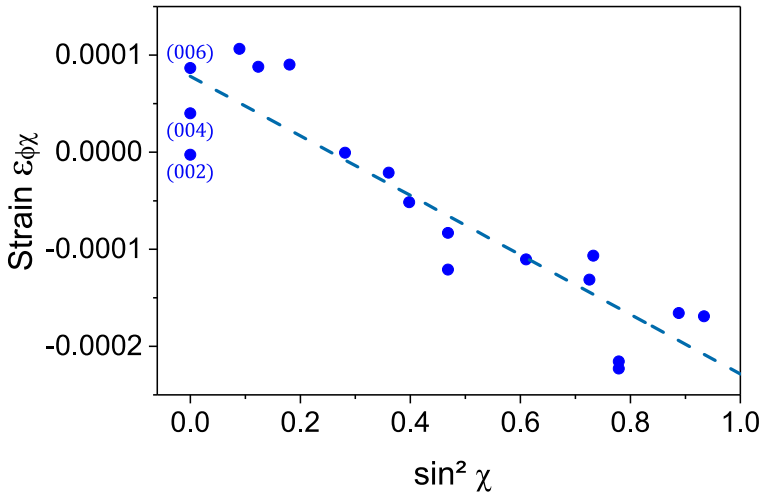

Figure 3.3 : Strain vs Sin²χ plot in a GaN-on-Si film. $2\theta - \omega$ measurements were carried out in skew symmetric mode on several planes tilted with respect to the surface with varying angles χ. Each data point corresponds to a measurement on one of the following reflections: (00l), (10l), (11l), (20l) and (302). XRD scans were fitted with split-Pearson7 functions to determine diffraction peak positions and calculate $\varepsilon_{\phi\chi}$ strain values. The linear fit (dashed line) shows the approximate linear behavior of the plot.

3.1.4. XRD peak shape measurements

Stress gradients may be considered as a succession of local deviations from the material mean stress, which corresponds to a second-order stress, as defined in the section 2.4.3. Following this definition, we can divide a thin film containing a gradient of in-plane stress into a set of sublayers, each associated with a local value of stress and thus with local values of strain. One can measure the crystal strain in the direction normal to the surface by carrying out a symmetric $\omega - 2\theta$ XRD scan. By doing so, all the local values of strain are measured at once, provided that the absorption of X-rays by the layer is low. The resulting diffracted signal can be seen in a first approximation as composed by an addition of diffraction peaks corresponding to each sublayer, whose position varies on the 2θ angles scale. The resulting diffraction profile is typically asymmetrical.

We use this sublayer description to extract a basic estimate of strain gradient in the studied GaN-on-Si sample. The low absorption assumption is verified by calculating the path length L of X-rays diffracted by the deepest sublayer of the GaN film of total thickness $t = 1.85\ \mu m$. For a (002) symmetric measurement with a beam incidence $\omega = 17.28°$, $L = 2t/\sin\omega = 12.46\ \mu m$, which is three times lower than the $1/e$ attenuation length of X-rays in GaN (for the Cu K_α radiation, see section 2.1.2). The strain gradient causes the (002) radial scan shown in **Figure 3.4** to have an asymmetrical shape on its left-hand side (low 2θ values). We treat each measured point on this left half-peak as the diffraction signal of one GaN sublayer. Hence, for each point of angle θ, we calculate a local strain ε by using a modified version of equation (2.21):

$$\varepsilon = \frac{\sin\theta_0 - \sin\theta}{\sin\theta} \tag{3.6}$$

where θ_0 is the angle at the top of the XRD peak. This is equivalent to considering that the surface of the sample is relaxed, as the surface sublayer has a strain value of zero. This treatment is sufficient to obtain a relative strain gradient, though an absolute strain gradient could be obtained by using the (002) Bragg angle of GaN given in **Table 2.1** for θ_0.

For each point, we also associate the measured intensity to the sublayer thickness, neglecting the absorption effect for the sake of simplicity. The calculation consists of a division of the local intensity by the sum of the intensities of all the experimental points. In this way, we obtain a set of relative thicknesses which equal to one when added together. We use these relative thicknesses to reconstruct the in-depth strain profile of **Figure 3.4**, by assuming that the gradient of strain is continuous from the AlGaN/GaN interface to the surface of the GaN layer.

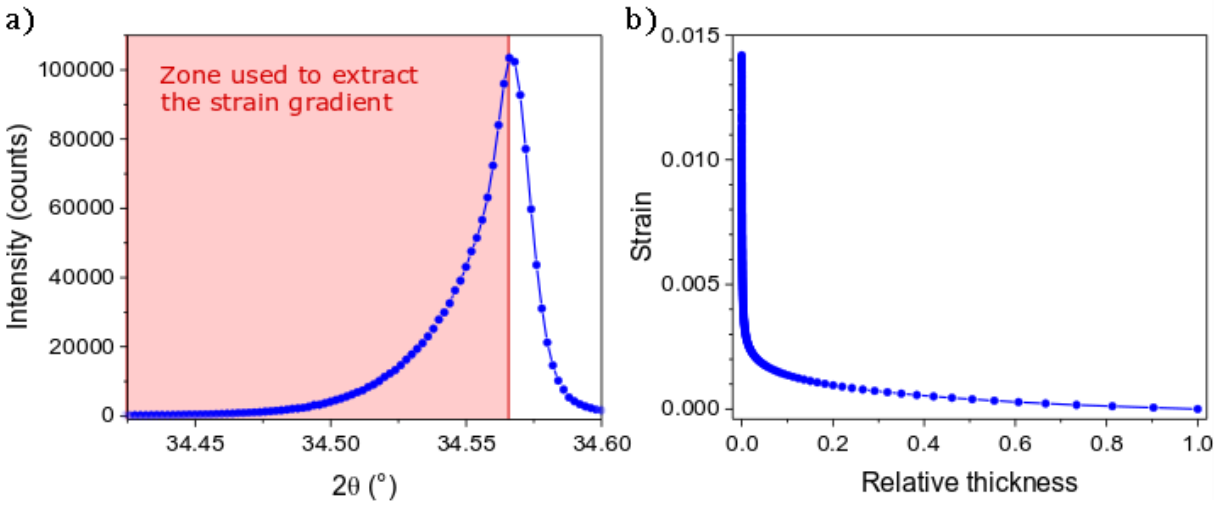

Figure 3.4 : Extraction of the stress gradient in a GaN layer by using the asymmetrical shape of a radial diffraction peak. a) (002) 2θ – ω scan measurement of the analyzed GaN-on-Si sample. b) Extracted strain gradient. The relative thickness scale varies from 0 (AlGaN/GaN interface) to 1 (GaN surface).

The gradient obtained is characterized by a dramatic decrease of strain in the deepest sublayers (90% drop in 9% of the film thickness). In our sample, this corresponds to a 90% variation of strain in the 170 nm above the AlGaN/GaN interface. We fitted this gradient with a polynomial of logarithms ($a_1 \ln x + a_2 \ln x^2 + a_3 \ln x^3\, a_4 \ln x^4$), which is adapted to the high curvature of the curve. Parameters $(a_1, a_2, a_3, a_4) = (-0.0012397, -0.0004661, -0.0000909, -0.0000044)$ were found.

Note that the method presented only gives a rough estimate of the strain gradient as it oversimplifies the reality of diffraction. Notably, X-rays absorption and background signal are not taken into account. Moreover, the intensity corresponding to each sublayer is treated as being entirely concentrated at a single 2θ angle, although it is actually spread across the reciprocal space. Along the $2\theta - \omega$ scan direction, it follows a Gaussian distribution with a

standard deviation depending on the Darwin width and the instrumental resolution (see section 2.4.2 a)). As shown in **Figure 3.5**, the intensity is also strongly spread in the transversal direction (corresponding to an ω scan cut of the reciprocal space), as the presence of TDs leads to a tilt of the crystal lattice (further details in section 4.1.1 a)). Close to the AlGaN/GaN interface, the higher number of dislocations increases this effect, thus lowering the measured intensity at the left-hand tail of the diffraction peak, eventually resulting in an underestimate of the thickness attributed to the sublayer. This might explain why the strain gradient of **Figure 3.4** is patently sharper than the strain gradient obtained from curvature measurements (**Figure 3.2**).

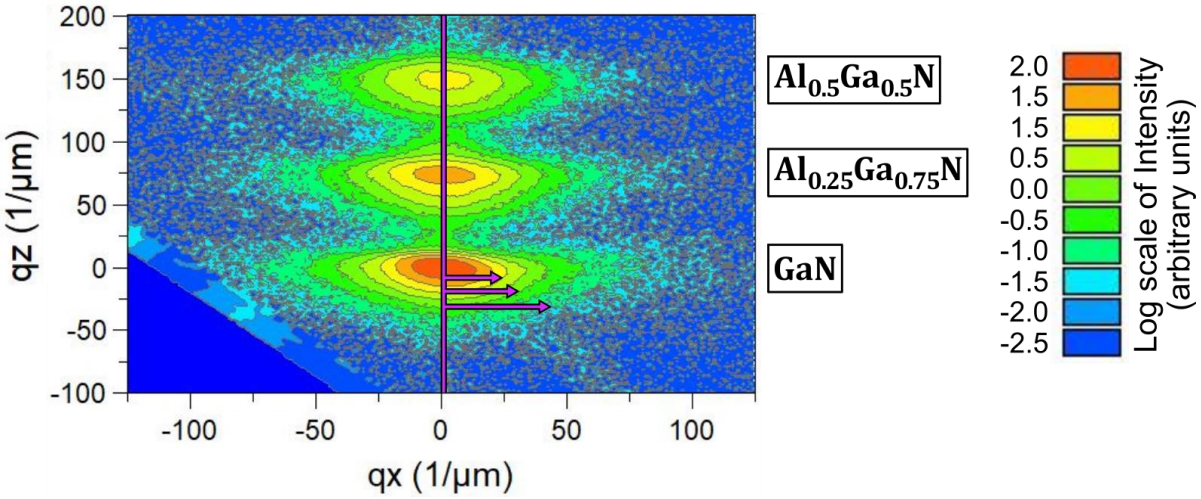

Figure 3.5 : Distribution on a reciprocal space map of the intensity diffracted by layers of GaN and AlGaN. The RSM is measured on a (004) refection. The path of a (004) $2\theta - \omega$ scan is depicted with a line along the q_z axis. On the GaN spot, the orthogonal spread of intensity (i.e. along the direction of an ω scan) is shown with arrows. Each arrow represents the distance away from the q_z axis where we observe a 90% drop of intensity, compared to the $q_x = 0\ \mu m^{-1}$ position. This spread of intensity, stemming from lattice tilt, increases when approaching the AlGaN/GaN interface (visible on the lower part of the diffraction spot).

3.2. Development of a simulation tool

3.2.1. Existing simulations

We have demonstrated the presence of a stress gradient in a GaN-on-Si sample, grown by MOVPE at Leti, by using micro-raman measurements, in-situ sample curvature measurements and the asymmetrical profiles of XRD scans. However, these techniques have their limitations and so we would like to develop a post-growth analysis to properly quantify these stress profiles. From a metrological point of view, XRD techniques appear as being ideal to carry out such measurements in a fast and non-destructive way. Yet, we have seen that conventional XRD stress gradient analyses, based on the evaluation of strain at different X-ray penetration depths, is not adapted to our samples and diffractometers, as well as being rather time consuming in terms of measurements. Extractions of stress gradients from asymmetric XRD

profiles is a non-conventional method which cannot be considered as a precise determination of stress states.

Alternatively, stress gradients in epitaxial films can be obtained from a least-squares fitting-based method of XRD peak profiles, using the kinematical or dynamical theory of diffraction to model diffraction profiles.[106] However, existing commercial XRD simulation software are designed for the modeling of quasi-perfect crystals and fail to reproduce the XRD signals observed for GaN-on-Si layers, which contain a wide set of defects.

In **Figure 3.6**, we illustrate this statement by comparing the XRD profiles measured on the studied GaN-on-Si sample with the ones obtained with the XRD simulation software of a diffractometer manufacturer. The GaN layer profiles of the symmetrical reflections (002), (004) and (006) are simulated by means of the dynamical theory of diffraction. As an input, the gradient of strain along the c-axis is given in the form of the polynomial of logarithms function of **Figure 3.4**. Note that this c-axis corresponds to the direction which matters in the calculation of interplanar distances to simulate the profiles of symmetric reflections. The modeled GaN layer is subsequently divided into a few hundreds of lamellae, each associated to a local strain calculated from the input function. We see that the commercial software profiles contain clear oscillations, stemming from interferences between the scattered X-rays, which is typical of high-quality materials and interfaces.

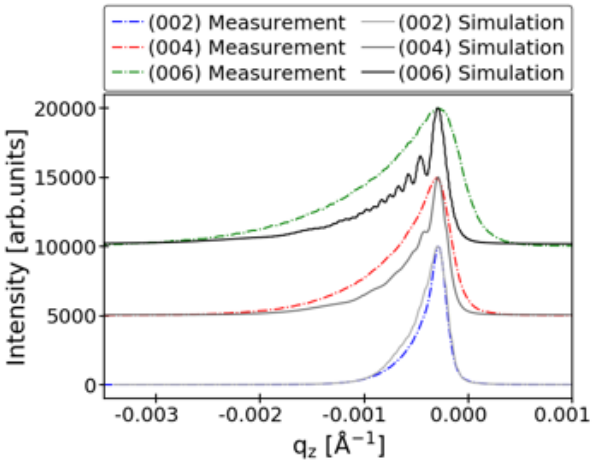

Figure 3.6 : Comparison of XRD peak profiles obtained by measurement and simulation on commercial XRD software. The comparison is shown for three symmetric reflections. Diffraction profiles are plotted in reciprocal space units along the q_z axis. For readability, intensities are normalized and shifted upwards for (004) and (006) reflections. For the same reason, the three profiles are plotted in relative units of q_z and shifted to the position of the (002) peak.

After the tests shown in **Figure 3.6**, we conclude that the available XRD modeling software are not adapted to the complexity of imperfect thin films. This motivated the development of a new simulation model for the study of stress gradients in GaN-on-Si samples.

3.2.2. Modeling principle

a) Introduction

In order to analyze stress gradients in GaN layers, we developed a simulation tool, in Python programming language. This program aims at simulating diffraction signals of a GaN layer containing a gradient of in-plane stress, so they can be compared to the experimental diffraction profiles.

The generated XRD profiles correspond to scans along the q_z axis of reciprocal space, around one or several of the symmetric reflections $(00l)$. These scans of reciprocal space correspond to radial $2\theta - \omega$ symmetric measurements, so that simulated and experimental data can directly be compared. This is convenient as (002), (004) and (006) are high intensity reflections, allowing for fast measurements. Furthermore, the main advantage of symmetric radial scans is that they are not affected by micro-strain and lattice rotational disorder stemming from TDs (see chapter 4 for further details).

Several material-related parameters are required to carry out the simulations, namely the lattice parameters and the structure factor. As stated earlier, we focus here on the analysis of GaN layer. We use the lattice parameters given in **Table 1.1** and the following structure factors calculated from equation (2.13): $|F_{(002)}| = 50.81\ \text{Å}^{-1}$, $|F_{(004)}| = 32.82\ \text{Å}^{-1}$ and $|F_{(006)}| = 27.05\ \text{Å}^{-1}$. Similarly, the sample thickness and the wavelength of X-rays are input as parameters ($t = 1.85\ \mu m$ and $\lambda(Cu\ K_{\alpha 1}) = 1.54059$ Å in our case).

Once the parameters are set, the core of the program is divided into two main steps:

- The calculation of the displacement field induced by an input strain gradient on each unit cell (UC) composing the GaN crystal.
- The calculation of the intensity scattered by such a distorted thin film, by means of the kinematical theory of diffraction. Although being simple, this theory is adequate to describe X-ray scattering in imperfect thin-film layers, as explained in section 2.1.3 e). The diffracted intensity is subsequently obtained by taking into account the instrumental resolution of the diffractometer and is plotted to be compared to the experimental data.

Detailed information about these simulation steps are given in the two following sub-sections. Additionally, the developed code is given in **Appendix 1**.

b) The displacement field

In-plane stresses cause a distortion of GaN thin films, in particular along the normal to the sample surface. In the simulation procedure presented below, we will characterize this distortion by means of the positions of UCs composing the GaN crystal. As this program aims at simulating symmetric $2\theta - \omega$ scans, only the position along the c-axis of the monocrystal is relevant. From the reference lattice parameter c_0 of GaN and the sample thickness parameter, we determine the number of UCs along the thickness of the GaN layer. Hence, the calculated

number of UCs corresponds to the one of a relaxed GaN layer. However, the actual measured thickness of the sample can be used as a parameter, as the difference of thickness between a relaxed and a stressed GaN layer is negligible compared to the total thickness of the thin film (typically a few nanometers vs a few micrometers).

The next step is to input a gradient of strain expanding along the thickness of the virtual crystal. We chose to define it on a relative thickness scale ranging from 0 to 1, so the strain profile is independent of the actual thickness of the layer. The physical parameter considered here is the strain ε_{zz} in the direction normal to the surface, so the strain profile can easily be calculated from a gradient of biaxial in-plane stress ($\sigma^b = \sigma_{xx} = \sigma_{yy}$), by means of the elastic constants of GaN ($\varepsilon_{zz} = 2S_{13}\,\sigma^b$, see section 1.1.2). The strain profile is subsequently used to calculate the displacement u_n field of each UC, which can be done in the following way:

$$u_n = c_0 \sum_{i=0}^{n} \varepsilon_{zz}(i) \tag{3.7}$$

where $\varepsilon_{zz}(n)$ is the strain around the n^{th} cell and u_n is given in units of the lattice parameter c_0, namely in ångströms in the code. The cell $n = 0$ corresponds to the interface between underneath GaN and buffer layers, while the cell $n = N_{UC}$ corresponds to the GaN surface. We apply the condition $u_0 = 0$, so the sample remains fix at its interface with bottom layers.

According to equation (3.7), the displacement field is calculated with a resolution depending on the number of points n considered for the strain profile. Due to the sum of strains performed, an error is introduced in the calculation of each value of u_n, which increases as n increases. As shown in **Figure 3.7**, such a calculation may lead to significant errors in displacement values, especially in thinner layers with a low total of UCs. In order to fix this issue, we used an oversampled calculation of the displacement field, where the number of points $n_{oversampled}$ is increased to $N_{oversampled} = 1 + D(N_{UC} - 1)$. Hence, we introduce a parameter D of definition, such that:

$$u_{n_{oversampled}} = \frac{c_0}{\mathrm{D}} \sum_{i=0}^{n_{oversampled}} \varepsilon_{zz}(i) \tag{3.8}$$

This definition of $N_{oversampled}$ is chosen so that the distance between two points $n_{oversampled}$ along the c-axis is equal to c/D. From equation (3.8), the displacement of each UC is easily obtained. At the m^{th} UC (starting from $m = 0$):

$$u_{\mathrm{m}} = u_{m \times n_{oversampled}} \tag{3.9}$$

For thicknesses of the order of the µm, which is typical of the GaN layers analyzed here, a definition parameter of $D = 16$ appears to be sufficient to obtain low errors in the displacement field (maximum error $< 0.5\%$, as shown in **Figure 3.7**). For thinner layers, a higher value of D may be chosen. The list of UCs displacement u_m obtained from equations (3.8) and (3.9), more precise than the one obtained from equation (3.7), is used in the following.

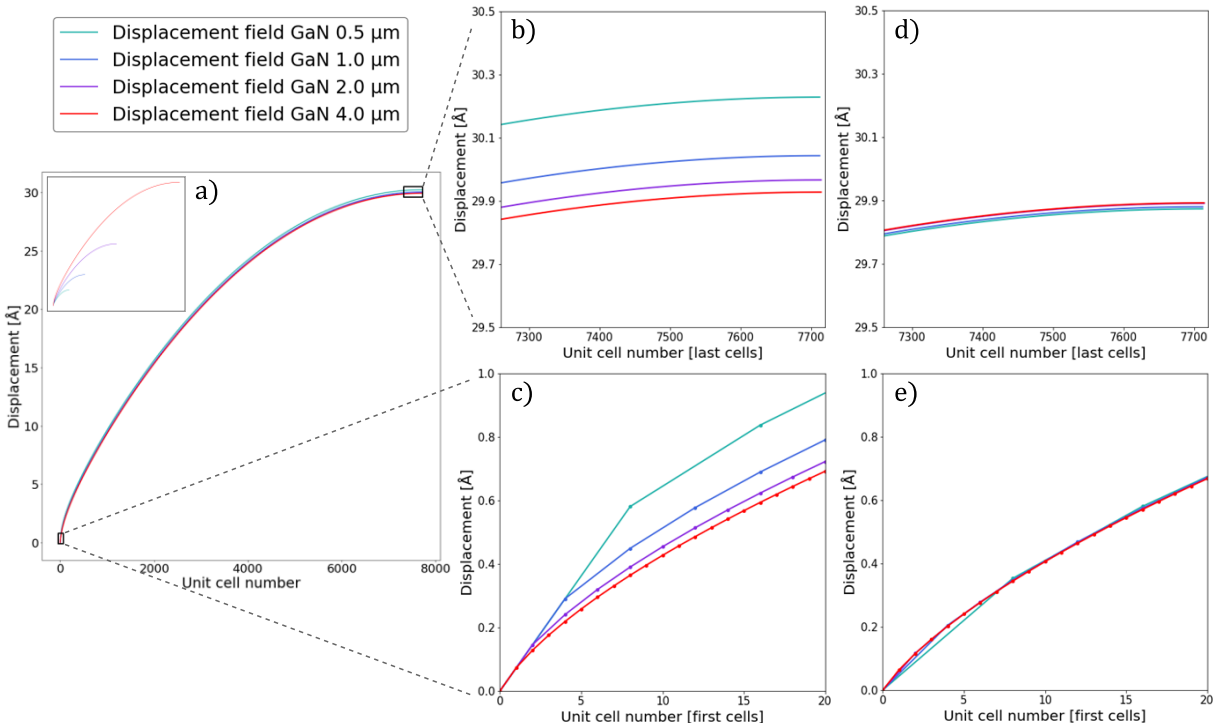

Figure 3.7 : Influence of the strain profile resolution on the calculation of the displacement field. a) Displacement profiles calculated from the strain gradient of **Figure 3.4** and from equation (3.7), for four GaN layers of thicknesses from 0.5 µm to 4.0 µm. For layers with lower thicknesses, x and y axes have been rescaled to show the divergence of profile shapes with respect to the 4 µm layer. Original displacement profiles are shown in the inset. b) – c) – d) – e) Rescaled displacement profiles calculated from equations (3.7) (b – c) and (3.8) (d – e), zoom on the top (c – e) and bottom (b – d) UCs of GaN layers. The displacement value of the top UC is 5.80% higher for the 4µm thick layer than for the 0.5µm thick layer when calculated with equation (3.7), but only 0.36% lower when calculated with equation (3.8), with D = 16.

The result of equations (3.8) and (3.9) is an average profile of UCs displacement. The actual displacement field may include variations of this profile along the x and y directions of the surface plane (**Figure 3.8 c)**), depending on the local characteristics of the crystal, like the presence or lack of TDs. In order to simulate these local variations, we introduce a surface plane size parameter and calculate a corresponding number of local strain profiles (see section 3.2.3.c)).

Formally, this surface size corresponds to the number of UCs in the surface plane, and a strain profile is calculated for each column of UCs irradiated by the X-ray beam. This represents a significant number of local strain profiles to calculate (1.1×10^{14} for a 1 mm $\times$ 1 cm beam footprint). Nevertheless, a representative distribution of strain profiles can be obtained for a much lower number of UC columns. We found that 5000 local strain profiles are typically sufficient to obtain a result identical to the simulation of a whole diffracting crystal.

Furthermore, if the displacement field does not significantly vary between two nearby columns of UCs, the surface plane can be divided in sub-areas containing a number of UC columns, each sub-area being associated with a uniform strain profile. In this case, the surface size parameter can be understood as the number of sub-areas in the diffracting crystal. This

consideration does not have any impact on the result of simulations, as (x, y) positions of UCs are not relevant for the simulation of radial symmetric scans. This is true as long as the lateral X-ray correlation length is high, which is typically the case in our samples (see section 3.2.3.b)). If lateral size effects become significant, one should define an (x, y) range within which the local strain is applied. For the sake of simplicity, we will keep speaking of columns of UCs in the following, even when they physically may correspond to lateral sub-areas.

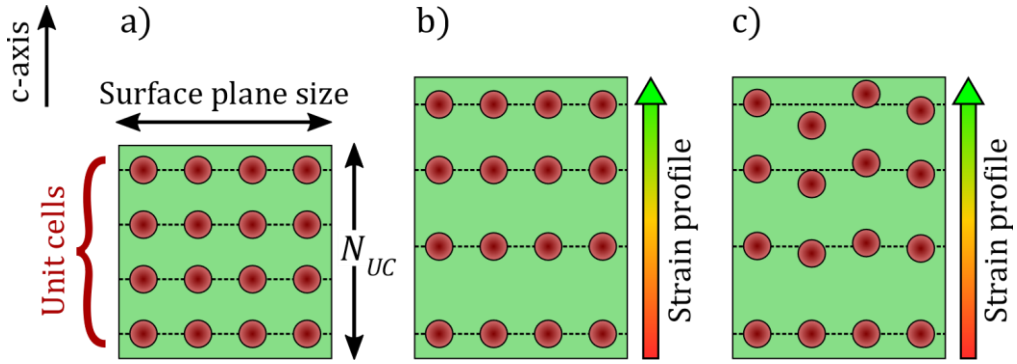

Figure 3.8 : Position of unit cells along the c-axis in the simulations. a) Unstrained crystal: the positions of UCs along the c-axis are calculated from the reference lattice parameter c_0 of GaN. b) A base strain profile is applied on every column of UCs, thus generating a displacement field. c) Local variations are applied on the base strain profile, so the displacement profile differs between each UC column / lateral sub-area.

c) Calculation of the diffracted intensity

Once the displacement field calculation is completed, the program calculates the amplitude of X-ray scattering within the GaN layer. To that end, the kinematical theory formula of amplitude within a distorted material, presented in equations (2.16) and (2.17) is used. In order to reduce computing time, we use for this calculation a fast Fourier transform (FFT) algorithm instead of a usual Fourier transform calculation. When computing Fourier transforms on a large number N of points (that is, UCs positions in this case), FFT calculations are associated with a low complexity, as computation time follows an $N \log N$ trend.[107] By contrast, simple Fourier transforms would instead follow a much less efficient N^2 trend.

Hence, for a position $\vec{q}$ of the reciprocal space, the calculation of scattered amplitude $A(\vec{q})$ is given by:

$$A(\vec{q}) = |F(\vec{q})| \, | \, FFT[V(\vec{r})G(\vec{r})] \, | \tag{3.10}$$

The values for the structure factor module $|F(\vec{q})|$ have been given in the initial parameters (see 3.2.2.a)). We recall that $G(\vec{r})$ is the correlation function containing the displacement field $u(\vec{r})$ applied on crystal UCs: $G(\vec{r}) = \exp\left(2\pi \overrightarrow{h_{00l}}.\overrightarrow{u(\vec{r})}\right)$ and $V(\vec{r})$ is the crystal shape function.

As we work with unpatterned thin films with thicknesses of the order of a few µm, we take $V(\vec{r})$ as a gate function equal to 1 within the crystal and to 0 outside of it. With this assumption,

$V(\vec{r})$ has no influence on the calculation of equation (3.10). This is valid as long as the variation of sample thickness due to surface roughness is negligible. This roughness stems essentially from steps at the surface of the layer, which originate at the point where screw TDs reach the surface. The typical height of this steps, as measured by atomic force microscopy, is of 3 – 4 Å. Hence, it is safe to neglect the impact of this roughness for films with a thickness above 100 nm. Nevertheless, if thinner layers are analyzed, one may simulate the variation of thickness by replacing in $V(\vec{r})$ the straight 0 to 1 transition of the gate function by a progressive transition following a complementary error function.[106]

The calculation of equation (3.10) is performed along a q_z axis scan of reciprocal space, centered on the reciprocal lattice point $\overrightarrow{h_{00l}}$. $A(\vec{q})$ is worked out for $N_{UC}^{coh} \times \mathcal{O}$ positions of $\vec{q}$, separated by a distance $c_0/(N_{UC}^{coh} \times \mathcal{O})$ in reciprocal space units. N_{UC}^{coh} is the number of UCs within a vertical domain of coherent diffraction, as will be detailed below. $\mathcal{O}$ is an oversampling parameter which allows the reciprocal space resolution of the simulation to be adapted. It is usually sufficient to set this parameter to $\mathcal{O} = 4$.

The next step of the simulation procedure is the computation of the scattered intensity. This calculation takes into account the lateral and vertical X-ray correlation lengths, which are set as parameters of the simulation. To this end, the crystal is divided into subdomains, both in the (x, y) plane and along the c-axis (see **Figure 3.9**). As shown in the equation (2.14), the scattered intensities corresponding to each of these subdomains are calculated separately and subsequently summed. This corresponds to a summation of squared amplitudes of each subdomain.

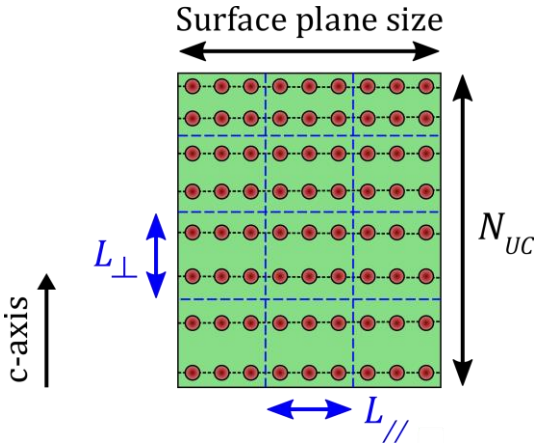

Figure 3.9 : Division of the simulated crystal in subdomains of coherent diffraction. The dimensions of subdomains correspond to the vertical and lateral correlation lengths $L_\perp$ and $L_{//}$. Note that the actual vertical size of subdomains slightly varies throughout the layer, owing to the displacement profile applied. However, this variation is negligible compared to $L_\perp$ (for example only a few ångströms for micrometric values of $L_\perp$).

In order to simulate the measured intensity, the simulated signal is then convolved with the instrumental resolution of the diffractometer, which is defined as a Gaussian function whose width depends on the Bragg angle of the selected reflection. The simulated diffraction scan can finally be plotted in reciprocal space units or in 2θ angle units. Note that the obtained intensity is arbitrary, as its real value depends on many parameters, such as the incoming X-

ray beam intensity and dimensions or which optics are placed in the path of the diffracted beam.

3.2.3. Evolution of simulations

With the aim of assessing the efficiency of the modeling tool, we have carried out several comparisons of diffraction profiles obtained by simulation and by measurements on the same GaN-on-Si sample that was studied in section 3.1. For these tests, we used the strain gradient shown in **Figure 3.4**, obtained from the asymmetrical profile of a (002) radial diffraction scan. In the following sub-sections, we will show the analysis of different refinements included in the program and their impact on the simulations.

a) Instrumental resolution

The experimental data to be analyzed was obtained on a Panalytical X'Pert Pro diffractometer, which allows for the measurement of the three symmetric reflections of GaN (002), (004) and (006). For these measurements, an asymmetrical 4-bounce Ge(220) monochromator and a 3-bounce Ge(220) analyzer crystal were used. These optics determine the instrumental resolution of the experimental setup, which constitutes one of the simulation parameters, as explained earlier. This experimental configuration is typical of measurements on III-N epitaxial thin films, as it permits to obtain very good instrumental resolution on ω scans. By using a four-bounce monochromator, the broadening component of these rocking curves is almost constant over Bragg angles θ, with a FWHM value close to 10 arcsec. However, this resolution is much worse in the case of $2\theta - \omega$ scans, especially at high 2θ angles for which the broadening of XRD peaks increases. The instrumental resolution of $2\theta - \omega$ scans is even more important as the corresponding XRD peaks are narrower than ω scans peaks (no broadening due to crystal misorientation stemming from TDs).

Hence, the instrumental resolution needed to be evaluated correctly. For this, we performed $2\theta - \omega$ measurements on a monocrystalline silicon sample. In **Figure 3.10**, we show the widths of diffraction peaks obtained for a wide set of reflections. Owing to the high crystalline quality of the sample, we can assume that these widths are only determined by the two broadening components β_d and β_0 of the instrumental resolution and the Darwin width (see section 2.4.2.a)). When calculating the Darwin width of each reflection, β_0 also appears to have a negligible impact on the measured widths, especially as broadening components add together quadratically (see equation (2.23)). Hence, we will consider that the data shown in **Figure 3.10** directly corresponds to the $2\theta - \omega$ instrumental resolution β_d of the diffractometer. From a fit of the evolution of β_d with the Bragg angle, we obtain the following instrumental resolutions for the three symmetric reflections: $\beta_d(002) = 20\ arcsec$, $\beta_d(004) = 30\ arcsec$, $\beta_d(006) = 84\ arcsec$.

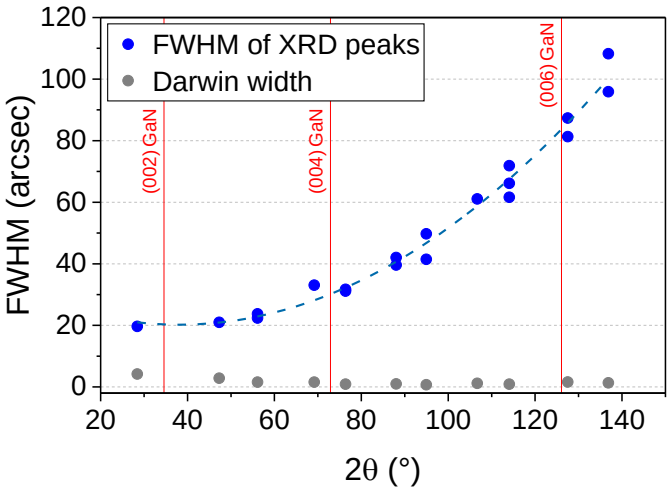

Figure 3.10 : Analysis of the experimental setup instrumental resolution for 2θ – ω scans. Radial scans were carried out in symmetric and skew symmetric geometry on a (111)-oriented sample of Si. The FWHM of the corresponding diffraction peaks is plotted in arcseconds against 2θ and fitted with a second-order polynomial function (dashed line): FWHM $\approx \beta_d = 0.00819 \times (2\theta)^2 - 0.622 \times 2\theta + 32.1$. The Darwin width of a silicon crystal is calculated for each reflection by means of equation (2.18) and shown for comparison. The 2θ reference values of the three symmetrical reflections of GaN are shown in red.

The first simulations of our program were performed by applying the base profile of strain to the whole sample, without any lateral variations in the (x, y) plane. These basic simulations did not either include the impact of instrumental resolution. As shown in **Figure 3.11 a)**, the result of this are diffraction peaks composed of a series of interference fringes, quite similar to the simulations of commercial software shown in **Figure 3.6**. Owing to its broadening effect, the instrumental resolution tends to annihilate these fringes, so the simulations become more comparable to experimental measurements. However, by inputting in the model the instrumental resolution measured above, the envelope of diffraction peaks still follows the global shape of previous simulations, which clearly differs from the measured profiles (**Figure 3.11 b)**). Despite being significant, the impact of instrumental resolution is not sufficient to obtain realistic simulations. We nevertheless note that the right-hand side of XRD peaks now fits much better with the experimental curves.

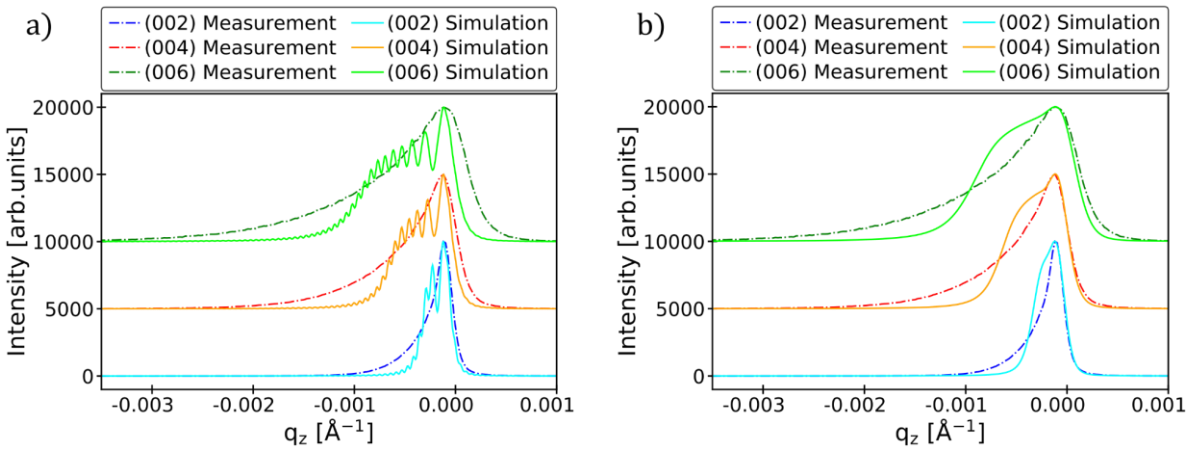

Figure 3.11 : Impact of the instrumental resolution on simulations. Simulations of 1.85 µm thick GaN sample, uniformly distorted by the strain profile of **Figure 3.4** compared to radial scan measurements. a) Instrumental resolution is not taken into account. b) The instrumental resolution extracted from **Figure 3.10** is taken into account.

b) X-ray correlation lengths

Another parameter which may have a significant impact on the shape of diffraction profiles is the X-ray correlation length. In the simulations, we distinguish the vertical correlation length along the normal to the surface of the layer and the in-plane lateral correlation length.

Figure 3.12 shows how the plots of **Figure 3.11** are substantially modified by dividing the layer into 10 lamellae diffracting incoherently with each other (i.e. by reducing the vertical X-ray correlation length to 185 nm). Once again, this process removes the oscillations of **Figure 3.11 a)**, but the diffraction profile does not follow the shape of the experimental measurements.

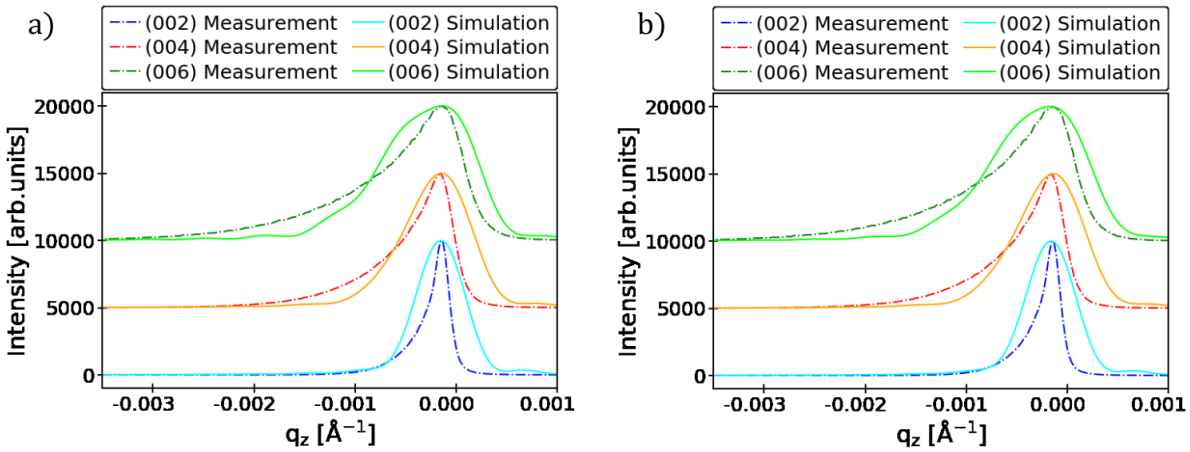

Figure 3.12 : Impact of the vertical X-ray correlation length on simulations. Graphs a) and b) correspond to the same simulations than those presented in **Figure 3.11**, but with the GaN layer being divided along the c-axis into 10 domains of coherent diffraction.

Conversely, the lateral correlation length has no impact on the outcome of the previous simulations. This is easily understandable as the position of UCs, and thus the scattered amplitude, are the same in each simulated column. Hence, the final simulation is just a multiplication of the elemental one column simulation, independently of whether the amplitudes or intensities have been added together.

In the case that the displacement field varies between UC columns (as in the following section 3.2.3.c), the lateral division of the layer may lead to different intensity profiles for each diffraction domain. However, this is only because the number of UC columns in a domain of coherent diffraction is so reduced that the intensity profile has not converged to its statistical average. This issue is simply fixed by simulating a greater number of UC columns, and thus a greater number of lateral domains (>5000). By doing so, the sum of intensities converges toward the intensity profile of a simulation with infinite correlation length.

The magnitudes of vertical and lateral diffraction size effects have both been analyzed on the studied GaN-on-Si sample, by means of Williamson-Hall plots of equation (2.28). It was found that these effects are negligible. Hence, in the following, a unique domain of coherent diffraction will be modeled, by choosing correlation lengths greater than the dimensions of the simulated crystal.

c) Variation of strain gradient

In our previous tests, we have seen that basic simulations are characterized by oscillation patterns, resulting from interference between X-ray waves, which are typical of quasi perfect materials. In practice, these patterns are not found experimentally. As GaN layers are rather imperfect, such interferences should simply not arise in the calculation of the sum of amplitudes. This is the reason why taking into account the instrumental resolution cannot be the full solution to obtain realistic simulations: the calculated scattered signal does contain oscillations, which are just attenuated by a convolution with the Gaussian function of

instrumental resolution. The impact of a reduced correlation length could explain the absence of oscillations, but Williamson-Hall analyses suggest that size effects are negligible in the tested samples.

The uniform displacement profile over the different UC columns appears to be a good candidate to explain the absence of oscillation patterns in experimental data. As shown in **Figure 3.8 b)**, the c-axis positions of UCs remain constant in all the simulated columns. By adding an additional local variation to UCs displacements (**Figure 3.8 c)**), interferences between scattered waves should not arise.

We identified three potential sources for local alterations of the base displacement profile:

1. A statistical dispersion of UCs positions around their expected position. This kind of displacement can result from thermal motion.
2. A shift of UC columns along the c-axis. This could be the effect of an irregular AlGaN/GaN interface, quite similar to the effect of roughness.
3. The local environment of the crystal. In the transmission electron microscopy image of **Figure 3.13**, we can see that the in-plane density of TDs is high in some regions of GaN layers and low in other ones. As TDs are known to relax surrounding stresses by recombining, we assume that densely dislocated areas will lead to a reduced local strain.

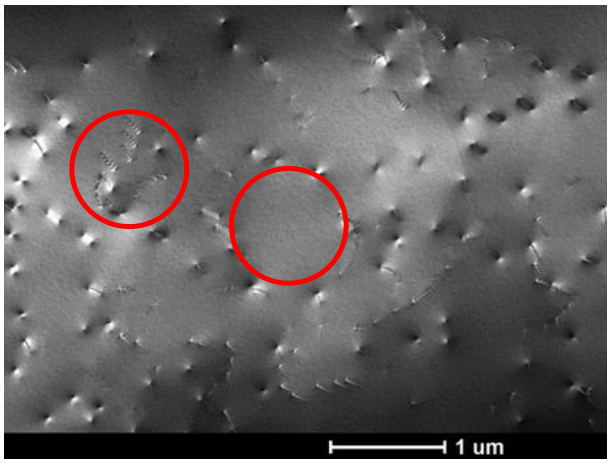

Figure 3.13 : Transmission electron microscopy image of the in-plane distribution of threading dislocations in a GaN-on-Si layer. This measurement was performed on a GaN-on-Si sample grown at CEA-Leti, which corresponds to the specimen GaN/Si(2) of chapter 4. The contrasted spots and lines visible on the image correspond to TDs (see section 4.2.1 for details). Two 1 µm diameter red circles highlight that these defects are unevenly distributed in the surface plane.

We tried to simulate each of these three local alterations of the displacement profile. For each UC column, the displacement field is calculated as the sum of the base displacement profile and its local modification.

For the dispersion alteration, this consists in adding a random value stemming from a normal distribution centered on zero to the displacement value of each UC (see **Figure 3.14 a)**). For the shift alteration (**Figure 3.14 b)**), a random number is similarly generated from a Gaussian distribution, but is applied to the whole UC column. These two procedures lead to

local strain profiles which do not differ from the base strain profile. In the corresponding simulations, we can see the characteristic oscillation patterns. Tests of UCs dispersion with random variable generated from other distributions, such as an exponential distribution, gave identical results.

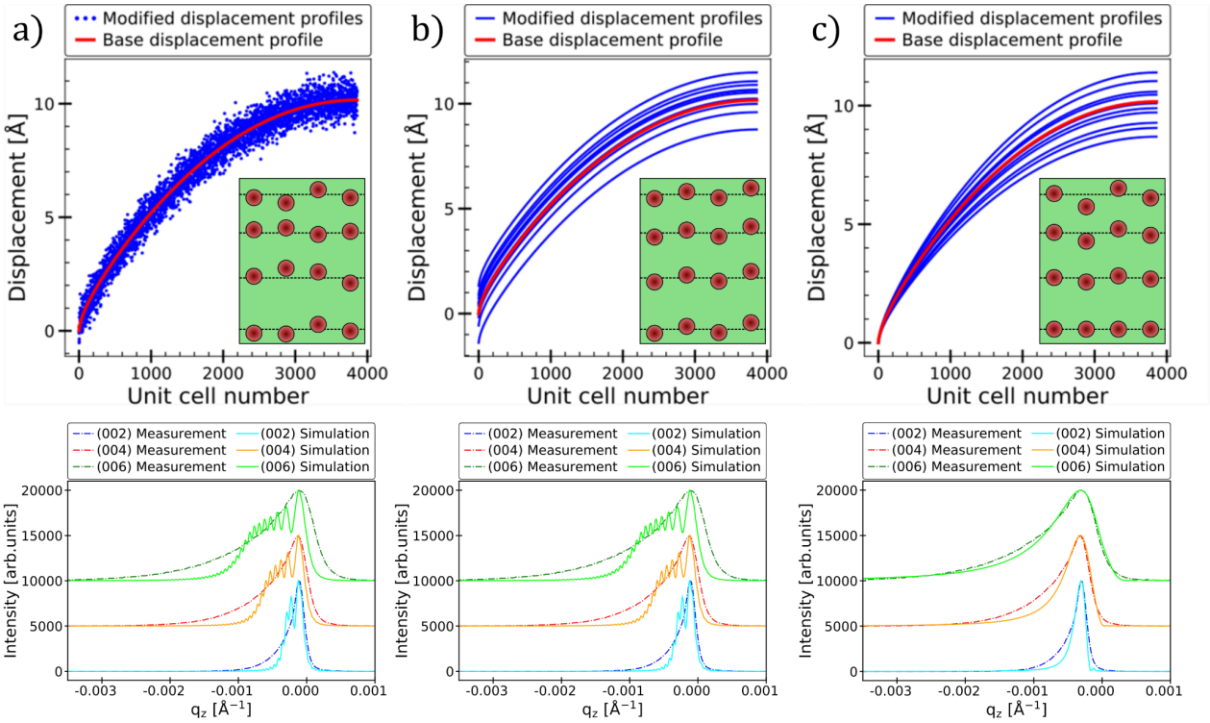

Figure 3.14 : Analysis of three kinds of local alteration of the displacement field. a) Statistical dispersion of UCs positions. b) Shift of displacement profiles. c) Attenuation of displacement profiles by surrounding TDs. For each kind of alteration, a graph shows the base displacement profile and a few local strain profiles. A representation of UCs position is provided in the insets. The corresponding simulations are plotted below. The instrumental resolution is not taken into account in order to better illustrate the annihilation of oscillation patterns.

The local attenuation of strain by surrounding TDs is more complex to model. The diagrams of **Figure 3.15** show examples of local strain and displacement profiles by assuming that the relaxation of stresses is fully determined by the recombination of TDs. However, such local displacement profiles are difficult to model as they require us to know the shape of the TD density profile along the c-axis, so that an appropriate distribution can be used for the position of inflection points in displacement profiles.

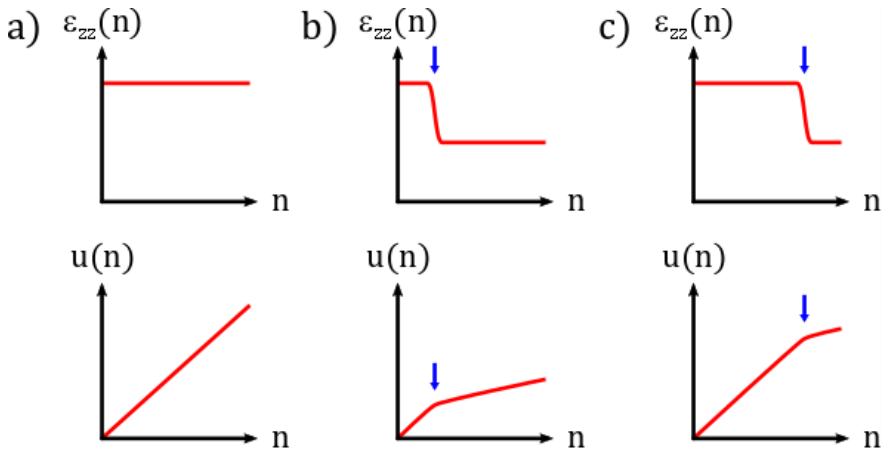

Figure 3.15 : Dependence on TD recombination of strain and displacement profiles. The diagrams show a model of the evolution of local strain profiles $\varepsilon_{zz}(n)$ and local displacement profiles u(n) (n is the UC index), when no surrounding TDs recombine (a), surrounding TDs recombine close to the GaN/AlGaN interface (b), surrounding TDs recombine close to the surface (c). Arrows mark the point where TD recombination takes place.

We chose to simplify the above model by simply multiplying, for each atomic column, the base strain profile $u_{ref}(n)$ by a random factor $(1 + X)$:

$$u_x(n) = u_{ref}(n)(1 + X) \tag{3.11}$$

where $u_x(n)$ is the local displacement profile of the x^{th} column and n stands for the n^{th} UC in the column. The random variable X is generated from a normal distribution centered on 0 and characterized by a standard deviation parameter σ. In the case that $X < -1$, $(1 + X)$ is taken to be equal to zero to avoid physically unrealistic negative local displacement profiles. The main benefit of this model is that σ is the only parameter that determines the local variation of strain/displacement.

As shown in **Figure 3.14 c)**, this model leads to simulated diffraction peaks with a shape similar to experimental measurements. This time, we note that the shape of each local displacement profile is different from that of the base displacement profile. This appears to be the condition required for the annihilation of interferences between X-ray waves.

The model of equation (3.11) can be used for the analysis of stress gradients in GaN layers. Provided that vertical X-ray coherence length effect is negligible (verified with Williamson-Hall plots) and that the sample thickness and the instrumental resolution are known, the outcome of simulations only depends on the shape of the stress/strain gradient and on the parameter σ, which quantifies the magnitude of local variations of strain.

According to our model, σ is characteristic of the set of TDs expanding through the layer. We assumed that in-plane variations of strain are the result of the local environment of UCs, which are located at varying distances from sites of TD recombination (and thus of strain relaxation). Hence, σ should be correlated to the standard deviation of the statistical distribution of in-plane distances between a UC and the closer site of TD recombination. In strongly dislocated layers, UCs have numerous TDs in their vicinity and σ should be high, and

vice versa. The distribution of TDs in the surface plane also plays a role on the distribution of UC-to-TD distances and the recombination of TDs might be favored when they are closely spaced.

The physically meaningful parameter to quantify local variations of displacement is the standard deviation $SD(u)$ from the base displacement profile, which is also the mean displacement profile. $SD(u)$ and σ are linked by:

$$SD(u) = \frac{\sigma}{\sqrt{N_{UC}}} \sqrt{\sum_{n=0}^{N_{UC}} u_{ref}^2(n)} \tag{3.12}$$

We recall that N_{UC} is the number of UCs in a column. Considering the parameter $SD(u)$ gives a better understanding of the outcome of simulations. For example, as shown in **Figure 3.16 a)** and **b)**, two simulations on layers of different thicknesses t will give similar results as long as the product $\sigma \times t$ stays constant (and t is in both cases large enough so that size effects remain negligible). The explanation is that when the thickness is multiplied by k, both the profile of displacement and the number of points composing this profile are multiplied by k, so $\sqrt{\sum_{n=0}^{N_{UC}} u_{ref}^2(n)}$ is multiplied by $k^{3/2}$. Hence, $SD(u)$ will remain the same only if σ is divided by k.

However, for simplicity and as the thickness of the layer is assumed to be known, we will use the parameter σ to find the best match between experiments and simulations. An Increase of this parameter leads to a broadening of the simulated profiles (**Figure 3.16 b) c)** and **d)**). For the studied sample, $\sigma = 0.125$Å appears to be a good fit, although the simulated peaks do not perfectly adopt the shape of the measured ones. The likely reason for this is that the rough estimate of strain gradient used for these simulations is not really accurate. In order to find the real gradient of strain, it is necessary to describe the strain profile by a function with adaptive parameters.

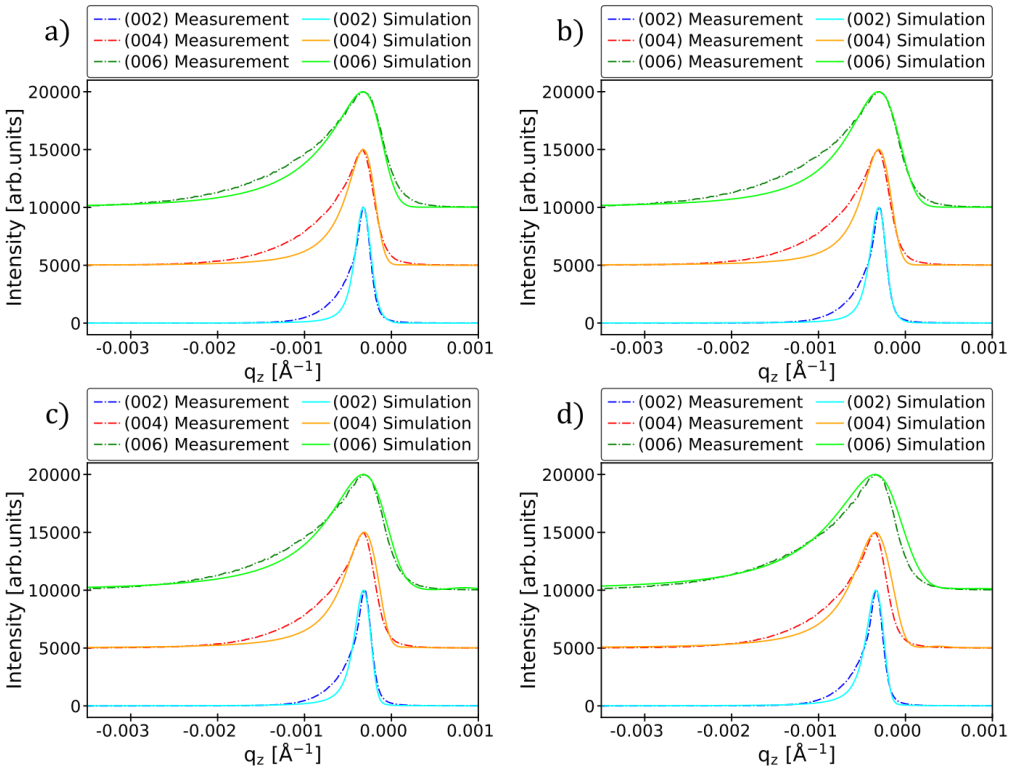

Figure 3.16 : Impact of the σ parameter on the simulated profiles. Thickness and local variation of displacement profile parameters are set to: t = 3.7 µm , σ = 0.05 Å (a) ; t = 1.85 µm , σ = 0.10 Å (b) ; t = 1.85µm , σ = 0.125 Å (c) ; t = 1.85 µm , σ = 0.15 Å (d).

d) Adaptive function for the strain gradient

According to the measurements of section 3.1 and the results obtained in the simulations of section 3.2.3, the decrease of strain in the thickness of GaN-on-Si layers appears to be quick close to the AlGaN/GaN interface and to progressively abate as reaching the surface. The input strain profile should therefore follow a curved trend, with a degree of curvature which needs to be determined.

Hence, we defined an adaptive function to describe strain profiles, based on two parameters: the root mean square (RMS) strain and the degree of curvature. The RMS of the strain profile is directly measurable by XRD, by means of a Williamson-Hall plot of $2\theta - \omega$ scans on the three symmetric reflections $(00l)$ of GaN. By using the integral breadth to extract peak widths from measurements on the studied sample, we found this RMS strain to be $\sqrt{\langle {\varepsilon_{zz}}^2 \rangle} = 0.00051$.

In the implemented function, the degree of curvature is defined by a single parameter K (without unit). We chose a logarithmic decrease to describe the strain profile $\varepsilon_{zz}(z)$ (defined on the relative thickness scale $z \in [0,1]$):

$$\varepsilon_{zz}(z) = \left(1 - \frac{\ln(Kz+1)}{L}\right)\varepsilon_{zz}(0) = \left(1 - \frac{\ln(Kz+1)}{L}\right)\sqrt{\frac{KL^2}{-L^2 - 2L + 2K}}\sqrt{\langle \varepsilon_{zz}{}^2 \rangle} \qquad (3.13)$$

where $L = \ln(K+1)$.

As shown in **Figure 3.17**, the profile obtained from (3.13) varies from a linear decrease for $K \to 0$ to a pronounced curvature for $K \to \infty$. We can see in this figure that the degree of curvature K is directly linked to the degree of asymmetry of the strain profile, which is easily understandable by following the logic detailed in section 3.1.4. However, by varying the parameters σ and K, we were not able to obtain a better match of experimental peaks than that achieved in **Figure 3.16 c)**.

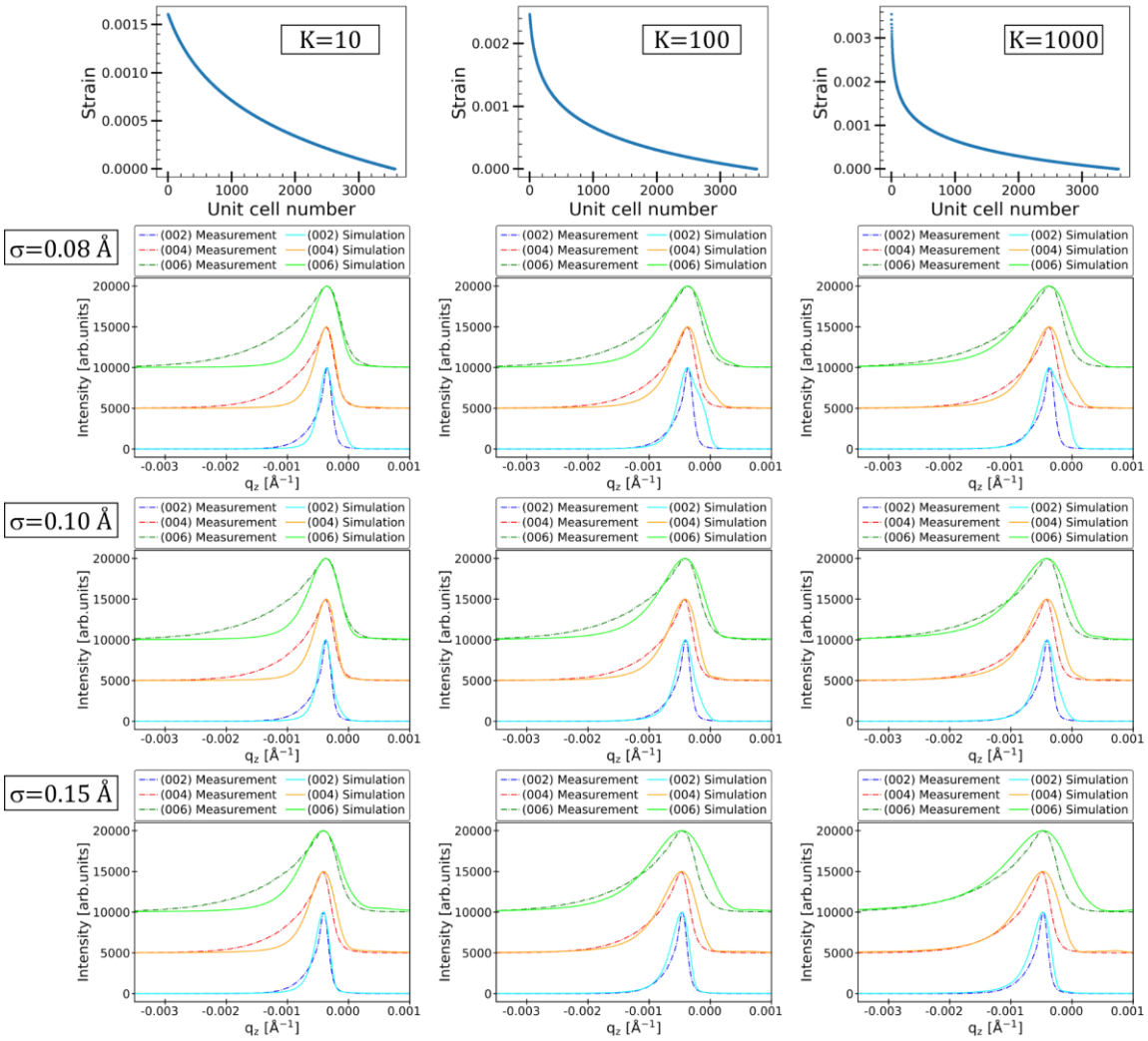

Figure 3.17 : Impact of the degree of curvature of the strain profile on the simulations. $\sqrt{\langle \varepsilon_{zz}{}^2 \rangle}$ is set at 0.00051, as found from a Williamson-Hall plot. At $\sigma = 0.08$ Å and $\sigma = 0.10$ Å, we see protuberances on the right side of some diffraction peaks, especially on (002) reflection, which originate from X-ray interferences. This indicates that the local variation of strain is underestimated, as confirmed by the disappearance of these patterns at $\sigma = 0.15$ Å.

In this chapter, we highlighted the presence of a stress gradient on GaN-on-Si samples grown at CEA-Leti by several XRD and non XRD techniques. We found that no ideal tool for the measurement of such a stress profile was available to us, so we accordingly developed a simulation program to reproduce the experimental diffraction curves.

We found that when simply modelling the displacement of columns of UCs under the action of a global stress gradient, oscillations appear in the simulated XRD curves, which are characteristic of interferences between the scattered X-ray waves. We fixed this issue by modelling local variations of the displacement profile, that we assume to be linked to local relaxations of compressive stress by TD recombination.

By using equation (3.13), we were able to model the diffraction profiles of a GaN layer of known thickness containing a gradient of in-plane stress by means of three parameters: the RMS strain $\sqrt{\langle {\varepsilon_{zz}}^2 \rangle}$ (in the direction normal to the surface), the degree of curvature K of this strain profile, and its local variations σ that we assume to be controlled by the surrounding distribution of TDs. This may be reduced to only two parameters by estimating the RMS strain with a Williamson-Hall plot. However, as illustrated in **Figure 3.17**, by following this procedure we were not able to obtain a combination of (σ, K) parameters matching with the experimental diffraction profiles for all three orders of diffraction at the same time. Several explanations can be suggested, such as the simplifications adopted to model the effect of TD recombination on local displacement profiles, or an unsuitable shape of the strain gradient.

In order to clarify the impact of these potential issues on simulations, it would be useful to determine whether the shapes of strain gradient obtained with equation (3.13) are physically realistic. Hence, we need a measurement of strain profiles in our GaN layers more accurate than those obtained in section 3.1. To this end, an in-depth measurement of strain gradients was carried out and is described in the fifth chapter of this thesis. Before this, the next chapter focuses on the analysis of the crystalline defects directly tied to the stress profiles, namely threading dislocations.

4. Threading dislocations analysis

The analysis of TDs is essential to assess the quality of III-N epitaxial films. These materials typically contain high densities of TDs, which usually reach 10^8 to 10^{10} cm^{-2} in the case of GaN-on-Si layers. TDs may affect the current leakage, breakdown voltage and electron mobility in III-N power devices, thus altering their performances (see section 1.3.1). Furthermore, a high density of TDs may induce a strong relaxation of compressive stresses, eventually leading to cracking of the GaN layer (section 1.3.1).

Different measurements can be used to quantify TD densities, such as Transmission Electron microscopy (TEM), Cathodoluminescence (CL) or X-Ray Diffraction (XRD).[108],[97] Among these, TEM is regarded as a reference measurement, as it combines reliable results, the advantage of observing the spatial distribution of TDs and the possibility to identify the different types of TDs (screw TDs, edge TDs and mixed TDs). However, TEM requires long and complex sample preparations, and the measured areas are limited to a few tens of µm.[109]

On the other hand, XRD has the advantage of being both easy to implement and non-destructive, and is therefore widely used. This technique takes advantage of the modification of the shape of the diffraction peaks, resulting from the distortion of the crystal by the set of TDs. The deduction of TD density is then either based on the observation of the diffraction peaks broadening, or on an analysis of the fitted peak profile.

A theoretical background of these analyses is given below, primarily focusing on XRD peak broadening methods, which are easy to implement in a metrological context. In particular, we study the peak broadening associated with the micro-strain field around TDs, which has not been commonly used to characterize III-N films in the past. Micro-strain measurements are carried out on GaN layers grown a wide range of substrates, including GaN-on-Si, and the results are compared to XRD misorientation measurements and complementary TEM and CL characterizations. For GaN-on-Si samples in particular, the layers have high macro stress gradients that complicate the analysis. This chapter shows how to bypass this additional effect and allow accurate TD densities measurements. The results presented here are largely based on a publication of the author.[110]

4.1. Theoretical background on XRD study of threading dislocations

4.1.1. Peak broadening methods

As we have seen in the section 2.4.2, the breadth of XRD peaks increases as the lattice of the analyzed samples deviates from the case of a perfect and infinite crystal. Hence, by disrupting the perfection of the lattice, TDs induce a symmetrical broadening of the diffraction

peaks in three different ways.[111] We will describe these effects using the notations introduced in the equation (2.17).

Firstly, dislocations induce a rotation of the crystal lattice that results in a broadening β_α of angular ω scans. The second kind of broadening is introduced by the local stress field of third order (see section 2.4.3), that surrounds dislocations. The resulting expansion and compression of the crystalline structure has a direct effect on the broadening β_ε of radial $2\theta - \omega$ scans. Finally, high dislocations densities can lead to the division of the crystal into several domains, separated by sets of dislocations forming boundaries between them. This results in a broadening β_L associated to the decrease of X-ray correlation length.

a) Misorientation measurements

XRD study of lattice rotations is one of the most popular techniques, in III-N materials community, for measuring dislocations densities of samples and devices.[112],[95],[4] Historically, the link between threading dislocations and mosaicity was studied for characterization of polycrystalline metals.

In 1953, working on annealed metals, *Gay et al.* used the mosaic block model (see section 2.4.2 a)) to describe the crystal as a set of subdomains, misoriented with respect to one another because of lattice rotations and separated by walls of TDs piled-up at grain boundaries. Assuming a Gaussian distribution for the orientation of the domains, they related the FWHM β_α of ω scan peaks, and the dislocations density ρ:[113]

$$\rho \approx \frac{\beta_\alpha}{3bt} \tag{4.1}$$

where b is the Burgers vector and t is the mean size of a mosaic block, which typically corresponds to the X-ray correlation length L.[91] As L is a parameter directly assessable in X-ray diffraction, by means of Scherer's formula or Williamson-Hall plots (see equations (2.25) and (2.28) in the section 2.4.2.b), we will use L instead of t in the following.

Four years later, *Dunn et Koch*[91] reassessed the work of *Gay et al.* In the calculation of the mean disorientation α between the blocks, they replaced a graphical evaluation of an integral by an analytical derivation, thus obtaining a new version of equation (4.1):

$$\rho = \frac{\beta_\alpha}{\sqrt{2\pi \ln(2)}\, b\, L} \approx \frac{\beta_\alpha}{2.1 b\, L} \tag{4.2}$$

In the two previous formulas assuming TDs piled-up at mosaic block boundaries, dislocation densities are correlated both to the FWHM β_α of radial scans peaks and to the X-ray correlation length L. An alternative approach consists in assuming a random distribution for dislocations, corresponding to an average spacing between dislocations equal to $1/\sqrt{\rho}$. This is equivalent to assume that each boundary between mosaic blocks contains only one

dislocation, so that the mean distance between dislocations is equal to the size of a mosaic block (i.e. $t = L = 1/\sqrt{\rho}$). Hence, for a random distribution of TDs, *Dunn et Koch* derived from equation (4.2) an estimation of the dislocation density independent of the block size (i.e. f the correlation length):[91]

$$\frac{\beta_\alpha}{\sqrt{2\pi \ln(2)}\, b\, \frac{1}{\sqrt{\rho}}} = \rho \;\Rightarrow\; \rho = \frac{\beta_\alpha^2}{4.35 b^2} \tag{4.3}$$

Previously, another formula was suggested by *Kurtz et al.*[114], again assuming a random distribution for dislocations, but starting from equation (4.1) from *Gay et al.:*

$$\rho = \frac{\beta_\alpha^2}{9 b^2} \tag{4.4}$$

The resulting TD density is approximately half of the one obtained with the equation (4.3) from *Dunn et Koch*. As the graphical-based derivation carried out by *Gay et al.* should be less precise than the analytical method of *Dunn et Koch*, the evaluation of TD density of equation (4.4) should be less accurate than the one of equation (4.3). Accordingly, the model from *Dunn et Koch* is usually chosen for density evaluation of randomly distributed TDs, such as in references.[97],[87],[88] Yet, the model from *Kurtz et al.* is also occasionally used in the III-N semiconductors community, such as in the articles.[115],[116]

On another note, both random TD distribution and piled-up TD distribution models have been applied to measurements on III-N layers. Some authors consider that the assumption of TDs being placed at the crystal domains boundaries is better suited than a random distribution in the case of epitaxial III-N layers,[117] which is supported by the observations of *Chechia et al.* on MOVPE (0001)-oriented GaN grown on sapphire substrates.[118] Working on similar samples, *Metzger et al.* treat the random and piled-up distributions as extreme cases, thus expecting a real TD density lying between the results of equations (4.3) and (4.2). Nevertheless, the comparison with TEM measurements carried out in the same study shows much better results for the random model of *Dunn et Koch*. A similar observation is made for edge TDs by *Lee et al.* on a set of MOCVD GaN-on-SiC, GaN-on-sapphire and AlGaN-on-sapphire samples.[97] A further limitation of piled-up distribution models is the difficult evaluation of the X-ray correlation length. This additional parameter is typically estimated with limited accuracy by using a Williamson-Hall plot, leading to errors in the calculated TD density.

In (0001) wurtzite III-N layers, threading dislocations are oriented along the c-direction normal to the surface. In this configuration, edge dislocations cause an in-plane rotation of the lattice about the normal to the surface, which corresponds to a lattice twist in the mosaic block model. Conversely, screw dislocations are responsible for an out-of-plane rotation associated with mosaic tilt. As a combination of edge and screw TDs, mixed dislocations generate both a mosaic twist and tilt. Consequently, we can measure independently the densities of dislocations with a screw component (i.e. screw + mixed types) and with an edge component (i.e. edge + mixed types) by respectively carrying out a tilt and a twist measurement.

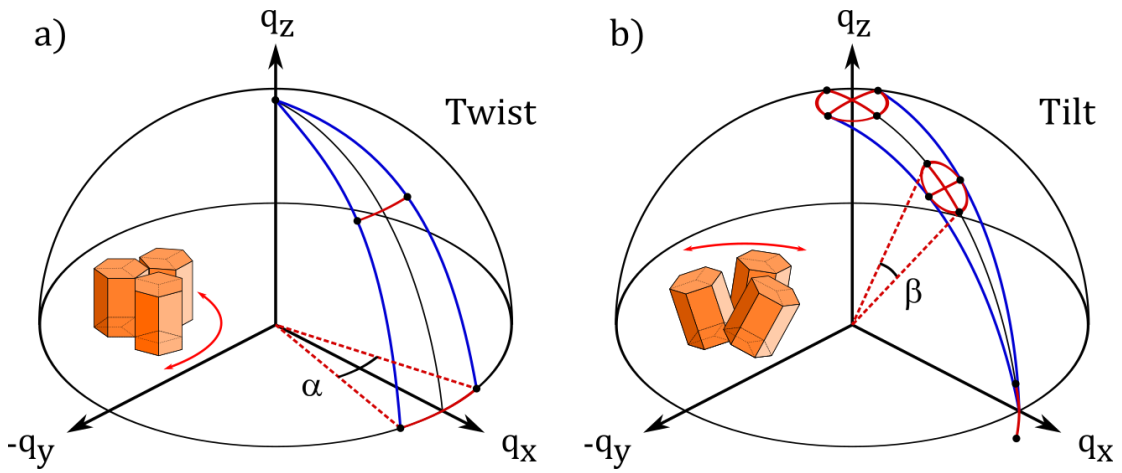

Figure 4.1 : Broadening of ω scans associated with lattice twist and tilt. a) Broadening owing to lattice twist of mean value α along on a sphere centered on the origin of the reciprocal space. b) Broadening owing to lattice tilt of mean value β along such a sphere. For both misorientations, the broadening is represented with red arcs for each of the following: a symmetric refection, an asymmetric/skew-symmetric reflection and a (hki0) reflection.

The diffraction spot broadening associated with a lattice twist is either measurable using a ϕ scan or an ω scan in skew symmetric geometry. Both measurements are equivalent on (hk0) reflections, although ϕ scans are affected by the axial divergence of the beam,[4],[119] which is normally higher than the equatorial divergence impacting ω scans. For example, measurements from *Heinke et al.*[119] on a GaN sample with TD density in the mid-10^9 cm^{-2}, suggest an approximate 10% increase of peak width when using a ϕ scan instead of an ω scan in skew symmetric mode. In practice, ϕ scans should therefore be reserved for measurements on highly twisted crystals.[4] As a rotation of the lattice about the normal to the surface, the twist leads to a high rotation of the crystal planes orthogonal to the surface. The rotation undergone by planes with an inclination $0° < \chi < 90°$ with respect to the surface is gradually reduced as χ decreases, until the extreme case of planes parallel to the surface (i.e. $\chi = 0°$), which are not affected by the lattice twist (see **Figure 4.1 a**). Therefore, the lattice twist should ideally be measured on (hki0) planes with an inclination $\chi = 90°$. However, these reflections require measurement geometries such as XRD in transmission or XRD with reflection geometry in In-plane mode, obtainable at a synchrotron facility but rarely on laboratory diffractometers.

As these measurements are not achievable on many laboratory diffractometers, and in particular on the ones used in this thesis, planes with high χ inclination are usually used instead. For GaN samples, the reflections $(30\bar{3}2)$ ($\chi = 70.45°$) and $(20\bar{2}1)$ ($\chi = 75.09°$) are often used as good indicators of the twist value. *Heinke et al.*[120] estimated that measurements on the $(30\bar{3}2)$ reflection give 85% to 91% of the real twist value, while the $(20\bar{2}1)$ gives an even better approximation, owing to its higher χ value. A more precise treatment relies on the measurement of a wide set of reflections at different χ values, as proposed by *Srikant et al.*[121] As shown in **Figure 4.2**, the breadth of a set of diffraction peaks is plotted against the angle χ. The data is fitted according to several possible models, which are detailed in

references[121],[122],[97] , and the real value of twist (i.e. 100% of twist) is obtained by extrapolation to $\chi = 90°$.

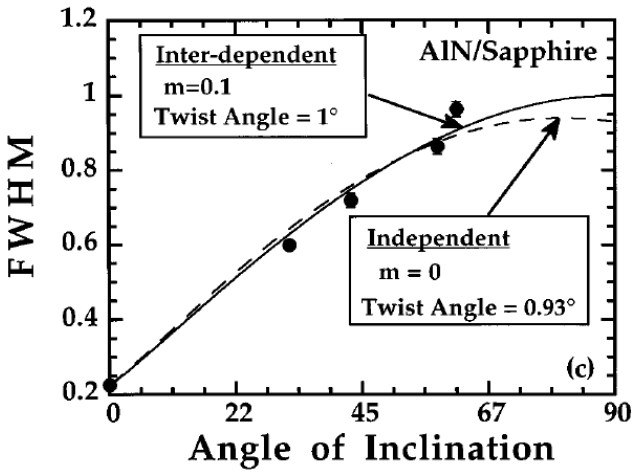

Figure 4.2 : Extrapolation of twist values. Figure reproduced from,[121] showing a twist assessment in an AlN layer grown on sapphire substrate. Srikant and al. used two different models to fit a plot of the peak breadth β_α against the angle of inclination ψ and extrapolate the corresponding twist values at $\psi = 90°$. The independent model (dashed line) is based on the assumption that the distributions of tilt and twist are independent. Conversely, the inter-dependent model assumes an influence of the twist distribution on the tilt distribution and vice versa. Hence, a factor m characterizing the tilt/twist interdependence is used. m lies between -1 and 1 and the interdependent model is equivalent to the independent model when m = 0.

A lattice tilt of mean angle α leads to a broadening β_α of symmetric and asymmetric ω scans. In skew symmetric mode, the impact of the tilt on ω scans is reduced as the inclination χ of the diffracting planes increases. On (0001) hexagonal III-N layers, the tilt is normally evaluated using ω scans on symmetric reflections, which have a high intensity and are not affected by the lattice twist.

It should be noted that the ω scans carried out for misorientation measurements can be affected by a number of additional sources of broadening, as detailed in the section 2.4.2. Among them, it is worth taking into consideration the X-ray correlation length and the sample curvature on III-N heteroepitaxial specimens. A limited lateral size $L_{//}$ broadens the peaks of symmetrical reflections used for tilt measurements, as well as skew symmetric measurements of twist, independently of the inclination ψ of the diffracting planes. The curvature of the sample affects both tilt and twist measurements. This effect can be lowered by reducing the beam height (see **Figure 2.8**) in the case of tilt measurements on symmetric reflections, and by limiting the beam width in the case of twist measurements on planes with high inclination ψ.[123]

Despite the wide use of misorientation measurements for the quantification of TD density, the potential errors in this analysis have been discussed in the literature. In reality, the impact of TDs on the lattice misorientations not only depends on their density, but also on their distribution in the plane parallel to the surface[95],[97] and on a correlation between the TDs, which is linked to the orientation of their Burgers vector.[124] Comparisons with TEM

measurements suggest a tendency to overestimate the density of edge dislocations, with a factor commonly reaching or exceeding two.[97] Conversely, a tendency to underestimate the density of screw dislocations has been observed, with values about four times lower when measured by XRD compared to TEM.[97]

b) Micro-strain measurements

An alternative method to quantify dislocations densities relies on the XRD measurement of the strain field created by dislocations. This strain extends locally around the dislocation line, its value decreasing rapidly when moving away from the dislocation core. Based on the description of stress fields detailed in the section 2.4.3, this kind of strain is associated to a third order stress. It is therefore called micro-strain, in contrast to the macro-strain induced by epitaxial biaxial stress of first order and its second order variations.

In 1961, *Hordon et Averbach* established the link between this micro-strain and the broadening of the $2\theta - \omega$ scan peak, within the context of polycrystalline metal characterization. Assuming an isotropic crystal and a Gaussian distribution of strain, they related this broadening β_ε, to the mean square strain $\langle \varepsilon^2 \rangle$ in the direction normal to the studied crystal plane:

$$\beta_\varepsilon{}^2 = 8 \ln(2) \langle \varepsilon^2 \rangle \tan^2\theta \tag{4.5}$$

In this formula, θ is the Bragg angle and β_ε is expressed in terms of FWHM. As the broadening contribution due to strain is assumed to have a Gaussian shape, the integral breadth could equivalently be used instead of the FWHM.

The measured expansion and contraction of the lattice are due to the radial micro-strain, coming from edge, screw and mixed dislocations, which extends in the plane normal to the dislocation line (see section 1.3.1). The stress field around a mixed dislocation is a sum of the stress fields around edge and screw dislocations.[51] In the following, we will decompose mixed dislocations into its screw and edge components, so that a mixed dislocation will account for two dislocations, of screw and edge types. *Hordon et Averbach* calculated the value of $\langle \varepsilon^2 \rangle$ by integrating the radial strain around dislocations between an initial core radius r_0 and a final radius R, such as represented in **Figure 1.6**.

For an edge dislocation with a Burgers vector length b_e, the mean square strain $\langle \varepsilon_e^2 \rangle$ along the diffraction plane normal is given by:[87]

$$\langle \varepsilon_e{}^2 \rangle = \frac{5}{64} \frac{b_e^2 (2.45 cos^2\Delta + 0.45 cos^2\Psi)}{\pi^2 R^2} \ln\left(\frac{\mathrm{R}}{\mathrm{r}_0}\right) \tag{4.6}$$

Δ and Ψ are geometrical terms. As depicted in **Figure A.1** of **Appendix 2**, Δ is the angle between the dislocation glide plane normal and the diffracting plane normal. Ψ is the angle between the Burgers vector and the diffracting plane normal.

In this formula, a Poisson ratio of 1/3 is assumed, as *Hordon et Averbach* derived them to analyze cubic metals.[87] Although a III-N crystal is an anisotropic media, GaN has a quasi-isotropic Poisson ratio (see section 1.1.2), which allows to use the procedure of calculation of $\langle \varepsilon^2 \rangle$ proposed by *Hordon et Averbach*. This may not be true for other III-N binary alloys, whose Poisson ratios are markedly anisotropic.[14]

Equation (4.6), with a Poisson ratio of 1/3, was used by *Metzger et al.* in a previous study of a GaN film grown on sapphire substrate[95] and by the author of this thesis and coworkers on a study of GaN samples on Si, SiC and sapphire substrates.[110] However, a Poisson ratio of 0.183 would be more suited for GaN layers with moderate TD density.[4],[16] Hence, starting from the initial work of *Hordon et Averbach,*[87] we recalculated the expression of $\langle \varepsilon_e^2 \rangle$, so the Poisson ratio ν appears as an additional parameter:

$$\langle {\varepsilon_e}^2 \rangle = \mathrm{A} \frac{b_e^2 (\mathrm{B}\, cos^2\Delta + (B-2) cos^2\Psi)}{\pi^2 R^2} \ln\left(\frac{\mathrm{R}}{\mathrm{r}_0}\right) \tag{4.7}$$

where A and B are two parameters depending on the Poisson ratio ν: $A = \frac{1}{16(1-\nu^2)}$ and $B = \frac{\nu^2 - 2\nu + 5}{2(1-\nu^2)}$.

The demonstration of equation (4.7) is provided in **Appendix 2**. We note that by applying the assumption of $\nu = 1/3$ on equation (4.7), we obtain parameters $A = 5/64$ and $B = 2.50$ slightly different than the ones obtained by *Hordon et Averbach* (i.e. $A = 4.5/64$ and $B = 2.45$). This result reveals an apparent inconsistency in the paper of *Hordon et Averbach*, which does not appear to have been pointed out in the subsequent literature. Equations (4.6) and (4.7) have both been tested, assuming $\nu = 1/3$, for the calculation of TDs on GaN layers (samples GaN/SiC and GaN/Si(2) in the following sections). The use of equation (4.7) results in a total density of TDs 6.5% - 8.5% higher than when using the result of *Hordon et Averbach*, almost independently of which sample or which reflection is used for the XRD measurement (an example is given in **Figure 4.12**).

In the following, we will replace equation (4.6) by equation (4.7), assuming a Poisson ratio of 0.183, corresponding to parameters $A = 0.0647$ and $B = 2.41$.

For the case of a screw dislocation with a Burgers vector length b_e, the integration of strain is carried out by taking into account the radial component arising from second order terms of nonlinear elasticity theory, as presented in equation (1.13). The radial strain in cylindrical coordinates $\varepsilon_{rr} = K b_s^2/(4\pi^2 r^2)$, with $K = 1$, is used for the calculations. The mean square strain $\langle \varepsilon_s^2 \rangle$ along the diffraction plane normal is given by:[87]

$$\langle {\varepsilon_s}^2 \rangle = \frac{b_s^2 sin^2\Psi}{4\pi^3 R^2} \ln\left(\frac{\mathrm{R}}{\mathrm{r}_0}\right) \tag{4.8}$$

As previously, the geometrical term Ψ corresponds to the angle between the Burgers vector and the diffracting plane normal.

In equations (4.6) to (4.8), a typical value of $10^{-7} cm$ is chosen for the lower radius limit r_0. Below this value, the elasticity theory is no longer valid and the theoretical strain tends to infinity. Atomic models must be used to study strain fields around the core of dislocations. For the sake of simplicity, strain in this area is simply not taken into account in this model.

Arrays of dislocations tend to reduce their energy by adopting spatial configurations for which the long-range stress field of each dislocation is cancelled out by the stress fields from surrounding dislocations. Hence, the stress field around each dislocation is considered to be effectively acting in a range corresponding to half the average spacing between dislocations, in a random distribution configuration.[51],[125] As this average distance is inversely proportional to the square root of the density of dislocations, we can relate the upper radius limit R to ρ.[87],[95]

For edge dislocations:

$$R_e = \frac{1}{2\sqrt{\rho_e}} \tag{4.9}$$

Similarly, for screw dislocations:

$$R_s = \frac{1}{2\sqrt{\rho_s}} \tag{4.10}$$

Note that the average spacing between dislocations depends on the distribution of the TDs in the surface plane. The values of R_e and R_s would therefore slightly vary for configurations of TDs differing from the random distribution framework described above, such as the case of a piled-up distribution of TDs. Furthermore, the real value of the screening range, i.e. the distance of cancellation of the strain fields, actually depends on the correlation of the dislocations, which is associated with the distribution of Burgers vectors orientations within the set of TDs.[124]

In the case of a material containing both edge and screw dislocations, a sum of the two mean squared strain contributions is made to obtain the global mean squared micro-strain responsible for the peak broadening:[95]

$$\langle \varepsilon^2 \rangle = \langle \varepsilon_e^2 \rangle + \langle \varepsilon_s^2 \rangle \tag{4.11}$$

Note that for a hexagonal (0001) oriented GaN crystal, there are three different edge dislocations systems, with Burgers vectors every 120° in the radial plane of the dislocation, and different values for the geometrical terms Δ and Ψ. By assuming that the density of each system is a third of the total edge TD density, $\langle \varepsilon_e^2 \rangle$ is taken as the average value of the mean squared strain of the three systems. This hypothesis is acceptable as identical diffraction peaks are measured when using the different reflections of a family of planes $\{hkil\}$ (i.e. by rotating the sample 120° about the normal to its surface).

Combining the above equations (4.5) to (4.11), we are able to calculate, for a given diffracting plane, the peak broadening associated with a density of screw dislocations and a

density of edge dislocations. *Metzger et al.* used this method to quantify threading dislocations densities in GaN layers grown on sapphire substrates.[95]

As for misorientation measurements, micro-strain measurements can be affected by other sources of peak broadening, such as a limited correlation length of X-rays. Nevertheless, the sample curvature has no effect on the radial scans used in this analysis. This allows for using large beams for this kind of measurements, even on highly bowed samples.

4.1.2. Peak shape methods

Peak broadening analyses have been extensively adopted as accessible methods to quantify dislocation densities in III-N crystals. Nevertheless, they rely on a rather simplistic treatment of the set of dislocations, which is only defined by the nature of the dislocations (edge/screw) and their densities, assuming straight dislocation lines with basic distributions (random or piled-up).

In order to treat the influence of dislocations on the diffracted signal more precisely, one can model the full shape of the diffraction peak, including the peak tails which correspond to the diffuse scattering component. This method may be referred to as *whole pattern diffraction line analysis*.[126] *Krivoglaz*[127] has provided a complete theory about this diffuse scattering based on the derivation, within the kinematical theory, of correlation functions (section 2.1.3.d)) for randomly distributed sets of straight dislocations, dislocation dipoles (i.e. pairs of close parallel straight dislocations with opposite Burgers vectors), dislocation loops or split dislocations associated to stacking faults.

As for the peak broadening analyses, the calculation of displacement fields of the lattice relies on basic assumptions about the position of dislocation lines within lattice, such as random or piled-up distributions. Additionally, these models take into account the size of the crystal, the orientation of dislocations in the lattice, and the distribution of Burgers vectors orientations.

Wilkens[128],[129],[130] noted that the model proposed by *Krivoglaz*[127] of a set of straight parallel dislocations completely uncorrelated with one another (i.e. with random distributions of positions and Burgers vector orientation), is not suited to describe the broadening of XRD peaks. In such a system, dislocations do not cancel out each other's strain field, so the mean square strain within the material increases with the size of the crystal. Hence, an infinite crystal would theoretically contain a diverging amount of energy and would lead to an infinite breadth of diffraction peaks.

To solve this issue, *Wilkens* introduced a new distribution model for dislocations, physically more accurate although mathematically simple, called "restricted random distribution". In this model, the lattice is divided in a set of sub-domains of equal size, each of them containing the same number of dislocations. Within a sub-domain, the positions of dislocations are random and their Burgers vectors are oriented in such a way that the total Burgers vector of the domain is zero. In this configuration, the dislocations screen each other's

strain fields, which thus only expand within the limits of the sub-domain. Consequently, the calculation of the strain fields in the lattice involves two parameters, namely the density of dislocations ρ and the size L of the sub-domains. The magnitude of the correlation between dislocations is given by a parameter $M = L\sqrt{\rho}$. Note that the shape of the diffraction profiles is determined by M, as this parameter defines the range on which the central part of the peak follows a Gaussian shape,[130],[124] thus meeting the basic assumption of the peak broadening theory (sections 2.1.4.2 and 4.1.1).

Kaganer et al.[124] used the restricted random distribution model to derive a description of double axis ω scans XRD profiles in crystals with straight and randomly distributed TDs. They obtained a function with two parameters depending on ρ and L, and used it to fit the whole diffraction profiles obtained on GaN samples on SiC substrates. This method allows to obtain both the dislocation density ρ and the correlation length of dislocations L. From this model, the authors derived an interesting analogy with the peak broadening analysis of *Dunn et Koch* (equation (4.3)). They rewrote the relationship between the broadening β of ω scans and the densities of edge and screw dislocations ρ_e and ρ_s in the following way:

$$\rho_e = \frac{18\,\beta_e^2 \cos^2\theta}{(2.8 + \ln M)^2 b_e^2} \tag{4.12}$$

$$\rho_s = \frac{36\,\beta_s^2}{(2.4 + \ln M)^2 b_s^2} \tag{4.13}$$

β_s is naturally measured on a symmetric reflection in the case of screw TDs and β_e on a highly tilted plane in the case of edge TDs. These equations show that the actual broadening of diffraction peaks depends both on the dislocation density and on the magnitude of the correlation between dislocations. In their study, *Kaganer et al.* extracted values of M between 1 and 2 from fitted experimental peaks, corresponding to strong screening of the dislocation strain fields. The corresponding estimates of TD densities are four times higher than for the model of *Dunn et Koch* for edge dislocations, and even one order of magnitude higher for screw dislocations densities, which shows the importance of the correlation between dislocations in misorientation measurements.

The model developed by *Kaganer et al.* is only valid at high density of TDs, owing to the use of Gaussian statistics when considering the distribution of TD positions.[124] This treatment is considered by the authors as sufficient for the analysis of their samples, with calculated TD densities of the order of the mid 10^{10} cm^{-2}. However, no discussion is provided about the lower limit of validity of the model, in particular whether it is suited for modern heteroepitaxial GaN layers, with TD densities of the order of $10^8 - 10^9 cm^{-2}$. It is worth noting that the TD density mismatch between the models of *Kaganer et al.* and *Dunn et Koch* is not consistent with TEM/*Dunn and Koch* comparisons provided in the literature for GaN layers with TD densities of $10^8 - 10^9 cm^{-2}$ (see section 4.1.1a)). In particular, *Kaganer et al.* found that *Dunn et Koch* model underestimates the density of edge TDs, while TEM observations conclude that this

model tends to an overestimate the number of TDs. This difference may be due to a higher correlation (i.e. a lower M) between TDs of the highly dislocated samples of *Kaganer et al.* Moreover, we observe that the model of *Kaganer et al.* predicts a strong dependence on the Bragg angle of the width of XRD peaks affected by edge TDs. For example, $(20\bar{2}2)$ and $(10\bar{1}1)$ reflections are affected by an equal component of ρ_e, as they have the same tilt with respect to the surface. According to equation (4.12), when measuring a GaN layer (with a given parameter M) with both reflections, $(20\bar{2}2)$ should give peaks 22% wider than $(10\bar{1}1)$. However, when we carried out this experiment on GaN-on-Si samples with TD densities of the order of $10^9 cm^{-2}$, we found identical peak widths for both reflections, such as predicted by *Dunn et Koch* model. These elements suggest that the accuracy of the model of *Kaganer et al.* for TD densities lower than $10^{10}\ cm^{-2}$ needs to be verified.

Working on GaN epitaxial layers, some authors developed an alternative method based on a Monte Carlo procedure of diffraction peak simulation. This technique relies on the random generation of a distribution of dislocation positions within a domain of coherent diffraction. For each dislocation, the displacement field of the crystal cells in the domain is calculated from the theory of elasticity. All these displacements are summed to calculate a global displacement field, which is used to work out the diffracted intensity with the equation (2.16). These operations are repeated on several domains of coherent diffraction, and the intensities are summed to obtain the simulated pattern. In principle, this method can be applied to every distribution of dislocations, such as randomly distributed straight dislocations[76] or a combination of threading and misfit dislocations, with dislocation correlation.[131] Furthermore, the conventional calculation method of *Krivoglaz*[127] raises some issues, due to the ensemble averaging performed for the calculation of intensity, which are fixed by the Monte Carlo process. Examples of thereby overcome limitations are the difficult numerical evaluation in the case surface relaxation associated to edge TDs,[74] or the non-validity of the averaging in the case of micro-beam diffraction.[76]

Whole pattern diffraction line analyses and Monte Carlo procedures aim to analyze the signal coming from both the center and the tails of XRD peaks. Another approach to study the dislocation density is to focus on the tails of the diffraction profiles. *Groma et al.*[132] extended the initial works of *Krivoglaz*[127] and *Wilkens*[133],[130] by calculating high order terms of the Fourier transform of diffracted intensity for a set of parallel straight dislocations. This enabled[134] the calculation of the second-order restricted moment $v(q) = \int_{-q}^{q} q^2 I(q) dq$, which is proportional both to the mean dislocation density and to $\ln q$, where q is the distance from the XRD peak in the reciprocal space. Hence, the intensity decay at peak tails follows a logarithmic trend, with an expected slope about -3 (in log scale). Further studies[124],[74] shown that this slope is actually comprised between -2 and -4 (in log scale), depending on the nature of the dislocations (edge or screw), on the size effect and on the integration of the signal in the reciprocal space (steeper slope when the measurement is made in triple axis mode than in double axis mode). Similarly, the calculation of third and fourth-order restricted moments gives access to the fluctuation of dislocation density and the polarization of the dislocation structure in the presence of dislocation dipoles. *Groma* and coworkers used this procedure to calculate the density of dislocations in a copper monocrystal.[134],[135]

The major advantage of XRD peak tails analyses is that the intensity measured in these zones corresponds to a diffuse scattering originating from areas strongly misoriented with respect to the rest of the lattice, namely the immediate vicinity of dislocation lines. In such an area, the lattice distortion is exclusively dominated by the nearest dislocation, which means that the distribution of dislocations and their correlation have no effect on the diffuse scattering signal. This is true even in the case of piled-up distributions, as long as the separation between the wave vector $\vec{q}$ and the diffraction peak is higher than the inverse mean distance between dislocations.[124] The main limitation of analyzing the tails of diffraction peaks is the low intensity of the corresponding signal, which can be difficult to distinguish from the measurement noise. Hence, on laboratory diffractometers, long measurements with high X-ray counting times are required. Additionally, to the author's knowledge, the procedure of *Groma*[134] has not been applied yet to III-N materials.

Table 4.1 summarizes the characteristics of the different XRD approaches for extraction of TD density detailed in the sections 4.1.1 and 4.1.2.

Method	**Analysis of misorientation**	**Analysis of micro-strain**
XRD peak zone	Center	Center
Hypotheses on TD distribution & correlation	Either random distribution or piled-up distribution	Random distribution
Parameters extracted	ρ_e , ρ_s	ρ_{tot}
Applications on epitaxial GaN	MBE,[120] MOVPE,[95] HVPE[136] GaN-on-Al_2O_3 GaN-on-SiC[117] GaN-on-Si[137]	MOVPE GaN-on-Al_2O_3[95]
Main limitations	Restrictive TD distribution assumptions TD correlation not taken into account ρ_e obtained by extrapolation or approximation	Restrictive TD distribution assumptions TD correlation not taken into account Assumption on ρ_s or ρ_s/ρ_{tot} required
Main advantages	Simple application Widely used method	Simple application Only one measurement needed Unaffected by sample curvature

Method	**Whole pattern diffraction line profile analysis**	**Monte Carlo (MC) procedure**	**Second-order restricted moment peak tail analysis**
XRD peak zone	Center + tails	Center + tails	Tails
Hypotheses on TD distribution & correlation	Restricted random distribution High TD density	Characteristics of the TD ensemble are defined by adapting the MC procedure	No hypotheses
Parameters extracted	ρ_e , ρ_s Correlation between TDs	ρ_e , ρ_s Other parameters defined in the MC procedure	2nd order moment: ρ_{tot}

			Higher-order moments: Fluctuation of ρ_{tot} and dislocations polarization
Applications on epitaxial GaN	MBE GaN-on-SiC[124]	MOVPE & HVPE GaN-on-Al_2O_3[74],[138],[75]	None
Main limitations	Complexity: numerical method Restrictive assumptions (random distribution, high TD density)	Complexity: numerical method	Complexity: numerical method Need for high quality measurements
Main advantages	Enables to quantify of the correlation between TDS	Easily adaptable model of TD distribution No ensemble averaging assumption	No influence of the TD distribution/correlation on the TD density

Table 4.1 : Characteristics of XRD procedures for extraction of TD density. Densities of edge TDs, screw TDs and the total density of TDs are respectively noted ρ_e , ρ_s and ρ_{tot}.

4.2. Additional characterization methods

Beyond XRD methods, TD densities can be measured by means of other characterization techniques, such as TEM and CL. These two techniques consist in imaging the dislocations on a determined area, so they can be counted and their density calculated. Hence, these characterizations constitute a more direct measurement of TDs than XRD. It should also be noted that TEM and CL are surface measurements, unlike XRD can usually be considered as a bulk measurement when considering layers with thicknesses of a few µm. Atomic force microscopy (AFM) also permits a similar counting of dislocations by detection of the pits forming at the point where TDs intersect the surface. However, this technique will not be used here, as it requires a wet etching of the sample surface[139] to clearly reveal small diameter pits of edge dislocations.

4.2.1. Transmission electron microscopy

Transmission electron microscopy (TEM) consists in the measurement of an electron beam transmitted through a thin material, with a typical thickness around 100 nm. While propagating through the material, the electrons undergo several interactions, such as absorption and diffraction. The electron beam absorption is critical in TEM measurements. It strongly limits the maximum thickness of the sample, to a value which depends on the atomic number of the atoms within the material, on the energy of the electron beam and on the temperature. For III-N materials, this critical thickness is normally of a few hundred of nm. Sample preparations are therefore required to thin the samples, by means of cleavage,

mechanical polishing and milling with a focused ion beam. Sample preparation is the main drawback of TEM characterization, as it is a long and delicate operation, especially for plan view measurements, such as those used to measure TD density.

In addition to an electron beam source and an electron detector, transmission electron microscopes are constituted of a set of lenses (see **Figure 4.3a)**), which modulate the incident and transmitted beam. The transmitted signal can be measured either on the focal plane of the objective lens or in the image plane of the projection lens. The first method is called diffraction mode, as it permits to observe the spots pattern of the diffracted beam. The second method, called the image mode, is used to obtain either bright field or dark field images.

Bright field images are performed by selecting the transmitted beam and blocking the diffracted beams, using a diaphragm placed in the focal plane of the objective lens. A contrast between atoms of different mass can be observed on this transmitted beam, while crystalline defects cause the electrons to deviate, and so result in a dark area. Conversely, by blocking the transmitted beam and imaging using a beam diffracted by an $(hkil)$ reflection, one performs a dark field image. In this case, the image is dark unless for areas of the crystal which follow Bragg's law, for which a diffracted beam is detected and the zone appears bright.

To obtain an image of the dislocations in III-N samples, a series of dark field measurements are carried out, while scanning an area of the thinned sample. A bright contrast is seen when dislocations strain the lattice in a direction which has a component along the diffraction vector $\vec{g}$. According to the theory of elasticity, this corresponds to the condition $\vec{g}.\vec{b} \neq 0$, where $\vec{b}$ is the Burgers vector of the dislocation.

TEM measurements can be performed out either on a cross section of the sample or on its surface. The latter method, called a plan-view measurement, is better suited to perform a quantification of TDs, owing to the greater quantity of measured dislocations. In plan-view mode, TDs are measured by using a $(hki0)$ reflection such as the $(11\bar{2}0)$.[109] According to the $\vec{g}.\vec{b}$ criterion, only edge and mixed dislocations should be visible. Nevertheless, the relaxation of screw dislocations at the surface induces a second strain contrast on the TEM images. This enables the measurement of the three types of TDs, and even to assess the nature of each dislocation. Indeed, by tilting the sample with an angle around 18°,[109] the contrast due to the horizontal component of Burgers vectors of edge and mixed dislocations is visible as a dark line along the core of the TD. On the other hand, the relaxation on the two interfaces of the film, associated to screw and mixed dislocations, appears as a doublet of black-to-white contrast perpendicular to $\vec{g}$. Mixed dislocations are therefore identifiable as they involve both contrasts. An example of this analysis is presented on the **Figure 4.6** of the section 4.3.1.

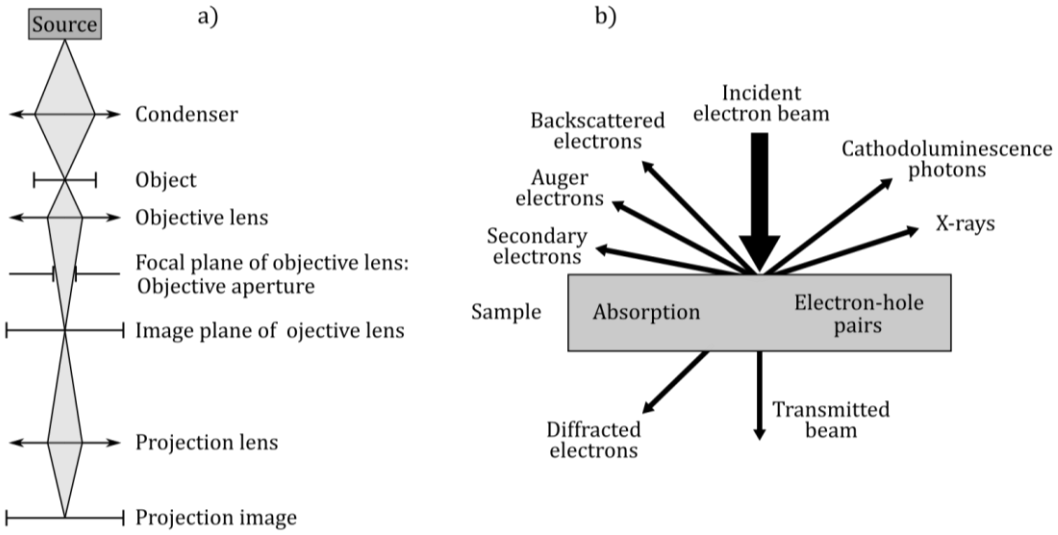

Figure 4.3 : Complementary techniques for threading dislocation characterizations. a) Scheme of a transmission electron microscope. b) Interactions between an electron beam and a semiconductor material.

4.2.2. Cathodoluminescence

Cathodoluminescence (CL) is another technique relying on the interaction between an electron beam and a material. As shown in **Figure 4.3b)**, one of the interactions between electrons and a semiconductor is the creation and subsequent recombination of electron-hole pairs, thus generating an emission of photons. CL technique consists in the measurement and analysis of this signal of photons.

This technique can be used to investigate the dislocations at the surface of a GaN crystal. In good quality GaN layers, the process of charge recombination leads to an emission of photons at an energy defined by the bandgap of the material. At TDs, non-radiative recombination occurs, and so there is no photon emission in the vicinity of dislocations.[140],[141] By scanning the surface of a sample with the electron beam while measuring the cathodoluminescence signal, we obtain an image of the sample, where the TDs appear as dark spots with a radius depending on the energy of the electron beam.[141] The quantification of TDs is then carried out by counting these dark spots.

Three examples of CL measurements are presented in the **Figure 4.5** of section 4.3.1. These images illustrate the main issue with CL measurements, namely the difficult measurement of high densities of TDs, as non-luminescent spots tend to overlap. This effect can be lowered by reducing the energy of the electron beam, as it is correlated with the vertical and lateral penetration of electrons in the crystal (see **Figure 4.4**), and therefore to the spot diameter. For low electron beam energies, TD densities of the order of $10^9\ cm^{-2}$ can be measured in GaN samples.

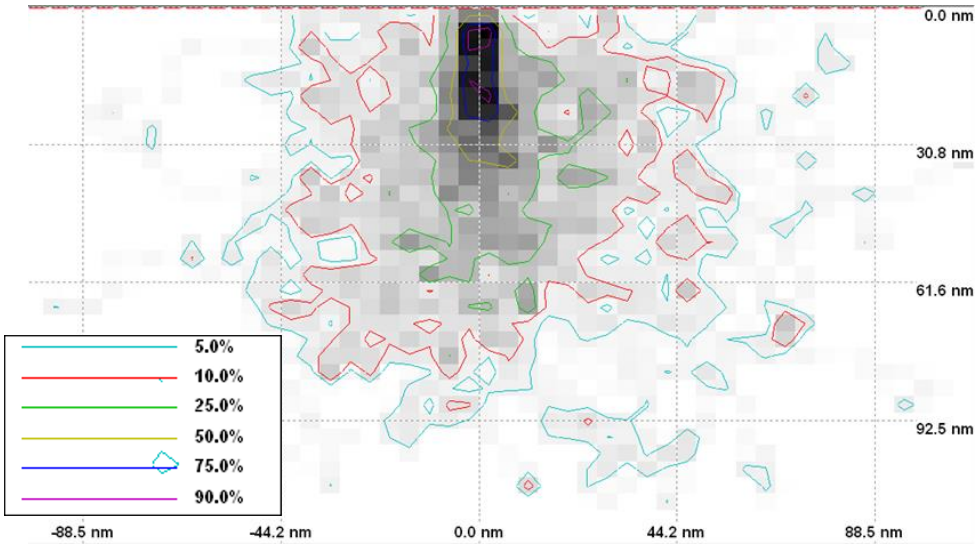

Figure 4.4 : Simulation of cathodoluminescence electron beam penetration in a GaN crystal. The simulation assumes an incident beam acceleration voltage of 3kV. The contour lines represent the intensity decay of the electron beam as penetrating into GaN.

4.3. XRD micro-strain measurements for the analysis of threading dislocations on GaN-on-Si layers

Despite being the most common XRD method to quantify TD densities, analyses based on the peak broadening of lattice misorientation measurements may lack accuracy. As seen in section 4.4.1, this is due to the restrictive assumptions made about the distribution of TDs, the distribution of Burgers vectors orientation not taken into account, a double counting of mixed TDs and a potential additional broadening linked to the sample curvature. On the basis of numerical simulations, *Kaganer et al.* suggested that misorientation analyses may give results more than four times underestimated for highly correlated dislocations.[124]

On the other hand, numerical approaches seek to model the shape of the diffraction peak, especially in the diffuse scattering region of the diffraction peaks. Accurate results are expected from these methods, as the diffuse scattering of peak tails is not influenced by the distribution of TDs nor by their correlation. However, these models involve complex mathematics, which are often considered too time consuming to implement for simple metrological studies. Further limitations are due to the low intensity of diffuse scattering, which can be difficult to distinguish from the measurement noise. Hence, on laboratory diffractometers, long measurements with high X-ray counting times are required.

In order to obtain a measurement that is both reliable and easy to implement, we decided to evaluate the alternative peak broadening method based on micro-strain measurements. As this analysis is based on the extension range of the strain field around a dislocation, the same issues as for misorientation measurements can be raised about the distributions of TDs and of

their Burgers vector. The impact on the results may however differ, as the radial micro-strain follows a specific $1/r$ decreasing trend extending away from the dislocation line (see section 1.3.1), and no comparison to a peak shape analysis has been made, such as in reference[124] for misorientation measurements. We can also note that micro-strain measurements rely on $(2\theta - \omega)$ $scans$, which are not affected by the sample curvature. This enables measurements on wafers highly bowed by thick heteroepitaxial layers, without reducing the size of the beam and thus increasing the measurement time.

4.3.1. Methodology

To carry out the study of micro-strain we used a set of samples of different types. Three 200mm diameter wafers of GaN(0001)-on-Si(111), grown by MOVPE, are designated as samples (1), (2) and (3). The growth parameters have been changed for each of these samples, to decrease their quality from GaN/Si(1) to GaN/Si(3). The thickness of the GaN layer is 1.20 µm for GaN/Si(1), 1.90 µm for GaN/Si(2) and 1.85 µm for GaN/Si(3). Note that sample GaN/Si(3) corresponds to the sample used for the stress gradient analyses of chapter 3.

We also used three samples with low stress gradients, namely a 3 µm thick GaN sample directly grown by MOVPE on a sapphire substrate, a 2 µm thick GaN sample grown by MOVPE on an AlN nucleation layer on SiC substrate and a freestanding GaN sample.

All the XRD data were acquired on the laboratory PANalytical X'Pert Pro diffractometer (see section 2.3.3). The measurements were made in high resolution mode, with an asymmetrical four bounce Ge(220) primary optic and an analyzer crystal in front of the detector, in order to minimize the impact of instrumental resolution and diffraction size effects on asymmetric reflections. Cross-slits were kept fully open, so the measured intensity is maximized. This configuration is the same than the one used for measurements in the chapter 3 and the instrumental resolution presented in **Figure 3.10** also applies to these measurements. In the following, the peak width of XRD micro-strain measurements is corrected accordingly, by using equation (2.23).

As detailed in section 4.1.1.b), TD quantification using their micro-strain relies on the measurement of $\omega - 2\theta$ radial scans of the reciprocal space. The scans were acquired in skew-symmetric geometry, allowing the measurement of a larger set of reflections on the diffractometer. The experimental peak width is linked to both the densities of screw and edge dislocations. Hence, an assumption has to be made on one of these two density parameters. As screw dislocations show typical densities significantly lower than that of edge dislocations,[4] their impact on the broadening of the diffracted peak is limited. The value of screw dislocations density extracted from tilt measurements by employing equation (4.3) is therefore used in the calculations of R_s and $\langle \varepsilon_s^2 \rangle$ (equations (4.10) and (4.8)).

This leaves the density of edge TDs ρ_e as the only remaining variable to calculate the peak broadening. However, according to equation (4.7), $\langle \varepsilon_e^2 \rangle$ has $a \ln\left(\frac{R_s/r_0}{R_s}\right) = -2\rho_e \ln(\rho_e) -$

$4\ln(2r_0)\rho_e$ dependence, which does not allow to write ρ_e in a simple algebraic form. Hence, we used two equivalent approaches to calculate ρ_e:

- We choose an initial guess for the value of ρ_e and calculate the values of R_e and $\langle\varepsilon_e^2\rangle$ (equations (4.9) and (4.7), with $\nu = 0.183$), and finally the total mean squared strain (i.e. from edge and screw TDs) and the corresponding peak broadening β_ε (equations (4.11) and (4.5)). The calculated β_ε is compared to the width of the measured peak, after correction of the instrumental broadening. These operations are repeated with different vales of ρ_e until β_ε corresponds to the experimental peak width. This procedure can easily be carried out with a spreadsheet software, but requires to manually change the parameter ρ_e.

- As the first procedure can be rather tedious when analyzing large datasets, we propose an alternative automatized approach. By using equations (4.11), (4.5), (4.7) and (4.9), we can write the density of edge dislocations under the form:

$$a\rho_e \ln(\rho_e) + b\rho_e + c = 0 \tag{4.14}$$

where:

$a = -2$

$b = -4\ln(2r_0)$

$$c = \frac{\langle\varepsilon_s^2\rangle - \dfrac{\beta_\varepsilon^2}{8\,ln\,2\,tan^2\theta}}{\dfrac{b_e^2 A}{3\pi^2}\left(B(cos^2\Delta_1 + cos^2\Delta_2 + cos^2\Delta_3) + (B-2)(cos^2\Psi_1 + cos^2\Psi_2 + cos^2\Psi_3)\right)}$$

Δ_n and Ψ_n, $n \in (1,3)$ being the geometric terms for each of the three edge dislocation systems.

Equation (4.14) can be resolved by means of a Lambert W function, as shown in **Appendix 3**. The density of edge TDs has two real number solutions, as $\frac{-c}{a}\exp\left(\frac{b}{a}\right) < 0$. The density of edge TDs is given by the $W_{-1}(z)$ branch of the Lambert W function:

$$\rho_e = \exp\left(W_{-1}\left(\frac{-c}{a}\exp\frac{b}{a}\right) - \frac{b}{a}\right) \tag{4.15}$$

Various numerical codes propose pre-built functions to evaluate $W_0(z)$, allowing a simple calculation of Equation (4.15).

For both solutions presented above, the total dislocation density is finally found by adding together ρ_s and ρ_e.

As a basis of comparison for the micro-strain measurements, we used several alternative measurements of TD densities, namely XRD misorientation, TEM and CL measurements. ω scan measurements of tilt and twist were carried out on the (0004) plane, for screw dislocations quantification, and in skew-symmetric mode on the highly tilted $(20\bar{2}1)$ plane for the

measurement of edge dislocations. As misorientation measurement is intended to be a fast analysis of the TD density, $(20\bar{2}1)$ is considered to give a good enough approximation of the twist value and no twist extrapolation is made (see section 4.1.1.b)). Both edge and screw TD densities are then added together to get the global result. The (0004) reflection has been chosen for tilt measurements owing to its higher Bragg angle and beam incidence angle than the (0002). As shown in the equation (2.24), this limits the additional broadening due to the curvature of the sample, without having to reduce the size of the beam with cross-slits.

CL measurements were carried out on an Allalin instrument from Attolight. In this tool, a focused electron beam scans the sample while the optical emission is collected and analyzed by a spectrometer. This spectrometer consists of a 320 mm monochromator, from Horiba Jobin Yvon, fitted with a 1024 × 1024 EMCDD high-speed camera adapted for UV-visible detection (200 nm -1100 nm). The camera enables near-instant acquisition of the entire emission spectrum. In all experiments, the sample is measured at room temperature.

For measurements on the samples GaN/Si(1), GaN/Si(2), GaN/SiC and GaN/Al_2O_3, the current and acceleration voltage of the incident beam are set to a few nA and 3 kV respectively, leading to a relatively low energy for the incident electrons. This reduces the diameter of the dark contrast spots around TDs, which is linked to the excited volume of crystal and therefore to the beam energy.[141] Hence, the overlap of dark spots on CL cartographies is reduced, enabling the counting of TDs up to a density of about 2×10^9 cm^{-2}. For each sample, two cartographies are measured, corresponding to a total investigated area of 105 μm^2. For the freestanding GaN sample, low dislocation density requires to image larger areas of the sample to increase counting statistics. Three measurements are carried out, on a total surface of 3840 μm^2. The beam acceleration voltage is raised to 10 kV in order to obtain well defined spots with an increased size of several pixels. **Figure 4.5** shows examples of three of our measured CL images. We can see that a higher density of dislocations on GaN/Si(2) sample makes the dislocation count more difficult than for GaN/SiC or freestanding GaN samples.

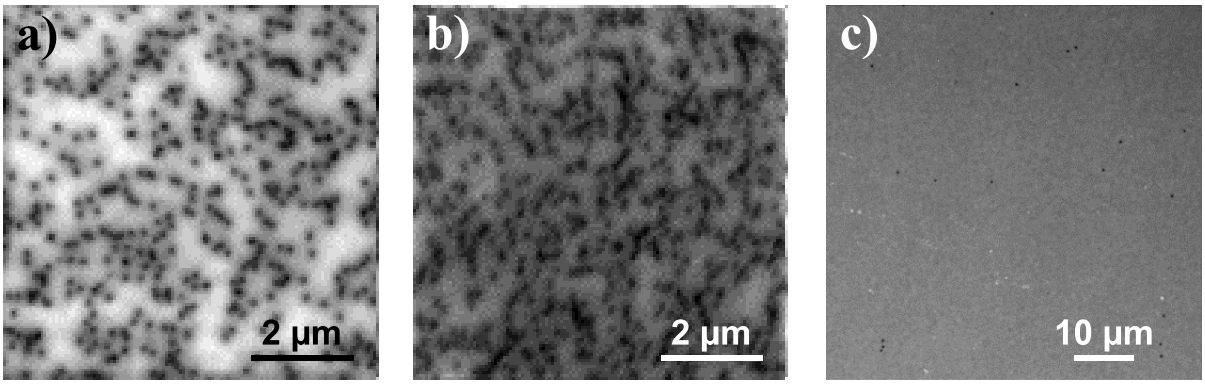

Figure 4.5 : Dislocation imaging using cathodoluminescence. a) GaN/SiC sample. b) GaN/Si(2) sample. c) GaN freestanding sample. Each dark spot corresponds to a TD.

TEM measurements were carried out in plan view mode to quantify the density of edge, screw and mixed TDs. The samples of GaN-on-Si (1) and (2) were prepared by means of a mechanical polishing and a milling with a 7° incidence ion beam, on a Gatan PIPS II machine, allowing measurements on areas between 5 µm² and 30 µm². TEM measurements were carried out on a ThermoFisher Osiris microscope. Bright-field plan view images were recorded in scanning microprobe mode, by using a condenser aperture of 50 µm. The images were recorded with a 15000-fold magnification for the sample GaN/Si(1) and a 11000-fold magnification for GaN/Si(2). A good counting statistic was achieved, ranging from 100 to 250 TDs per image, as shown in **Figure 4.6**.

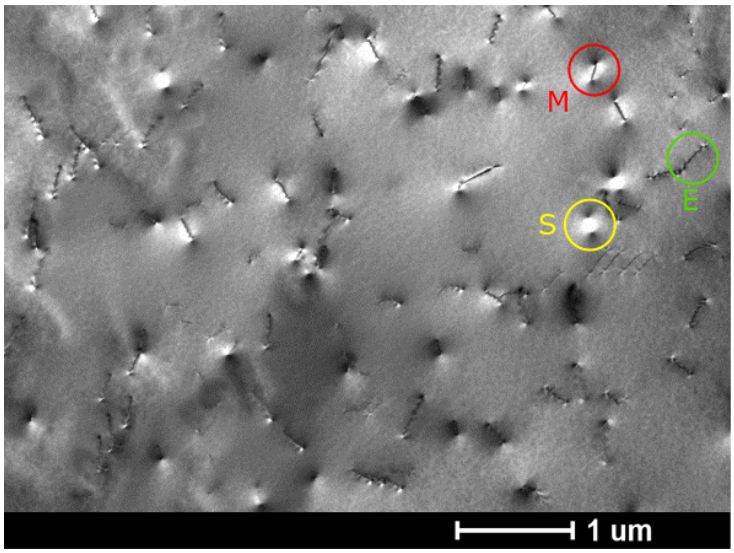

Figure 4.6 : Dislocation imaging using plan view TEM. Measurement carried out on the sample GaN/Si(2). Examples of edge (E), screw (S) and mixed (M) dislocations are shown.

4.3.2. Issues encountered in the case of layers with high stress gradients

As we have seen in the section 1.3.2 and the chapter 3, GaN samples may be unevenly strained, owing to the presence of in-depth stress gradients. This varying strain introduces a second source of broadening to the radial XRD peaks, which adds to the micro-strain broadening. Note that this broadening can be asymmetrical, depending on the gradient shape, while the broadening from micro-strain is always symmetrical (see section 2.4.3). The stress gradient is especially strong in GaN-on-Si samples and has therefore a large influence on the diffraction peak shape compared to GaN grown on SiC. As shown in **Figure 4.7**, the diffraction measurements show a quasi-symmetrical broadening of the peaks in the case of the GaN sample grown on a SiC substrate, likely indicating a broadening mainly induced by the micro-strain effect. By contrast, the GaN-on-Si sample shows a clear asymmetrical broadening, as the diffracting peaks are also altered by the stress gradient. Consequently, the width of the peak is not only affected by the micro-strain magnitude and so cannot be directly used to quantify the TD density.

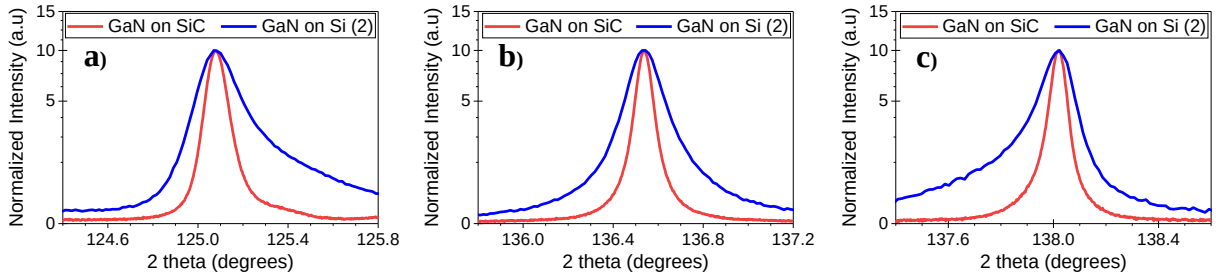

Figure 4.7 : Shapes of 2θ – ω peaks for different inclinations χ of the diffracting plane with respect to the surface. a) $(30\bar{3}2)$ plane, at $\chi = 70.45°$. b) $(20\bar{2}5)$, at $\chi = 36.91°$. c) $(10\bar{1}6)$ plane, at $\chi = 17.38°$. Blue line: GaN/Si (2) sample. Red line: GaN/SiC sample. The peaks of the two samples have been aligned to the same 2θ position.

Nevertheless, the value of the strain in these samples varies with the direction of observation. Assuming a biaxial in-plane stress acting on the layer, the resulting strain field for a hexagonal crystal like GaN, (0001) oriented along the z axis, is such that the strain value $\varepsilon_{\chi\phi}$ at a given orientation $(\chi\phi)$ is:[138]

$$\varepsilon_{\chi\phi}(z) = \sigma(z)((S_{11} + S_{12} - 2S_{13})\, sin^2\chi + 2S_{13}) \qquad (4.16)$$

where at a depth z, $\sigma(z)$ is the biaxial in-plane stress. $\varepsilon_{\chi\phi}$ is the resulting expansion or contraction of the lattice in a particular direction $(\chi\phi)$. This direction is defined by an angle χ, which is its inclination with respect to the surface of the layer, and an angle ϕ around the normal of the surface. S_{11}, S_{12} and S_{13} are the elastic constants of GaN.

Figure 4.8 illustrates the consequences of this equation. A tensile biaxial in-plane stress leads to a negative compressive strain in the direction normal to the surface, due to the Poisson

effect. The strain value progressively increases when tilting the direction of observation (increasing χ), until changing its sign and becoming positive when parallel to the surface. Necessarily, in between, there is a direction for which the strain is zero. This direction χ_0 can be calculated by a straightforward modification of equation (4.16):

$$sin^2\chi_0 = \frac{-2S_{13}}{S_{11} + S_{12} - 2S_{13}} \tag{4.17}$$

Using the elastic constants of GaN (S_{11} = 3.0067 TPa^{-1}, S_{12} = -0.9616 TPa^{-1}, S_{13} = -0.5217 TPa^{-1}),[12] we find this zero strain inclination to be 35.54°.

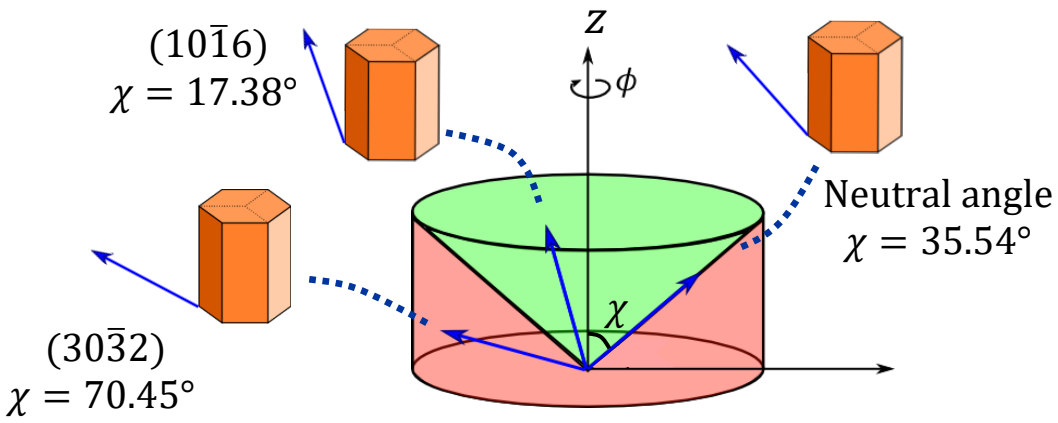

Figure 4.8 : Effect of a tensile biaxial stress on a hexagonal crystal of GaN. $\varepsilon_{\chi\phi}$ is negative in the ($\chi\phi$) directions represented by the green area and positive in directions represented by the red area.

As we saw in **Figure 4.7 a)**, using a diffracting plane with low tilt with respect to the surface leads to an asymmetrical broadening on the lower angle side of the peak of GaN-on-Si, as a result of the measurement of a negative macro-strain (a compression of the cell). The same measurement on a highly tilted plane (**Figure 4.7 c)**) leads to a broadening on the higher angle side of the peak, associated with a positive micro-strain (a dilation of the cell). If we choose a diffracting plane with an inclination close to 35.54°, such as the (20-25) reflection (36.91° with respect to the surface), the sample is observed in a direction for which the strain value is almost zero. Consequently, the broadening of the diffraction peak is no longer affected by the stress gradient, and so only influenced by the dislocations. The peak is therefore symmetrical and its width can be used for the micro-strain calculation of TD density.

4.3.3. Highlight of the stress gradient effect

To examine the effect of a stress gradient on micro-strain TD density measurements, we studied the trends of the different contributions to the mean absolute strain $\langle|\varepsilon|\rangle$ in the samples, when changing the inclination χ of the diffracted plane with respect to the surface.

In the micro-strain model, the strain distribution is assumed to be Gaussian, with a probability density function $P(\varepsilon) = k \exp(-c^2\varepsilon^2)$.[87] Hence $\sqrt{\langle\varepsilon^2\rangle} = 1/(\sqrt{2}c)$ and $\langle|\varepsilon|\rangle = 1/(\sqrt{\pi}c)$ (expectation of a half-normal distribution), which leads to:

$$\langle|\varepsilon|\rangle = \sqrt{2/\pi}\,\sqrt{\langle\varepsilon^2\rangle} \tag{4.18}$$

Using equations (4.8), (4.10) and (4.18), we obtain a linear relation for the screw dislocation contribution to the mean absolute strain $\langle|\varepsilon_s|\rangle$ versus $\sin\chi$, with a slope α_s depending on the screw TD density:

$$\langle|\varepsilon_s|\rangle = \alpha_s(\rho_s)\ sin\,\chi \tag{4.19}$$

For edge dislocations, we find that the average geometrical term $(2.45\,cos^2\Delta + 0.45\,cos^2\Psi)$ for the three dislocation systems is proportional to $sin^2\chi$. Hence, the contribution of edge type dislocations to the mean absolute strain $\langle|\varepsilon_e|\rangle$ has a slope α_e versus $\sin\chi$:

$$\langle|\varepsilon_e|\rangle = \alpha_e(\rho_e)\ sin\,\chi \tag{4.20}$$

The complete demonstration for equations (4.19) and (4.20) is given in **Appendix 4**. Equations (4.19) and (4.20) are used in **Figure 4.9** to fit the variation of the micro-strain influence with the inclination of the diffracting plane. The values of the slopes are chosen arbitrarily, with a factor of two between α_s and α_e, corresponding to a density of edge TDs about ten times higher than the screw TD one. The behavior of the mean absolute strain $\langle|\varepsilon_g|\rangle$ coming from the stress gradient is found directly from Equation (4.16):

$$\langle|\varepsilon_g|\rangle = \langle|\varepsilon_{\chi=0}|\rangle \left|1 + \frac{(S_{11} + S_{12} - 2S_{13})}{2S_{13}}\ sin^2\chi\right| \tag{4.21}$$

With $\langle|\varepsilon_{\chi=0}|\rangle$ the absolute mean value of the strain gradient in the direction normal to the surface.

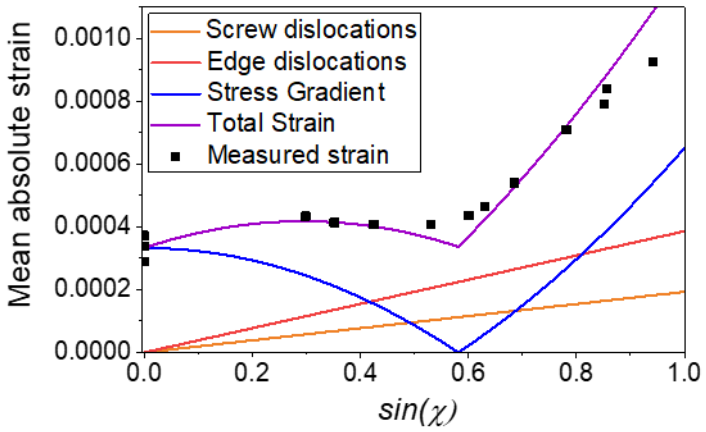

Figure 4.9 : Variation of different contributions to the mean absolute strain versus the inclination χ with respect to the surface.

In **Figure 4.9**, the total $\langle|\varepsilon|\rangle$ is assumed to be the sum of contributions $\langle|\varepsilon_s|\rangle$ and $\langle|\varepsilon_e|\rangle$ from dislocations and $\langle|\varepsilon_g|\rangle$ from the stress gradient. The corresponding curve is v-shaped, with a minimum close to the tilt corresponding to the $(20\bar{2}5)$ diffracting plane. The total strain measured on sample GaN/Si(3) has been added to the plot and matches quite well with the theoretical curve, implying that we can consider the strain to be dominated by the stress gradient and the dislocation density. The measured strain is extracted from the full width at half-maximum β of $2\theta - \omega$ diffraction peaks by using the equation (2.27). Note that the average strain value of the three symmetrical reflections (0002), (0004) and (0006) is taken as $\langle|\varepsilon_{\chi=0}|\rangle$ parameter for plotting the stress gradient behavior.

Having validated this preliminary analysis, we carried out micro-strain measurements on each of the five samples grown on hetero-substrates, on a set of diffracting planes with different inclinations χ, and calculated the TD densities corresponding to the measured widths, as detailed in the section 4.1.1.b). The results are plotted against the inclination of the diffracting planes in **Figure 4.10**. For each specimen, the magnitude of the stress gradient is estimated by extracting the RMS value $\varepsilon_{\chi=0}$ of the associated strain gradient, shown on the top of each graph. This value is derived from the slope of Williamson-Hall plots of the symmetric (0002), (0004) and (0006) reflections.

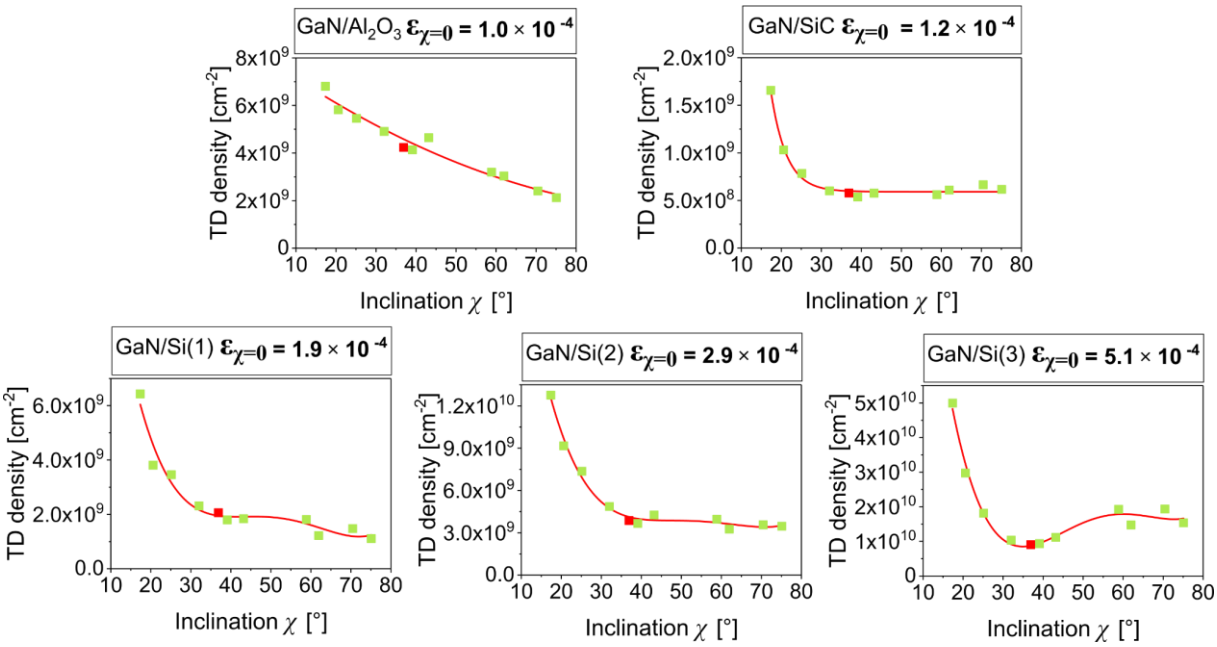

Figure 4.10 : Total density of threading dislocations calculated from micro-strain measurements on crystal planes with varying inclination χ with respect to the surface. At the top of each graph, $\varepsilon_{\chi=0}$ is the RMS value, in the direction normal to the surface, of the macro-strain induced by the stress gradient. The red points denote the $(20\bar{2}5)$ reflection, for which the stress gradient should have no effect on the calculated TD density.

By comparing the five graphs in **Figure 4.10**, we observe that the stronger the stress gradient of the sample is, the more the plots tend to adopt a V-shape, with a minimum for the $(20\bar{2}5)$ plane. This behavior is the result of an additional macro-strain broadening at high and low inclinations, as seen in **Figure 4.9**, which leads to an overestimation of TD densities for the corresponding reflections. This effect is increasingly apparent with the increase of $\varepsilon_{\chi=0}$. The shape evolution of the plots highlights the fact that, in some of the samples like GaN/Si(3), the stress gradient has a non-negligible effect and that the use of $(20\bar{2}5)$ planes is therefore essential to properly measure the micro-strain TD density.

On the other hand, when considering the peak broadening of GaN/Al_2O_3 sample, we assume the macro-strain contribution to be negligible compared to the micro-strain contribution, as this sample has the lowest stress gradient magnitude. On this sample, the V-shape was thus expected to be replaced by a constant value of TD density for all χ inclinations. Instead, a decreasing tendency is observed and seems to appear to some extent in the graphs of all the samples. The same trend has been observed when processing the data of the reference paper on micro-strain measurement on GaN from *Metzger at al.*[95] This may indicate that another effect, not considered in the model, is responsible for an additional broadening at low inclination with respect to the surface.

To address this issue, we carried out analyses on the magnitude of size effects in our samples by using Williamson-Hall plots. The results showed that dimensional effects were negligible. An example of this analysis is presented on **Figure 4.11** for sample GaN/Si(1), which gives very high correlation lengths of 1.9 µm for the lateral one ($L_{//}$) and 2.0 µm for the normal one ($L_{\perp}$).

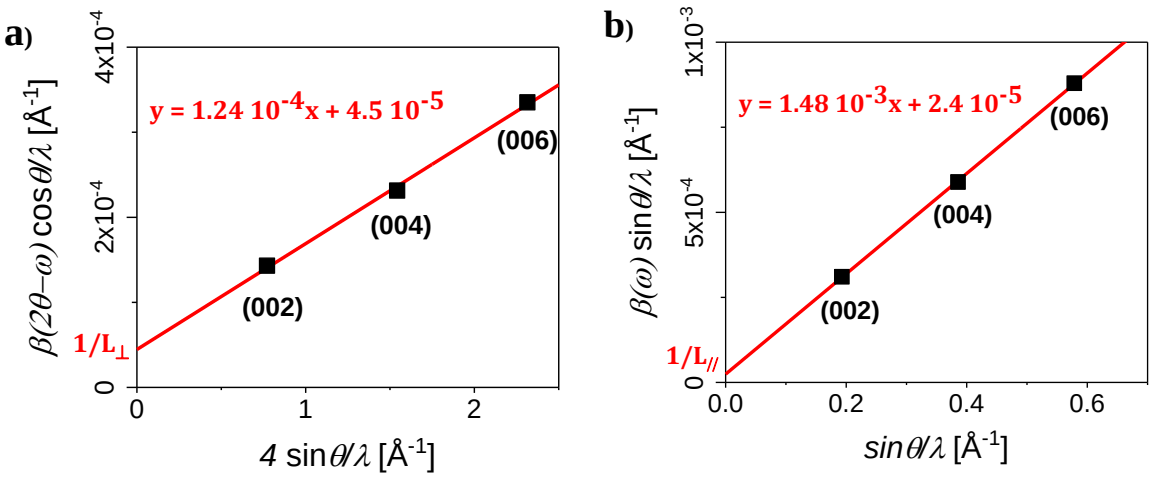

Figure 4.11 : Williamson-Hall plots for size effect estimate. The analysis is carried out for the sample GaN/Si(1), on symmetrical (0002), (0004) and (0006) reflections. a) Analysis of the full width at half maximum β(2θ − ω) of the diffracted peak of 2θ − ω scans. b) Analysis of the full width at half maximum β(ω) of the diffracted peak of ω scans. The lateral and normal correlation length $L_{//}$ and $L_{\perp}$ are found at the y-intercept of the linear fits.

The unexpected decreasing trend is neither due to the choice of the Poisson ratio value ν. As shown in **Figure 4.12**, the shape of curves in **Figure 4.10** does not vary with the value of Poisson ratio. This trend is also unaffected by the use of either equation (4.6) from *Hordon et Averbach* or the formula that we demonstrated (equation (4.7)), for the calculation of the mean squared edge TDs micro-strain. In fact, our GaN-suited results give an estimate of TD dislocation of GaN/Si(2) sample 22%-27% higher than if simply using the theory of *Hordon et Averbach* derived for copper crystals. This result is almost independent of the reflection used for the micro-strain measurement and similar results are found for the other samples. In details, the changeover to equation (4.7) at constant $\nu = 1/3$ accounts for a 6.5%-8.5% increase of the calculated TD density and the subsequent reduction of Poisson ratio to $\nu = 0.183$ for an additional 14%-17% increase.

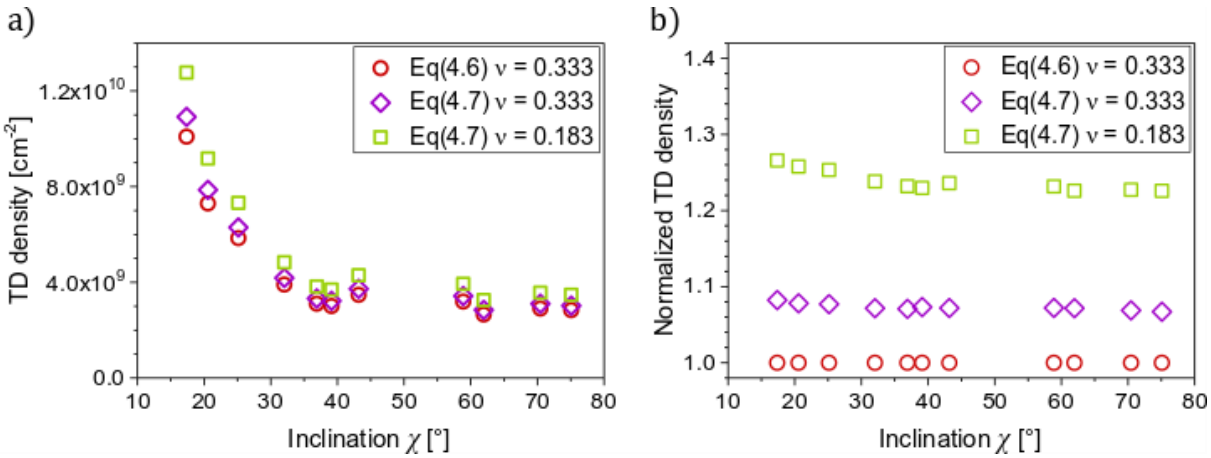

Figure 4.12 : Threading dislocation densities calculated with different formulas of edge threading dislocation mean squared micro-strain. The graphs are plotted using the data of GaN/Si(2) sample. a) The evolution of the total TD density with the

inclination χ of the diffracting plane is calculated using equation (4.6), which assumes a Poisson ratio $\nu = 1/3$ and equation (4.7), with Poisson ratios of $\nu = 1/3$ and $\nu = 0.183$. b) For each reflection, the TD density is normalized so the result of equation (4.6) is equal to unity.

Hence, no conclusive statement can be made about the origin of the observed decreasing trend. Further investigations would be needed to resolve this issue, which could affect the accuracy of micro-strain measurements.

4.3.4. Comparison with other measurement techniques

Along with the micro-strain measurements, we performed TD density quantifications with rotational disorder based XRD, CL and plan view TEM techniques. For the misorientations measurements, we show the results of two models, from *Dunn et Koch* and from *Kurtz et al.*, to highlight the diversity of existing calculations and the consequent variations in the results (about a factor 2 between these two models). These two models are compatible in terms of hypothesis with micro-strain analyses, as they assume a random distribution of TDs in the surface plane. Conversely, piled-up distribution models are not considered for the TD quantification, due to errors associated with the evaluation of the X-ray correlation length parameter (see section 4.1.1.a)).

The TD densities measured on GaN/SiC, GaN/Al_2O_3, GaN/Si(1) and GaN/Si(2) are compiled in **Figure 4.13**.

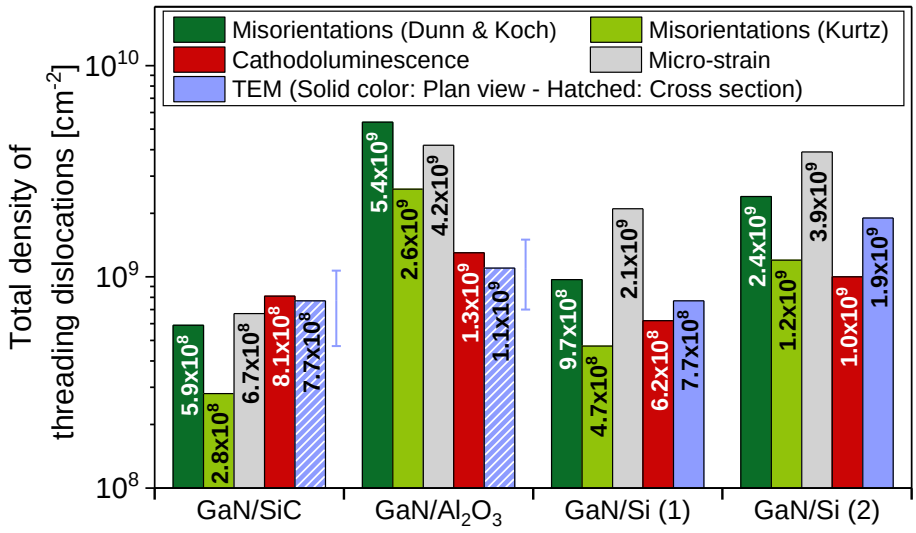

Figure 4.13 : Total density of threading dislocations found with XRD, CL and TEM characterization techniques for different GaN samples. Hatched bars correspond to cross section TEM counting of TDs, made on thin (~100 nm) samples prepared by focused ion beam. Due to the low number of TDs on these samples, these measurements are associated to a high statistical imprecision. The error bars shown on the graph correspond to a ± 3 TD count and a ± 5 nm sample thickness accuracy.

We observe that micro-strain and misorientations, especially with the Dunn and Koch model, give similar results, whereas CL and TEM measurements generally lead to lower

dislocations densities. This can be explained by at least three factors. Firstly, the counting of TDs in CL maps tends to underestimate the density of dislocations. This happens when the distance between two TDs is so short that the dark spots surrounding them in a CL image overlap. This effect is particularly strong when TDs form clusters, which is marginally observed in the CL images of **Figure 4.5**. A similar underestimate of dislocations within TD clusters may also happen, to some extent, when analyzing TEM images.

Secondly, we have seen that, in XRD measurements, each mixed dislocation is considered to be composed of one screw and one edge dislocation. The total TD density given by micro-strain and misorientations measurements is therefore overestimated, as mixed TDs are counted twice. This error can be estimated by using the plan view TEM images, which is the only measurement allowing to distinguish mixed TDs from screw and edge TDs. This analysis resulted in densities of mixed TD at the surface of $2.6\ 10^8\ cm^{-2}$ (34% of TDs) for GaN/Si(1) and $4.3\ 10^8\ cm^{-2}$ (23% of TDs) for GaN/Si(2). As a first approximation, we can subtract these values from the total densities of dislocations found by XRD. The value obtained by XRD misorientation measurements (Dunn and Koch model) and by TEM would then closely match for these two samples, while XRD micro-strain would still result in higher TD densities. Note that the count of mixed dislocations suffers from a further incertitude, due to the difficulty to distinguish between edge and mixed type for some TDs.

The third explanation arises from the difference in the measurement depths between the three techniques. Due to the low energy of its electron beam, CL is a surface measurement, with a collected signal coming from the top 70 nm of the GaN layer. Similarly, during TEM sample preparation, only the surface of the specimen is preserved, i.e. the top 80nm to 300nm. On the other hand, the attenuation length of the XRD beam in a GaN crystal exceeds 30 µm. Hence the whole GaN layer, which is 1 to 3 µm thick, is probed when diffraction measurements are performed. As the density of threading dislocations decreases from the buffer-GaN or substrate-GaN interface to the GaN surface, as shown in TEM images of **Figure 4.14**, it is normal to find a lower TD density for TEM and CL measurements.

However, for the GaN grown on SiC, the CL result is higher than those from XRD measurements. This is likely due to a different evolution of the TD density through the GaN layer in this sample. We expect samples on sapphire and silicon substrates to start with high dislocation densities at the nucleation layer, followed by a substantial density decrease when approaching the surface, while GaN on SiC substrate shows a good quality at the interface with the AlN buffer and less TD density variation. This assertion is supported by TEM cross section observations shown in **Figure 4.14**.

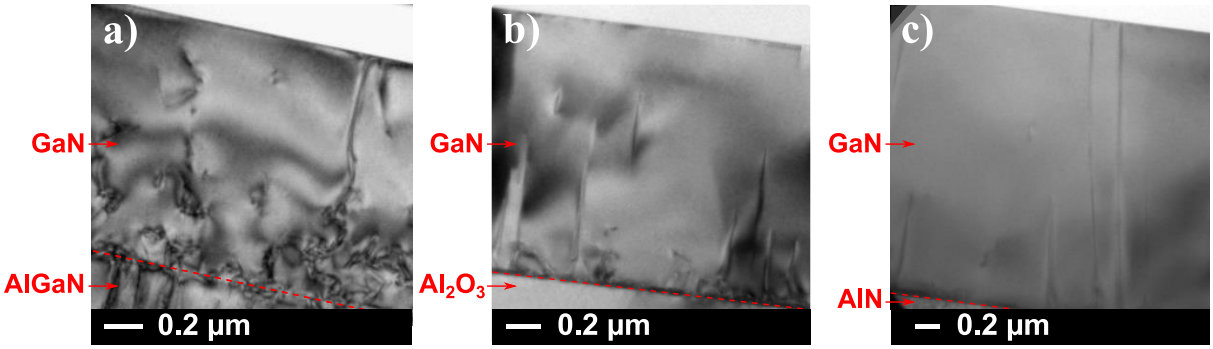

Figure 4.14 : TEM images of TDs in GaN layers measured in cross section. a) Sample GaN/Si(1). b) Sample GaN/Al2O3. c) Sample GaN/SiC. The separation between the GaN layer and the AlGaN buffer / the Al_2O_3 substrate / the AlN layer on SiC substrate is shown with a red line.

We also observe varying differences between misorientations and micro-strain measurements when changing the type of sample, probably due to differences in the dislocation arrangement. Despite the very common use of misorientations measurements for TD quantification, both XRD methods should therefore be used with care. We would therefore recommend using these techniques only to compare samples grown on the same substrates with similar epitaxy conditions.

Results of freestanding GaN sample are not included on **Figure 4.13** as we found that the widths of $2\theta - \omega$ scan peaks correspond to the instrumental resolution of the diffractometer. For the (205) reflection, it appears that the broadening components from instrumental resolution and from micro-strain are equal for a TD density of $3 \times 10^7 cm^{-2}$ (assuming respectively 90% and 10% of edge and screw TDs). We consider this value as being the low threshold of TD density measurable with micro-strain measurements with our material setup. Freestanding GaN specimens typically have TD densities below this limit, such as the value of $5.1 \times 10^5 cm^{-2}$ measured by CL on our sample. Micro-strain measurements are therefore not suited for this kind of sample, unless lowering the instrumental resolution of radial scans. At the cost of a reduction of the measured intensity, this might be achieved by using a monochromator/analyzer crystal with non-standard geometry, or made of crystals with a lower Darwin width than the Ge crystals used in these experiments. Conversely, according to equation (2.23), a 5% increase of peak width is induced by an FWHM instrumental resolution 3.12 times lower than the peak width predicted by the micro-strain model. On the (205) reflection, with the previous assumption on the screw/edge ratio, this corresponds to a TD density of less than $5 \times 10^8 cm^{-2}$. Above this limit, the effect of instrumental broadening may be neglected.

We have carried out an evaluation of XRD micro-strain measurement of TD density on a set of GaN samples grown on various substrates. In the case of GaN-on-Si layers, the presence of high stress gradients was shown to affect micro-strain measurements by inducing an

additional broadening on the diffracted peaks. We emphasized the impact of this issue in our measurements and solved it by using the $(20\bar{2}5)$ diffracting plane.

A comparison between XRD micro-strain, XRD misorientation, CL and TEM measurements has been carried out. For the XRD measurements, we show that micro-strain measurement is a complementary method to misorientation measurements for TD quantification, for densities $\gtrsim 3 \times 10^7 cm^{-2}$. The results confirm that Dunn and Koch model is better suited than Kurtz model for misorientation measurements in GaN layers, as expected from the literature. Both XRD measurements are easy to implement and could be combined to obtain an edge-screw TD ratio from misorientations, and the global dislocation density from micro-strain. However, the models associated with the XRD methods do not properly take into account all the existing distributions and correlations of the TDs.

When combined with CL and TEM data, these XRD analyses highlighted the difference of measurement depth between the different techniques. XRD gives a result averaged over the whole layer depth, while the low energy electron beam of CL enables the measurement of TD densities up to $2 \times 10^9 cm^{-2}$, but only probes the top 100 nm of the sample. TEM characterization, which can also be considered as a surface measurement, gives the TD density in the first few hundred nm of the layer, and is therefore roughly comparable to CL. The difference in analysis depth typically results in higher estimates of the TD density for XRD measurements. Furthermore, the variation of the mismatch between CL and XRD results, for samples grown on SiC, on Si and on sapphire, probably indicates a different behavior in the TD density reduction through the GaN layer. A full analysis of this issue should also take into account the differences in layer thicknesses, which probably explain the increased mismatch between CL and XRD results for the GaN/Si (2) sample, whose GaN layer is about 60% thicker than for GaN/Si (1). These analyses show that XRD measurements show varying behavior when very different samples are characterized and so they are most appropriate when comparing similar specimens.

To correctly compare the density of TDs measured by XRD and by complementary characterizations, such as TEM and CL, it is necessary to know the evolution of TDs through the GaN film. To better understand this limit, we present in the following chapter an in-depth XRD study of progressively etched GaN layers.

5. In-depth analysis of GaN layers

In the third and fourth chapters, we experienced difficulties when measuring TD densities and stress states in GaN-on-Si samples, as these values vary significantly within the thickness of GaN films, from the interface with buffer layers to the surface. The underlying problem is that the absorption of X-rays is low in this material, so XRD measurements typically probe the whole depth of µm-thick layers of GaN. The diffraction signal thus obtained is affected by all the conditions throughout the layer thickness and it is complex to extract each of these contributions to obtain a profile of stress, a profile of TD density, or even a value of TD density at the surface.

In order to obtain reliable measurements of profiles of stress and of TD density, we carried out a detailed measurement of these two properties on GaN-on-Si layers which were processed through cycles of etching and characterization. This chapter describes the principle of these measurements and of the subsequent analyses. The measured profile of strain is used to further assess the accuracy of our program of stress gradient analysis. The TD density profiles obtained from XRD lattice misorientation and micro-strain measurements are compared, and the discrepancy with CL measurements is analyzed. We finally study the close correlation between the reduction of TDs and the relaxation of compressive stresses within the GaN film.

5.1. Measurement Principle

The goal of this study is to analyze in-depth local characteristics of GaN-on-Si layers, by alternating cycles of characterizations and of reduction of GaN thickness by dry-etching the sample. As XRD based characterizations analyze the whole depth of remaining portions of GaN, several samples were used to perform etching from both the front-side and the back-side of the film.

To this end, a batch of 200 mm diameter GaN-on-Si samples were grown by MOVPE at CEA-Leti, with an intended thickness of GaN layers of 2300 nm. One of these samples was transferred onto a new (001) oriented substrate of silicon, by bonding it to the GaN surface by means of Ti/TiN layers. The initial (111) oriented Si substrate was subsequently removed by mechanical polishing and chemical etching. AlN and AlGaN buffer layers were also etched by reactive ion etching to reveal the face of the GaN film corresponding to the AlGaN/GaN interface, now located at the surface of the sample.

Measurement/etching cycles were then carried out on both the initial samples (**Figure 5.1 a)**) and the transferred sample (**Figure 5.1 b)**). On the initial samples, five etching cycles were performed on a first specimen (sample (1)), with respective intended etching depths of (30 – 470 – 500 – 500 – 500) nm. Since we found that the whole GaN layer was removed after the fifth etching, the process was repeated on a second identical specimen (sample (2)), with etching depths of (1500-100-150-150) nm. Etching steps were carried out in two phases: a

reactive ion etching followed by an atomic layer etching for the last 10 nm to be removed. This final phase aims at limiting the introduction of strain within the sample during etching steps. We used XRD measurements to verify that the first 30 nm etching on sample (1) had no significant impact on the stress state of the GaN layer.

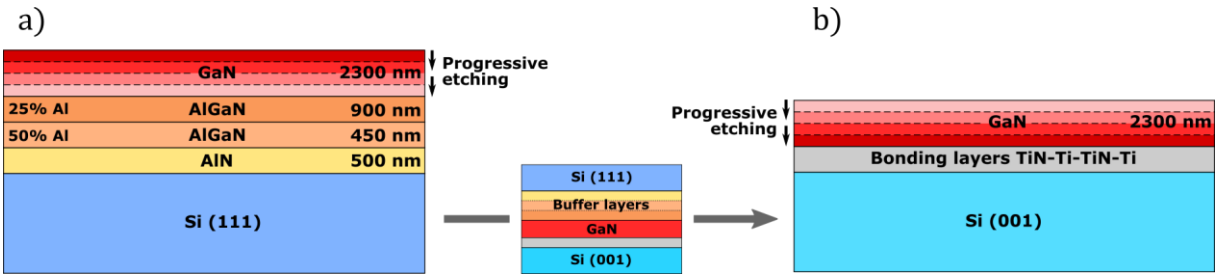

Figure 5.1 : Samples used for in-depth study of GaN-on-Si. a) Initial stack, as obtained by epitaxy. Corresponds to samples (1) and (2). b) Sample after transfer on a (001) Si substrate and removal of the initial (111) Si substrate and AlN/AlGaN buffer layers. Corresponds to sample (3). Each of the three samples is progressively etched from its surface.

Before each etching step and after the last ones, a series of characterizations was performed, including:

- Reflectometry and Ellipsometry measurements of the GaN layer thickness.
- XRD measurements of the density of TDs (micro-strain and lattice misorientation measurements), of the strain state and of X-ray correlation lengths in the GaN layer. The curvature of the sample was also measured to monitor the evolution of stresses within the sample.
- Raman measurements of the mean in-plane stress within the GaN layer.

On the transferred specimen (sample (3)), six etching cycles were performed. The first one corresponds to the removal of AlN/AlGaN buffers. During this operation, the aluminum content in the evacuated gas was monitored, so we could detect the moment when the last buffer layer was entirely removed. We stopped this first etching when a drop of the Al-concentration was detected. We observed that the etching rate was higher at the center of the wafer than at its edges. As a result, the GaN layer underwent a slight etching of around 140 nm, according to ellipsometry measurements. The intended etching depths of the five following cycles were respectively (45 – 75 – 150 – 300 – 600) nm, although the actual etching were measured to be 50%-70% deeper. This may be because we are etching the N-face of the GaN layer, which is more reactive than the standard Ga-face. The same characterizations as for samples (1) and (2) were performed, except for Raman measurements, due to time restrictions for processing the batch before the end of the thesis.

5.2. In-depth stress gradient analysis

5.2.1. Extraction of the stress gradient

a) Theoretical bases

As explained in the section 1.3.2, GaN-on-Si layers analyzed in this thesis are grown under compressive in-plane stress, as their lattice parameter is greater than the one of buffer layers beneath. As shown in the measurements and simulations of chapter 3, this strain is progressively relaxed during the growth, essentially owing to the recombination of TDs. During the post-epitaxial cooling phase, a tensile stress is introduced in the epitaxial layers, due to the mismatch of thermal expansion coefficients with the silicon substrate. This leads to a global shift of stress profiles within the epitaxial layers toward tensile values, as depicted in **Figure 5.2**. Note that there is a slight variation in the magnitude of this shift for each epitaxial layer, due to the different coefficients of thermal expansion of AlN and GaN. Besides the shift toward tensile values, we can assume that the shape of the stress profiles remain the same during the cooling process.[61]

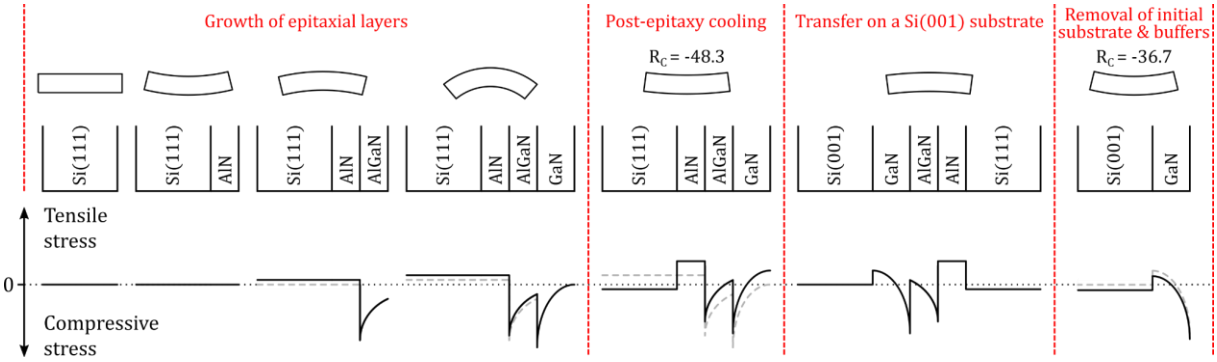

Figure 5.2 : Evolution of in-depth stress profiles within the sample GaN-on-Si (3) during its fabrication. For each step of fabrication of the sample, diagrams of the sample curvature, of the layer stack structure and of profiles of in-plane stress within these layers are shown. For the sake of simplicity, the second AlGaN buffer and the bonding layers are not depicted. The curvature is a direct image of the distribution of strain within the sample. A concave wafer corresponds to an average tensile stress within the surface layers, a convex wafer to an average compressive stress within the surface layers. The slight wafer curvature depicted after the growth of the AlN layer stems from a gradient of temperature within the sample. This additional curvature disappears after the post-epitaxy cooling step. R_c values correspond to curvature radii measured by XRD. A schematic shape of stress profiles is shown on the graphs below. Profiles corresponding to the previous step are depicted in dashed lines to easily follow the evolution of stress during the process. The introduction of tensile strain in the substrate during the epitaxial growth is exaggerated in the plots, so that it is noticeable. It is actually very slight, owing to the large thickness of the substrate compared to epitaxial layers.

The transfer of sample (3) on a relaxed Si(001) substrate does not lead to any modification of the stress state. We assume that no sliding of the GaN layer nor the Si(001) substrate over the bonding layers occurs during the process. The lattice parameter of GaN is therefore fixed at its interface with the new substrate. Hence, the subsequent removal of Si(111) substrate and buffer layers does not attenuate the stress gradient within GaN. This is confirmed by comparing XRD measurements performed before etching buffer layers and after etching the AlN layer, the $Al_{0.5}Ga_{0.5}N$ layer and about 90% of the last $Al_{0.25}Ga_{0.75}N$ buffer layer. As shown in **Figure 5.3**, the XRD profile of GaN remains the same, as its in-depth strain field is not modified. Hence, the shape of the stress gradient of GaN stays exactly the same in the transferred sample (3) as in samples (1) and (2). The stress profile is uniformly shifted toward

compressive stresses, as the tensile stress within epitaxial layers is slightly reduced when removing the initial Si(111) substrate, by compressing the Si(001) substrate.

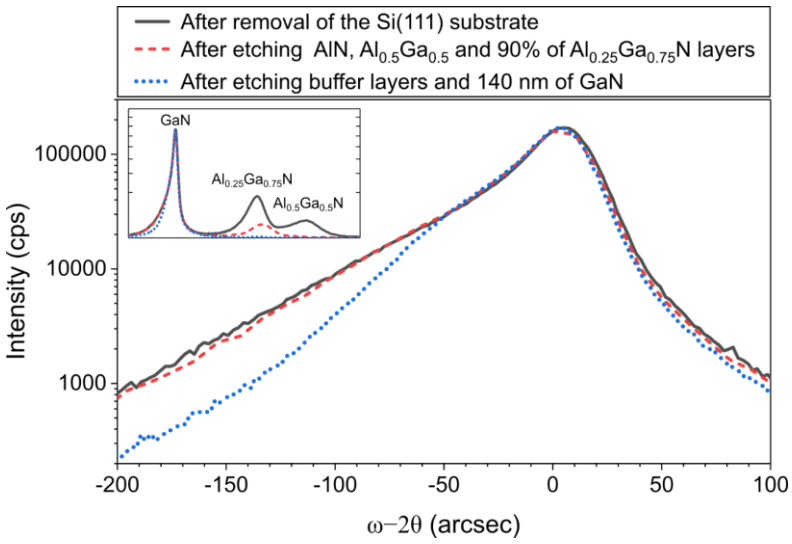

Figure 5.3 : Evolution of XRD profiles during the removal of buffer layers in the sample GaN-on-Si (3). Plot of (002) radial XRD scans centered on the GaN peak (relative angles measurement, intensity in log scale), before removal, after partial removal and after complete removal of the buffer layers. For the intermediate measurement, the etching operation was stopped for measurement just before completing the etching of the last buffer layer. From the full XRD profiles shown in the inset, we used the ratio of areas below $Al_{0.25}Ga_{0.75}N$ peaks to estimate that 90% of the layer was removed.

When progressively etching the GaN film, the stress profile in the remaining layer also appears unaltered, for the same reasons than discussed above to explain the result of **Figure 5.3**. A slight relaxation may occur at the GaN surface, especially at the edge of the sample. However, the in-depth extent of this relaxation should be limited to a few nanometers. We assume that it has a negligible impact on the XRD and Raman measurements at the center of the wafer presented in the following.

b) XRD Curvature measurements

As shown in in the section 3.1.2, it is possible to deduce the in-depth stress gradient in a GaN layer from the evolution of wafer curvature during the epitaxy process. Similarly, we can reconstruct such a stress gradient by monitoring the evolution of sample curvature between each cycle of GaN layer etching. The benefit of this second study is that the extracted stress gradient corresponds to that of the final GaN-on-Si specimen, with no need for assuming that no relaxation occurs in the lower part of the GaN layer during the growth process and that the shape of stress gradients remains unchanged during the post-epitaxy cooling phase.

We carried out this stress gradient reconstruction from the measurements on sample (3). On this sample, buffer layers have been removed, which means that the stress obtained using the Stoney equation corresponds to only the GaN layer. We used equation (3.3), by taking as

parameters the evolutions of thickness Δt and of curvature $\Delta\kappa$ between two etching cycles. The thickness is obtained from ellipsometry measurements. The curvature is derived from equation (3.2), based on XRD measurements along two orthogonal diameters of the wafer. At the edges of the wafer (i.e. at 90 mm away from the center), part of the $Al_{0.25}Ga_{0.75}N$ buffer appears to remain after the first etching cycle. Additionally, an uneven etching of the GaN layer is observed in the subsequent cycles of the process. This is visible on the reflectometry measurements of **Figure 5.4**, which show a shallower etching at the edges of the wafer. In order to obtain the value of stress at the center of the GaN layer, we restrict our analysis on curvature measurements within the range of -60mm to +60 mm away from the sample center.

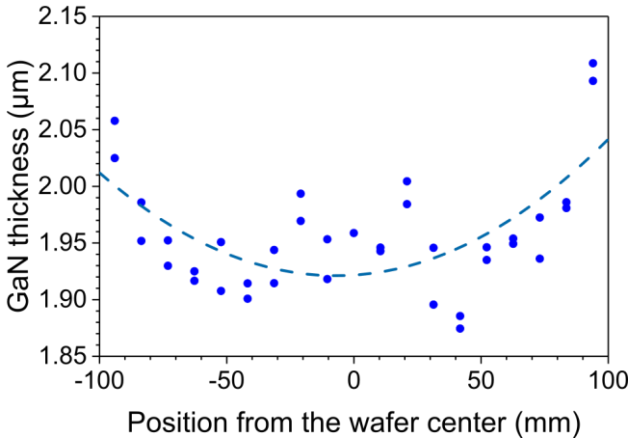

Figure 5.4 : Reflectometry measurement of the GaN layer thickness uniformity. Measurements were carried out along two diameters of the sample (3), after the second etching of GaN layer.

The stress gradient obtained is shown in **Figure 5.5**. Its general shape is coherent with the theoretical expectations depicted in **Figure 5.2**: the highly compressive stress close to the AlGaN/GaN interface rapidly decreases before flattening and becoming positive below the surface.

However, the profile lacks precision in the zone close to the initial AlGaN/GaN interface. The reason for this might be the high error bar on the value of Δt for the first etching cycles, due to shallow etching depths of less than 150 nm. This issue does not significantly impact the following cycles, as the relative error on Δt is limited for deeper etchings. The error bars shown in **Figure 5.5** correspond to an error of $\pm$ 10 nm on the ellipsometry measurements of thickness at the center of the GaN layer.

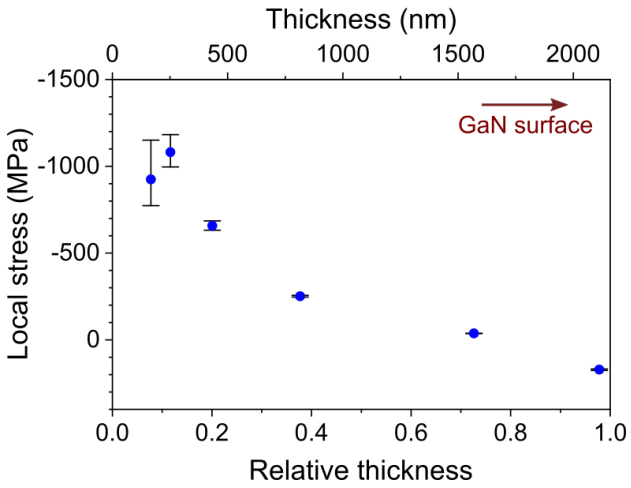

Figure 5.5 : Stress profile in a GaN layer, obtained from the evolution of curvature of the progressively etched sample (3). Negative stress values correspond to a compressive biaxial in-plane stress, positive values to a tensile stress.

Although the above procedure allowed us to obtain the global trend of GaN in-depth stress profiles, curvature measurements are significantly affected by small errors in the measurement of the GaN layer thickness. To obtain a more precise stress gradient, it appears to be necessary to work with alternative measurements of stress. These characterizations should be restricted to the center of the sample, where the thickness is constant. This can be readily achieved thanks to the millimetric beam sizes of XRD and Raman measurements.

c) XRD strain measurements

As discussed in chapter 3, radial XRD scans on symmetric reflections give a valuable representation of the stress profile within GaN layers. However, the reconstruction of a stress gradient from these data is complex, due to the asymmetric shape of XRD profiles. The in-depth study of GaN presented here allows to bypass this issue. We have seen earlier than etching cycles do not affect the strain profile within the remaining layer of GaN. Hence, the diffraction profiles obtained before etching can be approximated by the sum of the respective XRD signals of etched and remaining parts of GaN.

In our experiments, we use this approximation to obtain XRD profiles corresponding to the removed sublayers. For this, we use (002) diffraction profiles obtained at the center of sample (1), after the three first etching steps, and of sample (2) after the four etching cycles. The expected total etched depths are respectively of 30 – 500 – 1000 – 1500 – 1600 – 1750 – 1900 nm. Note that a total depth of 1500 nm is reached both on sample (1), after the fourth etching, and on sample (2) after the first etching. As the two corresponding XRD profiles fit well with each other, the data from both samples can be integrated together.

We first align the XRD profiles in 2θ by using the AlN peak, which is not affected by etching, as a reference peak. As several months separated the first and the last measurement, the intensity delivered by the X-ray source varied slightly between cycles of characterization.

We monitored these changes by measuring the intensity of the incoming X-ray beam. Each diffraction profile is modified accordingly, so measurements are comparable in terms of intensity. We finally apply an X-ray absorption correction to the intensity of each XRD profile. This allows us to simulate that the measured layer is still covered by the part of the GaN film already etched. Note that this absorption is not negligible (see **Figure 5.6 b)**) due to the use of the (002) reflection, which has a low beam incidence of 17.28°.

In this way, we obtained the set of diffraction profiles shown in **Figure 5.6 a),** which allows us to visualize the role of different parts of the GaN layer on the diffraction peak of the full GaN film. We subtracted from each of these profiles the diffraction peak measured after the next etching, thus obtaining a set of virtual diffraction peaks for each etched sublayer (**Figure 5.6 b)**). These peaks are quasi-symmetric, as the variation of strain within each sublayer is limited. Hence, we can use their 2θ position to reconstruct the strain gradient in the GaN film.

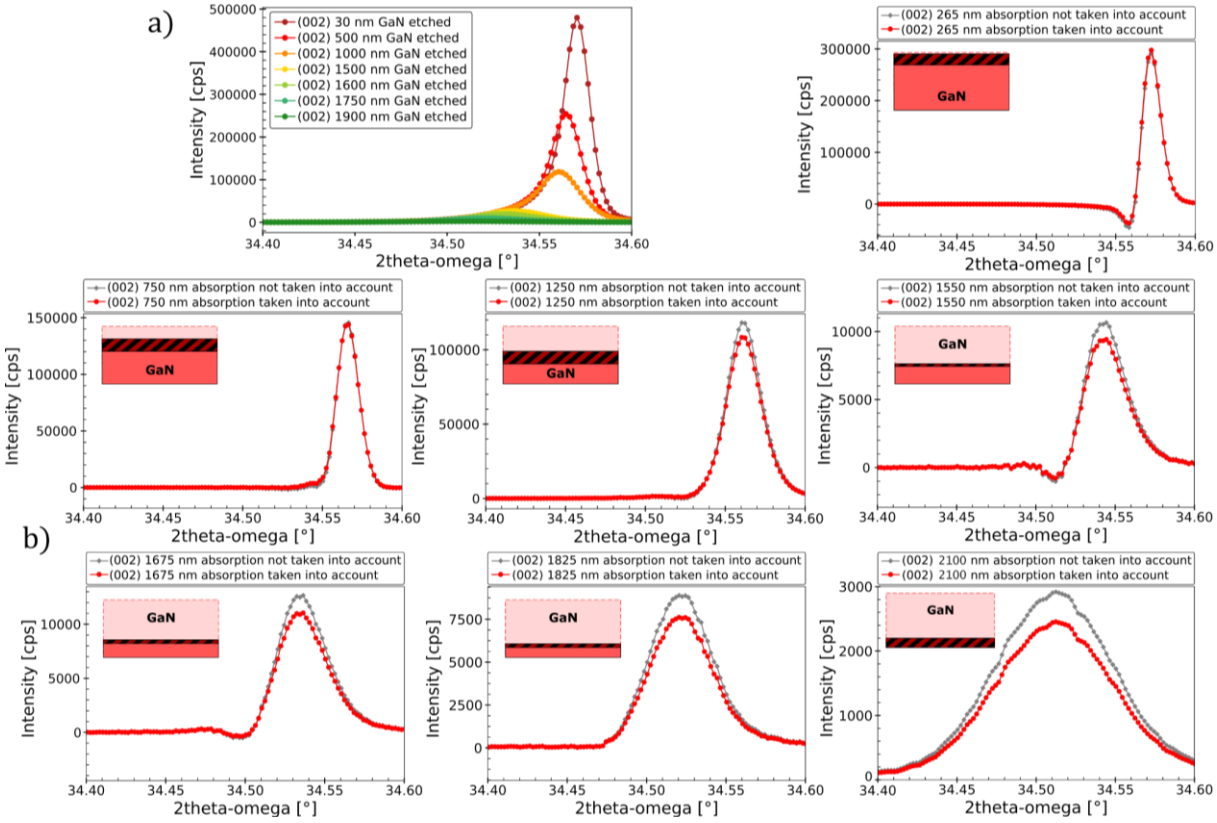

Figure 5.6 : In depth analysis of XRD profiles of a GaN-on-Si film. a) (002) radial scans measured after several etching cycles of samples (1) and (2), with intensity corrections of incident beam variations and X-ray absorption effects. b) Virtual XRD peaks corresponding to the etched sublayers of GaN. The impact of X-ray absorption is highlighted by the difference between plots taking this effect into account (red line) or not (grey line).

Note that the data from sample (3) is not used for a similar analysis, as the steep part of the strain gradient is removed during the first etching cycles. Hence, the diffraction peaks soon become really similar to each other, so that it is difficult obtain a proper XRD profile of sublayer by subtracting measurements with one another. Nevertheless, as no significant gradient of

strain remains once the layer is deeply etched, we directly use the XRD measurement after the last etching cycle to obtain the value of strain close to the interface with bonding layers.

The strain within each sublayer is calculated using equation (2.21) and the Bragg law. These values are considered as corresponding to the strain at half depth of the corresponding sublayers. We use ellipsometry measurements of GaN thickness to derive these in-depth positions and obtain the strain profile of **Figure 5.7**. A conversion to values of biaxial in-plane stress σ_b can be performed through elastic constants of GaN (from equation (1.6), $\varepsilon_{zz} = 2S_{13}(\sigma_{xx} + \sigma_{yy}) + S_{33}\,\sigma_{zz} = 2S_{13}\,\sigma_b$).

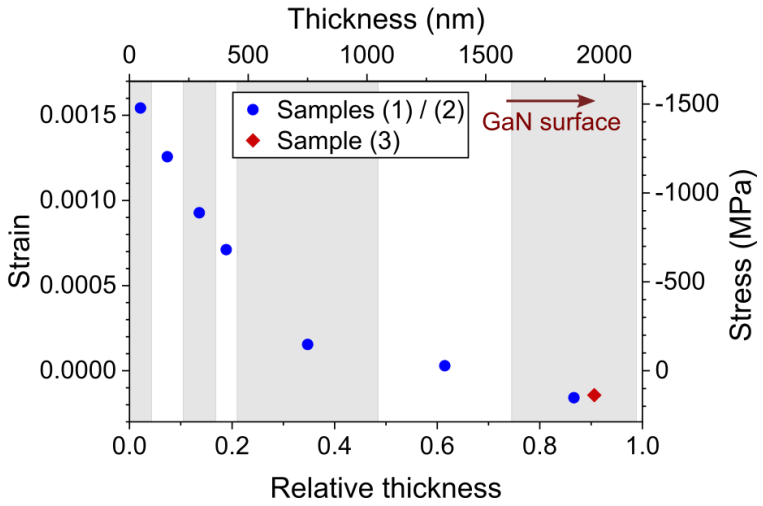

Figure 5.7: Strain and stress profiles reconstructed from in-depth analysis of XRD profiles. Strain values are obtained from the 2θ position of etched sublayer XRD profiles of **Figure 5.6 b)** (samples (1) and (2)), and of XRD measurement after the last etching cycle on sample (3). Values of biaxial in-plane stress σ_b are derived from elastic constants of **Table 1.2** ($\sigma_b = \varepsilon_{zz}/2S_{13}$). The extension of etched sublayers is shown with white and grey bands.

Compared to the curvature measurements, thickness measurement uncertainty is far less problematic, as it only leads to a small lateral error bar of the order of a few tenth of nm (not shown on the figure as it is negligible). We thus obtain a precise estimate of the stress decay close to the AlGaN/GaN interface. As expected, a tensile biaxial stress is observed close to the surface, with a good agreement between measurements on samples (1) and (3).

d) Raman measurements

Along with XRD, we performed Raman measurements of biaxial stress within the GaN layer between etching cycles. Unlike the cross-section measurements of section 3.1.1, these measurements are based on the E_2(high) mode of vibration, which is commonly used in the literature.[100],[99] This mode is capable of measuring distortions in the (0001) plane of GaN, which is convenient to measure the biaxial in-plane stress in (0001)-oriented GaN films.[138] The photon beam, a green laser with a power of 8 mW and a wavelength of 532 nm, is oriented

along the normal to the sample surface and the measurements were performed at the center of the sample.

In order to obtain an additional reconstruction of the stress profile of GaN, we use Raman data from samples (1) and (2), from the same etching cycles as for the XRD analysis. The second etching cycle (i.e. total of 500 nm of GaN removed) is however not included, as no Raman measurement was performed due to time limitations. Raman profiles are plotted on a Raman shift scale (**Figure 5.8 a)**). From the position $\omega_{E_2(high)}$ of a Raman peak, determined by means of a Lorentzian fit with an error of $\pm$ 0.1 cm^{-1}, we derive a mean value of biaxial stress σ^b in the GaN crystal:

$$\omega_{E_2(high)} - \omega^0_{E_2(high)} = K^b_{E_2(high)}\,\sigma^b \tag{5.1}$$

where $\omega^0_{E_2(high)} = 567.6\ cm^{-1}$ [100] is the peak position of an unstrained bulk GaN and $K^b_{E_2(high)} = -2.9\ cm^{-1}GPa^{-1}$ is the Raman biaxial pressure coefficient, derived by *Demangeot et al.*[101] assuming a biaxial stress in the (0001) plane.

By assuming that this measured stress corresponds to the stress at half the thickness of the measured layer, we plotted an estimate of the stress profile within the GaN film (**Figure 5.8 b)**).

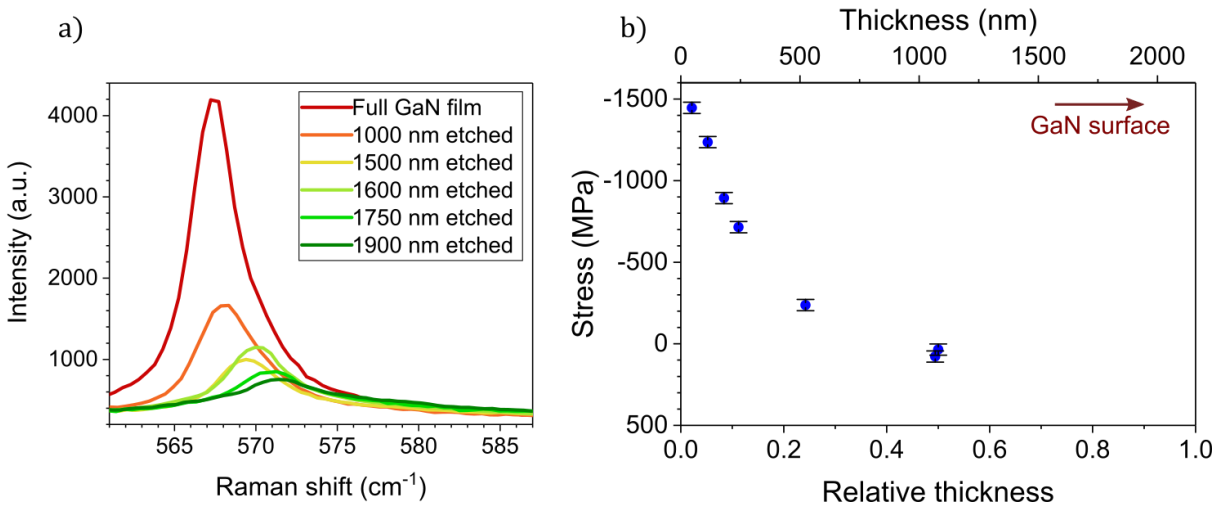

Figure 5.8 : Reconstruction of stress profile from in-depth analysis of Raman measurements. a) Raman shift curves. b) Stress profile obtained from the position of Raman peaks and equation (5.1).

The three stress gradient measurement obtained through sample curvature, XRD and Raman characterizations are in good agreement with each other, as shown in **Figure 5.9**. Far from the AlGaN/GaN interface, we notice that Raman results slightly diverge from the two other analyses. This is likely because we treated Raman measurements of the full GaN film as a measurement of stress at half the thickness of the layer. The accuracy of the Raman profile might be improved by following a procedure similar to the one detailed in section 5.2.1.d), for the construction of virtual XRD profiles of etched sublayers. Conversely, the stress analysis from curvature measurements lacks precision in the zone close to the AlGaN/GaN layer, as

discussed earlier. The stress profile obtained by XRD analysis of in-depth measurements correlates well both with Raman measurements, close to the interface with buffer layers, and with curvature measurements near the surface. It appears to be the most precise of our analyses and we will thus use this estimate of the strain/stress profile in the following.

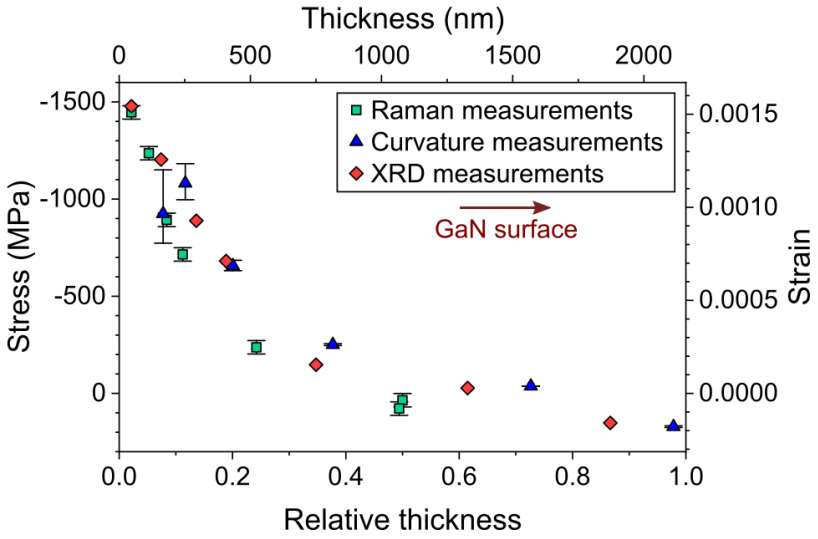

Figure 5.9 : Comparison of the stress profiles obtained through curvature, XRD and Raman measurements.

5.2.2. XRD simulation results

The strain profile obtained in **Figure 5.7** is an interesting opportunity to further assess the simulation tool developed in chapter 3. For this, we fitted the measured strain profile with a modified version of the logarithmic function of equation (3.13). We obtained the curve shown in **Figure 5.10 a)**, with a curvature parameter $K = 25$ and an RMS strain parameter $\sqrt{\langle {\varepsilon_{zz}}^2 \rangle} = 8.19 \times 10^{-4}$. The modification of the function consists in adding a parameter $s = -3.14 \times 10^{-4}$, which is a simple shift of the curve along the y-axis. This parameter allows us to fit the experimental absolute strain gradient, and is simply removed from the equation to transform the fit into a relative strain gradient (i.e. $\varepsilon_{zz}(1) = 0$), as used in the simulation tool. We then simulated a 2.16 µm GaN layer (i.e. the thickness of samples (1) and (2) as measured by ellipsometry) containing this strain profile and computed the corresponding diffraction peaks. The results, given in **Figure 5.10 b)**, are quite similar to experimental measurements performed on the full film of GaN, although not perfectly matching.

Although the logarithmic function fits rather well the experimental strain profile, the question arises of whether it is physically appropriate. We tried to obtain an answer by analyzing an easily measurable characteristic of the relative strain profile, namely its RMS value. The experimental RMS strain $\sqrt{\langle {\varepsilon_{zz}}^2 \rangle} = 3.78 \times 10^{-4}$, determined through a Williamson-Hall plot of the symmetrical reflections (002), (004) and (006), is clearly lower than fitted value. This result suggests that the real strain profile might have a lower amplitude and converge more rapidly to the surface value of strain.

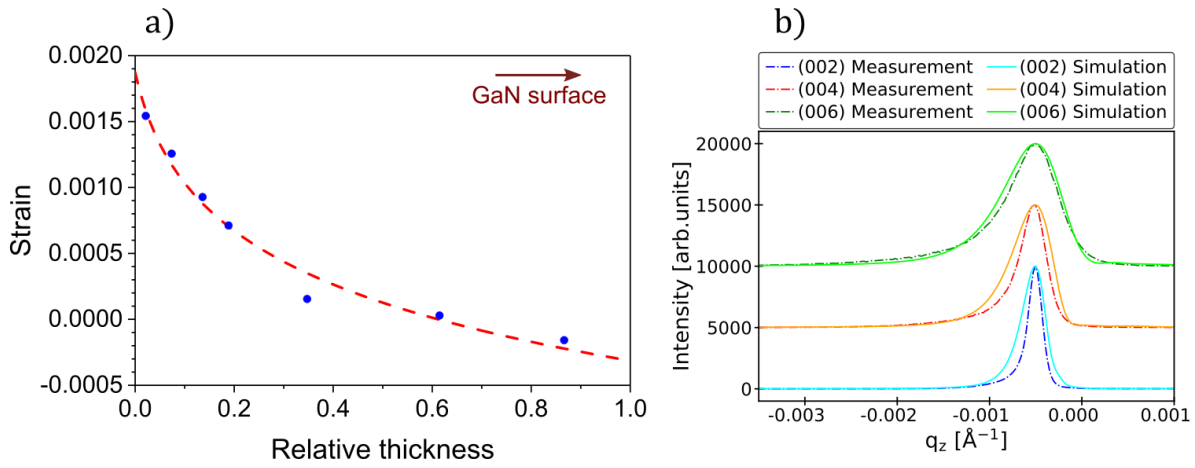

Figure 5.10 : Fit of the strain gradient with a logarithmic function. a) Strain profile obtained. b) XRD simulations of samples (1)/(2), with the fitted logarithmic strain profile as an input. This result is obtained with a parameter of local variation of displacement profile σ = 0.10, which gives the best match with experimental data.

Hence, we tried to use an alternative function to fit the experimental strain gradient, namely an exponential decay, with three parameters A, t, y_0:

$$\varepsilon_{zz}(z) = A \exp\left(\frac{-z}{t}\right) + y_0 \tag{5.2}$$

This function appears to give a slightly better fit of the strain gradient, as shown in **Figure 5.11 a)**. To confirm this, we compare the RMS strain $\sqrt{\langle {\varepsilon_{zz}}^2 \rangle}$ of this profile with the experimental RMS strain in the sample (2), obtained by means of a Williamson-Hall plot. The RMS of the profile is obtained by integration of the squared strain ${\varepsilon_{zz}}^2(z) = (A\,exp(-z/t) + y_0)^2$ on the [0,1] relative depth scale. We obtain:

$$\sqrt{\langle {\varepsilon_{zz}}^2 \rangle} = \sqrt{\frac{A^2 t}{2}\left(1 - \exp^2\left(-\frac{1}{t}\right)\right) + 2y_0 At\left(1 - \exp^2\left(-\frac{1}{t}\right)\right) + {y_0}^2} \tag{5.3}$$

With the parameters $A = 0.00193$, $t = 0.237$ and $y_0 = -0.00188$ obtained during the fit, we calculate an RMS strain of $\sqrt{\langle {\varepsilon_{zz}}^2 \rangle} = 5.52 \times 10^{-4}$, which is closer to that of Williamson-Hall analysis. From these observations, we conclude that the strain profiles in few µm-thick layers of GaN grown on silicon substrates by MOVPE follow an exponential decay.

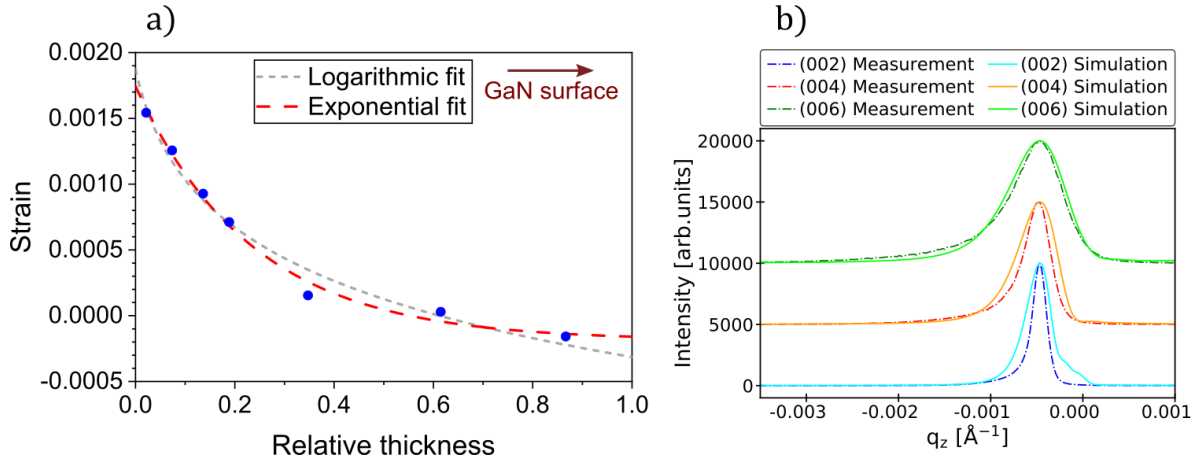

Figure 5.11 : Fit of the strain gradient with an exponential function. a) Strain profile obtained. b) XRD simulations of samples (1)/(2), with the fitted exponential decay strain profile as an input. This result is obtained with a parameter of local variation of displacement profile σ = 0.11, which gives the best match with experimental data.

As for the logarithmic profile, we tested the exponential decay fit as an input strain gradient in the XRD simulations. The obtained profiles do not either closely match the experimental data, especially on the (002) reflection, for which a remainder of oscillation patterns is observed on the right side of the peak.

It is important to note that, although the strain profiles fitted with logarithmic and exponential functions are quite similar, they lead to simulations with significant differences. Due to the strong flattening of the exponential strain gradient at a relative thickness above 0.7, the mean displacement profile and all the local displacement profiles computed with equation (3.11) follow a similar slope in a large zone below the layer surface (see **Figure 5.12 b)**). As discussed in the section 3.2.3 c), this favors the apparition of oscillations on simulated XRD curves. Conversely, the logarithmic fit of the strain gradient keeps decreasing until reaching the layer surface, so that the displacement profiles still slightly diverge below the surface (see **Figure 5.12 a)**). Consequently, the oscillations on XRD curves disappear at lower values of σ, even on the (002) curve.

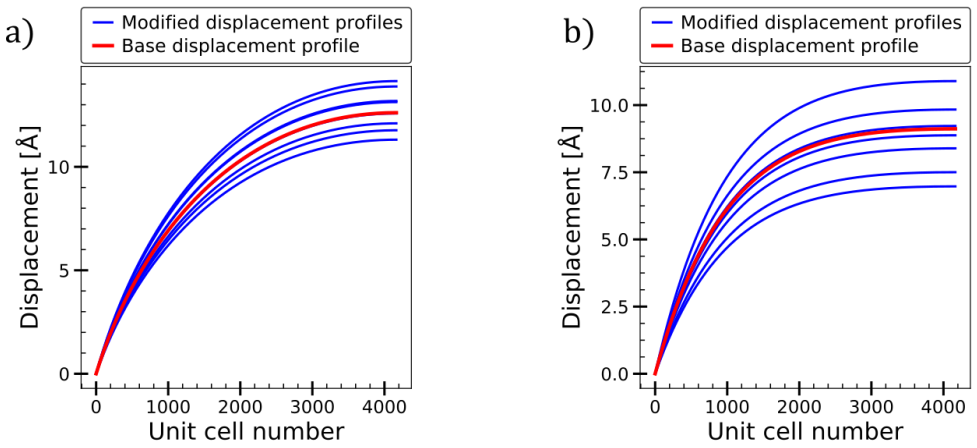

Figure 5.12 : Displacement profiles computed with logarithmic and exponential fits of the strain gradient. a) Mean and local displacement profiles obtained through the logarithmic fit of strain of **Figure 5.10**, with $\sigma = 0.10$. b) Mean and local displacement profiles obtained through the exponential decay fit of strain of **Figure 5.11**, with $\sigma = 0.10$.

The exponential decay function appears to give a satisfactory fit of the strain gradient within GaN, which suggests that the accuracy of our simulations is limited by our model. The remnants of oscillation patterns on the (002) simulation might be the sign of local variations of displacement not being truly adapted to the reality of the material. A new model for the computation of local displacement profiles, closer to diagrams of **Figure 3.15**, would be a promising track for further development of the simulation tool.

5.3. In-depth threading dislocations analysis

The evolution of TD density through the thickness of GaN was analyzed by means of XRD measurements of lattice misorientation and micro-strain. These characterizations were performed in accordance with the protocol detailed in chapter 4, with tilt, twist and micro-strain being respectively measured on (004), (201) and (205) reflections. Due to the decreasing intensity of XRD scans as the samples were etched, micro-strain measurements were fitted with a Split Pearson VII function to extract peak widths.

We combined this XRD data with ellipsometry measurements of thickness to plot a profile of TD density through the GaN film. We followed a simple approach by assuming XRD measurements to correspond to the TD density at half thickness of the analyzed layer. Hence, measurements on samples (1)/(2) and (3) are respectively used to extract the strain profile in the bottom half and the top half of the GaN film.

As micro-strain measurements are impacted by vertical X-ray correlation length, size broadening is subtracted from the width of diffraction peaks (equation (2.23)) when the thickness of GaN is lower than 1µm (size effects are negligible above this value). We use the Scherrer equation ((2.25)) to estimate this additional broadening, with the original Scherrer constant of $K = 0.94$.

As the precision of the Scherrer equation is often pointed out, we estimate the uncertainty associated to this equation by calculating the size broadening with the extreme values of the Scherrer constant ($K = 0.73$ and $K = 1.03$, see section 2.4.2.b)) derived in the literature for the usual crystallite shapes. As shown on **Figure 5.13**, this leads to a high error bar on the TD density of the last measurement of sample (2) (layer thickness of 93 nm). Note that an error in thickness measurements would lead to an additional uncertainty on the result of the Scherrer equation, thus further increasing the size of vertical error bars.

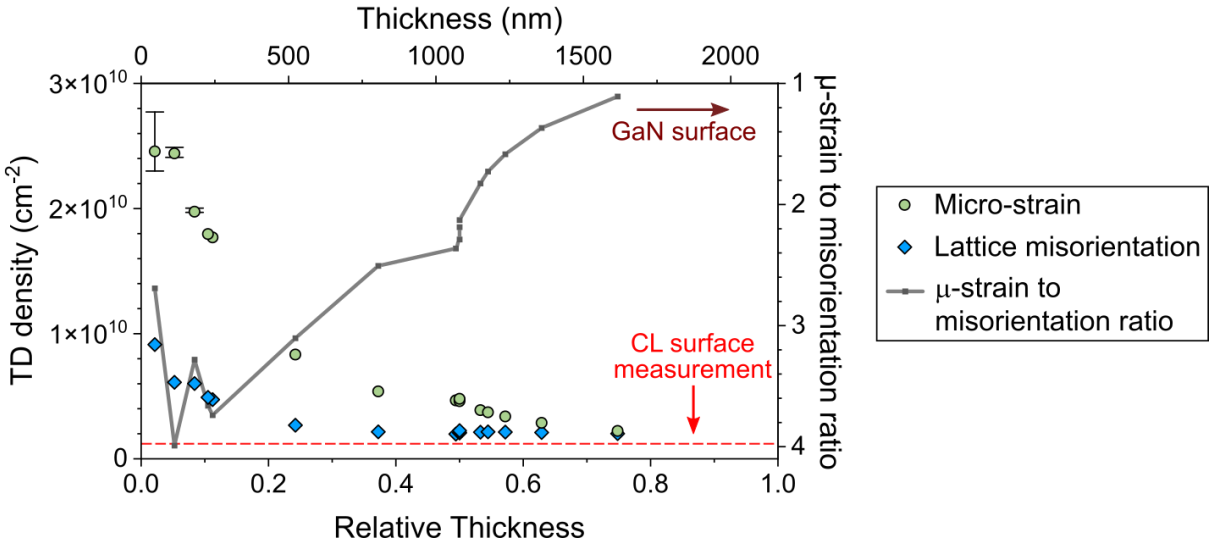

Figure 5.13 : XRD estimates of TD density profiles in a GaN-on-Si layer.

The graph in **Figure 5.13** compares the gradients of TD density obtained from misorientation and micro-strain measurements. We observe that both profiles almost converge in the high crystalline quality zone under the GaN surface. Despite the low variation of TD density in this area, measurements of the top 1080 nm of GaN layer give TD densities almost twice those found in CL measurements. This discrepancy between CL and XRD measurements is in part explained by the discussion of chapter 3: CL measurements tend to underestimate TD density due to an overlapping of diffraction spots and XRD measurements to overestimate it, owing to a double counting of mixed TDs. However, these arguments are not sufficient to explain the difference seen here between CL and XRD. In **Figure 5.14 a)**, we notice that individual CL spots are generally easily distinguishable. The impact of double counting of mixed TDs can be prevented by assuming that all of the contribution to tilt stems from mixed dislocations (i.e. there are no screw TDs in the layer, which is usually close to reality). With this hypothesis and the opposite extreme assumption (0% of mixed TDs, 100% of screw TDs), we obtain at a thickness $z = 1600$ nm a range of TD densities of $1.7 - 2.0 \times 10^9 cm^{-2}$ for misorientation measurements and $1.9 - 2.2 \times 10^9 cm^{-2}$ for micro-strain measurements, to be compared to the $1.2 \times 10^9 cm^{-2}$ obtained by CL at the sample surface. The remaining difference in the results can be explained by the limits of XRD models, notably the distribution of TDs that might not be perfectly random, and the correlation between TDs not taken into account. Nevertheless, we note that these results are much more convincing than the ones obtained by measuring the entire film of GaN, especially for micro-strain measurements which result in TD densities around $4.7 \times 10^9 cm^{-2}$.

In the bottom half of the GaN layer, the two XRD estimates of TD density profiles diverge to reach, close to the AlGaN/GaN interface, values of around $1 \times 10^{10} cm^{-2}$ and $2.5 \times 10^{10} cm^{-2}$ respectively for misorientation and micro-strain measurements. This divergence is probably due to a change in the structure of TDs with respect to the film surface, in terms of distribution and correlation. The presence of misfit dislocations, as reported for other AlGaN/GaN interfaces,[102],[142] might further broaden the diffraction profiles of the highly etched sample (2). However, their impact is probably small compared to that of the high number of TDs. Additionally, those misfit dislocations would lead to a comparable broadening of ω and $\omega - 2\theta$ scans for a given reflection,[124] which does not point toward diverging results between misorientation and micro-strain measurements.

A second CL measurement (**Figure 5.14 b)**) was performed after the last etching of sample (2) to try to determine which of the two XRD estimates of TD density at AlGaN/GaN interface is the more realistic. However, it was not possible to count the dislocations, due to the presence of micro-cracks at the surface of the sample, also visible on scanning electron microscopy (SEM) images (**Figure 5.14 c)**).

Sahonta et al.[142] previously measured the evolution of TD density in a similar MOVPE grown GaN/$Al_{0.28}Ga_{0.72}N$ heterostructure. These TEM measurements on a set of GaN layers with different thicknesses resulted in large variations of TD densities, from $4 \times 10^{10} cm^{-2}$ to $6.5 \times 10^{9} cm^{-2}$ for layers of 90 nm and 570 nm, which is quite comparable to our micro-strain measurements.

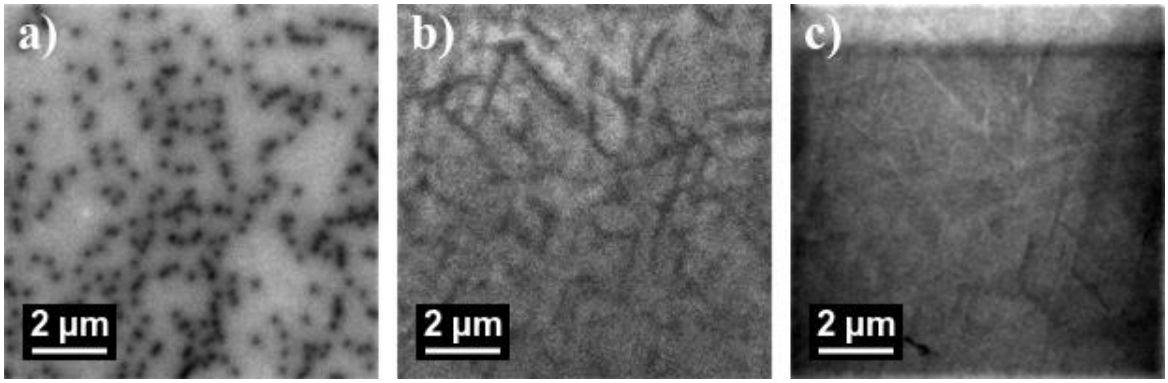

Figure 5.14 : Cathodoluminescence and scanning electron microscopy images of GaN layers. a) CL image of the surface of the non-etched GaN layer. b) - c) CL and SEM images of the GaN surface of sample (2) after the last etching cycle. Both images are recorded on the same area and show identical patterns identified as micro-cracks of the surface.

5.4. Correlation between in-depth dislocation density and strain gradient

Throughout this thesis, gradients of biaxial in-plane stress within GaN have been assumed to result from a relaxation of compressive stresses during the epitaxy phase, driven by the

progressive recombination of TDs. This effect has been observed several times in the literature.[142],[143] However, other mechanisms have been proposed to explain the progressive relaxation of wurtzite III-N layers, such as the formation of TDs inclined away from the [0001] direction at roughened hetero-interfaces between III-N layers.[58] Our in-depth measurements allow us to correlate profiles of strain and of TD density throughout the whole thickness of a GaN film. From the plot of **Figure 5.15**, we see that the relaxation of in-plane stress throughout GaN is proportional to the reduction of TD density, as quantified with XRD micro-strain measurements. This strongly suggests that the annihilation of TDs is the major mechanism of reduction of compressive stress in this layer.

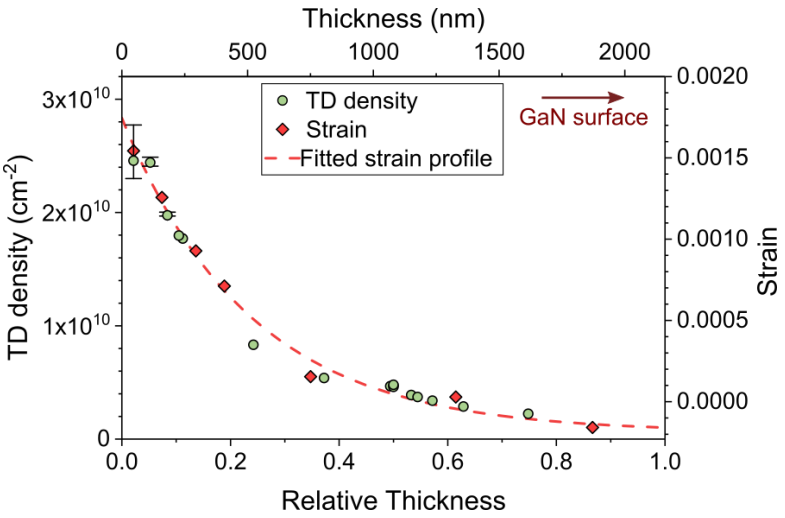

Figure 5.15 : Correlation of profiles of strain and of threading dislocation density. TD densities correspond to the XRD micro-strain measurements. Strain is obtained with the analysis of XRD measurements detailed in the sub-section 5.2.1.c), and fitted with equation (5.2).

The in depth-characterization of a progressively etched GaN layer allowed us to extract a gradient of in-plane stress, through analyses of XRD profiles, Raman and curvature measurements. These three characterizations give a similar strain profile, following an exponential decay trend. Thanks to these experimental measurements, we were able to confirm that the simulation tool developed in chapter 3 gives satisfactory results, although we noted an imperfect matching of the (002) curve.

From this study, we also obtained two profiles of TD density, relying respectively on lattice misorientation and micro-strain measurements. We notice that both measurements are in good agreement in the high crystalline quality area near the film surface. However, we find these values of TD density to be 40-80% higher than with CL measurements, even when assuming an absence of screw TDs, thus highlighting a somewhat limited precision of those XRD models. Nevertheless, the accuracy of these XRD measurements of TD density appears to be significantly better than what is often reported in the literature (i.e. typical errors of a factor two or greater, see section 4.1.1.b)), at least in the sparsely-dislocated zone near the surface. Close to the AlGaN/GaN interface, micro-strain and misorientation results diverge, probably

due to a TD structure departing from the ideal model in terms of distribution and correlation of Burgers vectors. In this zone, XRD analyses of TD density might be less reliable.

As the gradient of TDs given by micro-strain measurements is closer to the results of the literature, we used this profile for a comparison with measurements of the gradient of residual macro-strain, as obtained from XRD measurements. We observed that both TD density and strain profiles follow the same trend. This strongly suggests that the progressive relaxation of compressive stress in these GaN layers is driven by the recombination of TDs. This result might be used to implement in our simulation tool a model of variation of the local displacement profiles closer to physical reality. This would imply to model the local alterations of the displacement field as being proportional to the strain profile input instead of being linear through the sample thickness. As in equation (3.12), such a model would require a unique additional parameter σ to simulate the magnitude of the local deviations from the mean displacement profile.

General Conclusion

Development of high quality III-N semiconductor grown on silicon substrate, for power electronics applications, demands a comprehensive understanding of the behavior of crystalline defects associated with this material. More specifically, CEA-Leti would benefit from XRD methods of metrology for GaN-on-Si layer defects, adapted to characterizations within its cleanroom facility. During this PhD, we aimed to respond to this problem by focusing on the analysis of two important issues, namely gradients of in-plane stress and threading dislocations (TDs).

In-depth stress gradient is an issue specific to the special structure of GaN-on-Si layers, grown on top of a succession of III-N buffer layers. During our initial work, we obtained several basic estimates of stress gradients, from micro-Raman characterization, in-situ sample curvature measurement during layer growth, as well as from the analysis of XRD peak profiles. However, none of these techniques is satisfying: in-situ curvature measurements cannot be performed post-growth, cross section micro-Raman measurements are destructive and the XRD analysis only gives a rough estimate of the actual stress profile. Typical XRD analyses described in the literature are not satisfactory either, as they are not adapted to GaN-on-Si or require numerous high-quality measurements, often non-achievable with in-line diffractometers such as those found in the CEA-Leti cleanroom.

Hence, we proposed to study stress gradients by simulating XRD profiles, with a program that we developed in Python language. This numerical tool models the displacement field of the set of unit cells (UCs) composing a GaN layer affected by an in-depth profile of strain/stress. The diffracted intensity is computed by means of the kinematical theory of diffraction, which is adapted to the case of highly defective crystals. The first simulations were affected by oscillation patterns, which are also found in the results of commercial simulation software but that are not observed in experimental data. These oscillations correspond to interferences between the diffracted X-ray waves, which appear due to the long-range coherence of scattered X-rays.

We considered different physical phenomenon as potential sources of disruption of X-ray coherence, such as a limited X-ray correlation length, the thermal motion of UCs, the roughness of layer interfaces and a local variation of the strain field due to crystal defects. We showed that interferences are removed by implementing variations of the UC displacement field, so that the shape of local in-depth displacement profiles differ from the shape of the mean displacement gradient. We suggest that such variations are the result of an uneven relaxation of compressive stress within GaN, owing to the varying distance in the surface plane between UCs and sites of TD recombination. We model this phenomenon with an attenuation of the displacement field proportional to UCs depth, with the magnitude of attenuation being defined by a single parameter σ, characteristic of the density and distribution of TDs. With this procedure, we obtained a satisfying matching of experimental XRD profiles, largely improved in comparison with the results of the tested commercial software. Nevertheless, we still needed to verify experimentally that the tested in-depth strain profiles were realistic.

The high lattice mismatch between Si(111) and (0001) GaN leads to the generation of a high density of TDs, of the order of $10^9\ cm^{-2}$, within the thin films that we analyzed. The usual XRD method to analyze these dislocations, which relies on lattice misorientation measurements, has been discussed in the literature for its lack of accuracy. Hence, we decided to examine an alternative method, based on measurements of the micro-strain field surrounding TDs. This analysis is rarely employed in the literature of GaN characterization, even though it allows for simple estimates of TD density. The translation of micro-strain measurements into TD densities relies on a model derived for polycrystalline metals. We therefore adapted this model to the low Poisson ratio of GaN layers and provided a mathematical procedure for rapid calculations of TD densities. For GaN-on-Si samples, we found that the analysis is hindered by the presence of a strong gradient of stress. We demonstrated that this issue can be bypassed by performing XRD measurements on the (205) plane, whose normal is oriented toward a direction free of strain stemming from the stress gradient.

We validated this study by comparing the dislocation densities obtained from XRD micro-strain analysis with those from XRD lattice misorientation analysis and measurements with transmission electron microscopy (TEM) and cathodoluminescence (CL). In addition to GaN-on-Si samples, this comparison was performed on substrates of freestanding GaN and on heteroepitaxial layers of GaN on SiC and sapphire substrates. It was difficult to assess the accuracy of micro-strain analysis, due to the evolution of TD density through the GaN layer thickness. The lower number of dislocations close to the surface resulted in higher TD densities found with both XRD bulk GaN measurements than with TEM and CL surface measurements. We observed that the nature of sample substrate also had an effect on XRD results, which can be explained by differences in the spatial arrangement and correlation of TDs, and by a different evolution of the TD density through the layer thickness. In particular, layers with little strain gradient, such as GaN-on-SiC, showed lower dislocation density by XRD versus TEM and CL, while GaN-on-Si samples with a large gradient showed the opposite trend.

After the studies on TDs and stress gradients we performed an in-depth analysis consisting of a series of measurements on progressively etched layers of GaN-on-Si. This process allowed each part of the layer to be examined more accurately, so that we were able to better assess the results of our previous studies of TDs and stress profiles. TD density was measured by XRD lattice misorientation and micro-strain measurements. We found a good agreement between the two measurements in the zone of high crystalline quality, just below the sample surface. These XRD results are 40-80% higher than the corresponding CL measurements, which shows that there are still limits to the XRD analyses, likely due to the oversimplified models employed. Nevertheless, this result is satisfying compared to the large errors of a factor two or more often reported in the literature, thus reinforcing the interest of these simple XRD analyses. In the deeper levels of GaN layers, we observed a divergence between misorientation and micro-strain measurements, likely due to a non-ideal arrangement of the set of TDs. In this area near the buffer layers, the results of XRD analyses are thus less reliable.

The in-depth profile of stress was estimated by three methods during the cycles of etching and characterizations: sample curvature, Raman and XRD measurements. The three analyses are in good agreement with one another and result in a strain profile following an exponential

decay trend. In particular, the analysis of XRD data, which consists in the reconstruction of the diffraction curves stemming from the different parts of the GaN layer, appears to give a precise estimate of the stress gradient in both the bottom half and the top half of the thin film.

We used this XRD strain gradient measurement to replace the estimate of the strain profile previously employed in our simulation program, and computed the corresponding diffraction curves, which resulted in a satisfactory matching of the experimental data. However, some remnants of oscillation patterns were observed on the simulation of the (002) reflection. We propose that it is due to the oversimplified model used to simulate the local variations of the displacement profile. By comparing the measured gradients of strain and TD density, we found a very good correlation between the shape of both profiles. This suggests that the relaxation of in-plane stress within GaN layers is determined by the progressive recombination of TDs. Hence, the model of variation of displacement profiles could be reworked, so that the local alterations of the displacement field are not linear through the sample thickness, but rather proportional to the evolution of in-depth strain.

As profiles of TD density and strain are correlated, we could also consider using the stress gradients obtained with the simulations to improve the estimates of the surface density of TDs in GaN layers. This would enable a reliable picture of defects within GaN to be obtained from a small number of XRD scans.

Overall, the different methods developed during this PhD open the door to simple analyses of the main issues affecting GaN-on-Si layers. These techniques rely on quick and non-destructive XRD measurements that can be performed on almost every diffractometer equipped for high-resolution measurements. In the future, this work could also be extended to the analysis of III-N buffer layers below GaN, such as AlGaN layers, which are affected by similar distributions of TDs and stress. In addition, the simulation program could be complemented by the implementation of additional distortions of the lattice, stemming from distributions of crystalline defects. This would allow to handle complex cases, such as GaN-on-Si layers doped by ion implantation, which before annealing are affected by punctual defects in the zone near the surface. We could also consider the case of layers thin enough so that the strain field of misfit dislocations has a significant impact on the result of simulations. Finally, the inclusion of in-plane displacement fields associated to TDs would open the door to 3D simulations of reciprocal space maps.

One of the main limitations of our analyses might be that they are adapted to rather highly dislocated materials. For materials with low densities of dislocations, the kinematical theory that we use for our simulations might be limited and the use of dynamical theory simulations is recommended. Similarly, for TD densities below the mid $10^7\ cm^{-2}$, a proper measurement of the micro-strain would require diffractometer optics allowing for an improved resolution of radial scans compared to usual HRXRD setups.

Of course, as long as the high TD density condition is met, the analyses developed here are not restricted to nitride materials, but are interesting for a variety of thin films containing in-plane stress gradients. To this end, the developed program is fairly adaptable, as it essentially only requires knowing the lattice parameters of the studied material. For the conversion of

micro-strain measurements into TD densities, we provided a general formula which will help adapting this analysis to crystals with diverse Poisson ratios.

Bibliography

[1] A. Teke et H. Morkoç, « Group III Nitrides », in *Springer Handbook of Electronic and Photonic Materials*, S. Kasap et P. Capper, Éd. Boston, MA: Springer US, 2007, p. 753-804.

[2] H. Morkoç, « General properties of nitrides », in *Nitride Semiconductors and Devices*, Berlin Heidelberg: Springer-Verlag, 1999.

[3] G. A. Jeffrey, G. S. Parry, et R. L. Mozzi, « Study of the Wurtzite-Type Binary Compounds. I. Structures of Aluminum Nitride and Beryllium Oxide », *J. Chem. Phys.*, vol. 25, nº 5, p. 1024-1031, 1956.

[4] M. A. Moram et M. E. Vickers, « X-ray diffraction of III-nitrides », *Rep. Prog. Phys.*, vol. 72, nº 3, p. 036502, 2009.

[5] T. Deguchi *et al.*, « Structural and vibrational properties of GaN », *Journal of Applied Physics*, vol. 86, nº 4, p. 1860-1866, 1999.

[6] M. Tanaka, S. Nakahata, K. Sogabe, H. Nakata, et M. Tobioka, « Morphology and X-Ray Diffraction Peak Widths of Aluminum Nitride Single Crystals Prepared by the Sublimation Method », *Jpn. J. Appl. Phys.*, vol. 36, nº 8B, p. L1062, 1997.

[7] W. Paszkowicz *et al.*, « Lattice parameters, density and thermal expansion of InN microcrystals grown by the reaction of nitrogen plasma with liquid indium », *Philosophical Magazine A*, vol. 79, nº 5, p. 1145-1154, 1999.

[8] L. Weber, « IX. Kürzere Originalmitteilungen und Notizen », *Zeitschrift für Kristallographie - Crystalline Materials*, vol. 57, nº 1-6, p. 200–203, 1922.

[9] F. C. Frank, « On Miller–Bravais indices and four-dimensional vectors », *Acta Cryst*, vol. 18, nº 5, p. 862-866, 1965.

[10] D. Schwarzenbach, « Note on Bravais–Miller indices », *J Appl Cryst*, vol. 36, nº 5, p. 1270-1271, 2003.

[11] W. Voigt, *Lehrbuch der Kristallphysik (mit Ausschluss der Kristalloptik)*. B.G. Teubner, 1928.

[12] K. Kim, W. R. L. Lambrecht, et B. Segall, « Elastic constants and related properties of tetrahedrally bonded BN, AlN, GaN, and InN », *Phys. Rev. B*, vol. 53, nº 24, p. 16310-16326, 1996.

[13] K. Tsubouchi et N. Mikoshiba, « Zero-Temperature-Coefficient SAW Devices on AlN Epitaxial Films », *IEEE Transactions on Sonics and Ultrasonics*, vol. 32, nº 5, p. 634-644, 1985.

[14] J.-M. Wagner et F. Bechstedt, « Properties of strained wurtzite GaN and AlN: Ab initio studies », *Phys. Rev. B*, vol. 66, nº 11, p. 115202, 2002.

[15] D. Tromans, « Elastic anisotropy of hcp metal crystals and polycrystals », p. 22, 2011.

[16] M. A. Moram, Z. H. Barber, et C. J. Humphreys, « Accurate experimental determination of the Poisson's ratio of GaN using high-resolution x-ray diffraction », *Journal of Applied Physics*, vol. 102, nº 2, p. 023505, 2007.

[17] R. B. Schwarz, K. Khachaturyan, et E. R. Weber, « Elastic moduli of gallium nitride », *Appl. Phys. Lett.*, vol. 70, nº 9, p. 1122-1124, 1997.

[18] A. F. Wright, « Elastic properties of zinc-blende and wurtzite AlN, GaN, and InN », *Journal of Applied Physics*, vol. 82, n° 6, p. 2833-2839, 1997.

[19] D. R. Lide, *CRC Handbook of Chemistry and Physics, 86th Edition*. Taylor & Francis, 2005.

[20] O. Ambacher *et al.*, « Two-dimensional electron gases induced by spontaneous and piezoelectric polarization charges in N- and Ga-face AlGaN/GaN heterostructures », *Journal of Applied Physics*, vol. 85, n° 6, p. 3222-3233, 1999.

[21] R. Quay, Éd., « III-N Materials, and the State-of-the-Art of Devices and Circuits », in *Gallium Nitride Electronics*, Berlin, Heidelberg: Springer, 2008, p. 3-90.

[22] R. J. Trew, « SiC and GaN transistors - is there one winner for microwave power applications? », *Proceedings of the IEEE*, vol. 90, n° 6, p. 1032-1047, 2002.

[23] T. P. Chow *et al.*, « SiC and GaN bipolar power devices », *Solid-State Electronics*, vol. 44, n° 2, p. 277-301, 2000.

[24] S. Keller, « Substrates and Materials », in *Power GaN Devices: Materials, Applications and Reliability*, M. Meneghini, G. Meneghesso, et E. Zanoni, Éd. Cham: Springer International Publishing, 2017, p. 27-52.

[25] H. Amano, N. Sawaki, I. Akasaki, et Y. Toyoda, « Metalorganic vapor phase epitaxial growth of a high quality GaN film using an AlN buffer layer », *Appl. Phys. Lett.*, vol. 48, n° 5, p. 353-355, 1986.

[26] H. Amano, M. Kito, K. Hiramatsu, et I. Akasaki, « P-Type Conduction in Mg-Doped GaN Treated with Low-Energy Electron Beam Irradiation (LEEBI) », *Japanese Journal of Applied Physics*, vol. 28, n° 12, p. L2112-L2114, 1989.

[27] S. Nakamura, M. Senoh, et T. Mukai, « P-GaN/N-InGaN/N-GaN Double-Heterostructure Blue-Light-Emitting Diodes », *Jpn. J. Appl. Phys.*, vol. 32, n° 1A, p. L8, 1993.

[28] M. Kneissl, « A Brief Review of III-Nitride UV Emitter Technologies and Their Applications », in *III-Nitride Ultraviolet Emitters: Technology and Applications*, M. Kneissl et J. Rass, Éd. Cham: Springer International Publishing, 2016, p. 1-25.

[29] M. Asif Khan, J. N. Kuznia, A. R. Bhattarai, et D. T. Olson, « Metal semiconductor field effect transistor based on single crystal GaN », *Appl. Phys. Lett.*, vol. 62, n° 15, p. 1786-1787, 1993.

[30] M. Asif Khan, J. N. Kuznia, D. T. Olson, W. J. Schaff, J. W. Burm, et M. S. Shur, « Microwave performance of a 0.25 μm gate AlGaN/GaN heterostructure field effect transistor », *Appl. Phys. Lett.*, vol. 65, n° 9, p. 1121-1123, 1994.

[31] U. V. Bhapkar et M. S. Shur, « Monte Carlo calculation of velocity-field characteristics of wurtzite GaN », *Journal of Applied Physics*, vol. 82, n° 4, p. 1649-1655, 1997.

[32] R. Oberhuber, G. Zandler, et P. Vogl, « Mobility of two-dimensional electrons in AlGaN/GaN modulation-doped field-effect transistors », *Appl. Phys. Lett.*, vol. 73, n° 6, p. 818-820, 1998.

[33] M. Farahmand *et al.*, « Monte Carlo simulation of electron transport in the III-nitride wurtzite phase materials system: binaries and ternaries », *IEEE Transactions on Electron Devices*, vol. 48, n° 3, p. 535-542, 2001.

[34] D. Ueda *et al.*, « AlGaN/GaN devices for future power switching systems », in *IEEE InternationalElectron Devices Meeting 2005*, p. 377-380. *IEDM Technical Digest.*, 2005.

[35] F. Medjdoub, « Transistors à base de semi-conducteurs III-N sur substrat de silicium et applications », *Techniques de l'ingénieur Innovations technologiques*, p. IN146 V1, 2012.

[36] D. Ehrentraut, E. Meissner, et M. Bockowski, Éd., *Technology of Gallium Nitride Crystal Growth*. Berlin Heidelberg: Springer-Verlag, 2010.

[37] A. Dadgar, C. Hums, A. Diez, F. Schulze, J. Bläsing, et A. Krost, « Epitaxy of GaN LEDs on large substrates: Si or sapphire? », in *Advanced LEDs for Solid State Lighting*, vol. 6355, p. 63550R, 2006.

[38] K. Hiramatsu, T. Detchprohm, H. Amano, et I. Akasaki, « Effects of buffer layers in heteroepitaxy of gallium nitride », in *Advances in the Understanding of Crystal Growth Mechanisms*, p. 399-413, T. Nishinaga, K. Nishioka, J. Harada, A. Sasaki, et H. Takei, Éd. Amsterdam: Elsevier, 1999.

[39] H. Ishikawa, K. Yamamoto, T. Egawa, T. Soga, T. Jimbo, et M. Umeno, « Thermal stability of GaN on (111) Si substrate », *Journal of Crystal Growth*, vol. 189-190, p. 178-182, 1998.

[40] M. Khoury, O. Tottereau, G. Feuillet, P. Vennéguès, et J. Zúñiga-Pérez, « Evolution and prevention of meltback etching: Case study of semipolar GaN growth on patterned silicon substrates », *Journal of Applied Physics*, vol. 122, nº 10, p. 105108, 2017.

[41] M. Charles, Y. Baines, E. Morvan, et A. Torres, « Chapter 4 - III-N Epitaxy on Si for Power Electronics », in *High Mobility Materials for CMOS Applications*, p. 115-158,N. Collaert, Éd. Woodhead Publishing, 2018.

[42] Y. Tanaka *et al.*, « All MOVPE grown nitride-based LED having sub mm underlying GaN », *physica status solidi c*, vol. 5, nº 9, p. 3073-3075, 2008.

[43] D. Kapolnek *et al.*, « Structural evolution in epitaxial metalorganic chemical vapor deposition grown GaN films on sapphire », *Appl. Phys. Lett.*, vol. 67, nº 11, p. 1541-1543, 1995.

[44] P. Kozodoy *et al.*, « Electrical characterization of GaN p-n junctions with and without threading dislocations », *Appl. Phys. Lett.*, vol. 73, nº 7, p. 975-977, 1998.

[45] H. Yacoub *et al.*, « Effect of stress voltage on the dynamic buffer response of GaN-on-silicon transistors », *Journal of Applied Physics*, vol. 119, nº 13, p. 135704, 2016.

[46] X. A. Cao, H. Lu, S. F. LeBoeuf, C. Cowen, S. D. Arthur, et W. Wang, « Growth and characterization of GaN PiN rectifiers on free-standing GaN », *Appl. Phys. Lett.*, vol. 87, nº 5, p. 053503, 2005.

[47] A. Hinoki *et al.*, « Effects of Traps Formed by Threading Dislocations on Off-State Breakdown Characteristics in GaN Buffer Layer in AlGaN/GaN Heterostructure Field-Effect Transistors », *Appl. Phys. Express*, vol. 1, nº 1, p. 011103, 2007.

[48] S. W. Kaun, P. G. Burke, M. Hoi Wong, E. C. H. Kyle, U. K. Mishra, et J. S. Speck, « Effect of dislocations on electron mobility in AlGaN/GaN and AlGaN/AlN/GaN heterostructures », *Appl. Phys. Lett.*, vol. 101, nº 26, p. 262102, 2012.

[49] N. G. Weimann, L. F. Eastman, D. Doppalapudi, H. M. Ng, et T. D. Moustakas, « Scattering of electrons at threading dislocations in GaN », *Journal of Applied Physics*, vol. 83, nº 7, p. 3656-3659, 1998.

[50] D. Hull et D. J. Bacon, « Defects in Crystals », in *Introduction to Dislocations*, Fifth Edition, p. 1-20, Éd. Oxford: Butterworth-Heinemann, 2011.

[51] D. Hull et D. J. Bacon, « Elastic Properties of Dislocations », in *Introduction to Dislocations*, Fifth Edition, p. 63-83, Éd. Oxford: Butterworth-Heinemann, 2011.

[52] H. Stehle et A. Seeger, « Elektronentheoretische Untersuchungen über Fehlstellen in Metallen », *Z. Physik*, vol. 146, nº 2, p. 217-241, 1956.

[53] V. Volterra, « Sur l'équilibre des corps élastiques multiplement connexes », *Annales scientifiques de l'École Normale Supérieure*, vol. 24, p. 401-517, 1907.

[54] J. M. Burgers, « Physics. — Some considerations on the fields of stress connected with dislocations in a regular crystal lattice. I », in *Selected Papers of J. M. Burgers*, F. T. M. Nieuwstadt et J. A. Steketee, p. 335-389, Éd. Dordrecht: Springer Netherlands, 1939.

[55] A. Kelly et K. M. Knowles, *Crystallography and Crystal Defects*. John Wiley & Sons, 2012.

[56] J. Friedel, *Dislocations*. Pergamon Press, 1967.

[57] A. E. Romanov et J. S. Speck, « Stress relaxation in mismatched layers due to threading dislocation inclination », *Appl. Phys. Lett.*, vol. 83, nº 13, p. 2569-2571, 2003.

[58] P. Cantu *et al.*, « Role of inclined threading dislocations in stress relaxation in mismatched layers », *Journal of Applied Physics*, vol. 97, nº 10, p. 103534, 2005.

[59] S. J. Hearne, « Stress creation and relaxation during thin film depsoition », Ph.D. thesis, Arizona State University, 2000.

[60] S. Raghavan et J. M. Redwing, « Growth stresses and cracking in GaN films on (111) Si grown by metal-organic chemical-vapor deposition. I. AlN buffer layers », *Journal of Applied Physics*, vol. 98, nº 2, p. 023514, 2005.

[61] M. Charles, M. Mrad, J. Kanyandekwe, et V. Yon, « Extraction of stress and dislocation density using in-situ curvature measurements for AlGaN and GaN on silicon growth », *Journal of Crystal Growth*, vol. 517, p. 64-67, 2019.

[62] G. G. Stoney et C. A. Parsons, « The tension of metallic films deposited by electrolysis », *Proceedings of the Royal Society of London. Series A, Containing Papers of a Mathematical and Physical Character*, vol. 82, nº 553, p. 172-175, 1909.

[63] R. D. Deslattes, E. G. Kessler Jr, P. Indelicato, et E. Lindroth, « X-ray wavelengths », in *International tables for crystallography. Vol. C: Mathematical, physical and chemical tables*, 3. ed., Dordrecht: Kluwer Acad. Publ, 2004.

[64] S. N. Ahmed, *Physics and Engineering of Radiation Detection*. Amsterdam ; Boston: Academic Press Inc, 2007.

[65] W. Parrish et J. I. Langford, « Powder and related techniques: X-ray techniques », in *International tables for crystallography. Vol. C: Mathematical, physical and chemical tables*, 3. ed., Dordrecht: Kluwer Acad. Publ, 2004.

[66] R. Bardet, « Coefficients d'Atténuation Massique des Rayons X - Rendement d'une Diode Semi-conductrice ». Association Euratom-CEA, 1977.

[67] J.-Y. Duboz *et al.*, « GaN for x-ray detection », *Appl. Phys. Lett.*, vol. 92, nº 26, p. 263501, 2008.

[68] B. D. Cullity, « Diffraction I: the directions of diffracted beams », in *Elements Of X Ray Diffraction*, Addison-Wesley Publishing Company, Inc., 1956.

[69] M. A. Krivoglaz, « Distribution of the Scattering Intensity - General Aspects », in *X-Ray and Neutron Diffraction in Nonideal Crystals*, p. 1-73, M. A. Krivoglaz, V. G. Baryakhtar, M. A. Ivanov, S. C. Moss, et J. Peisl, Éd. Berlin, Heidelberg: Springer, 1996.

[70] E. N. Maslen, A. G. Fox, et M. A. O'Keefe, « X-ray scattering », in *International tables for crystallography. Vol. C: Mathematical, physical and chemical tables*, 3. ed., Dordrecht: Kluwer Acad. Publ, 2004.

[71] C. G. D. M.A, « XXXIV. The theory of X-ray reflexion », *The London, Edinburgh, and Dublin Philosophical Magazine and Journal of Science*, vol. 27, nº 158, p. 315-333, 1914.

[72] C. G. D. M.A, « LXXVIII. The theory of X-ray reflexion. Part II », *The London, Edinburgh, and Dublin Philosophical Magazine and Journal of Science*, vol. 27, nº 160, p. 675-690, 1914.

[73] B. E. Warren, « Perfect crystal theory », in *X-ray diffraction*, Reading, Mass.: Addison-Wesley Pub. Co., 1969.

[74] M. Barchuk *et al.*, « X-ray diffuse scattering from threading dislocations in epitaxial GaN layers », *Journal of Applied Physics*, vol. 108, nº 4, p. 043521, 2010.

[75] M. Barchuk, V. Holý, et D. Rafaja, « Density of bunched threading dislocations in epitaxial GaN layers as determined using X-ray diffraction », *Journal of Applied Physics*, vol. 123, nº 16, p. 161552, 2017.

[76] V. Holý *et al.*, « Diffuse x-ray scattering from statistically inhomogeneous distributions of threading dislocations beyond the ergodic hypothesis », *Phys. Rev. B*, vol. 77, nº 9, p. 094102, 2008.

[77] M. E. Vickers, M. J. Kappers, T. M. Smeeton, E. J. Thrush, J. S. Barnard, et C. J. Humphreys, « Determination of the indium content and layer thicknesses in InGaN/GaN quantum wells by x-ray scattering », *Journal of Applied Physics*, vol. 94, nº 3, p. 1565-1574, 2003.

[78] E. Prince et Internationale Union für Kristallographie, Éd., *International tables for crystallography. Vol. C: Mathematical, physical and chemical tables*, 3. ed. Dordrecht: Kluwer Acad. Publ, 2004.

[79] B. E. Warren, *X-ray diffraction*. Reading, Mass.: Addison-Wesley Pub. Co., 1969.

[80] W. Parrish, « Scintillation and solid-state detectors », in *International tables for crystallography. Vol. C: Mathematical, physical and chemical tables*, 3. ed., Dordrecht: Kluwer Acad. Publ, 2004.

[81] B. D. Cullity, « Diffractometer measurements », in *Elements Of X Ray Diffraction*, Addison-Wesley Publishing Company, Inc., 1956.

[82] J. R. Helliwell, « Single-crystal X-ray techniques », in *International tables for crystallography. Vol. C: Mathematical, physical and chemical tables*, 3. ed., Dordrecht: Kluwer Acad. Publ, 2004.

[83] T. Konya, « X-ray thin film measurement techniques III. High resolution X-ray diffractometry », *The Rigaku journal*, vol. 25, 2009.

[84] B. D. Cullity, « Appendix 1 - Lattice geometry », in *Elements Of X Ray Diffraction*, Addison-Wesley Publishing Company, Inc., 1956.

[85] H. Angerer *et al.*, « Determination of the Al mole fraction and the band gap bowing of epitaxial AlxGa1−xN films », *Applied Physics Letters*, vol. 71, nº 11, p. 1504, 1998.

[86] J. I. Langford et A. J. C. Wilson, « Scherrer after sixty years: A survey and some new results in the determination of crystallite size », *J Appl Cryst, J Appl Crystallogr*, vol. 11, n° 2, p. 102-113, 1978.

[87] M. J. Hordon et B. L. Averbach, « X-ray measurements of dislocation density in deformed Copper and Aluminum single crystals », *Acta Metallurgica*, vol. 9, n° 3, p. 237-246, 1961.

[88] J. E. Ayers, « The measurement of threading dislocation densities in semiconductor crystals by X-ray diffraction », *Journal of Crystal Growth*, vol. 135, n° 1, p. 71-77, 1994.

[89] W. F. Flanagan, « The effect of substructure on the cleavage fracture of iron cyrstals », Massachusetts Institute of Technology, 1959.

[90] P. Scherrer, « Bestimmung der Größe und der inneren Struktur von Kolloidteilchen mittels Röntgenstrahlen », *Nachrichten von der Gesellschaft der Wissenschaften zu Göttingen, Mathematisch-Physikalische Klasse*, vol. 1918, p. 98-100, 1918.

[91] C. G. Dunn et E. F. Koch, « Comparison of dislocation densities of primary and secondary recrystallization grains of Si-Fe », *Acta Metallurgica*, vol. 5, n° 10, p. 548-554, 1957.

[92] A. R. Stokes et A. J. C. Wilson, « The diffraction of X rays by distorted crystal aggregates - I », *Proc. Phys. Soc.*, vol. 56, n° 3, p. 174–181, 1944.

[93] W. H. Hall, « X-Ray Line Broadening in Metals », *Proc. Phys. Soc. A*, vol. 62, n° 11, p. 741, 1949.

[94] G. K. Williamson et W. H. Hall, « X-ray line broadening from filed aluminium and wolfram », *Acta Metallurgica*, vol. 1, n° 1, p. 22-31, 1953.

[95] T. Metzger *et al.*, « Defect structure of epitaxial GaN films determined by transmission electron microscopy and triple-axis X-ray diffractometry », *Philosophical Magazine A*, vol. 77, n° 4, p. 1013-1025, 1998.

[96] Th. H. de Keijser, J. I. Langford, E. J. Mittemeijer, et A. B. P. Vogels, « Use of the Voigt function in a single-line method for the analysis of X-ray diffraction line broadening », *Journal of Applied Crystallography*, vol. 15, n° 3, p. 308–314, 1982.

[97] S. R. Lee *et al.*, « Effect of threading dislocations on the Bragg peakwidths of GaN, AlGaN, and AlN heterolayers », *Appl. Phys. Lett.*, vol. 86, n° 24, p. 241904, 2005.

[98] V. Hauk, « X-ray diffraction », in *Structural and Residual Stress Analysis by Nondestructive Methods*, p. 17-65, Éd. Amsterdam: Elsevier Science B.V., 1997.

[99] F. Demangeot, J. Frandon, P. Baules, F. Natali, F. Semond, et J. Massies, « Phonon deformation potentials in hexagonal GaN », *Phys. Rev. B*, vol. 69, n° 15, p. 155215, 2004.

[100] V. Yu. Davydov *et al.*, « Phonon dispersion and Raman scattering in hexagonal GaN and AlN », *Phys. Rev. B*, vol. 58, n° 19, p. 12899-12907, 1998.

[101] F. Demangeot, J. Frandon, M. A. Renucci, O. Briot, B. Gil, et R. L. Aulombard, « Raman determination of phonon deformation potentials in α-GaN », *Solid State Communications*, vol. 100, n° 4, p. 207-210, 1996.

[102] J. A. Floro, D. M. Follstaedt, P. Provencio, S. J. Hearne, et S. R. Lee, « Misfit dislocation formation in the AlGaN/GaN heterointerface », *Journal of Applied Physics*, vol. 96, n° 12, p. 7087-7094, 2004.

[103] C. Genzel, « Problems Related to X-Ray Stress Analysis in Thin Films in the Presence of Gradients and Texture », in *Diffraction Analysis of the Microstructure of Materials*, p. 473-503, E. J. Mittemeijer et P. Scardi, Éd. Berlin, Heidelberg: Springer Berlin Heidelberg, 2004.

[104] P. Scardi et Y. H. Dong, « Residual stress in fiber-textured thin films of cubic materials », *Journal of Materials Research*, vol. 16, n° 1, p. 233-242, 2001.

[105] V. Honkimäki, « Utilisation du rayonnement synchrotron en sciences des matériaux », in *Rayonnement synchrotron, rayons X et neutrons au service des matériaux*, A. Lodini et T. Baudin, Éd. EDP Sciences, 2012.

[106] A. Boulle, F. Conchon, et R. Guinebretière, « Strain profiles in thin films: influence of a coherently diffracting substrate and thickness fluctuations », *J Appl Cryst*, vol. 42, n° 1, p. 85-92, 2009.

[107] J. Channagiri, « Strain and defects in irradiated materials : a study using X-ray diffraction and diffuse scattering », thesis, Limoges, 2015.

[108] M. Khoury *et al.*, « Imaging and counting threading dislocations in c-oriented epitaxial GaN layers », *Semicond. Sci. Technol.*, vol. 28, n° 3, p. 035006, 2013.

[109] D. M. Follstaedt, N. A. Missert, D. D. Koleske, C. C. Mitchell, et K. C. Cross, « Plan-view image contrast of dislocations in GaN », *Appl. Phys. Lett.*, vol. 83, n° 23, p. 4797-4799, 2003.

[110] V. Yon, N. Rochat, M. Charles, E. Nolot, et P. Gergaud, « X-Ray Diffraction Microstrain Analysis for Extraction of Threading Dislocation Density of GaN Films Grown on Silicon, Sapphire, and SiC Substrates », *physica status solidi (b)*, vol. 257, n° 4, p. 1900579, 2020.

[111] J. E. Ayers, *Heteroepitaxy of Semiconductors: Theory, Growth, and Characterization*, 1re éd. Boca Raton: CRC Press, 2007.

[112] B. Heying *et al.*, « Role of threading dislocation structure on the x-ray diffraction peak widths in epitaxial GaN films », *Appl. Phys. Lett.*, vol. 68, n° 5, p. 643-645, 1996.

[113] P. Gay, P. B. Hirsch, et A. Kelly, « The estimation of dislocation densities in metals from X-ray data », *Acta Metallurgica*, vol. 1, n° 3, p. 315-319, 1953.

[114] A. D. Kurtz, S. A. Kulin, et B. L. Averbach, « Effect of Dislocations on the Minority Carrier Lifetime in Semiconductors », *Phys. Rev.*, vol. 101, n° 4, p. 1285-1291, 1956.

[115] T. Ide, M. Shimizu, X. Q. Shen, K. Jeganathan, H. Okumura, et T. Nemoto, « Improvement of film quality using Si-doping in AlGaN/GaN heterostructure grown by plasma-assisted molecular beam epitaxy », *Journal of Crystal Growth*, vol. 245, n° 1, p. 15-20, 2002.

[116] X. H. Zheng *et al.*, « Determination of twist angle of in-plane mosaic spread of GaN films by high-resolution X-ray diffraction », *Journal of Crystal Growth*, vol. 255, n° 1, p. 63-67, 2003.

[117] M. Frentrup *et al.*, « X-ray diffraction analysis of cubic zincblende III-nitrides », *J. Phys. D: Appl. Phys.*, vol. 50, n° 43, p. 433002, 2017.

[118] R. Chierchia, T. Böttcher, H. Heinke, S. Einfeldt, S. Figge, et D. Hommel, « Microstructure of heteroepitaxial GaN revealed by x-ray diffraction », *Journal of Applied Physics*, vol. 93, n° 11, p. 8918-8925, 2003.

[119] H. Heinke, V. Kirchner, S. Einfeldt, et D. Hommel, « Analysis of the Defect Structure of Epitaxial GaN », *physica status solidi (a)*, vol. 176, n° 1, p. 391-395, 1999.

[120] H. Heinke, V. Kirchner, S. Einfeldt, et D. Hommel, « X-ray diffraction analysis of the defect structure in epitaxial GaN », *Appl. Phys. Lett.*, vol. 77, n° 14, p. 2145-2147, 2000.

[121] V. Srikant, J. S. Speck, et D. R. Clarke, « Mosaic structure in epitaxial thin films having large lattice mismatch », *Journal of Applied Physics*, vol. 82, n° 9, p. 4286-4295, 1997.

[122] Y. J. Sun *et al.*, « Determination of the azimuthal orientational spread of GaN films by x-ray diffraction », *Appl. Phys. Lett.*, vol. 81, n° 26, p. 4928-4930, 2002.

[123] M. A. Moram, M. E. Vickers, M. J. Kappers, et C. J. Humphreys, « The effect of wafer curvature on x-ray rocking curves from gallium nitride films », *Journal of Applied Physics*, vol. 103, n° 9, p. 093528, 2008.

[124] V. M. Kaganer, O. Brandt, A. Trampert, et K. H. Ploog, « X-ray diffraction peak profiles from threading dislocations in GaN epitaxial films », *Phys. Rev. B*, vol. 72, n° 4, p. 045423, 2005.

[125] D. Hull et D. J. Bacon, « Dislocation Arrays and Crystal Boundaries », in *Introduction to Dislocations*, Fifth Edition., p. 171-204, Éd. Oxford: Butterworth-Heinemann, 2011.

[126] L. Balogh, L. Capolungo, et C. N. Tomé, « On the measure of dislocation densities from diffraction line profiles: A comparison with discrete dislocation methods », *Acta Materialia*, vol. 60, n° 4, p. 1467-1477, 2012.

[127] M. A. Krivoglaz, « Scattering of X-Ray and Neutrons in Crystals with Dislocations », in *X-Ray and Neutron Diffraction in Nonideal Crystals*, p. 357-420, M. A. Krivoglaz, V. G. Baryakhtar, M. A. Ivanov, S. C. Moss, et J. Peisl, Éd. Berlin, Heidelberg: Springer, 1996.

[128] M. Wilkens, « Das Spannungsfeld einer Anordnung von regellos verteilten Versetzungen », *Acta Metallurgica*, vol. 15, n° 8, p. 1412-1415, 1967.

[129] M. Wilkens, « Das mittlere Spannungsquadrat $\langle \sigma 2 \rangle$ begrenzt regellos verteilter Versetzungen in einem zylinderförmigen Körper », *Acta Metallurgica*, vol. 17, n° 9, p. 1155-1159, 1969.

[130] M. Wilkens, « The determination of density and distribution of dislocations in deformed single crystals from broadened X-ray diffraction profiles », *physica status solidi (a)*, vol. 2, n° 2, p. 359-370, 1970.

[131] V. M. Kaganer, O. Brandt, H. Riechert, et K. K. Sabelfeld, « X-ray diffraction of epitaxial films with arbitrarily correlated dislocations: Monte Carlo calculation and experiment », *Physical Review B - Condensed Matter and Materials Physics*, vol. 80, n° 3, 2009.

[132] I. Groma, T. Ungár, et M. Wilkens, « Asymmetric X-ray line broadening of plastically deformed crystals. I. Theory », *J Appl Cryst*, vol. 21, n° 1, p. 47-54, 1988.

[133] M. Wilkens, « Theroretical aspects of kinematical X-ray diffraction profiles from crystals containing dislocation distributions », in *Proceedings of the Conference on Fundamental Aspects of Dislocation Theory*, vol. 2, 1969.

[134] I. Groma, « X-ray line broadening due to an inhomogeneous dislocation distribution », *Phys. Rev. B*, vol. 57, n° 13, p. 7535-7542, 1998.

[135] I. Groma et F. Székely, « Analysis of the asymptotic properties of X-ray line broadening caused by dislocations », *J Appl Cryst*, vol. 33, n° 6, p. 1329-1334, 2000.

[136] V. Soukhoveev, A. Volkova, V. Ivantsov, O. Kovalenkov, A. Syrkin, et A. Usikov, « Large area GaN and AlN template substrates fabricated by HVPE », *physica status solidi c*, vol. 6, n° S2, p. S333-S335, 2009.

[137] E. Arslan, M. K. Ozturk, Ö. Duygulu, A. A. Kaya, S. Ozcelik, et E. Ozbay, « The influence of nitridation time on the structural properties of GaN grown on Si (111) substrate », *Appl. Phys. A*, vol. 94, n° 1, p. 73-82, 2009.

[138] M. Barchuk *et al.*, « Correlation between the residual stress and the density of threading dislocations in GaN layers grown by hydride vapor phase epitaxy », *Journal of Crystal Growth*, vol. 386, p. 1-8, 2014.

[139] W. Hu *et al.*, « The substantial dislocation reduction by preferentially passivating etched defect pits in GaN epitaxial growth », *Appl. Phys. Express*, vol. 12, n° 3, p. 035502, 2019.

[140] S. D. Lester, F. A. Ponce, M. G. Craford, et D. A. Steigerwald, « High dislocation densities in high efficiency GaN-based light-emitting diodes », *Appl. Phys. Lett.*, vol. 66, n° 10, p. 1249-1251, 1995.

[141] S. J. Rosner, E. C. Carr, M. J. Ludowise, G. Girolami, et H. I. Erikson, « Correlation of cathodoluminescence inhomogeneity with microstructural defects in epitaxial GaN grown by metalorganic chemical-vapor deposition », *Appl. Phys. Lett.*, vol. 70, n° 4, p. 420-422, 1997.

[142] S.-L. Sahonta, M. Q. Baines, D. Cherns, H. Amano, et F. A. Ponce, « Migration of Dislocations in Strained GaN Heteroepitaxial Layers », *physica status solidi (b)*, vol. 234, n° 3, p. 952-955, 2002.

[143] S. Raghavan, X. Weng, E. Dickey, et J. M. Redwing, « Correlation of growth stress and structural evolution during metalorganic chemical vapor deposition of GaN on (111) Si », *Appl. Phys. Lett.*, vol. 88, n° 4, p. 041904, 2006.

Appendix 1: Python program for stress gradient analysis in thin film of GaN

```
"""
This program simulates the X-ray diffraction (XRD) signal stemming from a GaN layer
affected by a gradient of in-plane biaxial stress. The simulations correspond to
XRD radial scans (2theta-omega scans) of symmetric reflections [(002), (004),
(006)].
The function Main(order) computes the diffraction curve for one of the three
possible orders of diffraction (2,4,6). The main parameters of the simulation are
defined within this function.

Created on Wed Mar 21 2018
Author: Victor YON
"""

import numpy as np
import matplotlib
import matplotlib.pyplot as plt
import math as mt
import cmath as cmt
import random
from scipy.signal import fftconvolve
from scipy.signal import deconvolve
import time
import csv
pi = mt.pi
params = {'mathtext.default': 'regular'}
plt.rcParams.update(params)


#############################################################################
#                        INITIAL PARAMETERS CALCULATION
#############################################################################

def Interplanar_distance_calculation (reflection, a0, c0):

    # Computes the interplanar distances in the reciprocal space and real space and
returns the values obtained.

    # Distance in reciprocal space - Hexagonal system: d*² = (h²+k²+hk)a*² + l²c*²

    drec = mt.sqrt((reflection[0]**2 + reflection[1]**2 +
reflection[0]*reflection[1])/a0**2 + reflection[2]**2/c0**2)

    # Distance in real space - Hexagonal system: d² = 1/(4/3/a².(h²+k²+hk) + l²/c²)

    dreal = 1/mt.sqrt((reflection[0]**2 + reflection[1]**2 +
reflection[0]*reflection[1])*4/3/a0**2 + reflection[2]**2/c0**2)

    return dreal, drec

#############################################################################
#                        DISPLACEMENT FIELD CALCULATION
#############################################################################

def U_strain_gradient(d,z_size,R):

    # == Calculates the strain gradient, with a logarithmic shape, from parameters
K and RMS_strain defined within the function
    # == Calculates the base displacement profile along the thickness of the layer
    # == Returns the profiles of strain (strain_zsize) and displacement (u_zsize)

    definition = 16  # Parameter of oversampling of the stress gradient - A high
definition parameter enables a more accurate calculation of the displaement field
```

```
    size = (z_size-1) * definition + 1  # strain_zsize[i] = strain[definition*i] &
u_zsize[i] = u[definition*i]


    #== SETTING THE LOG-SHAPED STRAIN GRADIENT ==#

    K = 1000 # Coefficient of curvature of the logarithm
    RMS_strain = 0.00051 # Root mean square value of the strain profile - can be
estimated from a Williamson-Hall plot
    Max_strain = RMS_strain * (K*L**2/(-1*L**2-2*L+2*K))**0.5 # Max value of the
strain profile (=strain[0])

    X = np.linspace(0,1,size)
    strain = Max_strain * (1 - np.log(K*X+1)/np.log(K+1))


    #== DISPLACEMENT CALCULATION ==#

    u= np.zeros(size)
    #u[0] = strain[0]*d  # This shifts the position of the first atom in the column
to take into account the strain on this first atom
    for i in range (1,size):
        u[i] = u[i-1] + strain[i-1]*d/definition   # Unit:[Å] d=c0 for (001) -
between each step: ډ = ε × distance
                                                  # No strain is applied on the first atom
of the column(-> u[0]=0). The strain[0] is applied on the dispacement u[1] of the
second atom of the column. The strain[z_size] is equal to 0 and not applied to any
atom

    #== RETURNING TO A NORMAL DEFINITION FOR DISPLACEMENT AND STRAIN GRADIENTS ==#

    strain_zsize = np.zeros(z_size)
    for i in range(0, z_size):
        strain_zsize[i] = strain[definition*i]  # Array length: Number of atoms in
an atomic column

    u_zsize = np.zeros(z_size)
    for i in range(0, z_size):
        u_zsize[i] = u[definition*i]  # Array length: Number of atoms in an atomic
column

    return strain_zsize, u_zsize


def U_shift(u):

    # == Calculates the u displacement gradient at one of the (x,y) positions and
returns it
    # == This u_xy gradient is calculated by shifting the initial u gradient
    # == The distribution of shift is Gaussian
    # == Function not used by the program

    sigma = 1.0  # [Å] Standard deviation of the Gaussian distribution (68.2% of
the values lie between mean_value +-sigma)

    u_xy = np.zeros(len(u))  # The size of the u_xy gradient is the same that the
size of the domains along z
    u_xy = u + random.gauss(0,sigma)  # Distribution of shift centered in 0

    return u_xy


def U_dispersion(u):

    # == Calculates the u displacement gradient at one of the (x,y) positions and
returns it
    # == This u_xy gradient is calculated by dispertion of each z point of the
initial u gradient
```

```
    # == The distribution of shift of each z point is Gaussian
    # == Function not used by the program

    sigma = 0.45  # [Å] Standard deviation of the gaussian distribution (68.2% of
the values lie between mean_value +-sigma)

    u_xy = np.zeros(len(u))  # The size of the u_xy gradient is the same that the
size of the domains along z

    for i in range (len(u)):
        u_xy[i] = u[i] + random.gauss(0,sigma) # Distribution of shift centered in
0

    return u_xy


def U_factor(u, sigma):

    # == Calculates the u displacement gradient at one of the (x,y) positions and
returns it
    # == This u_xy gradient is calculated by multiplying the whole initial u
gradient by a factor
    # == The distribution of the factor value is Gaussian, centered in 1

    factor = random.gauss(1,sigma)
    if factor < 0:  # To avoid having a negative factor that would change the
global shape of the u gradient
        factor = 0
    u_xy = u * factor # Distribution of the factor centered in 1. 99.73% of values
in (u ±3σu) - 68.27% of values in (u ±σu)

    return u_xy


#########################################################################
#                    AMPLITUDE & INTENSITY CALCULATION
#########################################################################

def Calculate_shape_function(cryst_size_z):

    # == Calculates the crystal shape function along the normal to the sample
surface and returns it
    # == This function is equal to 1 within the crystal and to 0 outside of it
    # == Parameter: cryst_size_z: Whole size of the crystal along z

    Shape_function = np.ones(cryst_size_z)  # Defined as a gate function

    return Shape_function


def Intensity(q,domain_size_xy,size_z,G,U_XY,Shape_function,R,F0):

    # == Computes the amplitude scattered by a subdomain of coherent diffraction of
size domain_size_xy in the surface plane and size_z along the c-axis
    # == Computes the corresponding Intensity and returns it

    Ampl = np.zeros(len(q), dtype=complex)
    Total_Ampl = np.zeros(len(q), dtype=complex)

    # Calculation by means of a fast Fourier transform (Complexity N.log(N)):

    for i in range (domain_size_xy):

        Correlation_function = np.exp(-2*mt.pi*1j*G*U_XY[i,:])  # u for the (x,y)
position number i
        Ampl = F0*np.fft.fft(Shape_function*Correlation_function,n=len(q))   # n =
Length of the transformed axis of the output. If n is larger than the length of the
input, the input is padded with zeros
```

```
        Ampl = np.fft.fftshift(Ampl)                        # To center the signal
on G, the reciprocal space position of the diffraction spot for a relaxed crystal.

        Total_Ampl = Total_Ampl + Ampl

    Intensity = abs(Total_Ampl)**2

    return Intensity


def Total_Intensity(size_z, cryst_size_xy, nb_domains_xy, nb_domains_z, q, G, u, V,
R, F0, sigma):

    # == Call the functions to calculate the local strain fields in each subdomain
of coherent diffraction of size domain_size_xy in the surface plane and size_z
along the c-axis.
    # == Computes the sum of scattered intensities
    # == Returns the sum of intensities and the array of strain profiles

    cryst_size_z = size_z*nb_domains_z  # = lenght(u)
    dom_size_xy = cryst_size_xy//nb_domains_xy # number of unit cells in a
coherently diffracting domain of the surface plane (int=int//int)
    I = np.zeros(len(q))
    U_XY = np.zeros((cryst_size_xy,cryst_size_z))  # Matrice with all the
displacements of all the (x,y) positions in the whole crystal

    for h in range (cryst_size_xy):
#         U_XY[h,:] = U_dispersion(u)    # line 1: u(x1,y1) ; line 2 : u(x2,y2) ; ...
#         U_XY[h,:] = U_shift(u)    # line 1: u(x1,y1) ; line 2 : u(x2,y2) ; ...
        U_XY[h,:] = U_factor(u,sigma) #U_factor(u)    # line 1: u(x1,y1) ; line 2 :
u(x2,y2) ; ...

    for h in range (nb_domains_xy):  # Sum of intensities of all (x,y) domains
        for k in range(nb_domains_z):  # Sum of intensities of all domains along z
for a position (x,y)
            I = I +
Intensity(q,dom_size_xy,size_z,G,U_XY[h*dom_size_xy:(h+1)*dom_size_xy ,
k*size_z:(k+1)*size_z],V[k*size_z:(k+1)*size_z],R,F0)  # The u gradients for all
(x,y) positions, of the lenght of a domain along z


    return I,U_XY


#########################################################################
#                          INSTRUMENTAL RESOLUTION
#########################################################################

def Instrumental_resolution(theta):

    #== Calculates the Full Width at Half Maximum (FWHM) of the instrumental
    #== resolution for the Bragg angle θ of the simulated reflection and returns
    #== this value

    # Resolution = a0 + a1*2θ + a2*2θ^2  (polynomial degree 2)
    # Coefficients [arcsec/deg]:
    Coeff = [32.05,-0.6224,0.008185]
    fwhm = Coeff[0] + Coeff[1]*2*theta + Coeff[2]*(2*theta)**2

    return fwhm


def FWHM_Conv(fwhm_sec, theta, lamb):

    #== Converts the FWHM of the instrumental resolution in reciprocal space units
and returns this value

    fwhm_deg = fwhm_sec/3600  # Arcseconds to degrees
```

```
    delta_sintheta = mt.sin((theta+fwhm_deg)/180*pi) - mt.sin(theta/180*pi)

    fwhm_reciprocal = 2*delta_sintheta/lamb  # (Å-1) Instrumental resolution of
XRD3 at GaN peak angle (With ΔTheta=22": ΔG = 2/lambda*Δ(sin Theta) = 0.00013 Å-1)

    return fwhm_reciprocal


def f_gaussian(fwhm,d_rec,oversampling,size,range_factor):

    # == Creates a gaussian distribution with the same step between points than the
simulated scattered signal
    # == Returns this distribution and its x-axis

    x_step = d_rec/(oversampling*size-1)  # Step = TotalRange/Nb_point
    x_range = range_factor*fwhm  #Restricted range (Approx. n*FWHM_range)
    x = np.arange(-0.5*x_range, 0.5*x_range, x_step)
    gauss = np.exp(-4*mt.log(2)*(x/fwhm)**2)*0.9394/fwhm*x_step  # factor
0.9394/fwhm so the Area under the gaussian functions equal to 1 (See Langford &
Wilson 1978)
                                                                 # multiplied by x_step
so the Area is equal to one in the convolution space, where the step betwwen to
points is equal to unity
    return gauss,x


def Convolve_instrum_resolution(I,fwhm, d_rec, oversampling, size):

    # == Convolves the simulated profile of scattered intensity with the Gaussian
profile of intrumental resolution
    # == Returns the convolved profile of intensity

    instrum,x_instrum = f_gaussian(fwhm, d_rec, oversampling, size, 10.0)  #
Gaussian function for instrumental resolution: Range = last_param*FWHM_range

    Intensity = fftconvolve(I, instrum, mode = 'same') # Intensity array same size
as I

    return Intensity

#############################################################################
#                          GRAPHS PLOTTING & SAVING
#############################################################################

def Gradients_plot(strain, u, U_XY, Shape_function, size):
    t0 = time.time()

    # == Plots the strain profile, the base displacement profile plus a few local
    # == displacement profiles and the shape function
    # == Returns the figures of displacement and strain

    #-- Plot the strain gradient

    fig_strain=plt.figure(figsize=(5,3.5))    # Plot I vs. qz_order1
    fig_strain.patch.set_alpha(0.0)
    ax = fig_strain.add_subplot(111)
    plt.locator_params(axis='x',nbins=5), plt.locator_params(axis='y',nbins=5)
    ax.tick_params(width=1.5,direction='inout',length=8)
    ax.minorticks_on(),
ax.tick_params(which='minor',width=1,direction='in',length=4)
    plt.xlabel('Unit cell number', fontsize=20), plt.ylabel('Strain', fontsize=20)
    plt.xticks(fontsize=15), plt.locator_params(axis='x',nbins=5),
plt.yticks(fontsize=15)
    ax.tick_params(width=2,direction='inout',length=12)
    plt.plot(np.linspace(0,size,size), strain, linestyle= 'None', marker='o',
markersize=2)

    #-- Plot the Shape function
```

```
    fig_strain=plt.figure(figsize=(5,3.5))    # Plot I vs. qz_order1
    fig_strain.patch.set_alpha(0.0)
    ax = fig_strain.add_subplot(111)
    plt.locator_params(axis='x',nbins=5), plt.locator_params(axis='y',nbins=5)
    ax.tick_params(width=1.5,direction='inout',length=8)
    ax.minorticks_on(),
ax.tick_params(which='minor',width=1,direction='in',length=4)
    plt.xlabel('Unit cell number', fontsize=20), plt.ylabel('Strain', fontsize=20)
    plt.xticks(fontsize=15), plt.locator_params(axis='x',nbins=5),
plt.yticks(fontsize=15)
    ax.tick_params(width=2,direction='inout',length=12)
    plt.plot(np.linspace(0,size,size), Shape_function, color="grey")

    #-- Plot the displacement profiles

    fig_displacement=plt.figure(figsize=(5,5))    # Plot I vs. qz_order1
    fig_displacement.patch.set_alpha(0.0)
    ax = fig_displacement.add_subplot(111)
    plt.locator_params(axis='x',nbins=5), plt.locator_params(axis='y',nbins=5)
    ax.tick_params(width=1.5,direction='inout',length=8)
    ax.minorticks_on(),
ax.tick_params(which='minor',width=1,direction='in',length=4)
    plt.xlabel('Unit cell number', fontsize=20), plt.ylabel('Displacement [Å]',
fontsize=20)
    plt.xticks(fontsize=15), plt.locator_params(axis='x',nbins=5),
plt.yticks(fontsize=15)
    ax.tick_params(width=2,direction='inout',length=12)

    # Plot the displacement profiles for all the atomic columns
    plt.plot(np.linspace(0,size,size), U_XY[0,:], label='Modified displacement
profiles', linewidth=2, color='blue')#,linestyle= 'None', marker='o', markersize=2)
    for i in range (1,min(len(U_XY[:,0]),8)):  # limited to 20 plots
        plt.plot(np.linspace(0,size,size), U_XY[i,:], linewidth=2,
color='blue')#,linestyle= 'None', marker='o', markersize=2)

    # Plot the base displacement profile
    plt.plot(np.linspace(0,size,size), u, linewidth=3, label='Base displacement
profile', color='red')
    leg= ax.legend(loc='lower left', bbox_to_anchor=(0,1.01,1,0.2),
borderaxespad=0, mode='expand', fontsize=15.5,  handlelength=1.6,
handletextpad=0.2, labelspacing=0.3, edgecolor='black', numpoints = 3,
markerscale=1.5)

    tplot = time.time() - t0
    return fig_displacement, fig_strain

def Intensity_plot(Intensity,q,lamb):

    # == Plots the simulated profile (x-axis: q / y-axis: Intensity)
    # == Returns the figure and the x-axis

    Theta_Deg = 180/pi*np.arcsin(lamb*q/2)  # Conversion 1/Å to degrees
    Theta_Sec = Theta_Deg*3600  # Conversion degrees to arcseconds
    x = q  # Choice of the x-axis unit ( q: qz (1/Å) - Theta_Deg: θ (°) - Theta_Sec
(arcsec) )

    fig=plt.figure(figsize=(8,5))
    fig.patch.set_alpha(0.0)
    ax = fig.add_subplot(111)
    plt.locator_params(axis='x',nbins=5), plt.locator_params(axis='y',nbins=6)
    ax.tick_params(width=1.5,direction='inout',length=8)
    ax.minorticks_on(),
ax.tick_params(which='minor',width=1,direction='in',length=4)
    ax.set_xlim([-0.004,0.0000])
    plt.xlabel('qz [1/Å]', fontsize=20)
    plt.ylabel('Intensity [arb. unit]', fontsize=20)
    plt.xticks(fontsize=15)
```

```
    plt.yticks(fontsize=15)
    plt.plot(x,Intensity,color="purple",linestyle="-")

    return fig, x

def save_figures(figure, name):

    # == Saves the generated graphs

    fileformat = 'svg'
    fileformat2 = 'png'
    filename = name + "." + fileformat
    filename2 = name + "." + fileformat2
    figure.savefig(filename, format=fileformat, transparent=True,
bbox_inches='tight')
    figure.savefig(filename2, format=fileformat2, transparent=True,
bbox_inches='tight', dpi = 200)

#########################################################################
#                                MAIN PROGRAM
#########################################################################

def Main(order):

    # == Main function of the program
    # == Simulation parameters are defined at the begining
    # == Calls the functions to perform a simulation for the reflection (0,0,order)
    # == Returns the simulated profile of intensity (I), the corresponding x-axis
(x) and and the total time needed for the simulations (tf)

    t0 = time.time() # Measurement of the length of the simulation duration

    lamb = 1.54059  # Wavelength (Å) - kalpha1 Cu
    reflection = [0,0,order]  # Studied reflection

    #-- SIMULATION PARAMETERS

    a0, c0 = 3.1896, 5.1855  # Lattice parameters [Å]
    structure_factors_list = (50.81,32.82,27.05) # Respective structure factors of
(002),(004) and (006) reflections [1/Å]
    structure_factor = structure_factors_list[(order-2)//2]  # Structure factor
(Selection from the list)

    cryst_thickness = 1.85 # Crystal thickness [µm]
    cryst_size_z = round(cryst_thickness*10000/c0)  # Approximate number of unit
cells in the whole crystal along z ##### 2µm = 3857
    nb_domains_z = 1  # Number of incoherently diffracting domains along z
    size = int(cryst_size_z/nb_domains_z)  # Number of unit cells in the domain
along z
    cryst_size_z = size * nb_domains_z  # exact number of unit cells in the whole
crystal along z

    cryst_size_xy = 5000  # Approximate number of unit cells in the surface plane
    lateral_correlation_length = 20000.0  # Lateral correlation length (µm) - When
set to 20000.0: 1 (x,y) Domain for up to 38million of cryst_size_xy
    dom_size_xy = int(round(lateral_correlation_length/c0*10000)) # Number of unit
cells in a coherently diffracting domain of the surface plane
    nb_domains_xy = int(round(cryst_size_xy/dom_size_xy)) # Number of incoherently
diffracting domains in xy
    if nb_domains_xy == 0: # To avoid having it = 0
        nb_domains_xy = 1
    dom_size_xy = int(round(cryst_size_xy/nb_domains_xy))
    cryst_size_xy = dom_size_xy * nb_domains_xy # Exact number of unit cells in the
whole crystal in the surface plane

    sigma = 0.125  # Parameter of local variation of strain gradients
```

```
    oversampling = 4  # Oversampling factor (resolution of calculated curve).
Normally equals to 4 to see the fringes, sometimes 8 in practice
    display = 'rel' # 'abs' for absolute x-axis units / 'rel' for relative x-axis
units

    #-- CALCULATION OF BASIC PARAMETERS

    d_refl, G = Interplanar_distance_calculation (reflection, a0, c0)  #
Interplanar distance of the reflection in real and reciprocal spaces
    d_reel = order * d_refl  # Interplanar distance for the first order of
diffraction (distance between atoms = c0 for 001)
    d_rec = G/order  # d*001 (Interplanar distance in reciprocal space, 1st order
of diffraction -> =0.1928 for all symmetric reflections)
    R = np.linspace(0, (cryst_size_z-1)*d_reel, cryst_size_z)  # Whole crystal unit
cells basic positions [real space]
    theta = mt.asin(lamb/2/d_refl)*180/pi  # Bragg angle [Degrees]

    q = np.linspace(G - 0.5*d_rec, G + 0.5*d_rec, oversampling*size)  # the array
of positions along the qz axis of reciprocal space for which the scattered
amplitude is about to be calculated. Centered on G. Step between points =
c0/(oversampling*size)

    if display == 'abs':  # Absolute mode
        q = np.linspace(G - 0.5*d_rec, G + 0.5*d_rec, oversampling*size)  # Points
for Intensity computation in one domain [reciprocal space]
    elif display == 'rel':  # Relative mode
        q = np.linspace(-0.5*d_rec, 0.5*d_rec, oversampling*size)  # Points for
Intensity computation in one domain [reciprocal space]

    #-- CALLING THE MAIN FUNCTIONS

    Strain, u = U_strain_gradient(d_reel, cryst_size_z, R)  # Base strain field [no
unit] and Base displacement field [Å] computation
    V = Calculate_shape_function(cryst_size_z)  # Calculation of the crystal shape
function

    I,U_XY= Total_Intensity(size, cryst_size_xy, nb_domains_xy, nb_domains_z, q, G,
u, V, R, structure_factor, sigma)  # Intensity computation

# I is the sum of intensities of all the incoherently diffracting domains - U_XY is
the displacement ([Å]) matrix of the atomic columns in the whole crystal

    fwhm_arcsec = Instrumental_resolution(theta)  # Calculation of the instrumental
resolution of the diffractometer [arcsec]
    fwhm = FWHM_Conv(fwhm_arcsec, theta, lamb)  # Conversion of the fwhm in the
reciprocal space
    I = Convolve_instrum_resolution(I, fwhm, d_rec, oversampling, size)  #
Convolution of the diffracted intensity with the instrumental resolution
    tf = time.time() - t0

    figure_displacement, figure_strain = Gradients_plot(Strain, u, U_XY, V,
cryst_size_z)
    figure_intensity,x = Intensity_plot(I, q, lamb)

#    save_figures(figure_intensity, "Simul_(00"+str(order)+")_" +
str(cryst_thickness)+"µm_" + "xy="+str(cryst_size_xy) + "_ov="+str(oversampling) +
"_fwhm="+str(round(fwhm_arcsec)) + "_sigma-u-factor="+(str(sigma)))

    return I, x, tf
```

Appendix 2: Demonstration of equation (4.7)

The demonstration below is based on the work of *Hordon et Averbach*. It uses the angles and vectors defined in equation (4.6) and **Figure A.1**, where the use of the subscript 1 indicates that the first of the three equivalent edge dislocation systems of a wurtzite crystal is represented.

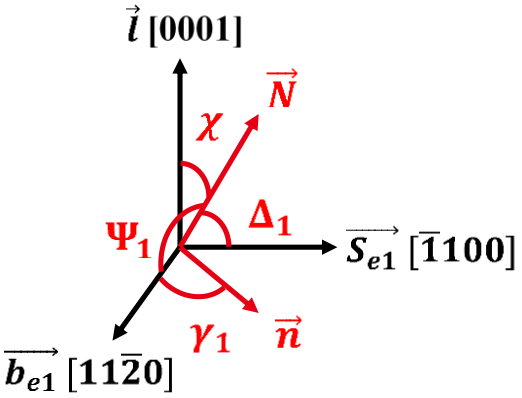

Figure A.1 : Sketch of the geometrical relationships around an edge threading dislocation with Burgers vector $\mathbf{b_e} = 1/3\,[11\bar{2}0]$. In this figure, we represented the angles($\Psi_1, \Delta_1, \gamma_1$) for the first of the three edge dislocation system (i.e. Burgers vector $\overrightarrow{b_{e1}}$ oriented in the [11$\bar{2}$0] direction and normal to the glide plane $\overrightarrow{S_{e1}}$ oriented in the [$\bar{1}$100] direction). $\vec{N}$ is the normal to the diffracting plane, $\vec{n}$ is the projection of $\vec{N}$ on the radial plane of the dislocation (i.e. the plane normal to the dislocation line directed along [0001]) and χ is the angle between the normal $\vec{N}$ and the normal to the surface $\vec{l}$.

The demonstration starts with the calculation of the mean square strain $\langle \varepsilon_{e\,\vec{n}}^{\,2} \rangle$ of an edge TD along $\vec{n}$. As shown in the figure above, $\vec{n}$ is the projection of the normal to the diffracting plane $\vec{N}$ on the radial plane of the dislocation. The calculation is based on an integration of the components ε_{rr} and $\varepsilon_{r\theta}$ of the strain field around an edge dislocation. *Hordon et Averbach* provided the expressions of $\varepsilon_{rr} = \frac{b_e \sin\theta}{4\pi(1+\nu)r}$ and $\varepsilon_{r\theta} = \frac{b_e \cos\theta}{2\pi(1-\nu)r}$ and the expression below, from where we will start the calculation. In the following, the inner radius r_0, the outer radius R, the geometrical angle γ (see figure above) and the Poisson ratio ν are constants independent of θ.

$$\langle \varepsilon_{e\,\vec{n}}^{\,2} \rangle = \frac{1}{\pi R^2} \int_{r_0}^{R} \int_{0}^{2\pi} (\varepsilon_{rr} + \varepsilon_{r\theta} \sin(\gamma-\theta) \cos(\gamma-\theta))^2 \, r \, dr \, d\theta$$

$$= \frac{1}{\pi R^2} \int_{r_0}^{R} \int_{0}^{2\pi} \left(\frac{b_e \sin\theta}{4\pi(1+\nu)r} + \frac{b_e \cos\theta}{2\pi(1-\nu)r} \frac{\sin(2\gamma-2\theta)}{2} \right)^2 r \, dr \, d\theta$$

$$= \frac{b_e^2}{16\pi^3 R^2} \int_{r_0}^{R} \int_{0}^{2\pi} \left(\underbrace{\frac{\sin^2\theta}{(1+\nu)^2}}_{①} + \underbrace{\frac{\cos^2\theta \, \sin^2(2\gamma-2\theta)}{(1-\nu)^2}}_{②} + \underbrace{\frac{2\sin\theta\cos\theta\sin(2\gamma-2\theta)}{(1+\nu)(1-\nu)}}_{③} \right) \frac{1}{r} \, dr \, d\theta$$

$$\textcircled{1}: \int_0^{2\pi} \frac{\sin^2\theta}{(1+\nu)^2}\, d\theta = \frac{1}{(1+\nu)^2}\int_0^{2\pi} \frac{1-\cos(2\theta)}{2}\, d\theta = \frac{1}{2(1+\nu)^2}\left[\theta - \frac{\sin(2\theta)}{2}\right]_0^{2\pi}$$

$$= \frac{1}{2(1+\nu)^2}(2\pi - 0) = \boxed{\frac{\pi}{(1+\nu)^2}}$$

$$\textcircled{2}: \int_0^{2\pi} \frac{\cos^2\theta\ \sin^2(2\gamma-2\theta)}{(1-\nu)^2}\, d\theta = \frac{1}{(1-\nu)^2}\int_0^{2\pi} \frac{1+\cos(2\theta)}{2}\ \frac{1-\cos(4\gamma-4\theta)}{2}\, d\theta$$

$$= \frac{1}{4(1-\nu)^2}\int_0^{2\pi} (1+\cos(2\theta)-\cos(4\gamma-4\theta)-\cos(2\theta)\cos(4\gamma-4\theta))\, d\theta$$

$$= \frac{1}{4(1-\nu)^2}\int_0^{2\pi} \left(1+\cos(2\theta)-\cos(4\gamma-4\theta)-\frac{1}{2}(\cos(2\theta-4\gamma+4\theta)+\cos(2\theta+4\gamma-4\theta))\right) d\theta$$

$$= \frac{1}{4(1-\nu)^2}\left([\theta]_0^{2\pi} + \left[\frac{\sin(2\theta)}{2}\right]_0^{2\pi} - \left[\frac{\sin(4\gamma-4\theta)}{-4}\right]_0^{2\pi} - \frac{1}{2}\left(\left[\frac{\sin(4\gamma+6\theta)}{6}\right]_0^{2\pi} + \left[\frac{\sin(4\gamma-2\theta)}{-2}\right]_0^{2\pi}\right)\right)$$

$$= \frac{1}{4(1-\nu)^2}(2\pi+0+0+0) = \boxed{\frac{\pi}{2(1-\nu)^2}}$$

$$\textcircled{3}: \int_0^{2\pi} \frac{2\sin\theta\cos\theta\sin(2\gamma-2\theta)}{(1+\nu)(1-\nu)}\, d\theta = \frac{2}{(1+\nu)(1-\nu)}\int_0^{2\pi} \sin\theta\cos\theta\sin(2\gamma-2\theta)\ d\theta$$

$$= \frac{2}{(1+\nu)(1-\nu)}\int_0^{2\pi} \frac{\sin(2\theta)}{2}\sin(2\gamma-2\theta)\, d\theta$$

$$= \frac{1}{(1+\nu)(1-\nu)}\int_0^{2\pi} \frac{1}{2}(\cos(2\theta-2\gamma+2\theta)-\cos(2\theta+2\gamma-2\theta))\, d\theta$$

$$= \frac{1}{2(1+\nu)(1-\nu)}\left(\left[\frac{\sin(-2\gamma+4\theta)}{4}\right]_0^{2\pi} - [\theta\cos(2\gamma)]_0^{2\pi}\right) = \boxed{\frac{-\pi\cos(2\gamma)}{(1+\nu)(1-\nu)}}$$

Hence:

$$\langle \varepsilon_{e\,\vec{n}}^{\,2} \rangle = \frac{b_e^2}{16\pi^3R^2}\int_{r_0}^{R} \frac{1}{r}\left(\frac{\pi}{(1+\nu)^2} + \frac{\pi}{2(1-\nu)^2} - \frac{\pi\cos(2\gamma)}{(1+\nu)(1-\nu)}\right) dr$$

$$= \frac{b_e^2}{16\pi^2R^2}\ln\left(\frac{R}{r_0}\right)\left(\frac{2(1-\nu)^2+(1+\nu)^2}{2(1+\nu)^2(1-\nu)^2} + \frac{1-2\cos^2\gamma}{(1+\nu)(1-\nu)}\right)$$

$$= \frac{b_e^2}{16\pi^2R^2}\ \frac{1}{(1+\nu)(1-\nu)}\ \ln\left(\frac{R}{r_0}\right)\left(\frac{2(1-2\nu+\nu^2)+(1+2\nu+\nu^2)}{2(1+\nu)(1-\nu)} + 1 - 2\cos^2\gamma\right)$$

$$= \frac{b_e^2}{16(1-\nu^2)\pi^2R^2}\ \ln\left(\frac{R}{r_0}\right)\left(\frac{2-4\nu+2\nu^2+1+2\nu+\nu^2+2-2\nu^2}{2(1-\nu^2)} - 2\cos^2\gamma\right)$$

$$= \boxed{\frac{b_e^2}{16(1-\nu^2)\pi^2R^2}\ \ln\left(\frac{R}{r_0}\right)\left(\frac{\nu^2-2\nu+5}{2(1-\nu^2)} - 2\cos^2\gamma\right)}$$

In the following, we will use two Poisson ratio depending parameters:

$A = \frac{1}{16(1-\nu^2)}$ $\quad$ $B = \frac{\nu^2-2\nu+5}{2(1-\nu^2)}$

The mean square strain $\langle \varepsilon_e^2 \rangle$ along the normal to the diffraction plane $\vec{N}$ is obtained by projection of $\langle \varepsilon_{e\,\vec{n}}^{\,2} \rangle$. We note that, geometrically, $(\cos\Delta = \sin\chi \sin\gamma)$ and $(\cos\Psi = \sin\chi\cos\gamma)$. Hence, as mentioned by *Hordon et Averbach*: $\cos^2\gamma = \cos^2\Psi / (\cos^2\Psi + \cos^2\Delta)$ and $\sin^2\chi = (\cos^2\Psi + \cos^2\Delta)$. This leads to:

$$\langle \varepsilon_e^2 \rangle = \langle \varepsilon_{e\,\vec{n}}^{\,2} \rangle \sin^2\chi = \langle \varepsilon_{e\,\vec{n}}^{\,2} \rangle (\cos^2\Psi + \cos^2\Delta) = A\frac{b_e^2}{\pi^2 R^2} \ln\left(\frac{R}{r_0}\right)(B - 2\cos^2\gamma)(\cos^2\Psi + \cos^2\Delta)$$

$$= A\frac{b_e^2}{\pi^2 R^2}\, ln\left(\frac{R}{r_0}\right)(B(cos^2\Psi + cos^2\Delta) - 2\,cos^2\Psi)$$

$$= \boxed{A\frac{b_e^2}{\pi^2 R^2}\, ln\left(\frac{R}{r_0}\right)(B\,cos^2\Delta + (B-2)\,cos^2\Psi)}$$

Appendix 3: Lambert W function - Demonstration of equation (4.15)

The Lambert W function, noted $W(z)$, is defined as the inverse function of $f(t) = te^t$, $t \in \mathbb{C}$.

Hence, for every complex number z: $z = te^t \Leftrightarrow t = W(z)$.

$W(z)$ is a multivalued function, which possess two branches of solutions for real arguments $z > -1/e$

- The principal branch, noted W_0, is defined on the interval $z \in [-1/e\,, \infty[$. It gives the unique solution of $W(z)$ for $z \geq 0$
- The W_{-1} branch, defined on the interval $\in [-1/e\,, 0[$. It gives a second solution of $W(z)$ for $-1/e < z < 0$. At the junction of both branches, $W_0(-1/e) = W_{-1}(-1/e) = -1$

The Lambert W function can be used to resolve equations of the form $ax\ln(x) + bx + c = 0$, in the following way:

$$ax\ln(x) + bx + c = 0 \quad \underset{X=\ln x}{\Longleftrightarrow} \quad aX\exp(X) + b\exp(X) = -\mathrm{c}$$

$$\Leftrightarrow \quad \left(X + \frac{b}{a}\right)\exp(X) = -\frac{\mathrm{c}}{\mathrm{a}} \quad \Leftrightarrow \quad \left(X + \frac{b}{a}\right)\exp\left(X + \frac{b}{a}\right) = -\frac{\mathrm{c}}{\mathrm{a}}\exp(X + \frac{b}{a})$$

$$\Leftrightarrow \quad X + \frac{b}{a} = W\left(-\frac{c}{a}\exp\frac{b}{a}\right) \quad \Leftrightarrow \quad \ln x = W\left(-\frac{c}{a}\exp\frac{b}{a}\right) - \frac{b}{a}$$

$$\Leftrightarrow \quad \boxed{x = \exp\left(W\left(-\frac{c}{a}\exp\frac{b}{a}\right) - \frac{b}{a}\right)}$$

Appendix 4: Demonstration of equations (4.19) and (4.20)

For a screw dislocation, using equations (4.8),(4.10) and (4.18):

$$\langle|\varepsilon_s|\rangle = \sqrt{2/\pi}\,\sqrt{\langle {\varepsilon_s}^2\rangle} = \sqrt{\frac{2}{\pi}\,\frac{b_s^2 sin^2\Psi}{4\pi^3 R^2}\ln\left(\frac{\mathrm{R}}{\mathrm{r}_0}\right)} = \sqrt{\frac{2}{\pi}\,\frac{4\rho_s b_s^2 sin^2\Psi}{4\pi^3}\ln\left(\frac{1}{2\mathrm{r}_0\sqrt{\rho_s}}\right)} = \alpha_s(\rho_s)\sin\Psi$$

For a screw dislocation, the Burgers vector $\overrightarrow{b_s}$ is oriented in the direction [0001] or $[000\bar{1}]$. Hence, the angle Ψ between the normal of the diffracting plane and the Burgers vector is either equal to the inclination χ of the diffracting plane with respect to the surface, or to $(\pi - \chi)$. Hence, we have:

$$\boxed{\langle|\varepsilon_s|\rangle = \alpha_s(\rho_s)\ sin\,\chi}$$

For an edge dislocation, we will use the angles defined in equation (4.6) and **Figure A.1** of **Appendix 2**.

Using equations (4.6) and (4.9), for the first edge dislocation system $(\overrightarrow{b_{e1}}, \overrightarrow{S_{e1}})$:

$$\langle {\varepsilon_{e1}}^2\rangle = \frac{5b_e^2(2.45cos^2\Delta_1 + 0.45cos^2\Psi_1)}{64\pi^2}\,4\rho_e\ln\left(\frac{1}{2\mathrm{r}_0\sqrt{\rho_e}}\right)$$

Geometrically, $(\cos\Delta = \sin\chi\sin\gamma)$ and $(\cos\Psi = \sin\chi\cos\gamma)$, which leads to:

$$2.45cos^2\Delta + 0.45cos^2\Psi = \sin^2\chi(\,2.45\sin^2\gamma + 0.45\cos^2\gamma) = \sin^2\chi(\,2\sin^2\gamma + 0.45)$$

Hence:

$$\langle {\varepsilon_{e1}}^2\rangle = \frac{5b_e^2(2\sin^2\gamma_1 + 0.45)}{64\pi^2}4\rho_e\ln\left(\frac{1}{2\mathrm{r}_0\sqrt{\rho_e}}\right)\sin^2\chi = K_1(\rho_e)(2\sin^2\gamma_1 + 0.45)\sin^2\chi$$

As we take $\langle {\varepsilon_e}^2\rangle$ as the average value of the mean squared strain of the three systems, if we write $\gamma_1 = \gamma;\ \gamma_2 = \gamma + \frac{2\pi}{3};\ \gamma_3 = \gamma - \frac{2\pi}{3}$:

$$\langle {\varepsilon_e}^2\rangle = \frac{K_1(\rho_e)}{3}\left[1.35 + 2\left(\sin^2\gamma + \sin^2\left(\gamma + \frac{2\pi}{3}\right) + \sin^2\left(\gamma - \frac{2\pi}{3}\right)\right)\right]\sin^2\chi = \frac{K_1(\rho_e)}{3}\,4.35\,\sin^2\chi$$

Finally, using Equation (4.18):

$$\boxed{\langle|\varepsilon_e|\rangle = \alpha_e(\rho_e)\sin\chi}$$

Abstract

CEA-Leti develops power electronics components with high energy efficiency, based on semiconductors of the III-N group (GaN, AlGaN, InGaN…), in particular in partnership with ST microelectronics. In order to minimize the costs and improve the compatibility with the standards of microelectronics industry, CEA-Leti chose to produce epitaxial thin films of GaN grown on silicon substrates. However, these two materials have large mismatches of coefficient of thermal expansion and lattice parameter. The resulting GaN layers are affected by strong gradients of mechanical stress and dislocation density throughout their thickness. As component performances and wafer fragility are linked to crystalline quality and stress state of these thin films, it is important to have access to effective, rapid and non-destructive metrology tools. To this end, this PhD focuses on the study of GaN layers by X-ray diffraction (XRD), which is an acknowledged and widely used technique for the analysis of epitaxial films. The effect of stress gradient on XRD measurements is an asymmetrical broadening of diffraction peaks. We suggest extracting this gradient by reproducing the experimental XRD signal, by means of a simulation of the diffracted intensity stemming from a distorted crystal. A good agreement between simulations and measurements is obtained when modelling local variations of the strain profile throughout the surface plane. For the quantification of dislocations extending through the thickness of GaN layers, we suggest a simple methodology, based on the measurement of the micro-strain field surrounding the dislocations. The study shows how to use this type of measurement on GaN layers with strong stress gradient. In addition, the results are compared to the dislocation densities obtained with alternative characterization techniques such as transmission electron microscopy, cathodoluminescence or XRD, via an analysis of crystal lattice misorientations. The studies of stress gradient and dislocation density, initially carried out on complete stacks of III-N layers, are enlighten by means of in-depth measurements on progressively etched films of GaN.

Résumé

Le CEA-Leti développe des composants de puissance à haut rendement énergétique à base de semi-conducteurs III-N (GaN, AlGaN, InGaN…), en particulier via un partenariat avec ST Microelectronics. Afin de minimiser les coûts et améliorer la compatibilité avec les standards de l'industrie microélectronique, le CEA-Leti a fait le choix d'élaborer des films minces de GaN hétéro-épitaxiés sur substrat de silicium. Cependant, ces deux matériaux présentent d'importants écarts de coefficient de dilation thermique et de paramètre de maille. Il en résulte des couches de GaN affectées par de forts gradients de contraintes mécaniques et de densité de dislocations dans leur épaisseur. Le niveau de performance des composants et la fragilité des plaques étant intimement lié à la qualité cristalline et à l'état de contrainte de ces films minces, il est important de disposer d'outils de métrologie performants, rapides et non destructifs. A ce titre, les travaux de cette thèse se concentrent sur l'étude de couches de GaN par diffraction de rayons X (DRX), technique reconnue et largement employée pour l'analyse de films épitaxiés. L'effet du gradient de contraintes sur les mesures de DRX est un élargissement asymétrique des pics de diffraction. Afin d'extraire ce gradient, nous suggérons de reproduire le signal de DRX expérimental par simulation de l'intensité diffractée par un cristal déformé. Une bonne adéquation entre simulations et mesures expérimentales est obtenue lorsque l'on modélise les variations locales du profil de déformation le long du plan de surface. Afin de quantifier les dislocations traversant les couches de GaN, nous proposons une méthodologie simple, basée sur la mesure du champ de micro-déformations entourant les dislocations. L'étude montre comment utiliser ce type de mesure dans les couches de GaN à fort gradient de contraintes. En outre, les résultats sont comparés aux densités de dislocations obtenues par des méthodes de caractérisation alternatives, telles que la microscopie électronique en transmission, la cathodoluminescence ou la DRX via l'analyse de la désorientation du réseau cristallin. Les études du gradient de contraintes et de la densité de dislocations, initialement menées sur des empilements complets de couches III-N, sont éclairées à l'aune de mesures en profondeur sur des films de GaN gravés progressivement.